Oscillations in Routing and Chaos

Agostina Palmigiano

From Buenos Aires

a dissertation
presented to the faculty
of Georg-August Universität
in candidacy for the degree
of Doctor rerum naturalium

Advisers: Theo Geisel / Fred Wolf / Demian Battaglia

2017

THESIS COMMITTEE MEMBERS

FIRST REFEREE AND SUPERVISOR
Prof. Dr. Theo Geisel,
Dept. of Nonlinear Dynamics
Max Planck Institute for Dynamics and Self-organization, Göttingen

SECOND REFEREE AND SUPERVISOR
Prof. Dr. Fred Wolf,
Theoretical Neurophysics Group
Max Planck Institute for Dynamics and Self-organization, Göttingen

Prof. Dr. Melanie Wilke,
Dept. of Cognitive Neurology
University Medical Center Göttingen, Göttingen

MEMBERS OF THE EXTENDED EXAMINATION BOARD

Prof. Dr. Alexander Gail,
Sensorimotor Group
German Primate Center, Göttingen

Prof. Dr. Siegrid Löwel,
Systems Neuroscience Group
Johann-Friedrich-Blumenbach-Institute of Zoology and Anthropology, Göttingen

Prof. Dr. Ulrich Parlitz,
Biomedical Physics Group
Max Planck Institute for Dynamics and Self-organization, Göttingen

DATE OF ORAL EXAMINATION:

Contents

0

Preface

The human brain is one of the most complex structures known to mankind, and arguably the most elaborate biological system that ever evolved. Studying such complex machinery whose precision and efficiency we witness in the simplest of acts, is a fascinating challenge. Neuroscience, as a historically rather young discipline, has adopted from the classical divisions of the natural sciences a wide array of experimental and theoretical approaches. A detailed account of the components, from the molecular level to the circuitry, is complemented by more abstract descriptions which aim to dissect the fundamental ingredients of neuronal dynamics. The large variety of approaches and complimentary levels of description add dimensions to the understanding of the brain and constantly reshape our view of the object of study. One among the possible perspectives, and that which was taken in this thesis, is to devote effort to studying classes of models that are broadly constrained by the statistics of the experimentally reported neuronal dynamics, and to investigate their implications on information transmission. Another possible perspective, which composes the last fraction of this work, is to dissect the elements that lead to the emergence of a certain dynamical behavior in models that allow one to make rigorous statements about their dynamics, in the hope that future research can push forward its frontiers.

Neurons in the cortex, when confronted with identical stimuli, respond rather unreliably. It was perhaps with some surprise, that the report of a reliable response to directly injected fluctuating inputs[164] arose, revealing that much of the observed variability derives from the large amount of recurrent inputs that each of the neurons receive[11]. This variability, which is certainly instrumental to the richness and flexibility of our behavioral output, nevertheless renders the general mechanisms underlying information encoding largely inaccessible. Approaches departing from the single neuron focus, which had been leveraged by the success of early mathematical models[123], embraced alternative proposals for the brain's building units and contributed to the exploration and development of population-level approaches[289]. In particular, the emergence and dissolution of coordinated activity at the population level have posed profound questions about its possible use in brain computation. Broad theories involving the role of collective rhythms in representation[71], coordination[267] and communication[216,86] have received as much supporting evidence as sharp criticism, while only few cases have provided compelling evidence for their role.

This thesis aims to shed light on the possible computational capabilities of oscillatory neuronal dynamics by investigating the properties of large heterogeneous networks with delayed interactions. For this purpose, Chapter 1 gives a detailed account of the experimental evidence linking oscillatory neuronal dynamics to behavior, with a particular focus on its role in attention and communication. Further, it reviews the mechanisms underlying the emergence of oscillations in network models, and its dynamical counterpart, the asynchronous irregular state. Finally, a review of the stability properties of these cases is offered.

Chapter 2 composes the first result section of this thesis. We investigated a class of network models in which neurons spike irregularly while the collective activity exhibits an irregular rhythm in the gamma band. This regime, in which short transient episodes of higher synchronization occur spontaneously, reproduces the frequency and power fluctuations found in cortical measurements. In order to determine whether this variability and irregularity presents an advantage or a limitation to flexible information transmission, we profited form small motifs of two or tree interconnected areas. When several circuits with these characteristics are connected by long range excitatory connections, the activity of the areas coordinate to spontaneously give rise to simultaneous gamma bursts of sparsely synchronized activity. Within each gamma burst, the areas transiently phase-lock, reproducing in the short bursts the out of phase locking patterns observed in higher synchrony regimes. Profiting from state resolved information theoretical tools we found that these transient patterns of coherence gate the information flow between the areas. Information flows in a direction determined by the phase relation and with a strength regulated by the fluctuating level of coherence. Externally injected inputs, representing sensory information or feedback from surrounding areas, are transmitted following the paths found by the analysis of the spontaneous activity. Finally, we found that weak external biases can modulate the pattern of relative phases, favoring particular directions of information transmission.

In Chapter 3, we advanced the tractability of large neuronal networks of exactly solvable neuronal models. We developed a framework that allows to study the delay-induced transitions from an initial asynchronous and irregular state to that of collective rhythmicity together with the changes in dynamical stability. Delayed systems, which in general have an infinite dimensional phase space, can be studied in equivalent systems of fixed and finite degrees of freedom. By introducing a single compartment axon for each neuron, delays arise from the extra steps of integration needed for the variable to reach threshold. We find that depending on the action potential onset rapidness and the level of heterogeneities, the asynchronous irregular regime characteristic of balanced state networks loses stability with increasing delays to either a *slow* synchronous irregular or a *fast* synchronous irregular state. In networks of neurons with slow action potential onset, the transition to collective oscillations leads to an increase of the exponential rate of divergence of nearby trajectories and of the entropy production rate of the chaotic dynamics. The attractor dimension, instead of increasing linearly with increasing delay as reported in many other studies, decreases until eventually the network reaches full synchrony. In the final chapter these results are discussed and understood in the perspective offered by other findings. Proposals for future work at the interface of the above perspectives are offered.

Both the possibility of information transmission in short transients of oscillatory activity and the coexistence of high dimensional chaos with perfect oscillatory behavior at the population level might in principle appear unintuitive. Reconciling our intuition with precise technical knowledge is the motor behind each small step in the direction of scientific progress[212], whose tangled paths have alternatively been found by disparate strategies such as specifying, generalizing, or simplifying previous approaches.

1

Introduction

The evolution of the nervous system in mammals lead to a disproportional growth of the cerebrum. The area occupied by its surface grows linearly with brain volume from insectivores to higher primates, leading to a convoluted neocortex for larger brain sizes[124]. This densely packed structure is a few millimeter thick, six layered sheet that occupies the larger fraction of the human cortex. It contains in the order of 10^5 neuronal cells per cubic mm, each forming on average $10^3 - 10^4$ synapses. Neurons in an area, project to tens of different other areas, receiving in turn projections from dozens of areas with probabilities resembling that of a log normal distribution, spanning 6 orders of magnitude[167].

Neurons in the cortex have generally an irregular spiking behavior whose rate can vary several tens of Hz depending on the neuronal type, the area they belong to and the nature of the presented stimulus[231]. This irregular spiking does not arise from single neuron dynamics which have been shown to be reliable[164], and neither does the trial to trial variability that is commonly observed in experiments. It is currently argued that the irregularity of neuronal spiking is a consequence of a dynamic balance of inhibition and excitation[223], an emergent property of the recurrent dynamics that allows for a regime sensitive to fluctuations. At the population level, neurons can engage in collective rhythms across the cortex[48], both in a spontaneous manner or induced by a stimulus. This oscillatory activity is compatible and shown to be coexistent with a dynamic balance[13]. In Figure 1.1, an example of how the collective activity of an intact macaque brain organizes in different areas is shown, exhibiting the high non stationarity and strongly oscillatory nature of brain activity. When looked at closely, irregular spiking from the recorded multi unit activity can be as well observed.

The high dimensionality, the large parameter space and intrinsic complexity of the components and the connections of neuronal networks pose a challenge to deciphering the neural code. Population rates of groups of 100 neurons[224] could respond rapidly and serve a robust, albeit redundant encoding mechanism.

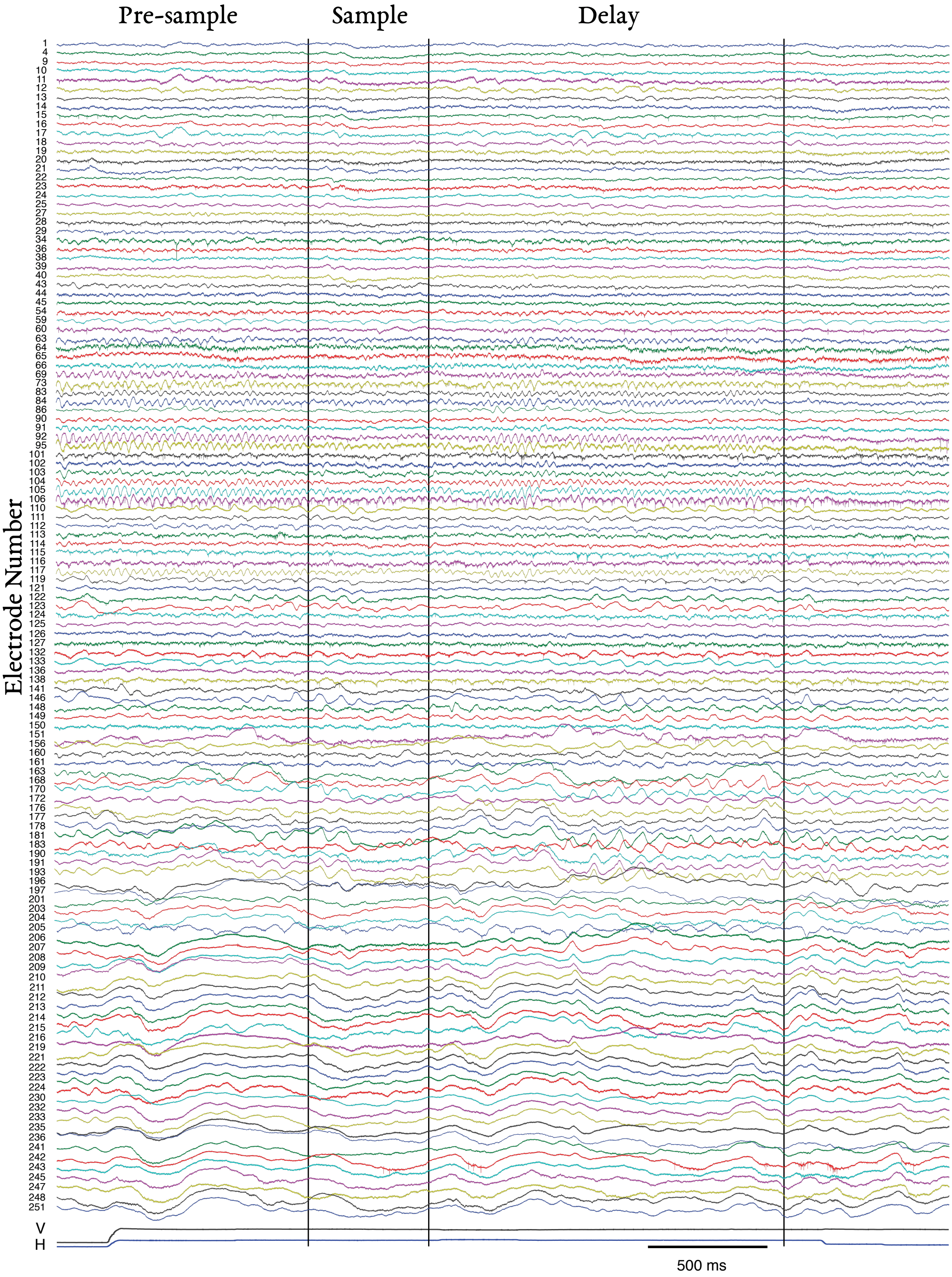

Figure 1.1: Cortical recordings from the macaque brain Raw local field potential (LFP) signals recorded from an macaque hemisphere while it performs a working memory task. Signals at the top correspond to anterior areas, while those at the bottom to posterior areas. The vertical black lines define, from left to right, the pre-sample, the sample, and a delay epochs. Note the highly oscillatory activity of the recordings in all three epochs. Modified with permission from Dotson et al. [64].

On the other end, non error-correcting combinatorial codes[189,219] with high encoding capacity might be too sensitive to small perturbations, given the possibly chaotic or highly sensitive nature of the activity's micro-structure[160]. Regardless of the underlying encoding paradigm, collective oscillatory activity could work as a modulatory mechanism to regulate local excitability and gate or enhance information transmission[86,220,261].

In this thesis we study different types of models of cortical circuits that exhibit collective oscillatory activity, and its role in information encoding and transmission. First, we will show in small motifs of coupled networks that transient coordination between rhythms together with the fluctuating oscillatory power observed *in vivo* act synergistically to flexibly route information between areas (see Chapter 2). Secondly, by means of simplified schemes we will show in delayed neuronal networks that high dimensional chaotic dynamics coexist with collective periodic rhythms (see Chapter 3). In order to contextualize these findings, a review of the possible relevance of oscillatory activity and of the mechanisms underlying the emergence of collective oscillations compose the following sections.

1.1 Functional role of oscillatory dynamics

Rhythmic activity is a ubiquitous feature of the collective behavior of neurons in the brain. Since its discovery by Hans Berger, brain rhythms have been reported in animal species from fish[40] to human[6], and have been related to cognitive, behavioral and perceptual tasks. In the mammalian brain, oscillatory activity has been found in the cortex and subcortical structures, while the behavioral and cognitive correlates of specific rhythms have been shown to be preserved across species[51]. Neural oscillations span more than four orders of magnitude[48]. From this broad spectrum[*], frequency bands aiming to reflect specific underlying cognitive or behavioral process have been defined and utilized for conjecture and analysis of brain function. A guide to the functional roles that have been correlated over time with each specific frequency band is shown in Figure 1.2 and briefly reviewed in the following section.

1.1.1 A brief summary

From the leftmost side of the spectrum, the delta rhythm with frequencies smaller than 5 Hz, is most prominent in non rapid eye movement (NREM, slow wave) sleep, and has been linked to memory consolidation: Performance of human subjects increases after sleeping and correlates with the slow wave activity in task related regions[239]. Also, slow oscillatory transcranial stimulation of human subjects during slow wave sleep improves the retention of declarative memories[168] (see Figure 1.2).

---

[*] This and the following sections will be largely focused, with very few exceptions, on the analysis of oscillatory activity reported from extra cellular recordings (local field potentials (LFP) and multi-unit-activity (MUA)) in mammals, generally rodents, cats or monkeys.

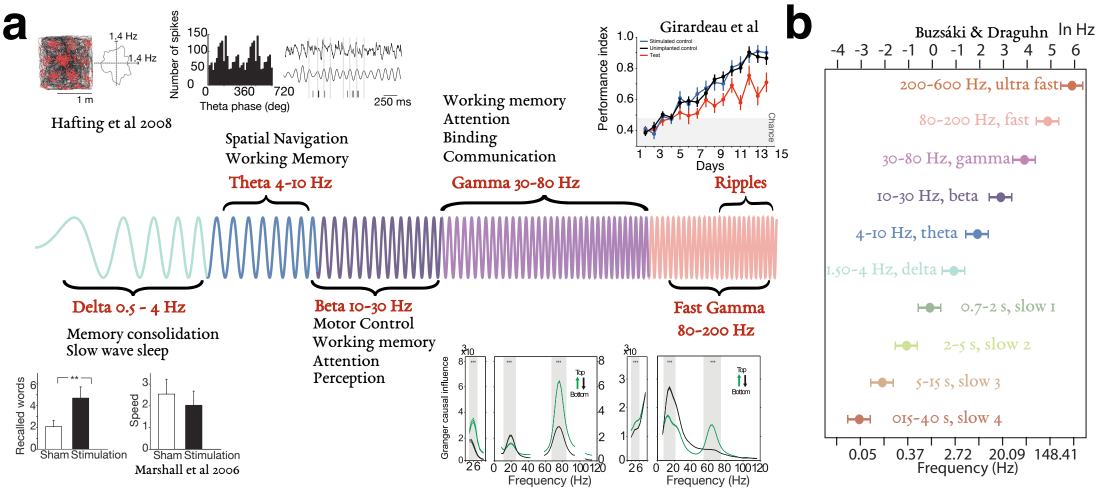

Figure 1.2: Functional role of brain rhythms. **(a)** Scheme representing some of the most prominent behavioral and cognitive roles assigned to each frequency range. Examples from selected studies are also reproduced: i) Delta rhythm: Transcranial stimulation to human subjects during slow wave sleep improves the retention of declarative memories Marshall et al. [168]. Theta rhythm: Phase precession of grid cells in entorhinal cortex is hippocampus independent Hafting et al. [107]. Beta rhythm: Granger causal influences reveal that top down modulations are predominantly in the beta band Bastos et al. [17]. High Gamma: Silencing hippocampal ripples during sleep impaired performances during a spacial memory task Girardeau et al. [93]. **(b)** The frequency span of each frequency band is constant in log Hz. Reproduced from Buzsáki & Andreas [50].

The faster theta rhythm (4-10 Hz) has been extensively investigated and discussed, and much like the gamma and the beta rhythm nowadays, dozens of possible roles have been assigned to it[47] [*]. Although the theta rhythm matches the frequency of whisking and sniffing in rats and the eye movements in humans Colgin[59], much of its role is currently linked to navigation and memory in the hippocampus and surrounding areas. A fundamental phenomena for navigation is that of phase precession by place cells in the hippocampus[184], grid cells in the entorhinal cortex[107] and by cells in medial prefrontal cortex (mPFC)[137], where neurons spike at successively earlier phases of the extracellular theta rhythm as transversing their own firing field. The theta rhythm has also been shown to be involved in working memory tasks[200,158].

The beta band (12-30 Hz) has been classically linked to motor tasks. It is prominent during muscle contraction and holding, and is generally linked to preparatory movements; disappearing during the execution (or even the thought of execution) of a movement[68]. It was shown to be prominent in the olfactory bulb[5] and in the visual cortex[87] in the absence of stimulus, and has been conjectured to be signaling the lack of change (or its prediction)[68]. Recently, work investigating the role of beta synchrony and coherence between pre frontal and parietal areas has shown that patterns of beta coherence can potentially store information about the objects identity during working memory tasks[215], and that modulations of beta coherence can be induced by top-down

---

[*] The distribution of functional roles linked to the theta band over time was presented in [47], more than thirty roles were linked to the rhythm in the 1960s

attention[46]. More recently and more generally the beta rhythm was proposed to mediate feedback (top down) interactions[17].

Gamma synchrony, with frequencies above the 30 Hz, was early described Adrian[5] as the response to odors (replacing prominent beta in the absence of stimulus) in the olfactory bulb. It was later shown that the appearance of gamma activity is a more general characteristic of the response to stimulus (evoked gamma) in the sensory cortices, as shown in the auditory cortex[21], the visual cortex[101], somatosensory cortex[228] and extensively reported afterwards. Induced gamma synchrony and coherence have been linked to attention[87,243,284,46,131,283,103,105,26,102,270,198,106], working memory[159,287,192] and even consciousness[71]. Gamma coherence lies at the core of theories aiming to explain the mechanisms mediating representation and inter-areal communication in the brain, that are central to Chapter 2 and will be discussed in detail in later sections.

Lastly, in the fast (140-200 Hz) range, sharp wave-ripples complexes appearing in the hippocampus during sleep or quiet rest are thought to play a role in memory consolidation. In the rat hippocampus, it was shown that pairs of place cells that active while performing a task are reactivated during post-learning sleep[280], and that the order of activation is preserved[229] in a phenomena called hippocampal replay. Furthermore, electrical stimulation applied to the hippocampus transiently silencing hippocampal ripples resulted in impaired performances during a spacial memory task[93].

As a closing remark, we consider it important to underline that in all but a few cases, experimental neuroscience has assigned functional roles to oscillatory activity by means of conditional experiments, as the ones summarized above. An animal is restricted to a particular behavioral state and conclusions of how the brain might either represent, store or transmit information are drawn by comparing the measured signals with those in control experiments. As stated by Varela et al,[267] “ The evidence available so far regarding the function of synchronization is only correlative.” [*]

1.1.2 Neuronal assemblies and gamma synchrony in representation

Experiments trying to unveil the role of gamma synchrony in visual processing showed that neurons within a cortical column, in either striate (primary) or extra striate visual cortices of the cat, and responding to the same stimulus (orientation or direction) engage in zero-lag gamma synchronization[101]. This stimulus specific synchronization in the millisecond range, measured as a multi-unit cross correlation, persisted between neurons in columns that were separated by several millimeters, with non overlapping receptive fields (RF)[100]. These studies also showed that synchronization was strongly enhanced when the same object covers both RFs compared to when two identical stimuli with the same characteristics are shown[100]. Inter-areal synchronization was further observed

---

[*] The quote continues: “ There is no direct proof that synchrony leads to changes in behavior when it is selectively altered. Such direct evidence has only been obtained in the olfactory system of insects. Stopfer et al[240] showed that odor discrimination deteriorates if synchronization patterns among olfactory bulb cells are disturbed. The search for similar evidence in the vertebrate brain is a daunting challenge, but future studies in this direction are a priority.” .

between neurons belonging to different areas, neurons in striate cortices present zero lag synchronization with those in exra-striate areas[70]. Moreover, in neurons belonging to the same area but located in different hemispheres, synchronization followed the same rules and was disrupted by sectioning of the corpus callosum[69].

These facts taken together, that i) synchrony is stimulus specific and that ii) inter-areal synchronization is strongly enhanced where a single stimulus spans both RFs compared to when two identical ones are presented, suggested that synchrony, both in the cat and the awake macaque[145], is sensitive to global stimulus features. These findings led to the hypothesis that neurons encoding the same stimulus form assemblies that are bound together by synchrony to form a representation of objects in the visual field and is known as the temporal correlation or the temporal binding hypothesis. Synchrony, would be the mechanism underlying integration of distributed cortical representations accounting for the perception of a single object. Although the finding of synchronization-mediated neuronal assemblies that codes for a particular feature continues to receive experimentally evidenced support[45,49,116], a key prediction of the temporal binding hypothesis successfully shown to hold in the anesthetized cat[54] failed to be reproduced in the awake monkey[245,157].

1.1.3 Synchrony in selective visual attention

The role of gamma synchrony, independently of the interpretation involving figure ground segregation and binding, could be seen as a mechanism for enhancing synaptic integration. Synchronous spikes with precision in the mili-second range enlarge the efficacy in driving a post synaptic neuron[9,259,238], and it could be conjectured that attention enhances synchrony among neurons coding for the attended stimulus as a means to facilitate its transmission. Prior to any experimental evidence, a model by Niebur & Koch[182] exploiting this idea and based on the temporal correlation hypothesis, showed that without changes in the mean firing rate of a lower area (V2, see Fig. 1.3), synchronous firing of the neurons coding for the attended stimulus in V2 would not only more effectively drive V4, but silence those inputs related to the unattended stimulus. This work motivated the first experimental work relating attention and synchrony, revealing that attention modulates the neuronal synchrony of firing in the somatosensory cortex of the macaque[236].

In the visual cortex, gamma synchrony in the context of selective attention was first investigated as an alternative or a complement to the biased competition theory (BCT) of selective visual attention. This theory arose from the observation that when attention is directed to one among other objects *within the same* RF, the firing rate response measured in extra-striate cortex (V4 or MT) equals that measured when only the attended stimulus is present; as if attention would *shrink* the RF of the neuron around the attended stimulus[176,254]. The biased competition theory states that stimuli inside a single receptive field *compete* for representation and that attention to a particular stimulus *biases* that competition to favor that relevant to behavior[63]. The experiments as well show that when stimuli do not compete for representation in the same RF, the firing rates in the ventral areas are unaffected by attention unless several distractors are present[176,177].

The fact that attention does not always modulate the firing rate of the attended stimulus in the presence of distractors outside the considered RF constrains the reach of the biased competition theory. BCT would ultimately have to rely on the unattended objects to be sequentially filtered out in later stages of processing, were RFs are large enough to cover a substantial portion of the visual field, effectively bringing all present stimuli to be in competition. These facts led to the search of alternative and possibly complementary mechanisms. Fries and collaborators[87] showed in the extra striate area V4 of the awake monkey that when attention is directed to one of two presented stimuli with non overlapping RFs (see Figure 1.3), synchronization (measured as spike-field coherence [*] and not only cross-correlations) is larger in the signal of the attended stimulus over the non attended one, even though no difference in their firing rates is appreciable in the first 500 ms[87].

That study was the first one to show that only neurons representing the attended stimulus exhibit enhanced synchronization and led to the conjecture that the local changes in synchronization may serve to amplify behaviorally relevant signals in the cortex[87]. Following analyses on those same experiments revealed that the spike-field coherence value was not only high during attention, but that in trials when coherence was high, the monkey would perceive a change in the stimulus faster, and then that spike-field coherence could work as a predictor of the speed of change detection[284].

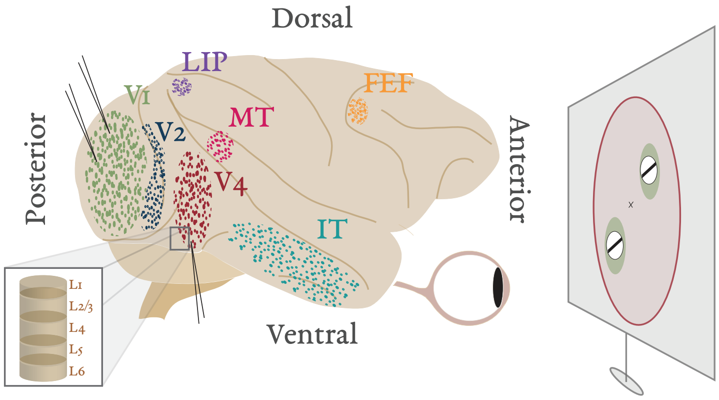

Figure 1.3: Some relevant brain areas for the study of the attention. Cartoon of a macaque brain with different areas shaded in colors (no exact design is intended) in a typical experimental set up for selective attention. From posterior to anterior, ventral pathway : Primary visual cortex (V1), Visual area V2, Visual area V4, Inferior Temporal lobe (IT). Dorsal pathway: Primary visual cortex (V1), Middle Temporal area MT, Lateral Intra-parietal Cortex (LIP). In the frontal lobe, the Frontal Eye Field (FEF). The inset shows the layered structure of the cortex. The screen shows two visual stimuli, as in a classic selective attention tasks. Each stimulus is enclosed by a green area representing two non-overlapping V1 receptive fields (measuring electrodes indicated over V1), and a red area, corresponding to a larger V4 receptive field.

Studies focusing on experimental configurations enforcing sustained attention[243] showed that the gamma power in macaque's V4 was accordingly modulated with the attentional demands of the task. A later study focusing on laminar differences Buffalo

---

[*] Spike Field coherence as used in[87], is defined as the power spectrum of the spike-triggered average normalized by the mean power spectrum over the LFP segments used to obtain the STA

et al.[38] showed that spike-field coherence (taken as a measure for synchronization) in the gamma range was predominant in superficial layers, while in the deep layers, low frequency synchronization predominates. In that study it was further shown, that attentional mediated changes in coherence in V1 and V2 are non significant [*], while they are in the gamma band in the superficial layers of V4 and in the alpha band in the deep layers of V4.

1.1.4 Inter-areal coherence in attention and communication

The studies of attention in the context of monkey electrophysiology accompanied the course of the field of human perception and attention. The latter, which had largely embraced the role of oscillations as a mechanism for long range coordination, advanced on the premise that areas communicate between each other by means of coherence between the population rhythms[210,267]. In particular those studies underscored the need and advantages of implementing tools that allow one to separate the contributions from the power fluctuations and those arising from phase locking[151,267,210], confounded in the coherence measure[†]. An early indication of the link between phase synchronization and attention was made in a magnetoencephalography study reporting that a difference in phase synchronization is seen in humans while performing an attentional blink[‡] task:

> *Our results reveal that communication within the fronto-parieto-temporal attentional network proceeds via transient long-range phase synchronization in the beta band.*[104]

This work already brings together the core concepts of what would later be coined as communication-through-coherence hypothesis (CTC). The hypothesis, as postulated by Fries[86], states that different, in principle distant populations of neurons can flexibly communicate depending on the patterns of phase locking of their oscillatory rhythms, and builds on two facts[86] : i) that neuronal populations do engage in oscillatory activity, and ii) that this oscillatory activity provides excitability and sensitivity peaks effectively creating windows enabling communication when aligned, and disrupting it when not [§].

---

[*] It has been previously found that gamma spike field coherence and power are decreased by attention in V1[57]

[†] The complex coherence γ_{xy} between two signals X and Y is the normalized cross spectrum:

$$\gamma_{xy}(\omega) = \frac{S_{xy}(\omega)}{\sqrt{S_{xx}(\omega)}\sqrt{S_{yy}(\omega)}} \tag{1.1}$$

Where $S_{xx}(\omega)$ is the power spectral density (the Fourier transform of the autocorrelation function) and $S_{xy}(\omega)$ is the cross spectral density (the Fourier transform of the cross-correlation function) Coherence, in this complex form can have larger values due to large phase locking or due to amplitude covariance, making the separation between this two contributions hard[151]. The measure called coherence as used in neuroscience is usually the real valued function $C_{xy}(\omega) = |\gamma_{xy}(\omega)|^2$.

[‡] Attentional blink is the phenomenon that human subjects are unable to report the presentation of a second object when the first one was presented less than 400 ms before

[§] Similar proposals and conclusions had been drawn in other (earlier) studies, detaching the role of gamma oscillations from representation towards a modulatory role helping to gate or regulate information flow. From work investigating the role of gamma oscillations in temporal coding in the hippocampus:

Correlational evidence for this hypothesis was first presented in the context of cortico-spinal interaction[220]. This work showed that coherence between motor cortex activity and electromyogram signals in human subjects correlates with the subject's readiness to respond, showing that coherence can be a predictor of the subject's reaction times. In the context of attention in monkeys[213], inter-areal (beta) spike-spike coherence in the dorsal pathway (between LIP and MT) is enhanced by attention. This work interestingly showed that the spikes of LIP preceded those of MT, as expected for a top down process. Further work, focused on the differences between the inter-areal coordination between LIP and frontal areas[46] in processes involving both bottom-up and top-down attention. In a scheme composed of two different attentional tasks i) visual pop-up (related to bottom-up attention) or ii) visual search (related to top-down attention), it was revealed that LFP-LFP coherence between LIP and frontal areas is enhanced by attention in the gamma range for the visual pop-up case, and enhanced in the beta band during the visual search task. This work importantly highlighted that information transmission between different hierarchical stages of processing could profit from different bandwidths depending on the top-down or bottom-up nature of the task.

Inter-areal coherence in the context of attention in the ventral stream[103] reported that inter-areal spike-field coherence and LFP-LFP coherence between V4 and FEF were significantly modulated by attention in the gamma band, and that they influence each other bi-directionally, as revealed by Granger Causality[*]. Interestingly, the firing rate in FEF is the first measure to be modulated by attention, followed by an increase in the gamma power of V4. Causal influences from FEF to V4 are faster than those from V4 to FEF, evidencing the prominent role of top-down processing in attention[†]. Further evidence in this direction was provided by simultaneous recordings along the ventral stream, where it was shown that firing rates in V4 were modulated by attention

---

> *In other words, it is the temporal relationship of firing patterns between communicating areas that dictates the responses of target regions [...] The present observations demonstrate that inhibitory gamma oscillations can powerfully gate afferent inputs to oscillating areas. This gating is dependent on the timing of the afferent input relative to the local population oscillation and is stable throughout a broad range of input amplitudes.*[41]

And from work reviewing the role of synchrony in information flow in the brain :

> *Synchrony is another form of temporal relationship between neurons that has been intensely studied. As with 'oscillations' and 'rhythmic activity', the term synchrony encompasses a spectrum of neuronal behaviors with various spatial and temporal scales. Here, we will label all of these phenomena as temporally correlated activity [...] We propose that correlations could be controlled independently of firing rate and that this would serve to regulate the flow of information rather than its meaning*[216]

[*] Granger Causality measures the reduction of unexplained variance of a process x at time t when considering only the past values compared to when also the past values of a process y are included. Significant Granger Causality is used here and elsewhere as a synonym of causal influence.

[†] FEF having faster responses than V4 was also reported in a feature-attention task, in which no frequency dependence was analyzed[290]

more strongly and earlier than those of V2, and those of V2 than those of V1[39].

Regarding the role of the thalamus, studies directed to unveil the interaction between the Pulvinar and the attentional network in the ventral stream, have arrived at somewhat different results. On the one hand, analysis of the delay period (i.e. when only a spatial cue is presented), found only a direct causal influence from the Pulvinar to both V4 and TEO in the alpha band[214]. On the other hand, in a classic attentional task with a target and two distractors (as that shown in Figure 1.3), it was shown that spike-field coherence between V4 spikes and the LFP signals in either IT or the Pulvinar are both significantly modulated by attention[291]. Causal influences measured with granger causality are significantly increased by attention from V4 to IT and from V4 to the Pulvinar only in the gamma band.

Although the above studies showed that attention modulates inter-areal coherence in a variety of configurations and areas, and that directed influences between areas are frequency localized, the core statement of the CTC hypothesis, that areas communicate aligning windows of excitability by establishing suitable phase relations, was only later directly addressed. Grothe et al[105] showed in a task requiring sustained attention that V1 and V4 LFP signals have transient periods of significantly increased phase locking only when the overlapping receptive fields of those areas enclose the attended stimulus. A follow up study, that will be used as a base for the models described in the second Chapter of this thesis, manipulated independently the luminance of the continuously morphing shapes used as stimuli[106]. The study showed that the spectral coherence between the LFP of V4 and the luminance of the stimuli was significant only for the stimulus that was being attended. This constrains the understanding of the mechanisms underlying attention, by showing that the non attended stimulus is already underrepresented in the activity of the V4 population. They further showed, via a simple phenomenological model, that gamma coherence solely as a routing mechanism can explain the selective spectral coherence between the attended stimulus and the V4 LFP. It as well predicts that the mechanisms underlying the underrepresentation of the non-attended object in V4 might be mediated by a mixture of anti-phase and drifting phase relations between upstream and downstream areas[106].

Further insights into the nature of oscillation mediated communication between areas was obtained from detailed layer-resolved measurements. As mentioned above, superficial layers preferentially synchronize in the gamma band while deep layers do so at lower frequencies[38]. The potential role of the frequency segregation in feedforward and feedback pathways was addressed in studies performing simultaneous recordings in distant areas over the visual hierarchy. These works unanimously stated in their conclusions that feedforward pathways, targeting the granular layer (layer 4) are mediated by gamma synchronization while feedback pathways, originating from deep layers and targeting superficial and deep layers of upstream areas are mediated by lower (alpha-beta) frequencies[209,17,261].

1.1.5 Causal links between oscillations and behavior

Compared to the vast amount of correlative evidence directed towards elucidating the role of coherence in situations of assumed enhanced communication (like attention), only a small body of work reports on the behavioral correlates of direct manipulation of the level of synchrony or coherence. This is in principle due to the intrinsic difficulties of independently manipulating the level of synchronization while leaving other possible confounded variables unaltered. A new avenue for controlled experimentation is due to optogenetic targeting of fast spiking (FS) interneurons[198], linked to the generation of gamma oscillations[16] (see section 1.3.1). Studies in anesthetized mice showed that inhibition of fast spiking interneurons suppresses gamma oscillations[232] and that optogenetic stimulation of that neuron type amplifies gamma oscillations[232,53]. Rhythmic stimulation of FS cells in the gamma band increased the LFP power in those frequency ranges, independently of the spiking probability (which can be independently manipulated by the intensity of the light impulses), showing that the oscillation frequency is a resonant-like network property[53]. Importantly, by rhythmically stimulating the FS cells in barrel cortex, it was also revealed that a whisker deflection evoked a response in regular spiking cells depending on the phase of the gamma stimulation. That study[53] demonstrates that the ongoing rhythm of a local circuit modulates the evoked response to stimuli, by maximizing its temporal precision in the release of inhibition and hindering it in its peak. A follow up study[228], reproduced these results in behaving mice and further revealed that FS gamma stimulation increases the mean detectability of hard to detect naturalistic stimuli. This result, in line with that showing that impaired oscillations in the antennal lobe of the locust hinders the discrimination of similar odors[240], suggest that when finer perception is required, cognitive modulations like attention might profit from oscillatory mechanisms[198].

1.1.6 A critical view on the role of gamma synchrony and coherence

The role of gamma oscillations in representation and routing as part of the binding and the communication through coherence hypotheses respectively, were prone to much skepticism and criticism, presumably because of the generality of their claims and the lack of detailed technical insights to support it. The concerns are detailed below, and while the first four focus on the nature of the induced gamma in primary visual cortex, the last two specifically refer to issues raised by the CTC hypothesis in attention and as a general communication scheme, respectively.

The concerns below, stem from a discrepancy between the supposed requirements that neuronal signals should accomplish for the communication through coherence hypothesis to operate in the brain and what is observed experimentally. In Chapter 2, we will incorporate some of the characteristics below described, which at first sight might appear as a limitation for the usage of oscillatory coherence in information transmission, and show that these features might actually facilitate the flexible gating of information flow.

i) Transient nature of gamma episodes

When a preferred visual stimulus is presented, the primary visual cortex exhibits a broadband increase in gamma power, which is not phase locked to the stimulus but *induced* by it[209,132,204,133]. This increase compared to baseline, is evident in the power spectra in a single trial basis. The time-dependent analysis usually performed in most of the studies that report induced increase in gamma power, involves a time-frequency analysis with a sliding window and consists an average spectrogram across many trials[141,157,204,203,286]. This type of analysis might falsely suggest a sustained and constant gamma increase during the stimulus presentation. This however, is far from the structure that can be seen in single trials where episodes of higher power have an average duration of 100-120 ms[286] in the awake and the anesthetized macaque. The fact that gamma power is localized in short epochs, constrains the temporal extent of gamma-mediated information processing in the brain, which would be restricted to only a few gamma cycles.

ii) Inconsistent power and drifting frequency of LFP signals

A second type of criticism, emphasizes the irregularity of the gamma oscillations observed in the cortex. It can be argued, that the lack of regularity of the gamma rhythm might preclude a proper alignment of communication windows, and that for gamma rhythms to be suitable for binding or communication they should present clock-like characteristics[44,43,286]. Single trial spectrograms as shown by Shapley and colleagues[286,43,44], have a fluctuating and inconsistent power, and a drifting frequency in the gamma band. In particular, work by Burns et al.[44] directed towards inspecting the regularity of these rhythms showed that gamma oscillations are far from periodic signals: the frequency and duration of transient episodes of elevated power in the gamma band (gamma bursts) are identical to those obtained by randomly shuffling the phases in Fourier space, both in the anesthetized[43] and the awake fixating macaque[286].

iii) Low induced gamma power

The LFP signals measured in the mammalian cortex in the absence of stimulus, as well as the EEG of primates, have a $1/f$ spectrum[48]. As previously mentioned, when a visual stimulus is presented, LFP recordings in the macaque V1 usually exhibit a modulation in the gamma frequency range[209,132,204]. This modulation nevertheless, lies on top of the characteristic $1/f$ spectrum, where low frequencies always have a larger power which can be enhanced or reduced comparatively depending on the behavioral task[17,103]. The fact that gamma fluctuations are small (10-20 μV on average) and that account for less than 10% of the total LFP power[132] suggests a weak role for gamma coherence in brain processing, and lead to presume that this spectral modulation is just a natural consequence of the imbalance of excitation and inhibition produced by increased excitation at the presentation of the stimulus[203,44,132,133,135].

iv) Stimulus dependence of gamma power

Gamma synchrony in the macaque V1 seems to be either better or solely induced by Gabor patches (gratings). The sole modification of superimposing two Gabor patches with different orientations and different contrasts (a plaid), disrupts the spike-spike synchrony in the gamma band observed in all the experiments agreeing with binding by synchrony[101,100,70,69], and it considerably lowers and shifts the gamma peak in the LFP[157]. This has not only been observed in macaques, but studies of human visual cortex report similar results[119]. Furthermore gamma synchrony might not be induced under naturalistic stimulation. Disparate results were obtained by different groups in this respect. While some[36] report a consistent increase of the narrow band gamma peak during naturalistic stimulation of the macaque V1, this is only found for specific natural stimuli in the human[119].

Besides the differences observed in the gamma activity of V1 depending on the type of stimulus, gratings or naturalistic, strong differences were as well observed in the neuronal signals depending on the characteristics of the gratings themselves:

- *The gamma power and peak are contrast dependent*[203,135]. Both the gamma peak and the power, together with the firing rate increase with stimulus contrast[135]. Despite these dependencies, the phases of spikes with respect to the LFP signal remain unaltered[203]. Time varying contrast induces dynamic changes in the gamma power and frequency that is history dependent, and furthermore, spatially varying contrast causes nearby assemblies to oscillate at different frequencies, unlike what is observed for a fixed contrast grating[203].

- *The gamma power and peak are depending on noise masking.* Similar changes are observed when masking the gratings with noise. Both the peak and the gamma power decrease with increasing noise masking, although in this case a modulation of the firing rate is not observed[135].

- *Gamma power and peak are dependent on the size of the grating*[132,204,133,135]. This is a particularly interesting manipulation, because increasing the size of the grating increases the power and the peak value of the induced gamma, but reduces firing rates due to surround suppression. Profiting from this difference, it was shown that there is a high correlation between the rate signal and the high frequency components of the local field potential (above 100 Hz) Ray2011.

v) inter areal phase relations do not match the expected synaptic delay

If collective oscillatory activity modulates network excitability, coordination between rhythms could align excitability windows and thus provide a flexible mechanism for routing. For the excitability windows to be *aligned*, a first intuitive constraint would be that the phase difference between the distant LFP rhythms ($\Delta\Phi$) times the average period (T) of the oscillation, is in the order of the inter-areal synaptic transmission delay d:

$$\delta := T\Delta\Phi = d \tag{1.2}$$

The estimation of the (mean) delay d is generally defined as the peak cross correlation between spikes in the different areas. Although there seems to be general agreement that spikes in an area usually spike in the trough of the local LFP signal[165,65,134,204], whether LFP-LFP delay matches the transmission delay d is still under active debate. Paired recordings between V1 and V2 in experiments designed to address this question, showed that the mean phase relation between V1 and V2 LFPs band pass filtered between 30 and 50 Hz is 90°, corresponding to a delay δ_{V1-V2} of 5-8 ms, much larger than the synaptic delay d of around 3 ms that they report[134]. Another study, investigated the inter-areal phase shift between V4 and FEF and found it to be between 8-13 ms similar to the estimated synaptic delay d of 10 ms[103].

A study by Vinck et al.[269] shows that contrary to other works reporting that spikes usually concentrate on the trough of the LFP, argue that actually spikes phase-lock to the rhythms depending on the orientation preference of the spiking cell or depending on the power of the rhythm, and show a wide-spread distribution of spike-LFP locking values. Other study by Dotson et al.[65], report that the LFP-LFP phase (in the beta band), in frontal and parietal areas, is bi-modally distributed with peaks at 0° and 180°, and that a full phase flip between rhythms can occur depending on the behavioral stage of a task.

Whether the inter areal delay is uniquely determined by the synaptic delay, and the implications of that difference on inter areal communication are still under debate. The perspective that can be added to the above exposed views, is that the effective time that it takes for a signal to propagate from one area to another might be effectively longer than the transmission delay d, and will generally depend on the response properties of the population per se. Work directed towards quantifying the time it takes for a stimulus to elicit a response in areas in the ventral stream[218] provided an estimate of the mean effective latency between two areas showed that the mean response in V1 is at 66 ± 10 ms, while in V2 it is 88 ± 21 ms, with a 16 ms difference in the mean, different from the 3 ms of synaptic delay, and form the 5-8 ms calculated form the phase lag[134].

vi) Lack of attentional modulation in V1

Beyond concerns regarding the nature of the induced gamma in primary visual cortex, there is no agreement on whether attention can modulate the gamma power in V1. While some studies[261] find an increase of gamma power and coherence with attention, some other[26] find either no change or a reduction[120,57]. Although the differences might be explained by changes in the stimulus paradigm, the concern that the induced power is at least not robustly modulated by attention still holds.

All the points raised above, in particular the stochastic and transient nature of gamma oscillations *in vivo*, appear hard to reconcile with a functional role of oscillatory coherence. Models incorporating these features and investigating their impact on inter-areal information transmission will be presented in Chapter 2

1.2 Theory of collective oscillations

Concomitant to the study and analysis of synchronization of neurons in the brain, efforts have been devoted for more than five decades to theoretically study the emergence of collective synchrony. Much of the early work was done in reduced and simplified systems of coupled oscillators, and aimed to have an overall understanding of the emergent dynamics of networks of periodic units. An early study by Winfree[281] laid the foundation of the study of a large number of almost identical coupled oscillators. Although providing substantial insight, a general theory for the study of collective synchronization under the weak coupling assumption only arrived with Kuramoto[150]. He showed that the dynamics of any network of coupled oscillators with natural frequencies ω_i, drawn from $g(\omega)$ have a universal form where the rate of change of the individual phases is proportional to a force that depends only on the pairwise difference between the oscillator's phase and its neighbors. Advancing on Winfree's intuition that mean field like simplifications in which the phases interact with the rest of the network only through a collective rhythm could strongly simplify the analysis, Kuramoto defined an order parameter r to study the simplest version of the model. The critical value of the coupling K at which the network shows synchronized collective behavior could be obtained analytically, although it was another 20 years before a rigorous derivation of the low dimensional dynamics of the order parameter was obtained[191].

1.2.1 Intuitions and the two neurons case

A step forward in the understanding of collective phenomena and towards a mathematical study of the interaction of neuron-like oscillators was taken by Mirollo and Strogatz[172]. Departing form the phase coupled approach by Kuramoto, they showed that a fully connected network of integrate and fire neurons with instantaneous excitatory pulse-like (delta) connections [*] always synchronizes. Excitation was then thought to be the required ingredient for network synchrony, and inhibition, specially delayed inhibition, was suspected to serve a stabilizing role of the asynchronous state[2,76]. A systematic study of the phase locking properties of two neurons depending on the sign and the time course of the synaptic current, revealed that contrary to this belief, for the leaky integrate and fire neuron (LIF[†]) non-instantaneous excitatory coupling leads to either

---

[*] By delta connections it is meant that the input current to a neuron at time t as a consequence of an incoming spike at time t_0 is modeled as $I \propto \delta(t - t_0)$.

[†] The LIF neuron is defined as $\tau_m \dot{V} = -V + I$, where τ_m is the membrane time constant, V is the voltage and I is a constant input current. For the model to be completed, a threshold V_t and a reset V_r voltage values have as well to be defined.

anti-phase or out of phase locking, approaching the zero lag synchrony only in the limit of instantaneous coupling[263]. This same analysis on inhibitory synapses showed that zero-lag synchronization is stable for inhibitory connections, not only for the simple integrate and fire neuron but as well for both a generic phase reduction and the Hodgkin-Huxley neuron [*][263]. Furthermore, even arbitrarily small delays give rise to stable, in phase synchrony when the interaction is an inhibitory delta pulse, as opposed to the out of phase locking obtained in the excitatory case[76,77].

1.2.2 Fully connected inhibitory networks

Generalizing these results to fully connected networks, the synchronous solution is always stable in the presence of *slow inhibitory coupling*, and for fast synapses it coexists with clusters of synchronized neurons, whose number increases as the coupling time constant becomes shorter, leading to an essentially asynchronous state for fast coupling[262]. For phase oscillators with instantaneous (delta) but delayed interactions, it was shown that the number of clusters formed in this case is inversely proportional to the delay of the interaction[76,77], therefore diverging for instantaneous coupling. It is worth mentioning that this cluster-like configuration allows for a population frequency *higher* than the single neuron rates, and is commonly observed in inhibitory networks, is stable and robustly preserved for a mild level of noise[96] or frequency heterogeneities[285,181]. By means of a powerful approach[34,90] Brunel and Hansel[32] made a comprehensive analysis of a fully connected inhibitory network with delayed interactions in the presence of noise. They calculated the instability boundaries as a function of the strength of the coupling, the mean firing rate of the neurons, the details of the synaptic coupling and the variance of the noise and explicitly showed, recovering the above results in the limit of small noise, up to which level of noise the n-cluster solutions would be stable. The transitions, obtained for the LIF, the exponential integrate and fire (eLIF [†]) and for a conductance-based model, not only separate the n-cluster regimes from the asynchronous state but they further show that even in these fully coupled networks a regime in which the frequency of the population oscillation is much larger than that of the single neurons, which fire in an irregular manner, can also exist (see section 1.2.6).

1.2.3 Fully connected excitatory networks

As stated by Hansel et al[112], to understand collective states of neural systems, one cannot separate the synaptic properties from cellular properties. A thorough investigation of excitation-induced synchronization in fully coupled networks with non delayed inter-

---

[*] Hodgkin-Huxley neuron refers to the 4-dimensional conductance based model as originally conceived in[123].

[†] The exponential integrate and fire model is $\tau_M \dot{V} = V + \Delta \exp\left((V-\theta)/\Delta\right) + I$ where τ_m is the membrane time constant, V is the voltage and I is a constant input current, θ is the threshold and Δ is a sharpness parameter.

actions revealed that excitation can be synchronizing for fast although not necessarily instantaneous synapses depending on the phase response curve of the neuron[112]. Type I neurons, characterized by an always positive phase response curve, can hardly be synchronized by slow excitatory connections even when the connections are strong. In the particular case of LIF neurons with synapses modeled by an alpha function, it was shown that for short (but not instantaneous) synaptic time constants there is a transition to a non synchronous oscillatory state, known as partial synchronization[262] where neurons fire irregularly with rates *larger* than the oscillation frequency. Type II neurons, on the contrary, can be synchronized if the synapses are fast enough. It was furthermore shown analytically in the weak coupling limit that this is a generic feature of Type I neurons[73]: They preferably synchronize through either delayed or slow inhibition. Type I neurons, transition to tonic spiking via a saddle node bifurcation on an invariant circle, and therefore correspond to neurons with a type I excitability (i.e. they can have achieve arbitrarily small rates). Given that the LIF is also a type I neuron, the above results make more intuitive that the inclusion of delays in the Mirollo-Strogatz scheme (delta coupled excitatory connections of phase oscillators) leads to other firing patterns than a synchronous state[251].

1.2.4 The role of heterogeneity

A further step in understanding synchronization in all-to-all pulse-coupled networks was made by studying the impact of heterogeneities in the neuronal frequencies. Unlike the case in which the coupling is a smooth function of the dynamical variables, in which mild heterogeneity doesn't break the synchrony in the population activity for a high enough coupling[150], heterogeneities introduced in the single neuron parameters of networks with pulse coupled interactions exhibit a wide range of behaviors. In networks of purely excitatory connections in a Mirollo-Strogatz like setting, it was shown that the inclusion of frequency heterogeneities breaks synchrony creating a subset of non-locked neurons, that remains finite even in the limit of vanishing inhomogeneity[256]. When the connections have a non instantaneous synaptic time course, and are therefore not initially in a synchronous state, the progressive increase of heterogeneities initially increases the fraction of locked neurons to a non-zero value, to later decay again. This non monotonic dependence of synchronization on the network's heterogeneity was reported both in integrate and fire[256] as in Hodgkin-Huxley neurons[110]. As discussed in White et al.[275], in an homogeneous network, the synaptic coupling only needs to align the phases of the neurons, while in the mild heterogeneous case, to achieve perfect synchrony it has to both entrain the frequencies and align the phases. White et al[275] showed in a pair of self and mutually inhibited Wang-Buzsáki like neurons [*], that mild heterogeneities could disrupt synchrony in basically two ways: by effective decoupling (asynchrony) or via suppression. They further showed that synchrony in a fully coupled network with

---

[*] The Wang-Buzsáki neuron[285] is a three dimensional conductance based model with fast sodium activation. See next section and Methods of Chapter 2

slow synapses, shown to be stable in an homogeneous configuration, can be also be disrupted by the above mentioned mechanisms. The robustness of synchronization in a looser definition including but not being limited to tight synchrony, was also studied in the weak coupling limit[181]. There it was shown that, unlike in inhibitory networks, excitatory networks could not bear even a small degree of synchrony at high firing rates when heterogeneities were included.

A clarifying view of the effects of heterogeneities in the dynamics of fully coupled networks was presented by Hansel and Mato[111]. They analytically derived the stability boundaries of the asynchronous state as a function of network parameters for mixed excitatory and inhibitory networks of quadratic integrate and fire neurons (QIF [*]). They showed, that for strong inhibitory conductances a transition to spike-spike synchrony was possible, in what they called mutual inhibition mechanisms. In another type of transition, called cross-talk mechanism, the excitatory-inhibitory loop gives rise to oscillations. Although in their fully coupled network they observed that the frequency of the oscillation was smaller than the rate in this case (bursting behavior), these two different routes to synchrony, one in which inhibition is the driving force for the collective oscillation, and the other one, in which excitation is needed to drive inhibition, will be further analyzed in section 1.3 of this chapter.

1.2.5 Synchrony in sparse inhibitory networks

Among the studies focusing on all to all connectivity, an interesting step was taken by Wang and Buzsáki[285] when considering on the one hand heterogeneities in the intrinsic neuronal frequencies, and on the other, in the connectivity. They showed that the synchrony of fully coupled inhibitory networks was fragile under the inclusion of 5% current heterogeneities (inducing heterogeneous firing rates) in a neuronal model with a broad and steep f-I curve [†] known as the Wang-Buzsaki model (WB). While keeping the neuronal firing rates uniform, they showed that there is a minimal amount of connections needed to achieve full synchrony. Under these two types of heterogeneity, the network was only coherent for frequencies (and firing rates) in the gamma range. In the presence of any of this two kinds of inhomogeneity, increasing the synaptic time constant didn't necessarily have a stabilizing effect, contrary to what was shown in the homogeneous case. A systematic and analytically tractable approach was devised by Golomb and Hansel[95]. By means of weak coupling approximation they could derive for the LIF an expression for the minimal amount of connections for which the asynchronous state looses stability in sparse inhibitory networks as a function of the firing rate and of the rise and decay time constant of the inhibitory synaptic coupling, providing an scaling low that keeps the degree of synchrony.

---

[*] The QIF neuron, defined as $\tau_M \dot{V} = V^2 + I$, will be studied in detail in Chapter 3.

[†] The f-I curve is the dependence of the firing rate of the neuron to an increasing input current. Neurons with a Type I neuronal excitability[122] as the one studied here, can achieve arbitrarily low firing rates

The studies mentioned above were no longer concerned with perfect spike to spike synchrony, but rather with the existence of some degree of synchrony, and the conditions to achieve collective oscillations in more realistic settings. Nevertheless, other theoretical work devoted to studying the mathematical aspects of the synchronous state, devoted effort in making rigorous statements about its stability. It was proven that pulse-coupled inhibitory networks with arbitrary connectivity and delayed interactions have a stable synchronous state in models with few constrains on the underlying voltage dynamics[250,249]. Although stable, the synchronous state is not the only attractor of the system. When the connectivity is random (keeping a fixed in-degree), this synchronized state is shown to coexist with a asynchronous irregular state. The inclusion of heterogeneities in the weights in this type of setting breaks the stability of the synchronous state and leads to periodic spiking patterns[62].

Spike-to-spike synchronization might appear to be unrealistic given the large variability of cortical activity. Nevertheless, fast spiking neurons, specially parvalbumin positive basket cells, are abundant, densely connected and can fire approximately once per gamma cycle[52]. These inhibitory subnetworks are believed to have a lead role in the development of neural rhythms[277,16,52]. In the above models, synchronization is sensitive to a minimal number of heterogenous parameters and is driven by a tonic form of excitation, implicit in phase neuronal models. The following subsections explore alternative or complementary mechanisms to the generation of collective oscillations exploring different types of synchronization and larger robustness to heterogeneity.

1.2.6 The synchronous irregular state

Pyramidal neurons in networks engaging in collective rhythms in hippocampal[253,27,278] and cortical[87] networks do not fire regularly in every cycle. Early models of the hippocampus[253] and the cortex[144], succeeded in modeling circuits that emulate this *synchronous irregular* (SI) or sparsely synchronized state, but not in unraveling its mathematical foundation. Brunel and Hakim[30], developed a theory to study the transitions to synchronous irregular states, as well as its behavior in the vicinity of the bifurcation. They studied the instability boundaries of the asynchronous state in sparse inhibitory networks of delta coupled LIF neurons with noisy inputs and delays, and found that the transition to a SI state is given by a supercritical Hopf bifurcation. The population frequency at the transition, is inversely proportional to the delay of the interactions, giving frequencies of the order of 200 Hz, well in the gamma range [*]. An immediate extension to this work to both excitatory and inhibitory neurons in an otherwise identical setting[29], showed that the synchronous irregular state emerges robustly for sufficiently large recurrent inhibition and delays. Interestingly, besides the high frequency synchronous irregular state, there is a low frequency synchronous irregular state, in which the population oscillates with in the alpha-beta band. For some parameter ranges, there

---

[*] They also studied the dynamics in the vicinity of the instability and provided analytical expressions for corrections to the oscillation frequency.

is a fraction of the phase space in which these two regimes overlap resulting in a nested beta gamma rhythm with low firing rates[29].

Extending these works, Brunel and Wang[34], developed a self-consistent framework to generally calculate the frequency of the oscillation of the SI state in more biologically realistic settings. They showed that when including temporal dynamics in the synapse, the frequency of the oscillation of the inhibitory network is a nonlinear function of the rise and decay time of the synapse and inversely proportional to the delay, and most prominently defined by the fast time scales. The inclusion of excitatory connections, generally slows down the oscillation frequency. Depending on the ratios of the inhibitory and excitatory synaptic time constants, different oscillatory regimes can be identified: An inhibition dominated one, characterized by a high 200 Hz frequency, where excitation is slow and hence almost tonic, and a E-I one, where excitation is faster than inhibition, with population frequencies of around 70 Hz. Further extension to account for the differences introduced when moving from an overly simplified model like the LIF to more complex neuronal models like the eLIF or conductance based ones, yielded similar results[90]. The SI state, that naturally accounts for the low firing rates and oscillation frequencies experimentally observed, seems to be of a universal kind given that it can be found for models with great variety of neuronal and synaptic characteristics[90]. The synchronous irregular state is the base of a large body of theoretical work modeling low synchrony network oscillations[143,15,37,56]. It will be used as a basis for the class of models presented in Chapter 2, and a transition similar to that described here will be obtained in a different framework in Chapter 3.

1.3 Mechanisms of gamma oscillations

The insights provided by theoretical work pointing to inhibition as a fundamental mechanism in the generation of collective oscillations was paralleled by the experimental corroboration of such a role. Nevertheless, although the existence of inhibition has been shown to be a necessary condition[82,277,278,52,276,53,228], whether it is a sufficient one for the generation of brain rhythms remains unknown. In hippocampal slices, gamma rhythms can be induced by a variety of pharmacological and electrical procedures. Depending on which one is performed, different conclusions have been drawn regarding the role of excitation have been drawn[16]. While the blockade of GABA_A receptors [*] usually disrupts the induced gamma rhythm[82,277,278,52], rhythms can be sensitive[82] or insensitive[277] to AMPA receptors [†] antagonists.

Two possible mechanisms for the generation of gamma oscillations can be then distinguished[278]. That in which inhibition is necessary and sufficient for the generation of gamma, known as interneuron network gamma oscillation (ING), or that in which the feedback from the excitatory population plays a crucial role, without which the rhythms would be abolished, named pyramidal-interneuron network gamma oscillations (PING).

---

[*] GABA_A mediates fast inhibition.

[†] AMPA is a glutamate receptor mediating fast excitation.

It is worth to point out however, that except in the case of the cerebellum where the principal cells are also GABAergic, or in optogenetically manipulated scenarios, in which fast spiking interneurons can be targeted directly[53,228], these mechanisms might coexist, either spatially segregated or contributing simultaneously.

1.3.1 PING ING models of gamma rhythms

Models of ING synchrony, are usually, but not necessarily, networks of interneurons driven by tonic excitation. Buzsáki & Wang[52] give three conditions for the existence of such a rhythm: i) Mutually connected inhibitory interneurons ii) a time constant provided by $\mathrm{GABA_A}$ receptors and iii) sufficient drive to induce spiking in the interneurons. Models have explored the ING mechanisms in "stripped down"[52] configurations in mainly two forms. One, in which excitation was present only tonically[285,95,244], and neurons fire, like fast spiking interneurons once per cycle giving rise to spike-spike synchrony. The other one, is in which the neurons receive a noisy poisson like input[34], and synchronization is sparse (SI state). In both cases, the collective frequency depends on the inhibitory synaptic time constant and lies in the gamma range. In the second scenario, the frequency, which is much higher than the single neuron firing rates is only weakly independent on the increase of the external excitatory input. Another possible exploration of ING models is that in which there are excitatory neurons in the network, but they play a secondary role. Examples with a tonic drive as in ter Wal & Tiesinga[244] and to some extent in one example in Börgers & Kopell[25] are determined by removing the feedback from excitation to inhibition and verifying that the rhythms still develops. As in the stripped down models, a noisy form of this version also exists[34]. In this case, making AMPA synapses slow enough, excitation reaches tonic levels and leads to an inhibition dominated oscillation.

The PING mechanisms that generate gamma, on the other hand, strongly rely on the role of excitation. Volleys of excitatory neurons drive the inhibitory ones, which should lag the former by a few ms. Heuristic arguments for the existence of a PING state have been outlined by Börgers & Kopell[25]. Their four conditions are: i) that the excitatory neurons are driven well over threshold, ii) E→I connections are strong enough and fast iii) that the inhibitory neurons only spike in response to excitatory neurons iv) I → E connections are strong enough for the inhibitory neurons to synchronize the excitatory ones. It is important to notice, that in some scheme of PING, specially those in which neurons are tonically driven, excitatory neurons also present spike to spike synchrony[25,244]. Noisy schemes of PING, can be obtained both for when the "noise" arises from the random connectivity or from an external source. These models, as developed in[34,90] allow for a deeper mathematical treatment and therefore different regimes can be identified. One, in which inhibition precedes excitation, in which decreasing the AMPA/GABA ratio increases the frequency of the oscillation, and another one, that is consistent with physiology, in which excitation precedes inhibition[13] and a decrease in AMPA/GABA ratio reduces the oscillation frequency as seen in vitro[278]. These models, precisely reproduce the lower spiking of pyramidal cells and the fast spiking of interneurons, while the population peaks at the gamma band. In both cases, noisy and tonic driven PING networks, the cornerstone of the rhythms lies in the feedback connections between excitation and inhibition, E→I and I→E. Regarding the other two types of connections, the role of recurrent excitation (i.e. E→E connections) in the generation of the rhythm is not well understood[25,52]. Recurrent inhibition (I→I connections) on the other hand, could serve to stabilize the rhythm in case the drive is too high[25], although large recurrent inhibition can lead to an ING rhythm instead.

1.3.2 Phase Locking of oscillating neuronal circuits

Neuronal populations as a whole can present in and out-of-phase locking patterns between them depending on the effective sign and delay of their interaction. In the cases in which populations behave like oscillators, their dynamics are well described by its phase evolution on the limit cycle. Small perturbations arising form interactions with other neuronal populations, can be calculated in the *weak-coupling limit* in a framework developed by Kuramoto[150,75]. Battaglia, Brunel and Hansel[19], analytically calculated the phase difference between two delayed rate units coupled by delayed "long-range" excitation. They showed, that depending on the level of inhibition and the ratio between the local and the inter-areal delay, transitions between in-phase and out-of-phase locking can occur, out-of-phase locking being predominant and occupying a significantly larger fraction of the parameter space. They further showed that the phase-locking patterns obtained with the reduced rate model can also be found in both purely inhibitory and both inhibitory and excitatory spiking networks coupled with long range excitatory connections. Further work by Battaglia et al. has shown how to reverse the phase relation of networks oscillating in a out of phase configuration by a strong excitatory pulse, both in rate models[20] and in spiking networks[20,282].

1.4 The balanced state

Among the large variety of dynamical behaviors that are observed in the brain and besides collective oscillatory activity, increasing interest was generated by the fact that neuronal activity, particularly in the cortex, can be highly irregular with statistics closely resembling that of a Poisson process[92]. This high variability, present in cortical circuits whose population can (or not) be embedded in a rhythm, is not due to lack of reliability at the single neuron level[164], indicating that it is due to input fluctuations arising from network interactions[11]. In principle, given that neurons in the cortex receive inputs coming from many different areas[167], these inputs could be expected to be nearly uncorrelated. If the large amount of synaptic inputs, of the order of $10^3 - 10^4$[193] are linearly summed in the soma, the net input to the cell can be expected to have a small variance and a nonzero mean. The small variance ($1/\sqrt{N}$ argument[255]) arises from the central limit theorem, while the non zero mean would result from to the comparatively small number of inhibitory synapses[61]. Constant inputs to neurons generate regular tonic spiking[164], indicating that a small variance on top of a high mean would result in a rather regular spiking output. On the contrary, correlated fluctuations could in principle survive the averaging and provide a source of neuronal variability; but neither the observed correlations in vivo are large enough, and if they were, models exploring that regime result in synchronized bursting activity[113].

Besides the interesting proposal that the variability observed in vivo probably arises as a consequence of synchronous inputs to a neuron[238], another is based on the premise that inhibitory and excitatory synaptic inputs cancel each other and that the residual fluctuations arising from the imperfect cancellation drive the neuronal firing. This last conceptual framework to explain the spiking variability finds its origins in models describing the dynamics of the membrane potential as a random walk. In those models, excitatory postsynaptic potentials drive the membrane potential towards the threshold while inhibitory ones drive it towards its reversal potential with equal or similar rate[92]. Shadlen & Newsome[223] developed this proposal, and argued in favor of the plausibility of a balance between excitation and inhibition being the fundamental mechanism behind variability. They reported its simple feasibility and argued that, contrary to all other models to explain spiking irregularity, the balanced state proposal does not contradict the experimental evidence. Mathematical and computational studies soon put on a solid footing possible schemes that could explain how from network models, irregular spiking activity could be obtained[257,265,264]. In particular, a mean field theory[265,264] for the balanced state was developed for sparse[*] and strongly connected networks. The dynamics of this type of networks, sometimes called balanced state networks, are asynchronous and irregular with a constant population mean, and will be used as a starting point to analyze the delay-induced transitions to collective rhythms in Chapter 3.

The hypothesis that cortical dynamics are characterized by a balance between inhibition and excitation, was tested experimentally in the ferret both in *in vitro* cortical slices[227] and *in vivo*[109]. In these studies they estimated, in a voltage-clamp configuration, the values of the inhibitory and excitatory conductances by a single recording of spontaneous activity and showed that *on average*, inhibition balances excitation. The understanding of the dynamics of this balance took a further step by performing paired-recordings in nearby neurons. It was shown, in the somatosensory cortex of anesthetized rat both in spontaneous activity and under stimulation[185], that inhibition and excitation track each other dynamically with inhibition lagging excitation by a few ms. Theoretical work aiming to explain the low correlations observed in cortical networks put forward a mathematical framework that accounts for this tight balance[206]. Dense[†] and strongly connected networks generate activity in which inhibition and excitation track each other allowing to cancel out most of the input correlations, leading to asynchronous and irregular dynamics. In this case, the inhibitory and excitatory input currents also present a lag of a few ms, but vanishes in the large N limit.

Interestingly, although the most prominent theoretical work describing the balance of excitation and inhibition[257,265,264,206] results in network dynamics that are asynchronous

---

[*] The number of connections K is much smaller than the number of neurons N

[†] The number of connections K is no longer required to be much smaller than N

and irregular, this balance has as well been experimentally observed in *in vivo* and *in vitro* oscillatory networks[13,23]. Atallah and Scanziani[13] showed in paired-recordings that excitatory and inhibitory conductances of neurons in hippocampal CA3 dynamically and proportionally track each other with a 2-3 ms lag while LFP recordings oscillates with frequencies in the gamma range. The inhibition-excitation balance and the gamma oscillations do not coexist independently. That study further showed that the modulation of the inhibitory and excitatory balance underlies the changes in amplitude of the gamma oscillations, that mediate (i.e. are correlated with) changes in the instantaneous frequency of the gamma oscillation[13]. This work shows that the balanced state, loosely defined as a state in which excitation and inhibition track each other dynamically, is in principle fully compatible with oscillatory activity at the population level.

1.5 Dynamical stability of neuronal networks

The characterization of the firing patterns that emerge as a collective phenomena in coupled networks as synchronous or asynchronous, regular or irregular is not sufficient to describe the dynamics of the network. Although complex, these patterns could live on a limit cycle, or present long and complex transients to it. A large body of work has been dedicated to study whether the microscopic dynamics of neuronal networks are sensitive to initial conditions or exhibit stable dynamics, and to explore the profound questions for brain computation that distill from the possibility of chaos in the brain.

In the origins, network models of rate units with Gaussian distributed weights were shown to have a sharp transition (in the large N limit) from a stable fix point to a chaotic state when the variance of the weight distribution equals a critical value[234]. In these type of networks, a particular type of mean field theory in which the input of the network to a single neuron is approximated by a gaussian noise term whose covariance can be found self-consistently, the first Lyapunov exponent[*] can be calculated analytically. The dynamics beyond the chaotic transition are characterized by a vanishing correlation, indicating asynchronous dynamics. Recently, this method has been extended to networks of 'realistic' connectivity, in which the rate of the units is restricted to have positive values and neurons obey Dale's law[170]. Further extensions incorporate external periodic[202] or stochastic[94] inputs. In both cases, it was shown that these external inputs suppress chaos. In Appendix A we will study, by means of a simple approximation, the impact of delayed interactions in networks of this type.

Another school of mean field theories is based on the analytical calculation of the order parameter in fully phase coupled networks[191]. The order parameter of a single population with the standard Kuramoto coupling and a Lorentzian distribution of intrinsic frequencies has been shown to be one dimensional, but extensions to uni-directionally coupled populations of those characteristics showed that the order parameter in that case exhibits chaotic dynamics[10]. Furthermore, this approach can also be used to study

---

[*] The first Lyapunov exponent is the rate of divergence of two trajectories as a consequence of an infinitesimal perturbation. Rigorous definitions will be given in the Methods of Chapter 3.

fully coupled theta neurons, as the ones studied in Chapter 3. Although the order parameter for the autonomous case with constant heterogeneous input has two dimensional dynamics, the periodically driven case is as well chaotic[230]. An extension to the fully coupled case for N populations can be found in Appendix B. Regarding the microscopic dynamics of the standard Kuramoto network, it was shown that the dynamics before the transition to full synchronization exhibit phase chaos for finite N. The maximum Lyapunov exponent vanishes for increasing N like $1/N$[196].

The precedent for the study of chaos in spiking neural networks was set by van Vreeswijk & Sompolinsky[265] in their landmark work on balanced state networks [*]. They showed that in these networks, the dynamics of binary neurons are chaotic with an infinitely large maximum Lyapunov exponent. The asynchronous and irregular dynamics characterizing the balanced state networks arise from the non vanishing variance of the large inhibitory and excitatory inputs received by each neuron in the network. Intuitions for this mechanisms will be outlined in section 3.1. Although the statistics of the balanced state networks appear to be largely independent of the single neuron model[265,128,174], its stability however is not common or intrinsic to the balanced state. Random networks of inhibitory LIF neurons with delta like synapses in the balanced state, have been shown to have stable dynamics[128,129]. After a transient of irregular activity whose duration scales exponentially with network size, the dynamics settle in a periodic orbit. However, finite size perturbations reveal a phase space of simultaneously diverging and contracting trajectories[175]. Trajectories initially separated on average by less than a critical value ϵ_{FT}, converge to each other exponentially (local stability), while those separated further diverge exponentially. Remarkably, this critical value ϵ_{FT} vanishes in the large N limit, leading to conjecture that is possibly the order of the limit of N to infinity what might underlie the difference in the mean field results[265] and those obtained for the inhibitory LIF[128,129]. Interestingly, networks of LIF neurons in the balanced state with more complex synaptic dynamics, like an exponentially decaying synapse, exhibit extensive chaos after a critical value of the synaptic time constant[173,199].

Quadratic integrate and fire neurons in the balanced state with non-delayed delta coupling, exhibit chaotic dynamics[174]. The trajectories of this dissipative system, settle on an attractor whose dimension increases linearly with network size (see Chapter 3), denoting extensive chaos, and it is independent of the initial conditions and the specific realization of the coupling matrix. The dynamics of these networks are also characterized by a non zero entropy production rate. This entropy production rate or source information rate is on the one hand a measure of how much new information about the initial conditions is provided by the successive iterations of the dynamics, the information contained in the micro-state of the system that is not available in the initial state measured with a finite precision. On the other hand, it is a measure of how much, given the finite resolution of the initial state, the next point in the trajectory is unpredictable; is the extra entropy generated by the unpredictable dynamics at finite precision. Further work on QIF neurons[174], showed that the number of neurons involved in the most unstable

---

[*] Generally, when referring to *balanced state networks*, the following is assumed: N neurons are connected with on average K other neurons, and the weight of the connections J scales like $1/\sqrt{K}$

direction (that of the -time dependent- first covariant Lyapunov vector, associated to the maximum Lyapunov exponent, see Chapter 3) is relatively small and changes variably over time.

The transition from stable dynamics presented by a network of LIF neurons and the chaotic behavior of otherwise identical networks of QIF neurons in the periodically spiking regime was studied by designing a neuron model with tunable spike onset rapidness, which allows to interpolate between these cases[173,72]. For a low and moderate spike onset rapidness, the dynamics of the network continue to exhibit high dimensional chaos as observed for the QIF neuron studied in Monteforte & Wolf[174]. Although the first Lyapunov exponent increases with a moderate increase in the rapidness, both the entropy production rate and the attractor dimension decrease monotonically. Past a critical rapidness value the stability is reached, meaning that even a finite albeit large action potential onset rapidness suffices to achieve stability. Theta neurons in the excitable regime, with a frozen noisy input can on the other hand present both chaotic and stable dynamics, depending on the characteristics of the input[152]. In the chaotic setting, it was also observed that the number of neurons contributing to the most unstable directions is usually low and that this participation is highly variable in time. This work importantly shows, that neurons can respond reliably to the same presentation of the stimulus despite the chaotic dynamics, depending on their alignment to the unstable directions.

Regarding the stability of networks presenting collective dynamics different from the asynchronous irregular state reviewed above, a few studies have pointed out the coexistence of chaos and collective rhythms. Differently to phase and complete synchronization of chaotic units[194], it is of interest to neuroscience to study the synchronous and/or oscillatory dynamics of coupled units that exhibit a periodically spiking response to a tonic input, as reported experimentally[164]. A synchronous chaotic state can be achieved with neuron models that can exhibit a wide variety of behaviors like chaos, bursting and periodic spiking[113], as with more canonical conductance based neurons[114]. In those networks, neurons present a high degree of synchrony (although the population activity is not necessarily oscillatory) while small perturbations change the trajectory of the network, from which its chaotic nature is concluded. Of particular interest for this thesis is coexistence of collective oscillations and chaos. A study[187] analyzing the microscopic dynamics of the partially synchronous state first described in[262] (see 1.2.3) reported that finite and densely connected networks of LIF neurons with temporally extended excitatory synapses, exhibit chaotic dynamics[*]. Nevertheless the maximum Lyapunov exponent vanishes with increasing network size, with the scaling depending on the type of disorder introduced (quenched or annealed). Surprisingly, further work showed that when the connectivity is *diluted* instead of dense, these same networks show extensive chaos[161]. It is worth to mention that in the partially synchronized regime described above, neurons fire quasi-periodically at rates slightly *higher* than the population rhythm. A picture conciliating irregular spiking, high dimensional chaos and collective oscillation at frequencies several times higher than the neuronal firing rates will be offered in Chapter 3.

---

[*] As opposed to the stable dynamics shown for the fully coupled case[262,187]

'The experimental evidence consistently shows that synchronous networks emerge and disappear in waves that last 100–300 ms; these transients represent a meaningful temporal scale of brain operation. The transient nature of coherence is central [...] as it underscores the fact that the system does not behave dynamically as having stable attractors, but rather metastable patterns — a succession of self-limiting recurrent patterns. In the brain, there is no settling down, but an ongoing change marked only by transient coordination among populations, as the attractor itself changes owing to activity-dependent changes and modulations of synaptic connections'

El compañero chileno[267]

2

Information routing with transient synchrony

Perception and cognition rely on context-dependent selection of relevant inputs and flexible inter-areal brain communication. However, despite its fundamental role, the basis of dynamic information routing remains an unsolved problem. In particular, the circuit mechanisms that underlie the fast reconfiguration of selective information transfer on behavioral time-scales are poorly understood. Proposals range from hypothetical circuitry dedicated to routing[188,271,272,273,292], to conditional signal propagation[147,3,108], to the hypothesis that neuronal oscillations direct inter-areal communication, either by enabling conditional readout through frequency filtering[7,8], or by exploiting coherence in networks of regular oscillations[115,37,20]. Windows for efficient communication along different pathways might potentially also arise from irregular fluctuations of local network excitability. In particular, this latter "communication through coherence" (CTC) hypothesis has been invoked in the interpretation of many experimental findings in which boosted inter-areal coherence seems to be associated with enhanced inter-areal communication[86,18]. For instance, increased inter-areal gamma-band coherence and phase synchronization are markers of selective attention, in which different input information streams have to be transmitted or filtered according to their relevance[103,105,106].

Conceptually, however, there are fundamental obstacles to the use of neuronal oscillations in routing. First, oscillatory synchronization is confined to short episodes lasting on the order of ∼100 ms, and the statistical properties of these short-lived oscillatory bursts bear strong signatures of stochasticity[43,44,286]. Second, neuronal spike firing is irregular and only weakly synchronized, with spikes emitted at every possible phase within the ongoing oscillation cycle[135]. Third, inter-areal synaptic transmission delays are long and diverse and may counteract reliable phase synchronization[205]. Fourth, the frequency of the transient oscillatory bursts fluctuates over time, varies between recording sites and depends on characteristics of the presented stimuli[134,205]. The likelihood of the bursts to spontaneously match a priory should be very low.

Here we investigate a class of circuit models that naturally exhibits extensive power, frequency and timing variability, and contain key types of heterogeneity including heterogeneous transmission delays. In these models, below the onset of developing oscillatory synchrony, collective oscillations are short-lived, having durations on the order of a few cycles, are weakly synchronized, and exhibit stochastically drifting frequency. When multiple circuits with these characteristics are coupled by long-range excitatory connections, the large-scale dynamics spontaneously generates temporally co-occurring bursts of synchrony. We find the drifting frequencies of each region to track each other giving rise to transient phase-locking within the gamma bursts. Through state resolved information theoretical analyses, we assessed whether these transient patterns of coherence can gate information flow. We further examined the propagation of external input signals relayed from different source regions and under which conditions these signals can be decoded from the activity of a downstream target region. We find that the transient coherence between the activity of the local circuits dynamically shapes the flow of information between them: Information transfer is either selectively boosted or suppressed along different routes according to the transient phase pattern. These distinctive routing states have a direction set by the transient phase relations and are modulated by the fluctuating level of synchrony. We find that the propagation of externally-supplied information can be selectively gated on or off along different pathways depending on the routing state. Surprisingly, the stochastic and fleeting nature of ongoing oscillations more effectively modulates information flow than stronger and more coherent forms of synchronized circuit activity.

This chapter is organized as follows: The section 2.1 details the mathematical and numerical methods, including definitions of the measures used and details of the numerical implementation. The section 2.2 contains the results summarized above, by increasing order of circuits integrating the small motifs. Finally, the results are summarized and briefly discussed in 2.3

2.1 Methods

2.1.1 Network Models

The network model used to model local brain regions consisted of 1000 excitatory and 250 inhibitory conductance-based Wang-Buzsáki neurons[285] with random connectivity. Each neuron in the network follows the equations:

$$C\dot{V} = (I - g_k n^4 (V - E_k) - g_{na} m_\infty^3 h (V - E_{na}) - g_l (V - E_l) + I_s^{\mathrm{E}} + I_s^{\mathrm{I}}) \tag{2.1}$$

$$\dot{n} = \phi(a_n(V)(1 - n) - b_n(V_i) * n) \tag{2.2}$$

$$\dot{h} = \phi(a_h(V)(1 - h) - b_h(V_i) * h) \tag{2.3}$$

where C is the membrane's capacitance, V is the voltage, I is an external input current, g_k is the potassium conductance, g_{na} is the sodium conductance, g_l is the leak conductance and E_k, E_{na} and E_l are respectively the potassium, sodium and leak reversal potentials. The $m_\infty(V) = a_m(V)/(a_m(V) + b_m(V))$ and $a_n(V)$, $a_m(V)$, $a_h(V)$, $b_m(V)$, $b_n(V)$, $b_h(V)$ functions together with all the single neuron parameters take the form originally defined by Wang and Buzsáki[285].

Synaptic conductances were modeled with a difference-of-exponentials time-course, proportional to a post-synaptic channel open probability P_s:

$$P_s = B[e^{(-(t - t_0 - d)/\tau_1)} - e^{(-(t - t_0 - d)/\tau_2)}] \tag{2.4}$$

where t_0 is the time of the pre-synaptic spike, d is a combined axonal and synaptic transmission delay, τ_1 , τ_2 are the synaptic time-constants and B is a normalization factor. Excitatory (E) or inhibitory (I) synaptic currents were then given by $I_s^{(E,I)} = g_s^{(E,I)} P_s^{(E,I)} (V_s^{(E,I)} - V)$, where $g_s^{(E,I)}$ is the peak conductance of the considered synapse and $V_s^{(E,I)}$ is the synaptic reversal potential. We used V_s^E = 0 mV and V_s^I = -80 mV, for excitatory and inhibitory synapses, respectively.

Both peak synaptic conductances and synaptic delays were chosen to be heterogeneous. Their values are Gaussian-distributed random variables, with prescribed means $g_s^{(E,I)}$ and $\overline{d}$ and standard deviations $\sigma_{g_s^{E,I}}$ and σ_d. The probability of establishing an excitatory (inhibitory) connection within each modeled brain region is denoted by P_E (P_I). The background drive to each neuron in the network was provided by external excitatory inputs, modeled as Poisson processes with rate ν_{in} and statistically independent for different neurons. Each spike injected by this external driving source induced in the target neuron a synaptic current as in equation (2.4). Peak conductances of the external drive were also heterogeneous and assumed values sampled from a truncated Gaussian distribution with mean g_s^ν and standard deviation $\sigma_{g_s^\nu}$. Long range synaptic connectivity between two or three brain regions was purely excitatory, targeting both excitatory and inhibitory neurons in the target region. In the two population scheme, the probability of having a long range excitatory projection, P_E^{LR}, was held equal between areas. In the network architecture comprising three areas, the central population Y received *feedforward* connections P_E^{FF} from X and Z that were stronger than or equal to the *feedback* ones P_E^{FB} from Y to both X and Z. Both feedforward (and feedback) connections had equal strength. No connection was present between X and Z. Long-range excitatory synaptic conductance values were drawn from the same distribution as for recurrent excitation within each local area.

Excitatory Synaptic time 1	τ_1^E	3 ms
Inhibitory Synaptic time 1	τ_1^I	4 ms
Excitatory Synaptic time 2	τ_2^E	1 ms
Inhibitory Synaptic time 2	τ_2^I	1 ms
Mean Synaptic delay	d	1.5 ms
Mean Synaptic Excitatory Conductance	g_s^E	5 nS
Mean Synaptic Inhibitory Conductance	g_s^I	200 nS
Mean Input Synaptic Conductance	g_s^ν	3 nS
Standard deviation delay	σ_d	0.1 ms
Standard deviation Synaptic Excitatory Conductance	$\sigma_{g_s^E}$	1 nS
Standard deviation Synaptic Inhibitory Conductance	$\sigma_{g_s^I}$	10 nS
Standard deviation Input Synaptic Conductance	$\sigma_{g_s^\nu}$	1 nS
Local Inhibitory probability connection	P_I	0.2
Local Excitatory probability connection	P_E	0.3
Inter-Areal Excitatory probability connection	P_E^{LR}	0.08
Inter-Areal Excitatory FF probability connection	P_E^{FF}	0.08
Inter-Areal Excitatory FB probability connection	P_E^{FB}	0.01
Poisson input rate	ν	$10 \cdot P_I$ kHz

Table 2.1: List of default network parameters.

The default set of network parameters is summarized in Table 2.1. These default values were used, unless specified otherwise (specific parameter variations are listed in the following). The probability of establishing a (local) inhibitory connection was changed depending on the considered working point. Simulations were performed: with $P_I = 0.3$ in Figures 2.2, 2.6, 2.27 and 2.28; with $P_I = 0.6$ in Figure 2.10 and 2.29 a-c,e, and with $P_I = 0.1$ in Figures 2.18 and 2.22 d,f,h. The probability of establishing a local excitatory connection deviated from default values in Figures 2.13, 2.23, 2.24, 2.26, 2.28 with $P_E = 0.35$, in Figures 2.18a, 2.22, 2.1 with P_E=0.25 and in Figure 2.18 with $P_E = 0$. In Figure 2.27 and 2.29d, we also adopted a smaller degree of input conductance heterogeneity, $\sigma_{g_s^\nu} = 0.1$ nS; in Figures 2.15, 2.16, 2.20, 2.26 was $\sigma_{g_s^\nu} =$ 0.5 nS and in Figures 2.24 and 2.28 $\sigma_{g_s^\nu}$ =0 nS. Typical simulation runs were performed with a fourth order Runge-Kutta method (fixed time step $dt = 0.1$ ms) when the input was continuous or simple Poisson spike trains, and lasted 10 min of real time, unless otherwise indicated (details found in the corresponding section). When the input was modeled as an Orstein-Uhlenbeck process, an Euler-Maruyama integration scheme with

$dt = 0.01$ ms was used. To sample neuronal activity distributions, we combined multiple simulations with quenched heterogeneity and connectivity but different realizations of the stochastic drive to the system.

All simulations and information theoretical analysis were made with custom code written in C++. Analysis and illustration of simulation's output were made in Matlab.

2.1.2 *Characterization of network activity*

The synchronization index was chosen to be χ^2, where $\chi^2 = \frac{\sigma^2_{V(t)}}{\sum_{i=1}^{N} \sigma^2_{Vi(t)}/N}$ [95]. Here, $V(t) = \sum_{i=1}^{N} V_i(t)/N$ is the so called LFP-like signal. The variables $\sigma_{V(t)}$ and $\sigma_{V_i(t)}$ denote the standard deviation of LFP amplitudes over time or, respectively, of the membrane potential traces $V_i(t)$ of each individual neuron i. The χ^2 coefficient is bounded to the unit interval, with vanishing values indicating asynchronous dynamics. The frequency of the collective oscillation of a region was calculated as the inverse of first peak position of the autocorrelation function of a multi-unit rate signal, obtained by convolving the raster plot of each local network with a Gaussian kernel of standard deviation of 2ms. The rate signal in Figure 1b was calculated as a histogram with a 1 ms bin width. Single neuron rates were calculated as the inverse of their mean inter-spike interval. Spectrograms of LFP activity were calculated using a standard time-frequency Fourier analysis with overlapping Hamming windows (300 ms size, 50 ms step, 250 ms overlap) and the time-averaged spectra through the multi-taper method (sixteen tapers).

2.1.3 *Analysis of gamma burst properties and coordination*

To extract the joint distribution of frequencies and durations of oscillatory burst (Fig. 2.2 and 2.10b) we thresholded the LFP spectrograms at the 95% percentile of instantaneous power values. The thresholded spectrograms were then scanned at different frequencies (i.e. line by line) to extract the durations of time intervals over which power at the given frequency was continuously sustained above threshold. Sampling of these burst duration was performed combining 80 long trials (overall 800 min of signal). We then studied time and frequency coordination between oscillatory bursts occurring in different coupled regions (Fig. 2.6 c–d). As before, LFP spectrograms of each region were thresholded at 95 percentile and scanned line-by-line, creating a binary string for each frequency. Each of them was then cross-correlated against the analogous strings obtained from the other population, resulting in a distinct correlation value for each different pair of frequencies. The calculation was made by pulling together 50 trials for Figure 2.6 c, ands 10 trials for Figures 2.10, 2.20. Significance of the estimated correlations (Fig. 2.6c) was assessed by comparing bootstrap with replacement confidence intervals (c.i.) for each correlation value with the associated permutation-based chance levels (5000 replicas).

2.1.4 Analysis of transient phase-locking

We calculated time-resolved cross-correlograms (XC) adopting an overlapping sliding window of 50 ms length (roughly two average oscillation periods) and 0.1 ms step. Within each time-window, standard cross-correlation was performed between chunks of LFPs of each of the coupled populations:

$$\mathrm{XC}(t,\tau) = \left\langle (V_X(t') - \overline{V}_X) \cdot (V_Y(t'-\tau) - \overline{V}_Y) \right\rangle_{t' \in W(t)} \tag{2.5}$$

where $\langle \cdot \rangle_{t' \in W(t)}$ denotes averaging over a 50 ms time window $W(t)$ centered on time t, and $\overline{V}_{X,Y}$ are LFP averages over this same window.

The instantaneous phase of each LFP signal Φ_X and Φ_Y was calculated by interpolating a straight line over the unit phase interval $0 < \Phi < 1$ between consecutive maxima of population activity of a single repetition. A peak in population activity was considered as such if it was the maximum in a neighborhood of a half-period radius of the central oscillation frequency of the population activity. Such a fast approach avoids band-pass filtering and leads to similar results as a Hilbert Transform analysis, as shown in[282]. The relative phase $\Delta\Phi$ was then found by a subtraction (mod 1) of the instantaneous phases Φ_X and Φ_Y, $\Delta\Phi_{XY} = \Delta\Phi = \Phi_Y - \Phi_X \mod 1$. The joint probability distribution of time-dependent phase difference $\Delta\Phi$ and the time dependent peak of XC, denoted as $\mathrm{XC}^*(t) = \max_\tau[\mathrm{XC}(t,\tau)]$ was sampled by pulling together 100 simulated trials (overall 1000 min of signal). The conditional probability distributions shown in Figure 2.8C (right) were obtained by independently normalizing each row of the probability matrix in Figure 2.8c (left). The XC* threshold for the Figure 2.8d was the 99 percentile (XC* = 0.37).

The circular variance of Figure 2.9 was calculated as follows: Given $\{s_i\}_x$ with i=1,...,N the set of spike-times in a window of time W(t) centered at t, coming from neurons belonging to a defined subset of the region X, $\mathfrak{S}_x$, we define $\theta_i^x(t)$ as the phases of the area's LFP (Φ_X) at spike-times: $\theta_i^x(t) = \Phi_X(s_i)$. The local circular variance of the subset $\mathfrak{S}_x$, $CV_{\mathfrak{S}_x}(t)$ is then the circular variance of the set $\theta_i(t)$. The full $\mathrm{CV}(t) = \frac{1}{2}(\mathrm{CV}_{\mathfrak{S}_x}(t) + \mathrm{CV}_{\mathfrak{S}_y}(t))$ was evaluated considering two different conditions for the subsets $\mathfrak{S}$. In Figures 2.11c (top) and 2.11d-e (left), $\mathfrak{S}_x$ was the full network X, and $\mathfrak{S}_y$ was the full network Y. In right panels of Figure 2.11d-e, $\mathfrak{S}_{x,y}$ was taken to be 10 randomly chosen neurons. This measure of CV, quantifies how much the spikes from the regions are locked to its own LFP, and therefore giving an alternative measure of joint synchrony. In both cases, the length of the sliding window W was seven oscillation periods. Two hundred noise realizations with the same network architecture one minute each were used to obtain the joint distribution of CV(t) and XC∗(t). As before, the conditional probability distributions shown in Figure S6d-e (bottom) were obtained by normalizing each row of the probability matrix in Figure 2.9d-e (top).

2.1.5 *Analysis of information transfer*

We evaluated Transfer Entropy[221,279] (TE) between discrete time-series of the simulated LFP signals $V_X(t)$ and $V_Y(t)$. These signals can take values from the sets Ξ_X and Ξ_Y respectively, and have distributions $\mathrm{p}(x)$ and $\mathrm{p}(y)$ over these sets. These sets correspond to signal values measured within a selection of specific temporal windows in which certain conditions which define a consistent functional state are properly fulfilled. The state-selection filtering procedure defining the pooling of time epochs into states is described later in this section.

Transfer Entropy from the region X to the region Y is defined as a deviation from the following Markov condition[268]:

$$p(y_t|\boldsymbol{y}_t^k) = p(y_t|\boldsymbol{y}_t^k, \boldsymbol{x}_t^l) \tag{2.6}$$

This reads: the probability of V_Y taking a value y_t at time t given that the k past values of V_Y were $\boldsymbol{y}_t^k = (y_{t-t_1}, ..., y_{t-t_k})$ equals the probability of V_Y taking a value y_t at time t, given that the k past values of V_Y were $\boldsymbol{y}_t^k$ and that the l past values of V_X were $\boldsymbol{x}_t^l$. This condition is only fulfilled if there is no influence of the past of V_X on the current values of V_Y; in other words if the distributions are statistically conditionally independent. TE is a measure of the deviation from the Markov condition in (2.6):

$$\mathrm{TE}_{X\to Y} = \sum_{\substack{y_t,..,y_{t-t_k}\in\Xi_Y \\ x_{t-t_1},..,x_{t-t_l}\in\Xi_X}} p\left(y_t, \mathrm{y}_t^k, \mathrm{x}_t^l\right) \log_2\left(\frac{p\left(y_t|\mathrm{y}_t^k, \mathrm{x}_t^l\right)}{p\left(y_t|\mathrm{y}_t^k\right)}\right) \tag{2.7}$$

Here we relaxed the Markov condition adopting a commonly used simplification[98,125,162,237,20] (but see Fig. 2.19). We replaced in the previous expression the past activity history V_Y^k and V_X^l with observations at a single past time $V_{X,Y}(t-\tau)$, with a variable interaction latency τ. With this approximation, TE in (2.7) can be written as:

$$\mathrm{TE}_{X\to Y}(\tau) = H\left[V_Y(t)|V_Y(t-\tau)\right] - H\left[V_Y(t)|V_X(t-\tau), V_Y(t-\tau)\right] \tag{2.8}$$

An analogous (but not identical) expression for TE in the opposite Y-to-X direction is obtained by exchanging the indices X and Y. Similar results are obtained when transfer entropy is estimated by considering different interaction delays for sender and receiver, or when considering more than a single interaction delay (see Fig. 2.19). The formulation (2.8) makes clear that in the isolated scheme of two connected populations, TE from X to Y measures information present in the collective activity of target region Y which cannot be accounted for by the past activity of the target region Y itself, but must have been transferred from X to Y. TE is the reduction of uncertainty in estimating the current state of a given region Y by including the history of an afferent region X.

When more than two areas constitute the interacting system, the above expression for transfer entropy must be modified to account for the possibility of non direct functional interactions (e.g. transfer from X to Z via Y, etc.). We used partial transfer entropy[260] to uncover the direct interactions between pairs of populations when embedded in a larger multi-areal system. Given a set of three populations X, Y and Z, partial Transfer Entropy with a single interaction delay is defined as:

$$\mathrm{pTE}_{X\to Y}(\tau) = H\left[V_Y(t)|V_Y(t-\tau), V_Z(t-\tau)\right] - H\left[V_Y(t)|V_X(t-\tau), V_Y(t-\tau)V_Z(t-\tau)\right] \tag{2.9}$$

This expression reduces to Equation (2.8) when the activity of Z is statistically independent from that of X and Y, as can be seen in the equivalent expression of discrete time series below.

$$\mathrm{pTE}_{X\to Y}(\tau) = \sum_{\substack{y_t, y_{t-\tau_y} \in \Xi_Y \\ x_{t-\tau} \in \Xi_X \\ z_{t-\tau} \in \Xi_Z}} p\left(y_t, y_{t-\tau}, x_{t-\tau}, z_{t-\tau}\right) \log_2\left(\frac{p\left(y_t|y_{t-\tau}, x_{t-\tau}, z_{t-\tau}\right)}{p\left(y_t|y_{t-\tau}, z_{t-\tau}\right)}\right) \tag{2.10}$$

All the probability densities required for the evaluation of Equation (2.8-2.10) can be straightforwardly derived from the three-terms or the four-terms joint probability distribution $p\left(y_t, y_{t-\tau}, x_{t-\tau}\right)$ in the TE case, or $p\left(y_t, y_{t-\tau}, x_{t-\tau}, z_{t-\tau}\right)$ in the pTE case. These probabilities must be sampled over the sets Ξ_X, Ξ_Y, Ξ_Z, constituted by the values assumed by the time-series of neural activity, only over selected temporal epochs.

Sampling these probability distributions by pooling LFP epochs which fulfill a specific set of conditions $\mathfrak{G}$ allows evaluating TE and pTE within a consistent regime, specified by the choice of the filtering conditions $\mathfrak{G}$ themselves. The information theoretical analysis with a specific filtering condition based on the instantaneous inter-areal phase-difference $\Delta\Phi$ is what we call a *state-specific directed functional connectivity* (or, in short, *routing state*). When considering a two region circuit in Figures 2.13b–c, 2.27, 2.14a–c and 2.28, the $\Delta\Phi$ range is split into five relative phase bins of equal size (TE vs τ and $\Delta\Phi$ surfaces were then smoothed by linear interpolation). Figure 2.27 and 2.28 show the Anisotropy index from single trials. The separation in just two *Top* and *Bottom* routing states (Fig. 2.13e, 2.14d–e, 2.15-2.18, 2.22, 2.28) was based on the relative phase to fall, respectively, in the coarser ranges $\Delta\Phi_\uparrow$, i.e. $0 < \Delta\Phi < 0.5$, or $\Delta\Phi_\downarrow$, i.e. $0.5 < \Delta\Phi < 1$.

In Figure 2.14, we adopted an additional filter conditional to the strength of inter-areal coherence, on top of the instantaneous phase relation. Conditions on the instantaneous value of XC* were imposed to be larger than median+0.5 (Fig. 2.14d, third dashed line in Fig. 2.14b) or smaller than the median-0.5 of its distribution (Fig. 2.14e, first dashed line in Fig. 2.14b).

In the three regions case in which a pairwise analysis was performed (Figs 2.27 and 2.28), the procedure was identical to that described above for the two regions case. More complex state-filtering conditions were devised for the complete analysis of the dynamics of the three regions. The six possible hierarchical configurations that the LFP signals can take define six filtering conditions numbered from $\Delta\Phi_1$ to $\Delta\Phi_6$ that give rise to six routing states, as illustrated in Figure 4d. The conditions can be written in terms of the pairwise phase relations in the following way:

$$\Delta\Phi_1^{xzy} = V_X, V_Y, V_Z \mid \Delta\Phi_{XY} > 0.5, \Delta\Phi_{XZ} > 0.5, \Delta\Phi_{XZ} > \Delta\Phi_{XY} \tag{2.11}$$

$$\Delta\Phi_2^{xyz} = V_X, V_Y, V_Z \mid \Delta\Phi_{XY} > 0.5, \Delta\Phi_{XZ} > 0.5, \Delta\Phi_{XZ} < \Delta\Phi_{XY} \tag{2.12}$$

$$\Delta\Phi_3^{zxy} = V_X, V_Y, V_Z \mid \Delta\Phi_{YZ} < 0.5, \Delta\Phi_{XZ} < 0.5, \Delta\Phi_{XZ} < \Delta\Phi_{YZ} \tag{2.13}$$

$$\Delta\Phi_4^{zyx} = V_X, V_Y, V_Z \mid \Delta\Phi_{YZ} < 0.5, \Delta\Phi_{XZ} < 0.5, \Delta\Phi_{XZ} > \Delta\Phi_{YZ} \tag{2.14}$$

$$\Delta\Phi_5^{yxz} = V_X, V_Y, V_Z \mid \Delta\Phi_{XY} < 0.5, \Delta\Phi_{ZY} < 0.5, \Delta\Phi_{XY} < \Delta\Phi_{ZY} \tag{2.15}$$

$$\Delta\Phi_6^{yzx} = V_X, V_Y, V_Z \mid \Delta\Phi_{XY} > 0.5, \Delta\Phi_{ZY} > 0.5, \Delta\Phi_{XY} > \Delta\Phi_{ZY} \tag{2.16}$$

For the two regions model, we estimated histograms (within the two possible top and bottom routing states): in Figures 2.13e–f and 2.14d–e based on 5000 minutes of signal, from 50 trials of the same network instance; in Figure 2.13b, Figure 2.27b,2.14c and 2.28, based on 10 min of signal from a single network realization (while the mean over a total of 150 min, from 15 different network instances is shown in Figure 2.14a); for Figures 2.15 and 2.16, based on single trial simulations each lasting 10 min; in Figure 2.17, based on 40 different network instances (10 min of LFP signal for each considered parameter configuration); in Figure 2.18, based on 10-min simulations from 50 different network instances (while in Figure 2.18a, only 10 network instances were used, with the same simulation time). When analyzing a three regions motif, we estimated histograms (within each of the six state filtering conditions): in Figure 2.24, based on simulations each lasting 18000 minutes each from twelve different network instances; in Figure 2.26, based on twenty simulations each lasting 9000 min from different network instances; while Figure 2.22 is based on simulations lasting each 50 minutes from 40 different network instances. We note that qualitatively similar conclusions for most analyses may been obtained using smaller data sets, but the associated confidence intervals for the computed quantities would have been larger.

TE values obtained by plugging sampled histograms into the definition (2.8) were then further corrected against finite-size bias by quadratic extrapolation toward infinite sample size[242] in the following way: Given a set of time series of length L from which we want to estimate TE, we take three subsets of the same length L_i, with $L_i = \frac{L}{i}$ where $i = 1, ..., 10$. For each length L_i, TE is calculated from each of the three subsets ($\mathrm{TE}_i^{j=1,2,3}$), and the mean of these, $\mathrm{TE}_i = \langle \mathrm{TE}_i^j \rangle_j$ is obtained. The infinite sample size value of TE is the y-intercept of a second order polynomial fit of TE_i vs i.

The 95% confidence intervals (c.i.) for TE values were approximated as two times the standard deviation above and two times below the mean, over the considered network instances or trials (95% rule). These c.i. were then compared to the 95% c.i. obtained under the null hypothesis of functional uncoupling, providing a baseline TE range for significance testing. We adopted a resampling bootstrap with replacement building a distribution out of 1500 surrogates for network realization, and collecting them together. In order to keep the oscillatory nature of the analyzed time-series, we built bootstrap surrogates using LFP blocks of a mean length Λ. This value should preserve the signal's autocorrelation structure. To choose this value, we analyzed the behavior of the bootstrapped TE vs the chunk length size Λ. For oscillatory signals in the transient synchrony regime, the value of the bootstrapped TE initially increases and then saturates at around Λ=100 ms. We chose Λ=300 ms for the TE baseline calculations, and we kept it for the MI calculations, although as the random input has no oscillatory nature, the value of the bootstrapped MI were independent of Λ. TE values whose 95% c.i. fell completely above (below) the baseline range were indicative of significantly enhanced (damped) information transfer with respect to chance level.

We finally defined the Functional Anisotropy Index:

$$\Delta\mathrm{TE} = \frac{\mathrm{TE}_{Y\to X}(\tau) - \mathrm{TE}_{X\to Y}(\tau)}{\max\limits_{ij}(|\mathrm{TE}_{X\to Y}(\tau)_{ij}|, |\mathrm{TE}_{Y\to X}(\tau)_{ij}|)} \tag{2.17}$$

bounded in the $-1 \leq \Delta\mathrm{TE} \leq 1$ range, as a simpler indicator of different efficiency of information transfer in the two possible reciprocal communication senses between regions in a considered pair.

2.1.6 Generation of Input Signals

Exogenous sources of information were first modeled as scalar gaussian random field (GRF) input currents. GRFs were generated as follows: N discrete values were taken from a continuously smooth correlation function given by

$$C(\tau) = \frac{2}{\cosh(\tau/\tau_s)} \tag{2.18}$$

at regularly spaced times $\{\Delta\tau_i\}$, i=1,..,N, and then used to obtain its Fourier transform $FC(\tau) = \hat{C}(k)$, with $k = k_0, ..., k_{N-1}$, evenly spaced with $\Delta k = \frac{2\pi}{\Delta\tau N_\tau}$. The scalar random field in Fourier representation was then obtained by

$$\hat{\Phi}(k) = \sqrt{\frac{\pi}{\Delta k}\hat{C}(k)}(A_k + iB_k) \tag{2.19}$$

The real part of Eq (2.19) in real space, i.e. $\Re\left(F^{-1}\hat{\Phi}(k)\right) = \Phi(\tau)$, provided the desired GRF stochastic variable.The current conveying the externally injected signal $S(t) = g\Phi(t)$ was generated independently for each area. Each has a power spectrum given by:

$$\hat{C}(f) = \frac{2\pi g\tau_s}{\cosh(\pi^2\tau_s f)} \tag{2.20}$$

The fraction of power p contained in the spectrum up to a cut off frequency f_c, is given by

$$2/\pi\mathrm{gd}(f_c) = p \qquad \text{where} \qquad \mathrm{gd}(x) = \int_0^x \frac{1}{\cosh(y)}dy. \tag{2.21}$$

A stochastic realization of the GRF variable was first generated within Matlab and then fed as an input to each neuron in a single region through the RK4 integrator in custom code as described above. The parameters used in Figures 2.20, 2.22 and 2.26

were $\tau_s = 1$ ms and the gain factor g=2. Similar results are obtained for τ_s ranging from 0.5 ms to 5 ms.

In Figure 2.22 (right column), we confirmed our results adopting a different model for the stochasticity of the external signals, and modeled inputs as Ornstein-Uhlenbeck processes. The input signal was given by the following equation:

$$\dot{S}(t) = -\gamma S(t) + g\eta(t) \tag{2.22}$$

where η is a Gaussian white noise with zero mean and unit variance. The variance of the input signal was given by $\sigma^2 = \frac{g^2}{2\gamma}$. In this figure we took g=0.1 and γ=1. An Euler Mayurama method was used to simulate the input and the network dynamics, with a time step dt=0.01 ms.

2.1.7 Probing the propagation of input signals

Information theory functionals can be evaluated also on the continuous time-series provided by the external current sources $S(t)$. In particular it is possible to evaluate state-resolved Transfer Entropy between injected currents $S(t)$ and LFP time-series, as we do in Figures 2.22–2.24.

Sharing of information between the two endpoints of a communication line is assessed via the classical measure Mutual Information (MI)[60]. In the case of MI between an injected signal S and LFP from a region X we write:

$$\mathrm{MI}_{S\leftrightarrow X}(\tau) = \sum_{t\in\mathfrak{G}} \sum_{s,x} p\left(x(t), s(t-\tau)\right) \log_2 \left(\frac{p\left(x(t), s(t-\tau)\right)}{p\left(x(t)\right) p\left(s(t-\tau)\right)} \right) \tag{2.23}$$

The estimation of MI can be state-filtered, by pooling only input and response value pairs within the epochs fulfilling the filtering criteria specified by the chosen filter $\mathfrak{G}$. When analyzing tri-areal motifs in Figures 2.11 and 2.26, as for TE, we computed partial (also called conditional) mutual information[85,60].

2.1.8 Baseline estimation

Information theoretical estimators, as many other estimators, are sensitive to the statistical structure of the time series over which they operate. In order to asses the significance level, i.e. the information transmission that we could expect from chance, we compared the information transmission of our networks with that of the 95% boundaries of the distribution of the estimators obtained when randomly shuffling of the time series. The advantages of this procedure in contrast to the comparison with the TE values obtained from disconnected networks, is that bootstraps methods are independent of how the parameter to be studied modifies the dynamics of the network. For example, the extra amount of excitation received from the external connections might change the level of synchrony and the statistical structure of the dynamics, and therefore the disconnected estimation can in principle be under or over estimated compared to a bootstrap. In Figure 2.1 it is shown how the 95% band of the distribution of TE values of randomly shuffled series depends on the length of the chunk Λ used for the randomization. If the chunk is too short, then the series seems more asynchronous than it actually is, and the estimators give a small value. For chunks over the $\approx$ 100 ms, the value saturates. For all the simulations we used a value of Λ well inside the saturation area.

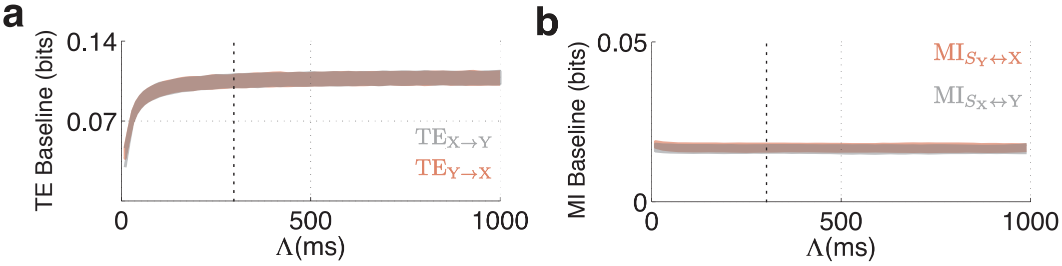

Figure 2.1: Baseline estimation for information theoretical quantities on signals of oscillatory nature. We used a bootstrap with replacement for shuffling the series. This was done as follows: Iteratively, we chose a chunk starting in random point of the considered time series, and a random length from a gaussian distribution of mean Λ and we sequentially relocated it to a new string. Given the oscillatory nature of our signals, a short chunk length disrupts its structure, leading to surrogates that do not respect the statistical structure of the original time series. **(a)** 95% limits of the distribution of Transfer Entropy surrogates, from X to Y (grey) and from Y to X (pink) of a in a *Top* state as a function of the mean chunk length Λ. We see that for lengths bigger than 150 ms (i.e. longer than the mean burst length) the values of TE for this surrogates saturate. We used an average length of 300 ms (dashed line), well into the saturation area. **(b)** Mutual information between input noise to a source area and the LFP-like signal of a target one. As the input signal $S_{x,y}$ has no periodic structure, this transient is not observed in this case and the saturation is reached immediately. We kept the choice made for TE also in this case for practical reasons.

2.2 Results

2.2.1 Transient synchrony

Oscillatory neuronal activity *in vivo* is comprised of epochs of synchronous activity arising from an overall poorly synchronized state. We identified and characterized a regime of local circuit dynamics, below the onset of oscillatory synchrony, that mimics this fundamental feature and reproduces the substantial fluctuations in both frequency and power seen experimentally in local field potential (LFP) recordings[44,286].

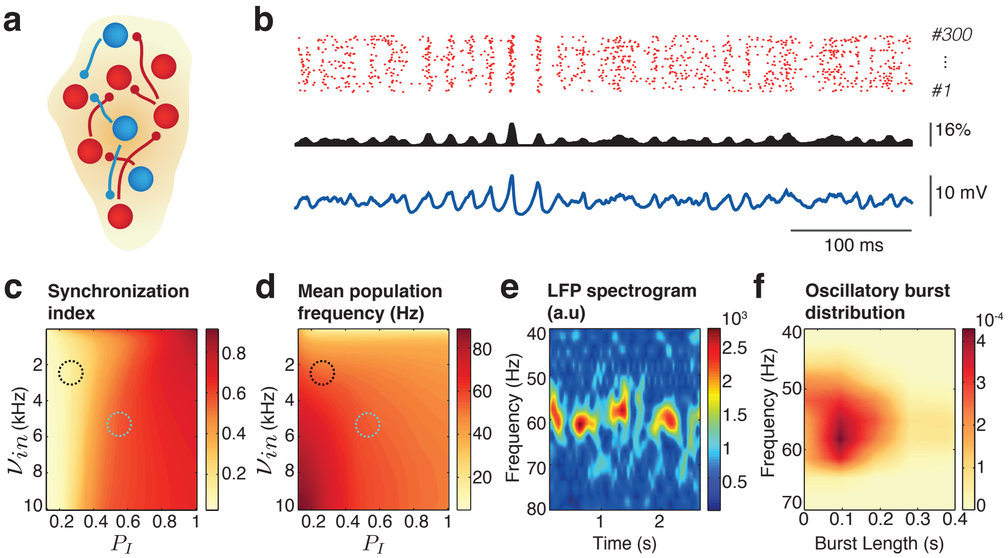

Figure 2.2: Transient synchrony regime. (a) Cartoon of the local connectivity of a brain region or area, modeled as a random network of heterogeneous inhibitory and excitatory conductance based neurons. **(b)** Simulated activity at the edge of synchrony. Transient oscillatory bursts are noticeable in LFP time-series (bottom) and in multi-unit activity (middle, measured as percentage of active neurons). Individual neurons however fire irregularly and not at every oscillation cycle, as indicated by the raster plot of 300 excitatory neurons (top). **(c)** The degree of synchronization of local neuronal activity, as quantified by the synchronization index (see *Methods* 2.1.2), grows with the probability P_I of recurrent inhibitory connection and the rate ν_{in} of the Poisson background drive to the region, revealing a smooth transition from asynchronous to synchronous behavior. **(d)** Dependency of the frequency of collective regional oscillation from P_I and ν_{in} (see Fig. 2.3a for single neuronal firing rates). Dashed circles in panels **c–d** highlight two working points, with similar collective oscillation frequencies in the gamma range but very different synchronization levels. Upper left dashed circle (edge of synchrony working point) P_I :∼0.25 and ν_{in} :∼2.5kHz, the high synchrony working point P_I :∼0.55 and ν_{in} :∼5.5kHz. **(e)** Transient gamma bursts are evident in the spectrogram of LFP activity at the edge of synchrony. **(f)** Joint distribution of the frequencies and durations of these gamma bursts. Note the predominance of short-lived bursts covering a band of frequencies in the gamma range.

The dynamics of a local circuit (or region) with transient synchrony is characterized in Figure 2.2. A circuit is modeled as a large network of excitatory and inhibitory spiking neurons with a random local connectivity (Fig. 2.2a) and heterogeneous synaptic conductances and latencies (see *Methods*). Figure 2.2b depicts the time evolution of the average membrane potential in the local circuit, together with a raster plot of individual neurons and a histogram of the multi-unit activity rate (see *Methods* 2.1.2). In the following, we call the population-averaged membrane potential, a convenient descriptor of the collective neuronal activity, an "LFP-like" signal[186]. As indicated in Figure 2.2b, the amplitude of the LFP trace exhibits transient epochs of increased oscillatory amplitude. These oscillatory events are more difficult to detect inspecting the spike traces of a few single units whose firing always remains stochastic[30,29,35,246]. Individual neurons can fire at every phase of the ongoing oscillation, as revealed by an average circular variance of ∼0.6 of the overall distribution of the phases of firing.

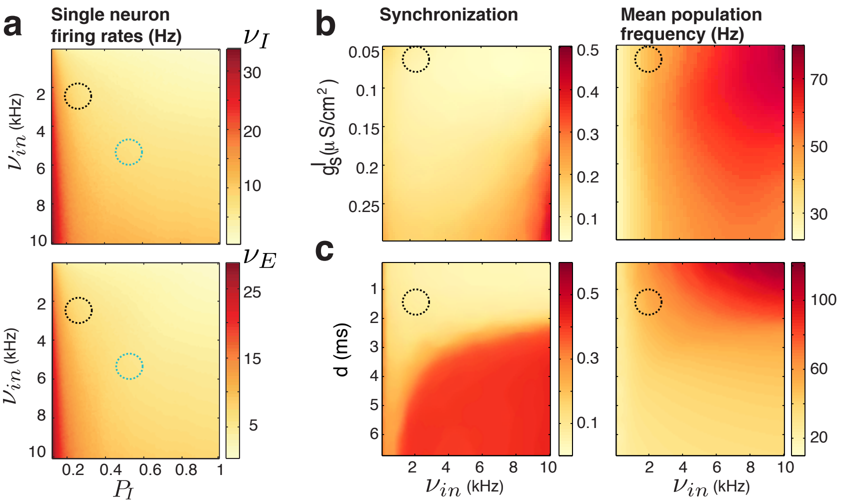

Figure 2.3: Additional characterizations of the edge-of-synchrony regime. (a) Dependency on ν_{in} and P_I of the average firing rate of individual excitatory and inhibitory neurons. The dashed circles in all panels represent the same working points of Figure 2.2. **(b)** Synchronization index (left) and collective oscillation frequency (right) as a function of the mean inhibitory conductance strength g_s^I (top row), or the mean synaptic delay d (bottom row) and of the local background Poisson drive rate ν_{in}.

In our local circuit, similar to experimental observations[16], the generation of oscillatory activity relies on delayed recurrent interactions, either occurring through direct delayed connections or mediated by inhibitory-excitatory-inhibitory loops[35,247,244]. The level of recurrent inhibition controls the overall level of synchrony of the network. Enhancing recurrent inhibition induces a graded transition toward higher synchrony. In Figure 2.2c this is shown via an increase of the probability P_I of establishing local inhibitory connections, as captured by the network synchronization index[97,95] (see *Methods* 2.1.2). Increasing local inhibition also leads to an overall reduction of the mean frequency of the collective population oscillation (Fig. 2.2d) and of the firing rates of individual neurons (Fig. 2.3a). Delayed recurrent inhibition can as well be modulated, beyond the probability of establishing a local inhibitory connection, by increasing either the peak inhibitory conductance (Fig. 2.3d) or the synaptic delay (Fig. 2.3c).

Proportionally increasing both the strength of recurrent inhibition and the background drive, along the diagonal of Figure 2.2c–d, essentially maintains the value of population frequency (Fig. 2.2d) and firing rates (Fig. 2.3a), but increases the synchronization level, rising smoothly along this line. The rise of the synchronization index along this line is smoother and less steep the larger the adopted parameter heterogeneity, as can be seen in Figure 2.4a-b. The increase of synchronization with increasing input drive is slow, as shown in Figure 2.4c. The population frequency and the mean firing rates, on the other hand, increase monotonically (Figure 2.4d-f).

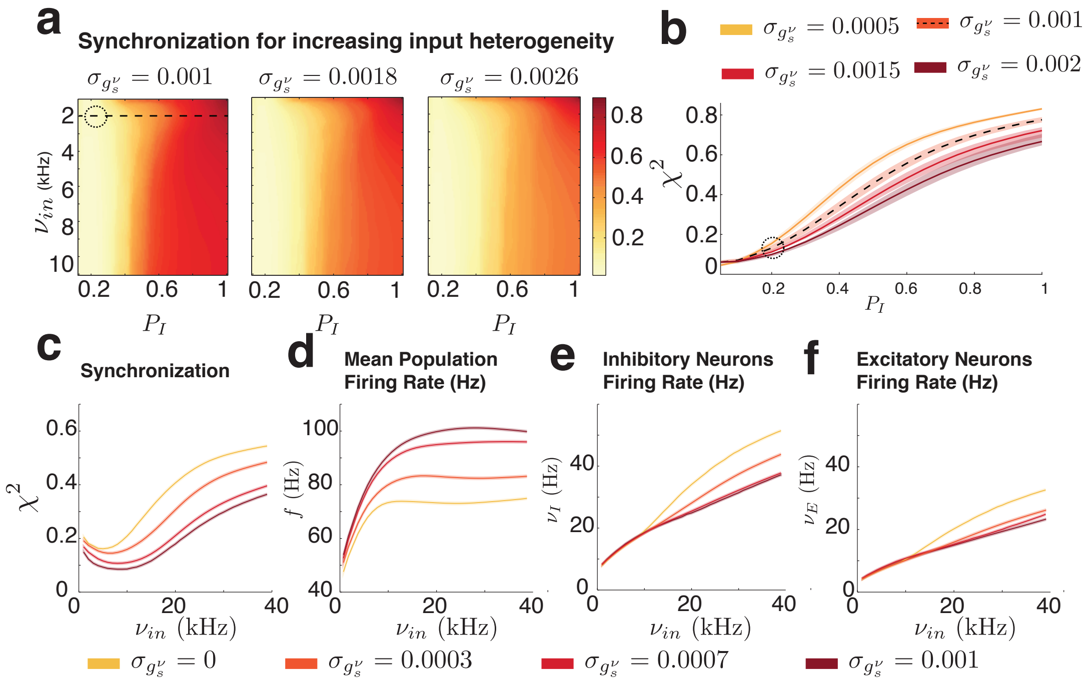

Figure 2.4: Edge-of-synchrony regime dependence on input heterogeneity. Synchronization index for different levels of heterogeneity of the input conductances of the background drive, as measured by the standard deviation $\sigma_{g_s^\nu}$ of the Gaussian-distributed input conductances. **(a)** Dependency of the synchronization index on the rate ν_{in} of the Poisson drive and the probability of making a local inhibitory connection P_I, repeating and extending Figure 2.2 **(a)** for different values of heterogeneity. **(b)** Synchronization index as a function of P_I, for different levels of $\sigma_{g_s^\nu}$. The dashed curve is a cross section of the left panel of **(a)** at a rate $\nu_{in} = 2$ kHz, also indicated with a dashed line . Shaded areas are one standard deviation from the mean of 50 trials. **(c)** Synchronization index (left column) **(d)** Collective oscillation frequency **(e-f)** Single neuron firing rates as a function of the mean Poisson rate of the input for the chosen level different levels of heterogeneity $\sigma_{g_s^{in}}$. The heterogeneity generally favors the synchronous irregular states of the network, while as well reducing the level of synchrony.

We define two working points (circles in Fig. 2.2c–d, 2.3 and 2.4): One with transient synchrony (in black) and a second one at a stronger synchrony level (in light blue), both giving rise to a collective oscillation frequency close to 60 Hz.

Bursts of transient oscillatory power are visible in the LFP spectrogram in the black working point (Fig. 2.2e), while higher synchrony levels, which will be analyzed in detail later, lack this transient nature. Statistical analysis of the duration and frequency of these bursts, (joint distribution is shown in Figure 2.2f) shows that the edge of synchrony regime gives rise to gamma bursts with frequencies broadly distributed over a range between 45 and 75 Hz and a short mean duration close to 100 ms (i.e. four to six oscillation cycles). The simulated distribution is in good agreement with *in vivo* LFP recordings[44,286].

Figure 2.5 shows some classic network statistics of the transient synchrony regime. For a chose neuron the excitatory and inhibitory input currents from the recurrent connections tightly track each other (Fig. 2.5a), and are strongly anti-correlated (Fig. 2.5b). The mean zero lag correlation for the shown set is of ≈ -0.86. The oscillatory nature of the input currents is also appreciable from the cross correlation functions. The spike correlations in the networks are low (Fig. 2.5c), consistent with irregular spiking. The distribution of firing rates, strongly modulated by the heterogeneity in the network, is broad and similar for excitatory and inhibitory neurons, although this last have a higher mean and a longer tail. Despite low spike correlations, membrane's pairwise correlations are higher, and its mean closely follows the value of the synchronization index ξ (Fig. 2.5e). The inter spike interval (panel f), has a heavy tail and differs from exponential by a noticeable bump around ≈ 20 ms, indicating collective oscillatory activity.

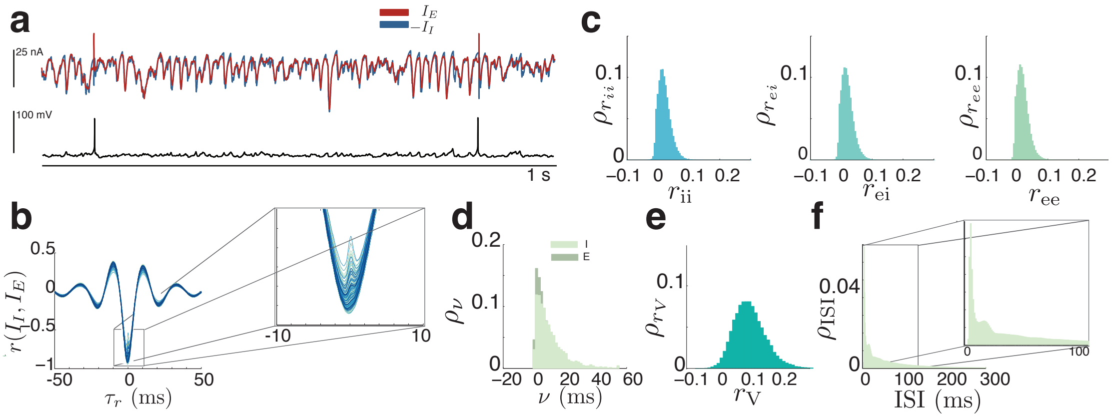

Figure 2.5: Fast tracking of inhibition and excitation at the Edge-of-synchrony regime. Synaptic excitatory (red) and inhibitory (blue, flipped for comparison) current to a randomly chosen excitatory neuron (top). Corresponding membrane potential of the chosen neuron (in mV). **(b)** Cross-correlation between the inputs for 300 excitatory neurons. The inset shows the decrease in absolute correlation due to spikes. **(c)**. Distribution of Pearson correlation coefficient between spike trains of inhibitory neurons, excitatory and inhibitory neurons (middle) and excitatory neurons (right). **(d)** Firing rate distributions, for inhibitory neurons in light green and for excitatory neurons in dark green. **(d)** Distribution of Pearson correlation coefficients between voltage traces of 300 randomly chosen excitatory neurons. **(e)** Inter-Spike-interval distribution. Notice the bump in the inset that hints oscillation.

It is important to underline that the transient synchrony regime should not be considered as a sharp transition line separating two qualitatively distinct regimes. It rather represents a range of parameters (cf. Figs. 2.2–2.4) leading to a qualitatively similar mixed dynamics in which asynchronous and synchronous epochs can both occur stochastically.

In the following we consider multiple brain regions with transient synchrony, linked into simple structural connectivity motifs and analyze their emergent dynamics. In particular, we study their coordinated oscillatory bursting dynamics, their phase locking properties and, finally, test whether these features can subserve the selective and flexible routing of information.

2.2.2 Simultaneous emergence of phase-locked gamma bursts

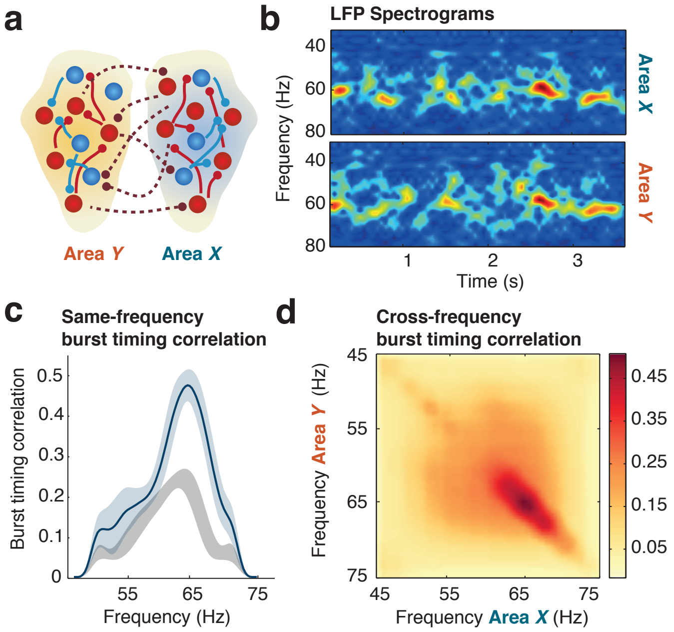

Figure 2.6: Emergent gamma burst tracking. (a) Cartoon of a canonical circuit of two brain regions reciprocally connected through weak long range excitation. **(b)** Spectrograms of LFP activity for coupled networks with transient synchrony. The time and frequency of emergent coordinated bursts are approximately matching in the two coupled regions, as visible in this example. **(c)** Burst-timing correlations between same-frequency gamma bursts in different regions (blue), compared with chance level expectations (grey). Shaded bands denote 95% c.i. **(d)** General burst-timing correlations between oscillatory bursts with dissimilar frequencies. Strict frequency matching is not required for burst timing correlation.

We treated the simplest case of two local circuits (corresponding to two generic areas or regions X and Y), coupled by long range excitatory projections (Fig. 2.6a) that are established with equal probability (P_E^{LR}) and strength in both directions (i.e. X-to-Y and Y-to-X). The seemingly haphazard nature of gamma bursts appears as an obstacle for communication. If the duration and the frequency of oscillatory epochs fluctuate independently in each brain region, observing simultaneous oscillatory bursts in a source and a target region, aligned in a well defined phase relation, might be extremely unlikely. To analyze the inter-region coordination (or lack of thereof) we examined the relative timing, frequencies and phase relationships of gamma bursts in the two connected regions.

Interestingly, we found that our model gives rise to correlated episodes of spontaneous timing and frequency tracking between stochastically-emitted gamma bursts in the two connected regions. This is depicted in the spectrograms of Figure 2.6b. This phenomenon of *burst-tracking* can be quantified by the correlation between the times of occurrence of oscillatory bursts in distinct regions, as a function of their instantaneous frequency (see *Methods* 2.1.3). Figure 2.6c–d reveal that for frequencies in the gamma band, correlations between the timing of bursts with matching frequencies can reach relatively high values, peaking at ~0.5 for nearby collective oscillation frequencies of 60 Hz. Analogous frequency tracking has been observed experimentally[209]. We find that coordination between oscillatory episodes occurs not only between bursts with an exactly matching main frequency (Fig. 2.6c), but even in a cross-frequency manner (Fig. 2.6d).

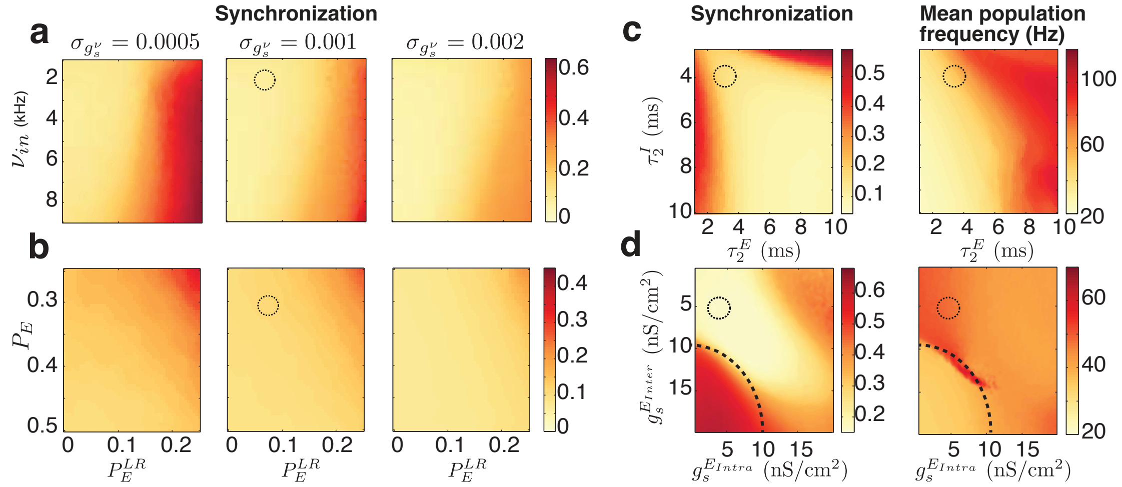

Figure 2.7: Robustness of the transient synchrony regime in coupled networks. (a) Dependence of the synchronization index on the probability of establishing a long range excitatory connection P_E^{LR} and the rate of the Poisson input ν_{in}.**(b)** Dependence of the synchronization index on the probability of establishing a long range excitatory connection P_E^{LR} and the probability of establishing a local excitatory connection P_E. In the range of the studied parameters, synchrony remains low despite the presence of long range excitatory connections, for various levels of input heterogeneity. **(c)** Synchronization index (left) and collective oscillation frequency (right) as a function of the synaptic decay time of inhibition τ_2^I and excitation τ_2^E (See *Methods* eq. 2.4). **(d)** Synchronization index (left) and collective oscillation frequency (right) as a function of the mean excitatory conductances within the network ($g_s^{E_{Intra}}$) and the excitatory conductances for the long range projections ($g_s^{E_{Inter}}$). The dashed line represents a sharp transition to spike-spike synchrony.

It is relevant to underscore, that the level of synchronization of the transient synchrony working point depicted in Figure 2.2, is robust to the extra external input each network receives in the two area motif. The level of synchronization is robust to moderate changes in parameters that depends on the long range excitatory coupling, as the long range probability connection (Fig. 2.7a–b) or the synaptic time constants (panel c). In particular, while an inter-areal excitatory conductance twice as large as a local one induces a transition to spike-spike synchronization, when kept similar in value the level of synchronization in the network remains unaffected (panel d).

Beyond time and frequency coordination, we find that oscillatory bursts also exhibit transient phase synchronization (Fig. 2.8). A time-resolved cross-correlation (XC) analysis of the LFP signals from the two coupled regions of the structural motif is shown in Fig. 2.8a (see *Methods* 2.1.3). Transiently rising values of XC denote the onset of epochs of increased inter-region oscillatory coherence. The time dependent maximum of XC (denoted XC*(t)) occurs at a fluctuating time-lag $\tau^*(t)$, generally different from zero (in-phase, dashed white line) and from the average half period (anti-phase, dashed black line), indicating out-of-phase locking as frequently observed empirically[18]. To quantify this further, we calculated the phases of each of the LFP signals and defined the relative phase between the rhythms, $\Delta\Phi$ (see *Methods* 2.1.4). The relative phase is a strongly fluctuating quantity whose distribution $P(\Delta\Phi)$ is spread out (Fig. 2.8(**b**)).

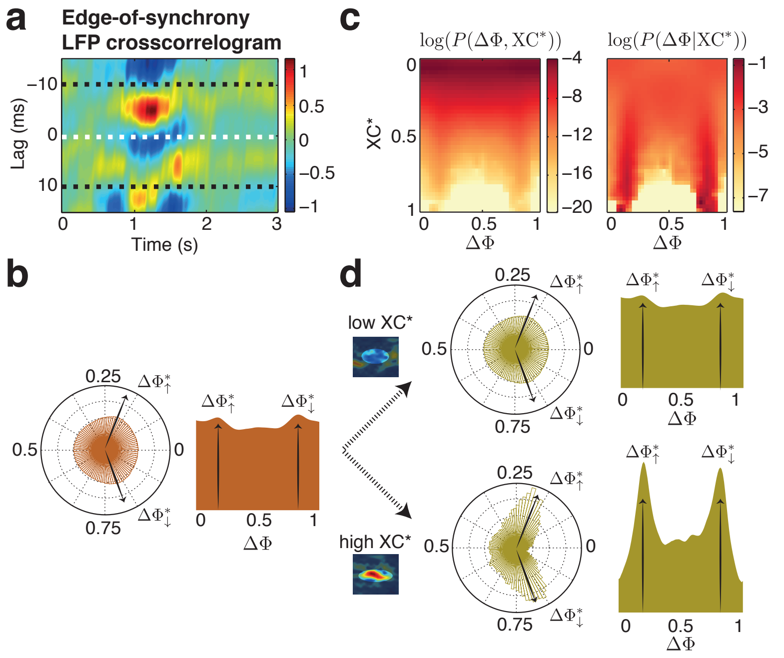

Figure 2.8: Transient phase locking. **(a)** Time-resolved Cross-Correlogram (XC) between simulated LFPs of the two coupled brain regions of Figure 2a (50 ms sliding window). Networks are set at the same synchrony working point. Horizontal dotted lines mark $\tau^* = 0$ ms and $\tau^* = \pm\langle T\rangle/2$, with $\langle T\rangle$ equal to the average period length. The positions of the highest XC maxima, displaced with respect to these guiding lines, reveal the occurrence of transient episodes of inter-areal phase-locking with *out-of-phase* relations. **(b)** Distribution of instantaneous inter-areal phase differences between simulated LFPs, in polar (left) and linearly unwrapped (right) histogram forms. Two peaks at relative phases $\Delta\Phi^*_\downarrow > 0.5$ and $\Delta\Phi^*_\uparrow < 0.5$ can be observed. **(c)** Joint probability distribution of the inter-areal relative phase $\Delta\Phi$ and of the time-dependent maximum XC* of the cross-correlation XC (left). To the right of the same panel, this joint distribution is conditioned on the instantaneous peak cross-correlation XC*. **(d)** Polar histograms of relative phase, conditioned on XC* being lower (upper panel) or higher (bottom panel) than threshold levels (see *Methods* 2.1.5). Relative phases close to $\Delta\Phi^*_\downarrow$ or $\Delta\Phi^*_\uparrow$ tend to be visited when XC* is high.

The precision of phase-locking markedly increases with the instantaneous level of cross-correlation (Fig. 2.8c). As shown by the joint probability distribution of $\Delta\Phi$ and of XC* (Fig. 2.8c, left), events of higher values of XC* are less frequent than low values, but tend to occur at specific relative phases. This phenomenon is revealed by conditioning the joint distribution on the values of XC* (Fig. 2.8c, right). For low values, corresponding to a poorly synchronized baseline activity, the distribution of the relative phase $\Delta\Phi$ remains spread out (Fig. 2.8d). During epochs of strong cross-correlation, however, it becomes prominently bimodal (Fig. 2.8d, bottom).

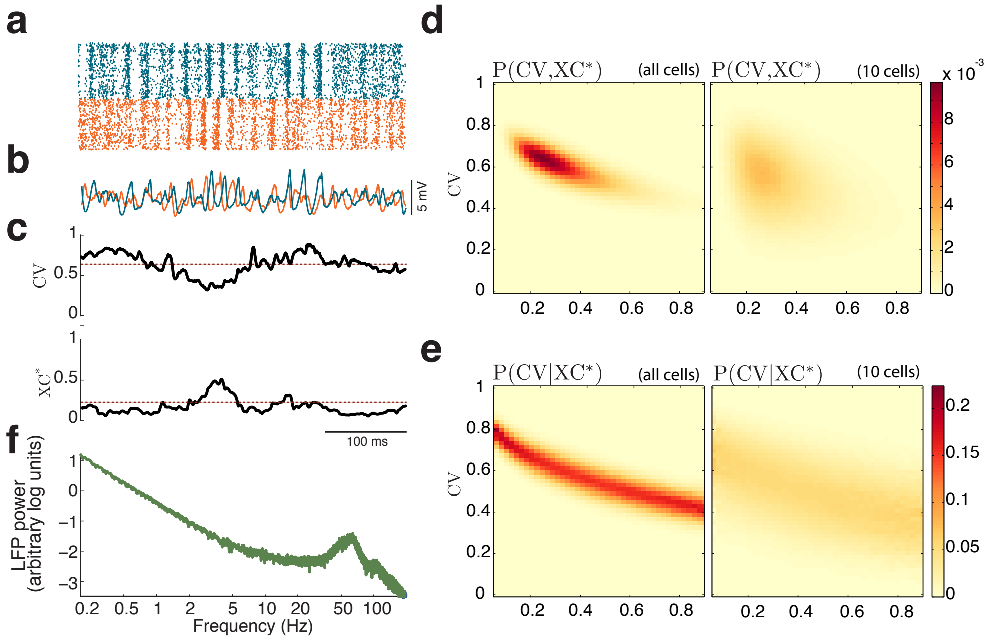

Figure 2.9: Transient modulations of neuronal firing phase-locking. (a) Raster plot of the 2000 excitatory neurons of the X and Y regions in the bi-areal circuit of Figure 2.6. **(b)** Associated LFP traces. Transient oscillatory burst are visible both in the global spiking activity raster and in the LFP. **(c)** The circular variance (CV) of the coupled system as a measure of joint synchrony is be obtained by considering the mean of the circular variances from spikes of 1) all the neurons in each of the populations (CV_{all}), or 2) the spikes coming from only 10 cells of each population(CV_{few}). The full-population circular variance is on average elevated, however it transiently decreases below its average level (dashed line) in correspondence of transients rise of inter-areal oscillatory coherence, as tracked by the time-resolved cross-correlation peak XC* (cf. Figure 2.8). Notice how a single burst in a population but not in the other one is not reflected in the measures of joint synchrony. **(d)** The joint distribution of time-dependent CV_{all} and XC* (left) reveals a very marked peak at low oscillatory coherence and poor phase concentration of firing when the spikes from the complete area are used. The joint distribution of time-dependent CV_{few} and XC* (right) on the other hand shows a diffused peak. **(e)** The distribution of CV_{all} (left), conditioned on observing increasingly larger values of XC* confirms the tendency toward stronger phase-locking of firing during high synchrony transients, commented in panel **c**. The distribution of CV_{few} conditioned on XC* presents a smeared out dependency. **(f)** Time-averaged spectrum of the LFP signal (of region X). The logarithmic scale reveal a gamma-resonance on top of a $1/f$-type decay of LFP power.

High synchrony transients can be appreciated both in the rastergram of the coupled networks as well as in the LFP-like signals of Figure 2.9a-b. Spiking activity is only weakly modulated by oscillations on average. Nevertheless we found that the phase-concentration of neuronal firing, as quantified by the circular variance (see *Methods* 2.1.4) transiently rises to higher values during high XC* transients. The instantaneous circular variances of the distribution of firing phases drops to ∼0.3 during the strongest coherence oscillatory bursts, and rises as high as ∼ 0.8 during inter-burst periods (2.9c). These transients of coordinated synchronization can be estimated both from the maximum value of the time resolved cross correlation XC* or from the CV (panel d). The structure of the distributions of CV estimated based on small cell pools (CV_{few}) is a highly blurred version of the analogous distributions built based on whole populations (CV_{all}). The values of CV estimated based on a few cells will, although matching population-based averages, have a much larger variance, making a precise CV estimation from a few single units more difficult.

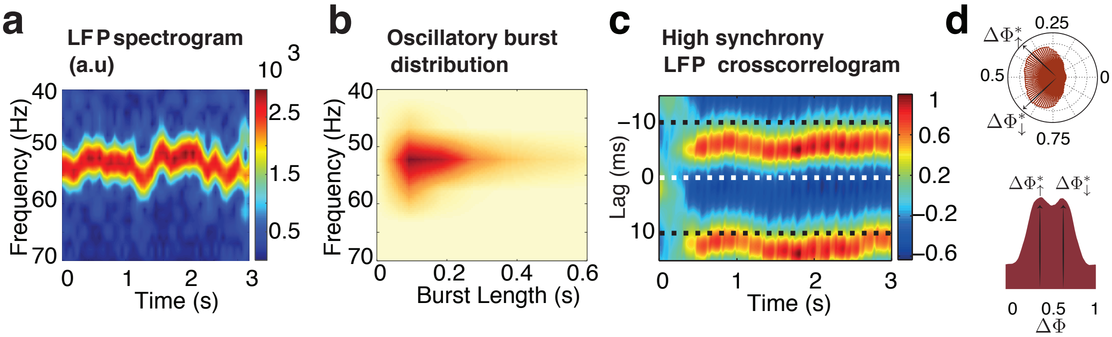

Figure 2.10: High synchrony working point. (a) Spectrogram of LFP-like activity for a single population in a high synchrony regime. The transient oscillatory bursts characteristic from the transient synchrony regime are no longer present in this working point. **(b)** Distribution of gamma bursts for the high synchrony regime. Given that this distributions are obtained by thresholding to the 95% percentile, transitions are still observed, but the length of this episodes of high synchrony are significantly longer. **(c)** Time-resolved XC analysis of simulated LFPs manifest very long lasting episodes of out-of-phase inter-regional phase locking. **(c)** The relative phase distribution reflects strong persistent locking between the activity of the areas. The mild peaks of Figure 3b can be interpreted as "ghosts" of the two prominent out-of-phase peaks shown here.

A summary of the analysis performed in the high synchrony working point of Figure 2.2 can be found in Figure 2.10. This regime generates a persistent power peak in the spectrogram (panel a). The power fluctuations, which do still occur, are nevertheless not enough to reach seemingly desynchronized states (Fig. 2.10a–b). In this working point a similar preference for out-of-phase inter-areal phase-locking is observed. Nevertheless, the simulated LFPs are persistently oscillating and the two phase-locking configurations are close to stable attractors (Fig. 2.10c), giving rise to a bimodal $\Delta\Phi$ distribution, even without conditioning on the values of XC* (Fig. 2.10d). The edge-of-synchrony oscillatory dynamics can be then seen as transiently replicating oscillatory modes that would be stable in the high synchrony regime.

Comparing Figures 2.10d and 2.8d, beyond the evident difference in the locking, it is apparent that the peaks of the bimodal phase distribution are closer to anti-phase ($\Delta\Phi = 0.5$) the higher the level of local inhibition. This feature, that different levels of inhibition lead to different phase locking properties, can be better understood in a rate model of analogous characteristics. In Figure 2.11, the dependence of the phase locking is shown in panel (a) for coupled inhibitory populations connected by long range excitatory axons. Each population obeys an equation of the form $\dot{r}_i = -r_i + [h_{\text{ext}} + K_0 r_i(t - D_{\text{local}}) + K_1 r_j(t - D_{\text{long-range}})]_+$, where r is a rate variable, h_{ext} is an external source of tonic excitation, K_0 is a parameter regulating the self-inhibition and K_1 modulates the long range excitatory interaction. The analytical solution of the phase locking values between the two populations of the rate model was obtained by Battaglia et al.[19] and is reproduced here in Figure 2.11. Including independent white noise in such a model, allows to have a bi-modal distribution of the phase distributions (not shown).

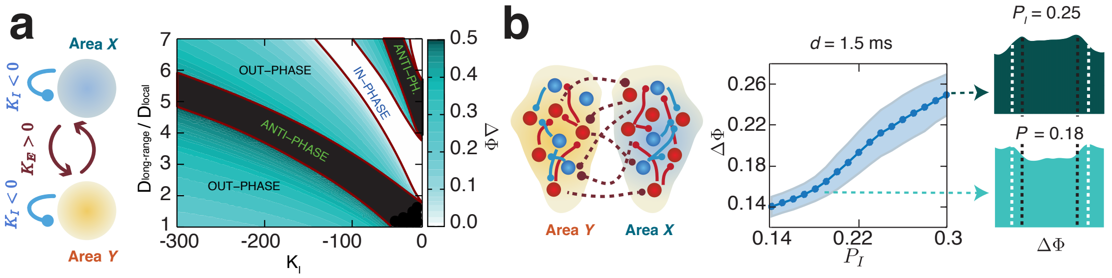

Figure 2.11: Inter-areal phase locking depends on local inhibition. (a) We reproduce here results already published in[19] about a mean-field version of the canonic bi-areal model of Figure 2. The two regions are modeled as simple rate units, with a threshold-linear transfer function, local self-inhibition of strength K_I and mutual long-range excitation of strength K_E. Both local and long-range interactions are delayed, respectively with delays D_{local} and $D_{\text{long-range}}$. The system is predicted to develop phase-locking configurations, with a stable relative phase $\Delta\Phi$ which is not only a function of $D_{\text{long-range}}$, but also of K_I itself, allowing virtually any phase-relation to be stabilized for a given value of conduction delay. Out-of-phase locking tend to be dominant for strong local inhibition. **(b)** Left: canonical circuit as in Figure 2A. Middle column: Mean values of $\Delta\Phi_{\uparrow}$ as a function of local inhibition. Changes in the probability of establishing a inhibitory connection affects the position of the meta stable peak in simulations of the spiking network at the transient synchrony regime studied in Figure 2.

This fact shows that the phase locking properties of coupled networks is not a sole consequence of the synaptic delay, but that is am emergent property of the self organized neuronal dynamics.

2.2.3 Emergence of routing states

Although generic, the canonic two regions motif of Fig. 2.6a may be viewed as representing two interconnected brain regions at two different levels in the cortical structural hierarchy, such as e.g. a sensory and a prefrontal cortical regions (cf. cartoon in Fig. 2.12a) interacting in an attention-modulated manner[103] or a fronto-parietal pair of regions involved in motor planning[55]. It has been observed that the direction of influence can be modulated between such region pairs depending on task and behavioral states[103,46]. We examined how the transient dynamics of gamma bursts emerging in our models (Fig. 2.8) modulate the direction and strength of information flow. We quantify the efficiency and direction of inter-region information exchange of spontaneous activity depending on the system's states, by means of information theoretical analyses.

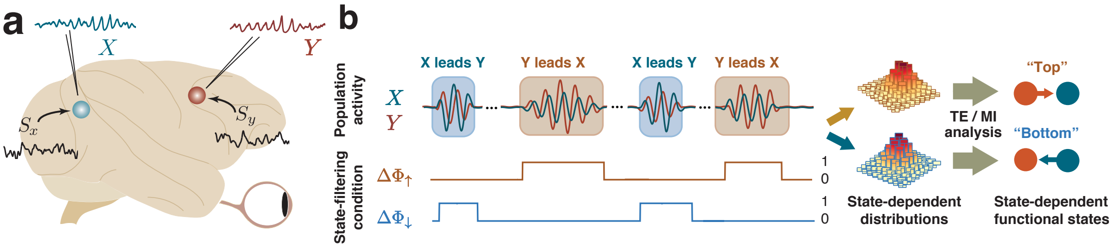

Figure 2.12: Information transfer during transient burst events, the approach. (a) Cartoon of a macaque brain illustrating areas potentially interacting is a manner similar to X and Y, e.g. visual area V4 and frontal eye field FEF, respectively. Inputs to these areas, modeled as correlated random signals S_x and S_y, account for input activity to the cortical areas. **(b)** Cartoon depicting the state-filtering pipeline. LFP epochs fulfilling the tested constraints (in this case concerning the relative phase $\Delta\Phi$) are pooled across time and trials, sampling separate neural activity distributions. State-dependent information transfer direction and efficiency is evaluated using these distributions.

A useful measure is provided by Transfer Entropy (TE)[221,279], here computed based on LFPs from different regions. TE, in a model-free fashion, quantifies how much the knowledge of the past activity of a putative source region improves the prediction of the future activity of a target system and constitutes in this sense a generalization of the Granger Causality approach[28]. The information theoretical setting naturally allows to condition the estimation of Transfer Entropy to an arbitrary set of constraints. We designed *state-selecting filters* that condition information measures on consistent dynamics features and so define a *state-specific directed functional connectivity* (or, in short, *routing state*). As sketched in Figure 2.12b, transients of a system's activity fulfilling specific state-filtering conditions are pooled, through time and trials, into separate statistical samples. Different distributions of activity were obtained from these separate samples, and quantified information theoretically (see *Methods* 2.1.5). Using this approach we probed information transfer through state filters selecting epochs in which the relative phase between the region's rhythms, $\Delta\Phi$, falls in different ranges.

By means of a TE analysis in which the relative phase is constrained to a narrow band, we study state-specific directed functional connectivity between the collective neural activity of the regions X and Y (Fig. 2.13a). For both directions of interaction, TE exhibits a broad peak centered around a specific combination of the interaction delay τ and $\Delta\Phi$ (Fig. 2.13b, see *Methods* 2.1.5). In both panels, the interaction delay τ that maximizes information transmission corresponds to the lag of ~4 ms at which XC(t) peaks during coordinated bursting events (Fig. 2.8a). This optimal delay τ depends on the meta-stable phase of locking ($\Delta\Phi^*_{\uparrow,\downarrow}$, see Fig.2.8) and differs therefore from the mean inter-areal transmission delay $\bar{d}$ of 1.5 ms, as previously discussed (Fig. 2.11).

Optimal functional coupling occurs at different relative phases for different directions

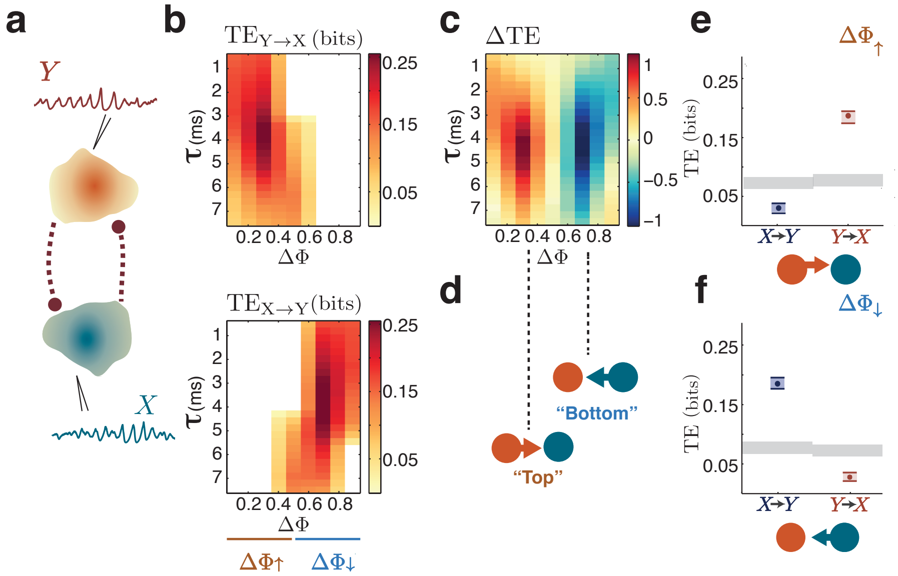

Figure 2.13: Information transfer during transient burst events. (a) Cartoon illustrating the model examined in panels d–h (see also Fig. 2a). **(b)** Maps of Transfer Entropy (TE) between LFPs of the X and Y region, resolved as a function of $\Delta\Phi$ and of different interaction delays τ. White background indicates that TE values do not rise above chance-level. Information transfer is always significantly higher from the phase leading to the phase lagging region than vice versa. **(c)** Functional Anisotropy Index ΔTE. Two lobes of different sign indicate the existence of two distinct *routing* states: *Top* and *Bottom*. They are associated to effectively unidirectional information transfer in opposite directions (graph motif representation in panel **(d)**). **(e–f)** Information transfer in different directions, in a $\Delta\Phi_\uparrow$ configuration (*Top* state, panel **e**) or a $\Delta\Phi_\downarrow$ configuration (*Bottom* state, panel **f**), for the optimal interaction lag. Boxes and shaded bands give 95% c.i. of, respectively, actual TE and chance-level values.

of influence. This phenomenon can be better visualized by the *Functional Anisotropy Index* ΔTE, proportional to $(\mathrm{TE}_{Y\to X} - \mathrm{TE}_{X\to Y})$ (Fig. 2.13c), see *Methods*). Two patches with equal absolute value $|\Delta\mathrm{TE}|$ but different signs correspond to effectively unidirectional configurations with opposite directions (Fig. 2.13d), supported by the same fixed bidirectional structural connectivity. We refer to the states corresponding to these two configurations, filtered by the $\Delta\Phi_\uparrow$ (Y leads X, $0 < \Delta\Phi < 0.5$) and $\Delta\Phi_\downarrow$ (X leads Y and $0.5 < \Delta\Phi < 1$) conditions, as *Top* and *Bottom* routing states respectively. Information transfer proceeds from the region leading in phase to the region lagging in phase, as if long-range synaptic connections from the laggard to the leader region were effectively not functional. This information transfer is in a "top-down" sense (from Y to X) in the *Top* state and "bottom-up" (from X to Y) in the *Bottom* state. Based on the analysis of the relative phase dependency of TE in Figures 2.13(b–d), we also adopted coarser state filtering criteria based solely on the $\Delta\Phi_\uparrow$ and $\Delta\Phi_\downarrow$ conditions. Figure 2.13(e–f) show the net directed information transfer, in the *Top* (Fig. 2.13e), or the *Bottom* routing states (Fig. 2.13f) compared to chance-level expectations (grey band, see *Methods* 2.1.5).

Complementary information to that of Figure 2.13, is presented in Figure 2.14. Figure 2.14a shows the mean TE map as a function of the relative phase for interaction delays lasting a complete gamma cycle. It could be argued that the same hierarchy seen from

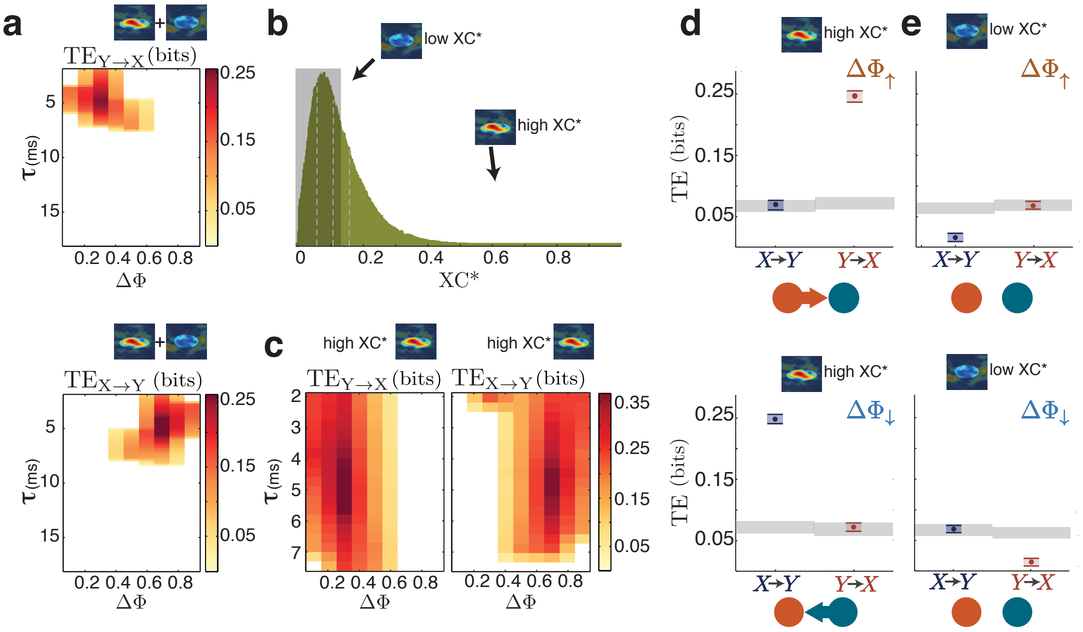

Figure 2.14: Additional characterizations of directed information transfer. **(a)** Maps of mean TE as a function of inter-areal relative phase $\Delta\Phi$ and interaction latency τ, up to larger values of τ. Note that information transfer at a longer latency corresponding to the time between a laggard population oscillation peak and the next oscillation peak of the leader population is not significant. **(b)** Distribution of instantaneous peak crosscorrelation values XC*. Shaded background indicate XC* smaller than the distribution mean. The three vertical dashed lines are, from left to right, -0.5 + median, the median and 0.5 + the median respectively (see *Methods*). **(c–d)** To illustrate the role of the high synchrony episodes in the uni-directionality of information transmission, a phase resolved analysis was performed for epochs in which XC* is larger or smaller than threshold levels (larger or smaller than 0.5 $\pm$ the median, as indicated in panel b, see *Methods*). While information transfer during high-synchrony bursts is boosted, no significant transfer occur in between the bursts epochs. **(c)** Same maps of TE as in Figure 4d, (single trial) but evaluated limited to higher-than-average XC* epochs. Such phase-resolved maps correspond to the coarser analyses of panels d–e. **(d–e)** Information transfer in different directions, in a $\Delta\Phi_{\uparrow}$ condition (*Top* state, upper row) or a $\Delta\Phi_{\downarrow}$ condition (*Bottom* state, lower row) limited to high XC* values, i.e. *within* coordinated gamma bursts **(d)** or to low XC* values, i.e. *between* coordinated gamma bursts **(e)** for the optimal interaction lag. Boxes and shaded bands give 95% c.i. of, respectively, actual TE and chance-level values.

leader to laggard could be established from laggard to leader with an optimal interaction time of the order of a period minus the average distance between the peaks, i.e. of the order of 15-16 ms. In Figure 2.14a we show that information transmission is only statistically significant up to latencies smaller than half an average oscillation cycle and fails to reach significance otherwise.

As episodes of jointly synchronous activity are plausibly those that transmit the larger fraction of information, we further constrained the analysis of information transmission only to transients with large values of joint synchronization. We analyzed epochs of activity in which the value peak XC* rising above (Fig. 2.14d , "inside the bursts") or dropping below (Fig. 2.14e, "outside the bursts") specified threshold levels (see *Methods* 2.1.5). TE is shown as a function of phase and the interaction delay for a "inside the

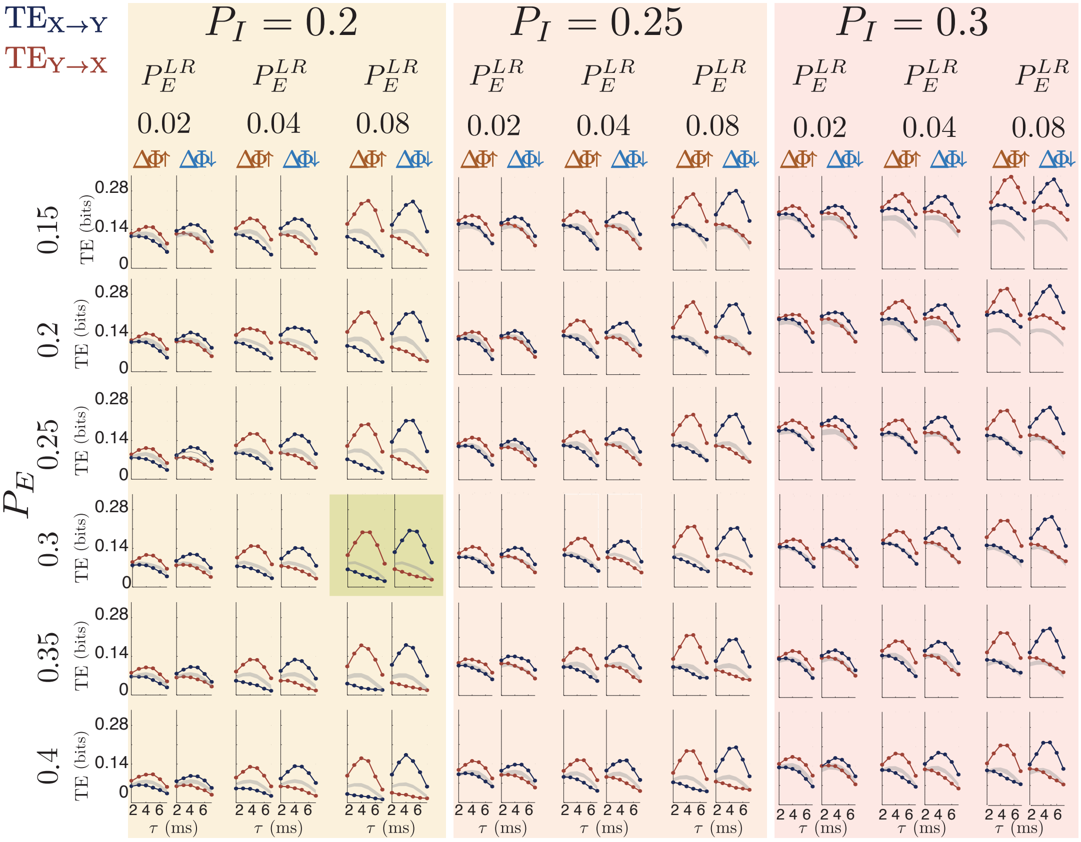

Figure 2.15: Full characterization of directed information transfer (Part 1). For three different values of inhibitory probability connection P_I (in shaded light yellow, orange and red), Transfer Entropy analysis is performed in the *Top* ($\Delta\Phi \uparrow$) and the *Bottom* ($\Delta\Phi \downarrow$) states, as a function of the interaction latency τ. For each P_I value, the dependence of the state dependent information transmission is shown for different values of local excitatory probability connection P_E and inter-areal excitation P_E^{LR}. The panel shaded in green corresponds to the parameters chosen in Figure 2.13. Gray band indicates chance level. We see that for a wide range of parameters (all giving rise to edge-of-sync dynamical behavior) information flows uni-directionally from the phase leading to the phase lagging area.

bursts" configuration in Figure 2.14c. In the "outside the bursts" configuration TE is nowhere significant. As before, a corse grained analysis in which the information transmission is analyzed in the *Top* and the *Bottom* configurations only, reveals that the information anysotropy induced by the phase relation is modulated by the level of synchronization. The instantaneous level of inter-areal synchrony works as a gain control that boosts information transfer in both directions when synchronization is high, and limits it during asynchronous epochs. The areas are functionally disconnected when synchrony is very low, and directed information transfer occurs primarily inside the bursts. This dual mechanisms that can work independently makes the problem of routing conceptually accessible. The direction of information flow can be set by the phase relation while possible distractors can be muted by a suitable regulation of the level of inter areal synchronization. The modulations of functional interactions are explained by the enhanced phase concentration of spiking during high coherence transients (Fig. 2.8 and 2.9), which facilitates post-synaptic depolarization.

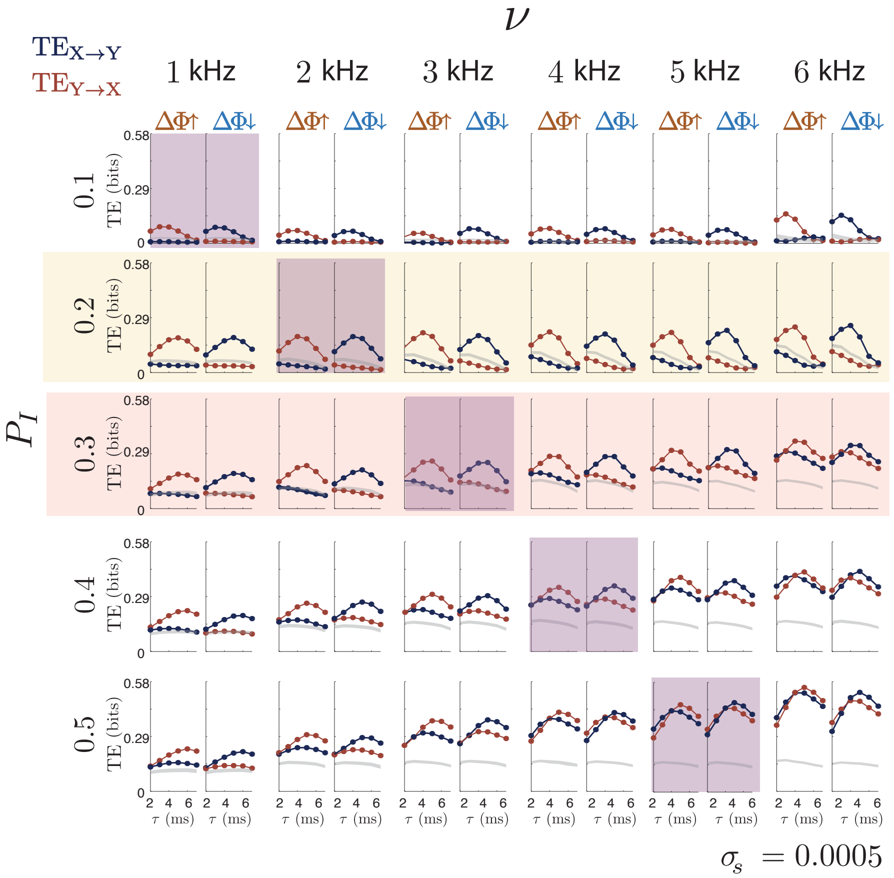

Figure 2.16: Full characterization of directed information transfer (Part 2). For five different values of inhibitory probability connection P_I, single trial Transfer Entropy analysis in the *Top* ($\Delta\Phi\uparrow$) and the *Bottom* ($\Delta\Phi\downarrow$) states, as a function of the interaction latency τ are here shown for different values of the Poisson input rate ν_{in}. The shaded areas in yellow and pink correspond to those shown in Figure S9. The values along the diagonal, shaded in lilac, have a monotonic increase in the synchronization level, and correspond to different points along the curves shown in Figure 2.17)a

Information transfer in the leader-to-laggard direction is highly significant despite the coarseness of the $\Delta\Phi_\downarrow$ and $\Delta\Phi_\uparrow$ conditions. This indicates that the emergence of information transfer anisotropy requires just a weak degree of phase locking. In fact, we find unidirectional transfer of information during *Top* and *Bottom* transients to be robust, persisting within extended ranges of the analyzed parameters (Figs. 2.15 and 2.16). In Figure 2.15, Transfer Entropy in the *Top* and the *Bottom* configurations are shown as a function of the delay for several values of local inhibitory (P_I) and excitatory (P_E) probability connections, as well as long range excitatory connections P_E^{LR}. The higher P_E^{LR}, the larger the difference in information transmission in the *Top* and the *Bottom* states. The effect of the local excitation, on the other hand, is to bring "balance", by effectively reducing the level of local synchronization and therefore restoring the flexibility in schemes that would other wise be too synchronous for it. That balance, does not diminish the difference between the TE values in a single *Top* or *Bottom* state, which remains similar. The increase in the local inhibition P_I form 0.1 (yellow shaded area) to 0.3 (red shaded area) pushes the values of TE above baseline when the values of local excitation are low. To investigate further the effect of inhibition, we computed Transfer Entropy for some of the values of the synchronization map shown in Figure 2.15.

Figure 2.16 explores the impact on the information flexibility as a function of the external input drive and the strength of the local inhibition. The values indicated in 2.15 are shown in shaded yellow and red in . We see that for values of P_I smaller than 0.3, the increase in the drive does not break the flexibility of information transfer. The "diagonal" of this TE matrix, which corresponds to moving along the panels in lilac in Figure 2.16, is shown in Figure 2.17. Figure 2.17a shows TE as a function of synchronization with shaded color bands representing the 95% c.i. and the chance level expectations in gray. As indicated above, the lack of compensatory balance increases the synchronization and disrupts the flexibility of transfer. Effectively unidirectional information transfer is found for broad ranges of inter-areal coupling and synchronization levels (black arrows indicate parameter values in Figure 2.13), replaced by bidirectional but unbalanced functional interactions at strong coupling and/or synchrony. The strength of inter-areal information transfer grows monotonically with the level of synchronization[37]. This growth, however, is fairly slow. Operating at the transient synchrony regime synchrony brings only a small quantitative loss of communication capacity with respect to higher synchrony regimes.

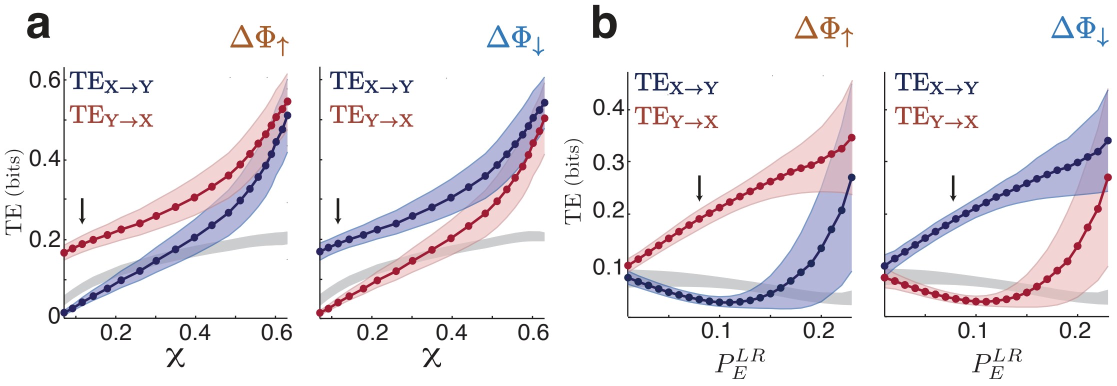

Figure 2.17: Information transfer dependence on synchronization and coupling strength . (a) TE in the *Top* (left) or the *Bottom* (right) states as a function of local networks synchronization (obtained by growing P_I and adjusting ν_{in} to maintain constant firing rate, as following the diagonal of Figure 2.16, shaded lilac area). **(b)** TE in the *Top* (left) and the *Bottom* routing state (right), as a function of the strength of structural inter-areal coupling (growing P_E). This curves correspond to an extended exploration of the parameters corresponding to the green shaded area in Figure 2.15. In both panels, colored lines and surrounding shadings indicate mean TE values and 95% c.i., in comparison with chance-level expectations (gray bands).

As discussed in the Introduction section 1.3.1, two main scenarios have been identified for the generation of oscillations in recurrent networks of spiking neurons. Oscillations can either emerge as an interplay between inhibition and excitation via the pyramidal-interneuron gamma (PING), or by the activation of an inhibitory network in the interneuron gamma (ING). All simulations performed elsewhere in this Chapter correspond to a situation in which both excitatory and inhibitory neurons contribute to determine the oscillation frequency. In Figure 2.18a we focus on a different scenario, enforcing a strictly ING mechanism for oscillation generation by artificially suppressing any local excitatory interaction. By performing a Transfer Entropy analysis on this configuration we show that the routing states associated to different effectively unidirectional information transfer profiles continue to robustly exist.

We have focused so far on using a local field potential (LFP) like signal as a descriptor of the population activity of each of the considered local circuits. This measure, derived as a direct average of the membrane potential of the individual neurons, captures both spiking activity and the sub-threshold oscillations of the neuron's membrane. In the following, we show that the information anisotropy introduced by the relative phase can also be obtained by population measures only based on spiking activity. In Figure 2.18b we show that the TE analysis for multi-unit activity (MUA) like signal (the network's rastergram convolved with a gaussian kernel) yields similar results to those obtained with the LFP-like signal.

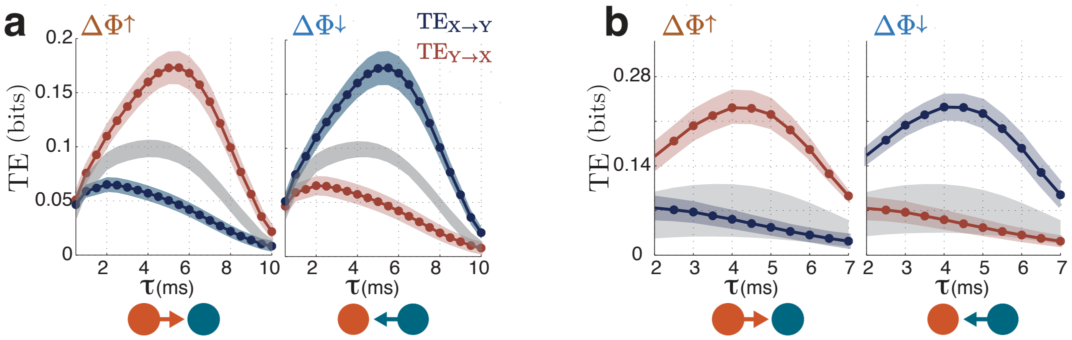

Figure 2.18: Information transmission with ING oscillation mechanisms and with MUA signals instead of LFP. (a) Information transmission as measured by transfer entropy as a function of the interaction latency τ, in a top ($\Delta\Phi\uparrow$, left) and the bottom ($\Delta\Phi\downarrow$, right) states, in a purely inhibitory network. Shaded areas represent the 95% confidence interval, and the grey band the chance level. **(b)** We have so far described the population activity of each of the considered local circuits by an LFP-like signal. Here we show transfer entropy analyses analogous to those of Figure 2.13 e–f, but performed in terms of a Multi-Unit activity-like (MUA) signal. **a** Transfer entropy between MUA signals as a function of the interaction latency τ, in a top ($\Delta\Phi\uparrow$, left) and the bottom ($\Delta\Phi\downarrow$, right) states in a network in the transient synchrony regime. The MUA signals were obtained, as described in the methods, by convolving the spiking activity of each network with a gaussian kernel with standard deviation = 2 ms.

Transfer entropy and delayed mutual information are measures designed to estimate increases in predictability between coupled Markov processes of order k. These measures, by definition, depend on the k previous steps and not only on a single interaction delay as was used in the figures of the present Chapter. More specifically, the estimation of Transfer Entropy was based on the approximation of the past activity history V_Y^k and V_X^l

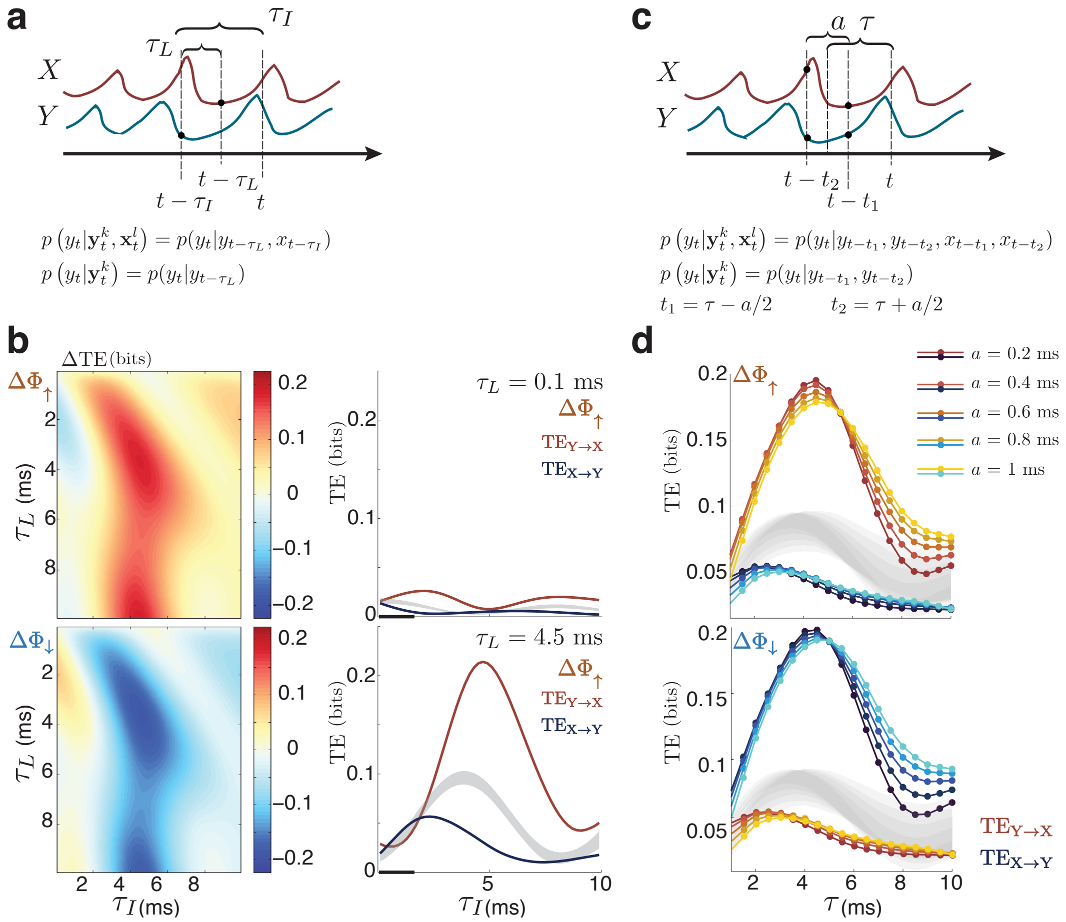

Figure 2.19: Alternative estimation methods for Transfer Entropy. **(a)** The history terms of V_Y^k and V_X^l are evaluated at t-τ_L (local delay) for the target and at t- τ_I (inter-areal interaction time) for the source, instead of a single interaction delay τ for both. The joint probabilities $p\left(y_t|\boldsymbol{y}_t^k,\boldsymbol{x}_t^l\right)$ and $p\left(y_t|\boldsymbol{y}_t^k\right)$ are replaced by $p(y_t|y_{t-\tau_L},x_{t-\tau_I})$ and $p(y_t|y_{t-\tau_L})$ respectively. **(b)** Left panels: ΔTE= $T_{Y\to X}-T_{X\to Y}$ as a function of the local τ_L and the inter-areal interaction delay τ_I in the top (upper row) and the bottom (lower row) states. In a top state TE is predominant from Y to X for all values of τ_L, and markedly peaks at an interaction delay of τ_I around 4 ms. Right panels: TE in both directions in an *Top* state at slices of constant τ_L. In the top row, $\tau_L=0.1$ ms, the sampling time. **(c)** The history terms of V_Y^k and V_X^l are taken at two different past times separated between them by a ms : $t_1=\tau-a/2$ and $t_2=\tau+a/2$. The interaction delays t_1 and t_2, unlike the in panels a-b, are the same for both time series. The joint probabilities $p\left(y_t|\boldsymbol{y}_t^k,\boldsymbol{x}_t^l\right)$ and $p\left(y_t|\boldsymbol{y}_t^k\right)$ are replaced by $p(y_t|y_{t-\tau+a/2},y_{t-\tau-a/2},x_{t-\tau+a/2},x_{t-\tau-a/2})$ and $p(y_t|y_{t-\tau+a/2},y_{t-\tau-a/2})$ respectively. Notice that now a 5-dimensional histogram is needed to estimate the joint probability distributions. **(d)** Transfer Entropy from Y to X (red palette) and from X to Y (blue palette) in a *Top* (upper row) and a *Bottom* (bottom row) states as a function of the intermediate interaction delay τ for different values of separation between the considered points a. The estimations are based on a single 10 min long trial, for clarity of illustration.

with observations at a single past time $V_{X,Y}(t-\tau)$ (see Methods 2.1.5). The inclusion of such simplification meant replacing the joint histogram terms $p\left(y_t|\boldsymbol{y}_t^k,\boldsymbol{x}_t^l\right)$ and $p\left(y_t|\boldsymbol{y}_t^k\right)$ in eq. (2.7) by $p(y_t|y_{t-\tau},x_{t-\tau})$ and $p(y_t|y_{t-\tau})$ respectively. This figure explores two different ways of approximating the history of the time series V_Y^k and V_X^l. In Figure 2.19a-b, we show that the estimation is robust to taking different interaction delays to evaluate the history of the activity of the coupled networks. One interaction delay, τ_L is taken to evaluate the history of the *local* circuit (i.e. when analyzing $TE_{Y \to X}$, τ_L refers to the interaction delay of X). τ_I on the other hand, is the inter-areal interaction delay. We can see that for all values of τ_L, $= TE_{Y \to X} - TE_{X \to Y}$ peaks at a value of τ_I=5 ms. For the minimum possible interaction delay (the integration time), and as discussed in[130], taking the local delay equal to the sampling time allows to re obtain the (mean) synaptic delay between the areas (d=1.5 ms, indicated as a black bar in the x-axis) at the peak of the inter-areal interaction delay τ_I. In the bottom row, a slice at τ_L=4.5 ms is shown. In Figure 2.19c-d, an analogous analysis is made, while taking into consideration two possible interaction delays, instead of a single one. The inclusion of several past times essentially leaves unchanged the TE estimation values.

2.2.4 Emergent routing of information streams

The existence of a phase gated dynamic switching between *Top* and *Bottom* routing states only starts to address the question of routing. In particular, it is not obvious that streams of external information entering the circuits are routed in a fashion similar to the spontaneous activity analyzed so far. To examine this aspect in our models, we introduce external input currents S_x and S_y modeling incoming activity from surrounding areas or carrying information about sensory stimulation (Fig. 2.20a). We modeled the input signals as $S(t) = g\Phi(t)$ where $\Phi(t)$ is Gaussian random field (see *Methods* 2.1.6) with autocorrelation $C(t) = 1/\cosh(\frac{t}{\tau_s})$. The fraction of power p contained in the spectrum up to a cut off frequency f_c, is given by Eq (2.21) (for example, for $p = 0.9$, $f_c \approx \frac{5}{2\pi^2\tau_s}$). For a value of $\tau_s = 0.5$ ms, that cut off is around the 500 Hz, while when $\tau_s = 5$ ms, f_c will be around 50 Hz. For an intermediate value of $\tau_s = 1$ ms, we re-analyzed the burst coordination properties observed in the isolated case of Figure 2.6. The inclusion of external signals does not interfere with the burst tracking phenomenon (Fig. 2.20b), but enlarges the frequency range in which this coordination takes place (Fig. 2.20c). The frequencies of the LFP signals, together with the frequency range in which they coordinate, is shifted to lower values (panels b-d).

We then study how these injected input streams propagate through the interconnected regions conditional on the instantaneously active routing states. An exhaustive analysis as a function of the sensory input parameters g and τ_s, unveils that there is a broad parameter range in which information about the input to a source area S_x (or S_y) can be read out from an output area Y(or X) (colored panels around Fig. 2.21a). When the input becomes too strong (the gain parameter g is large), the network becomes synchronous, driving the single units strongly (Fig. 2.21a-b). We note that the increase of the amplitude of the input signals generally decreases the frequency of the network while increasing the firing rates (Fig. 2.21b-c), leading to states of higher synchrony. This frequency reduction should be contrasted to the effect in the population frequency that has an increase in the rate of the *independent* Poisson process that every neuron receives (see Fig.2.2d). An increase in the input to the neurons, leads in both cases to increasing firing rates and synchronization levels, but while an independent input leads to higher population frequency, a fully correlated one, in this case leads to a frequency reduction.

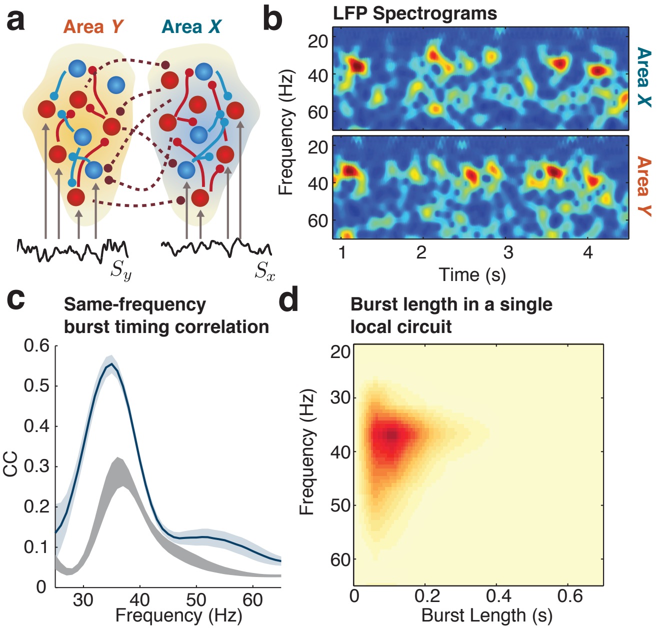

Figure 2.20: Characterization of the transient synchrony regime with input streams. (a) Cartoon of a canonical circuit of two brain regions receiving a continuous random signal. All neurons of each network receive, besides the independent background Poisson input, the *same* random input signal S_x in X and S_y in Y independent between them. **(b)** Spectrograms of LFP activity for coupled networks with transient synchrony receiving independent input. The time and frequency of emergent gamma bursts remains coordinated. **(c)** Burst-timing correlations between same-frequency gamma bursts in different regions (blue), compared with chance level expectations (grey). Burst timing correlations are significant over a frequency range further expanded with respect to Figure 2.6c. Shaded bands denote 95% c.i.. **(d)** Joint distribution of the frequencies and durations of gamma bursts. The average duration of bursts remains short, of the order of 100 ms, but the frequency spread is even larger than in the not-driven case featured in Fig. 2.2(f). Note also that the frequency range is shifted toward lower values.

The addition of external smooth inputs, even for a intermediate level of synchrony ($g = 2$,$\tau_s = 1$ ms) does not modify the system's states defined by TE, which remain markedly unidirectional (Fig. 2.22c). Nevertheless, non-smooth inputs like OU processes (see Methods 2.1.6) lead to high synchrony levels that cannot be compensated by reducing the local inhibition, and therefore TE is significant both from leader to laggard and form laggard to leader, although a marked asymmetry between the *Top* and *Bottom* states still persists (Fig. 2.22d). State-resolved information theoretical analysis between the input streams S_y (or S_x) to the receiver region Y (or X) and the neuronal activity of the target region X (or Y), revealed that the information injected into a source region propagated towards an inter-connected distant target following the path imposed by the

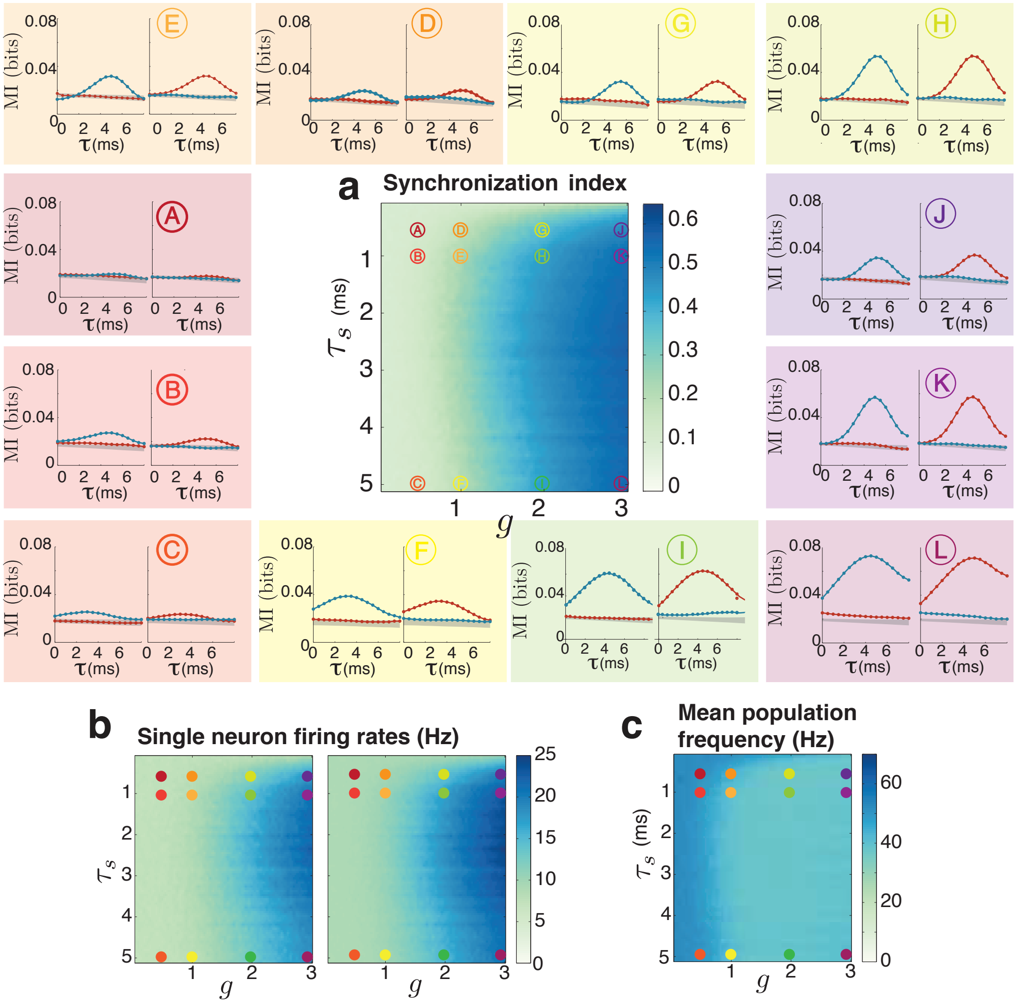

Figure 2.21: Characterization of the transient synchrony regime response to input streams of different characteristics. (a) Synchronization index as a function of the input gain g and the correlation time τ_s of the input. For some selected configurations, the Mutual Information between the input to an area S_x (or S_y) and the LFP signal of the target one Y(or X) is as well shown as a function of the interaction delay τ_s in the *Top* and *Bottom* states, still defined through the phase relation $\Delta\Phi$ of the LFP-like signals. **(b)** Mean firing rate for the excitatory (left) and inhibitory (right) neuronal populations. **(c)** Mean frequency of the LFP signal.

routing states, defined by the state-specific TE analysis. As shown in Figure 2.22e for smooth inputs and Figure 2.22f for OU inputs, when in a *Top* state, information about the input injected into a the source area Y is uni-directionally transmitted to X, while there is no information being transmitted about the input injected into X. This is also seen by the state-filtered MI information measure as shown in panels g and h. Although in the OU case, the directed functional connectivity between the regions estimated by TE between LFPs is bidirectional, the propagation of the externally-supplied signals remains to be unidirectional.

To summarize, the analysis of transfer entropy between LFP like signals allows to

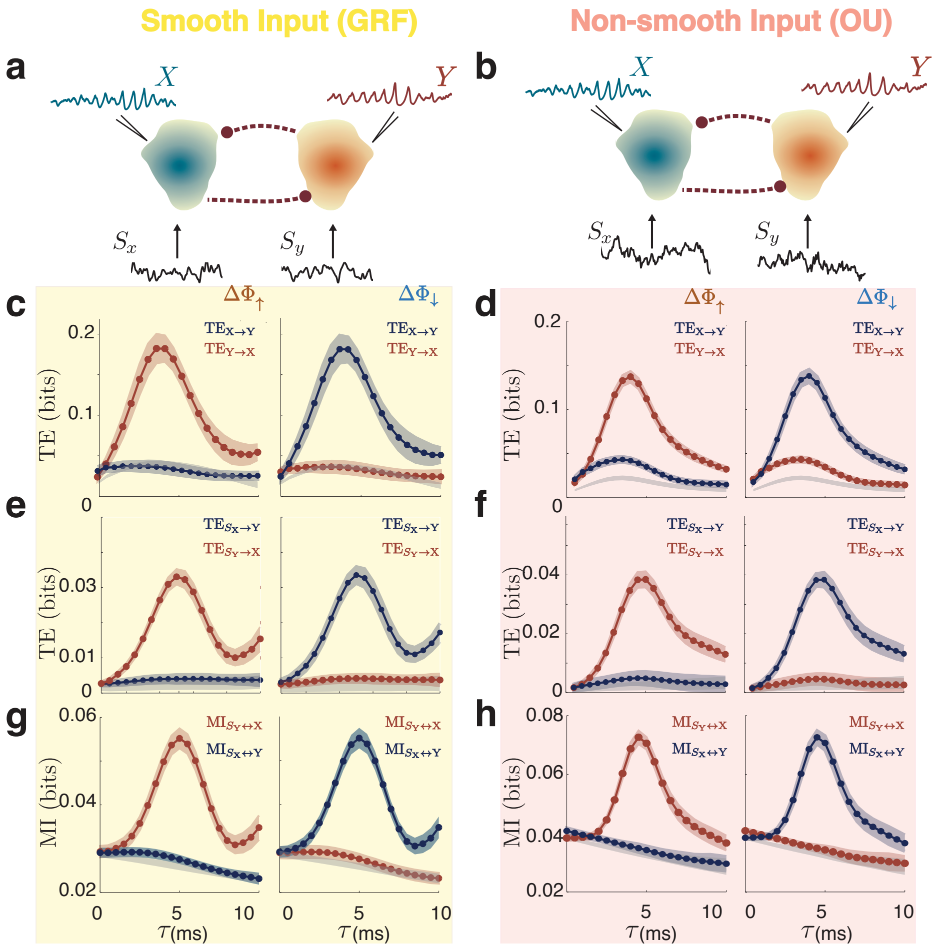

Figure 2.22: Routing of input signals between two coupled regions. **(a)** Architecture as in Figure 2.6, networks are symmetrically connected with long range excitatory projections to both inhibitory and excitatory neurons. In this case the input is modeled as a gaussian random field (see *Methods* 2.1.6 and text). **(b)** Mutual Information (MI) between the input signal to the source region and the LFP-like activity signal from the target region as a function of the interaction latency (see *Methods*). They are shown for the *Top* (left) and *Bottom* (right) states, still defined through the phase relation $\Delta\Phi$ of the LFP-like signals. MI between the input to the source region and the target area's activity is only significant when the source region is leading the target region in phase. Transmission of the externally-supplied input signals is regulated by the phase relation between the interacting regions. **(c)** Transfer Entropy between the LFP signals of the interacting regions as a function of the interaction latency τ, for this driven case in *Top* (left) and *Bottom* (right) states. **(d)** Transfer Entropy from the input signal to the source region to the target area, in *Top* (left) and *Bottom* (right) states. Input specific information is selectively gated deepening on the phase configuration of the LFP rhythm. **(e-h)** Same analyses as in panels **(a-d)** but performed with a different input noise model. Input signals are modeled as an Orstein-Uhlenbeck process (see *Methods* 2.1.6) with variance $\sigma^2 = \frac{g^2}{2\gamma}$ with $\gamma = 1$ and $g = 0.1$. Note that in the case of OU inputs, the levels of synchronization reached by the network are higher(0.6) and far from transient synchrony .

quantify how much information about the spontaneous activity is transferred from a source region to a target one without specifications on the nature of the information being transmitted (functional connectivity). Here we showed that the same mechanisms that regulate the information transmission of endogenously generated network activity, is the one that regulates the transmission of specific, input-related information.

2.2.5 The routing problem in a selective attention setting

Next, we extended the model to include three interconnected regions with transient synchrony, X, Y and Z. As shown in Figure 2.23, the state-selection procedure can be extended straightforwardly to this case. The three region architecture enabled us to study a setting typical of visual selective attention experiments[106,26,105], as the ones described in the Introduction in section 1.1.4. For instance, we considered a situation in which two distinct visual stimuli —potentially with super-imposed noise flicker[106]— are coded for by distinct populations X and Z in lower-order areas such as parts of V1, whose distinct receptive fields both fall within the larger field of a third population Y in a higher order area such as V4 (Fig. 2.23b). With increasing number of involved areas, the complexity of the states defined by the rhythm's phase relations increases, requiring a refinement of the state filtering conditions to match the new possible configurations.

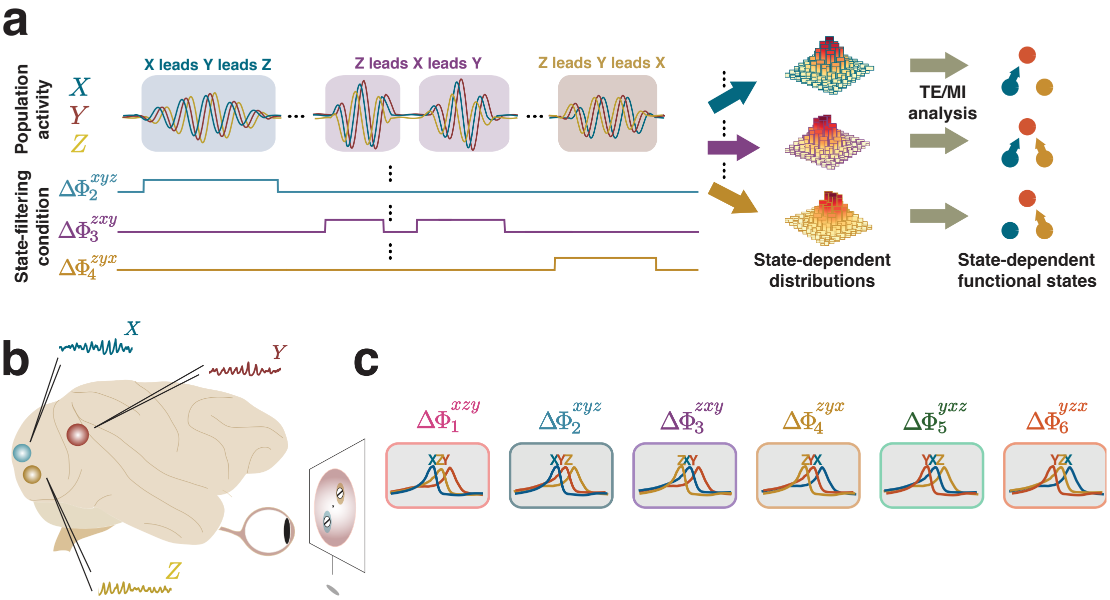

Figure 2.23: State selecting filtering conditions of three regions architectures. **(a)** Cartoon showing the state filtering pipeline for three interconnected regions. Six state filters are defined for all the permutations of XZY.**(b)** Cartoon of a macaque brain, with three recoding sites, the brown and the blue in primary visual cortex V1, and the red one in extra-striate cortex V4. Also indicated: screen with two stimuli and a fixation point and the receptive fields of the recording sites in matched colors. **(c)** In systems involving N regions, the quantity of state selecting filters scales as $N!$. In a three population area, there are six possible phase hierarchies, which define six information constraining filters denoted by $\Delta\Phi_1^{xzy}$ to $\Delta\Phi_6^{yxz}$ (superscript indicates the 'order' of the signals in the given configuration, $\Delta\Phi_1^{xzy}$ reads: Phase configuration in which X leads Z that leads Y. (See *Methods*, equation (2.11)).

The six state selecting filters for a three region scheme, numbered from $\Delta\Phi_1$ to $\Delta\Phi_6$, are shown in Figure 2.23c. Each one represents a dynamic configuration constraining the routes of information transmission. A directed functional connectivity analysis of the three region model is shown in Fig. 2.24 for two different network architectures.

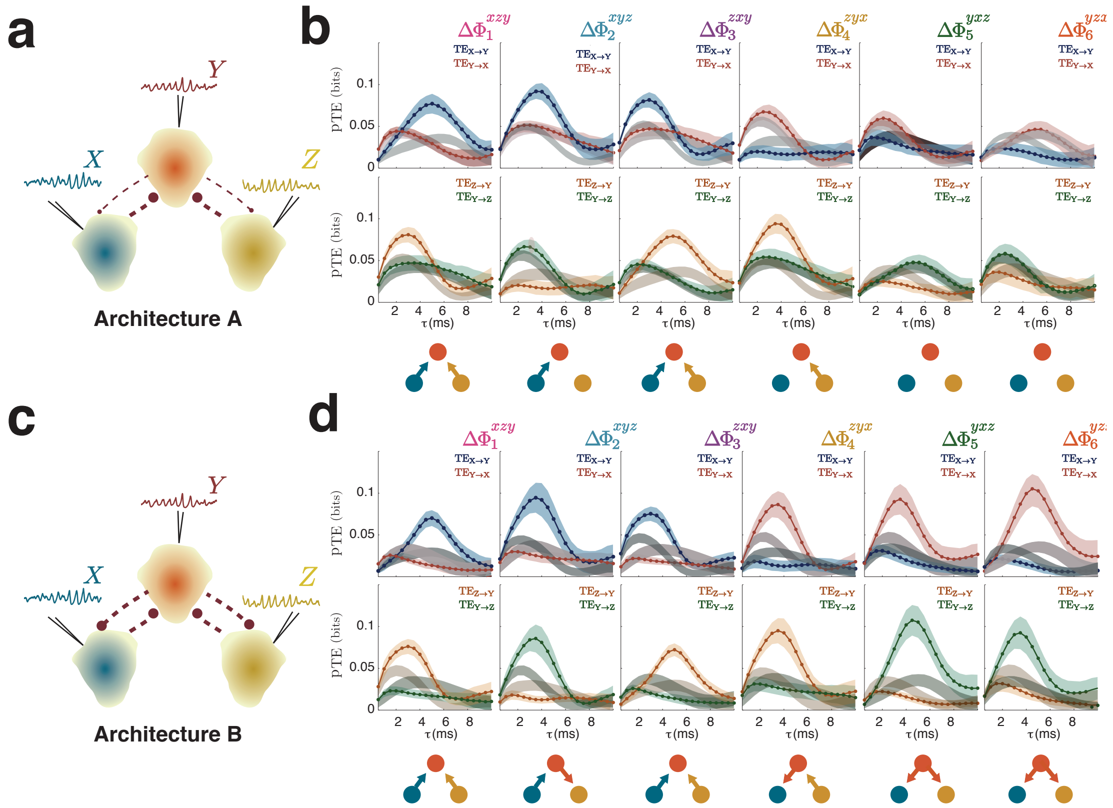

Figure 2.24: Information transfer between three regions. **(a)** Three region circuit in which feed-forward connections from upstream regions X and Z are stronger than feed-back connections from the downstream region Y. **(b)** Partial Transfer Entropy (See Methods, equation 2.10) from X to Y (blue), from Y to X (dark red), from Z to Y (brown) and from Y to Z (green) in the six possible configurations. The dark shading bands correspond to chance levels, different for each of the directions in matching colors. We see that when X and Z are both leading in phase on Y (states $\Delta\Phi_1$ and $\Delta\Phi_3$), both regions can transmit information to Y, while pTE from Y to X and Z remains at chance level. Depending on which is the phase configuration the optimal lag for information transmission differs. When the activity of the target region Y is between the senders, we can recover uni-directional information transmission from a single region (states $\Delta\Phi_2$ and $\Delta\Phi_4$). **(c)** Symmetric, three-region structural motif in which feed-forward and feed-back structural projections are equally strong. In this case, as shown by panel **(d)**, additional routing states arise, associated to new directed functional connectivity motifs. Significant information transfer can also occur from the downstream region Y to one of the upstream regions (states $\Delta\Phi_2$ and $\Delta\Phi_4$), or to both (states $\Delta\Phi_5$ and $\Delta\Phi_6$).

A predominantly feed forward architecture (**A**), in which two primary areas (X and Z) project to a downstream target Y with a higher strength than that of the feedback (i.e from Y to X and Z), is depicted in a cartoon in Figure 2.24a. A second possible, 'symmetric' architecture (**B**), in which the strength of the long range excitatory connections is equal between the areas, is shown in Figure 2.24c. TE analysis between the LFP signals of the three coupled regions show that multiple routing states can arise depending on the phase pattern. The routing states defined by the phase configurations $\Delta\Phi_2^{xyz}$ and $\Delta\Phi_4^{zyx}$, exhibit a unique asymmetry between the primary areas, in which one of them is leader and the other one is laggard with respect to the target area Y. These phase configurations allow for a selective control of the information transmission from afferent inputs, effectively blocking competing information channels during the transient episodes. In architecture (**A**), uni-directional information transmission is of a merely bottom up nature, as TE is only significant from X to Y ($\Delta\Phi_2^{xyz}$) or from Y to X ($\Delta\Phi_4^{zyx}$). In architecture (**B**), there is as well a top-down like control from Y to the area lagging in phase. Configurations in which both the primary areas lead in phase the downstream area ($\Delta\Phi_1$ and $\Delta\Phi_3$), result in convergent (bottom-up like) information transmission in both architectures (**A**) and (**B**), as represented by the convergent motif obtained from the transfer entropy analysis. It is worth to highlight, that although the downstream area simultaneously receives and therefore integrates information from its afferent inputs, the peak information transmission occurs at different interaction latencies, keeping a temporal segregation between them. The configurations in which the target area Y leads in phase to both X and Z ($\Delta\Phi_5$ and $\Delta\Phi_6$), leads to either a disconnected motif in the architecture (**A**) or to a purely top-down like control in the symmetric network (**B**).

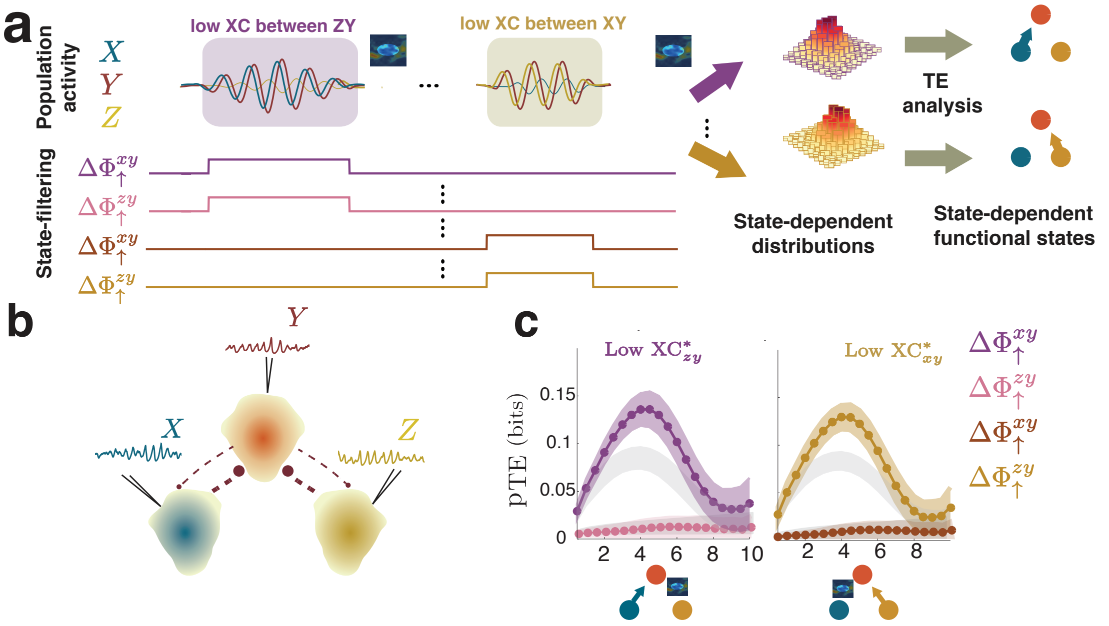

Figure 2.25: Information transfer between three regions, alternative model. (a) Alternative state selecting filtering procedure for a three area scheme. Episodes with low XC* between Z and Y (i.e. XC$^*_{ZY}$) are pulled separately, and later classified in *Top*$_{\mathrm{XY}}$, *Bottom*$_{\mathrm{XY}}$, *Top*$_{\mathrm{ZY}}$, *Bottom*$_{\mathrm{ZY}}$ in the . Analogously, this four states can be as well defined when XC$^*_{XY}$ is low. Transfer Entropy is then calculated in this eight states. **(b)** Three region circuit in which feed-forward connections from upstream regions X and Z are stronger than feed-back connections from the downstream region Y. **(c)** (left) Partial Transfer Entropy between X and Y, while X leads Y (i.e. a *Top*$_{\mathrm{XY}}$, in violet) and between Z and Y, while Z leads Y (i.e. a *Top*$_{\mathrm{ZY}}$, in pink), in a low XC$^*_{ZY}$ configuration. Information transmission is only significant from X to Y. All the other configurations (i.e. both *Bottom* and TE from Y to Z and X) are non significant. (right) Partial Transfer Entropy between Z and Y, while Z leads Y (i.e. a *Top*$_{\mathrm{ZY}}$, in light brown) and between X and Y, while X leads Y (i.e. a *Top*$_{\mathrm{XY}}$, in dar brown), in a low XC$^*_{XY}$ configuration. Information transmission is only significant from Z to Y.

The routing scheme shown in Figure 2.24 is based solely on constraining the phase relation between the LFP signals of the involved areas. Although at the transient synchrony regime such a scheme offers configurations that enable unidirectional information transmission despite the presence of distractors, it does not exploit the fluctuating coherence of the rhythms for such a selection. Analogously to the two population case, an alternative routing mechanism, based both on the phase relation and the level of synchrony of the involved regions can be proposed. In this scheme, we analyze the information transmission form X (Z) to Y, depending on their phase relation but conditioned on Z (X) and Y to have low joint synchrony. The state-selecting filtering pipeline is shown for this case in Figure 2.25a. For each pair (X and Y or Z and Y), *Top* and *Bottom* states can be obtained constrained on the level of coherence of the competing population. For a asymmetric three area architecture (panel b), is shown that when Z and Y are "outside the burst", information is transferred uni-directionally from X to Y in a *Top* state, while no information is being transferred from Z to Y, and neither form Y to X or Z in the bottom state, given the asymmetry of the connectivity. When X and Y are "outside the burst", then information is transmitted uni-directionally from Z to Y. The level of synchronization and the phase relation can work as separate mechanisms that gate information in a selective manner. By relaxing the conditions on the phase relations, the scheme becomes scalable to large amount of connected areas.

In order to fully address the routing problem in a selective attention like set up, input streams were injected to each neuron in the lower (V1-like) areas modeling sensory input, and in the V4 area, representing feedback information (Fig. 2.26a–b). Typically in these experiments (see Introduction section 1.1.4), the focus of attention is alternatively directed to one stimulus or the other, defining an information routing problem in which the transmission toward Y of the input stream S arising to X (or Z), associated to the attended stimulus must be enhanced, while the other unattended stream arising to Z (or X) should be gated off.

An information theoretical analysis of the full model is shown in Figure 2.26c–d. We focus first on the routing of the signals S_x and S_z, coding for different stimuli. In a phase configuration in which X leads Y, being Z a laggard of the dynamics, only information about the input streams S_x is present in the downstream region Y (panel c, left) although no other mechanism besides an unsuitable phase relation prevents information about S_z to be present in Y. Analogously, when Z leads Y, being X a laggard of the dynamics, only information about the input streams S_z is present in the downstream region Y (panel c, right). Switching between the transient phase-locking patterns associated to the two $\Delta\Phi_2^{xyz}$ and $\Delta\Phi_4^{zyx}$ conditions thus produces rerouting effects analogous to the ones which would be associated to a re-orientation of the attentional spotlight. The complete analysis of the system is shown in panel d. We see that, as in *autonomous* case where no input signals was included (Fig. 2.24), there are routing states ($\Delta\Phi_1$ and $\Delta\Phi_3$) in which the downstream area Y receives information coming from both sensory stimuli, that can still be segregated temporally.

A full repertoire of dynamical states and corresponding information motifs are found through the conditions imposed by the phase hierarchies. Information can be selectively and uni-directionally transmitted by a single input area among several afferent inputs to a target area depending on the phase relation between the rhythms.

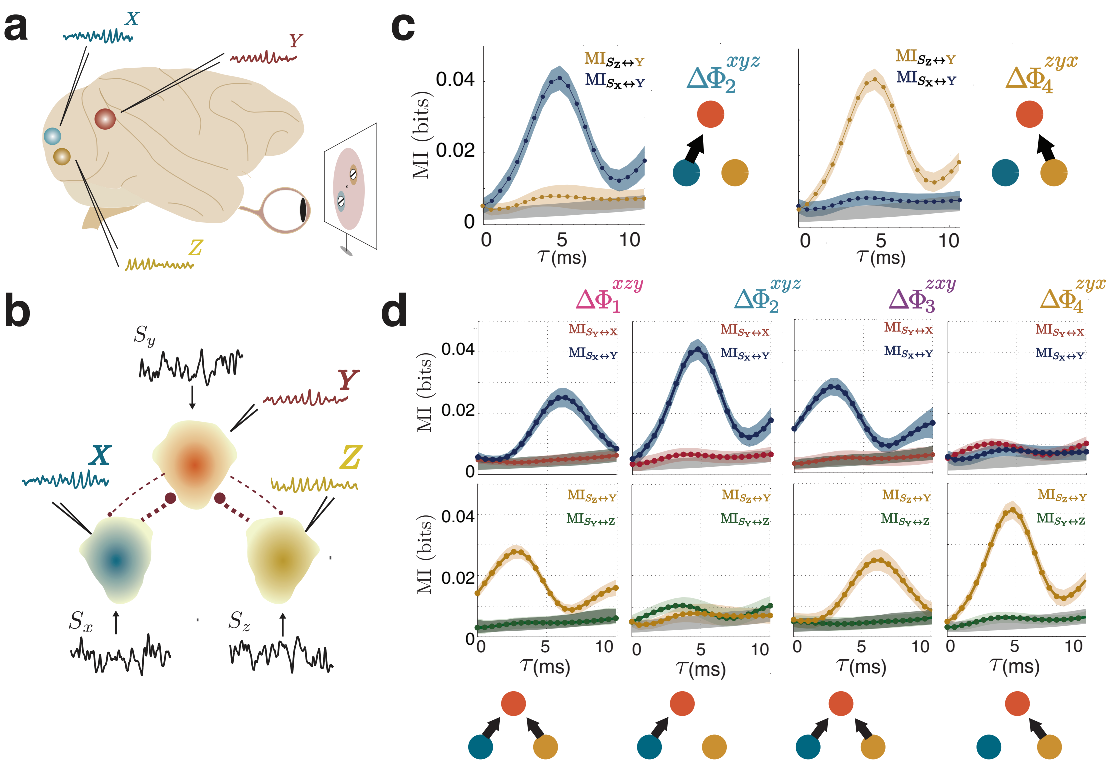

Figure 2.26: Routing of input signals in a selective attention paradigm. Sensory input $S_{X,Z}$ to primary regions X and Z, or top down input signals to Y S_Y, are integrated in the system of Figure S14a and modeled as independent and smooth random fields identical to those of Figure 14a–d. Information conveyed by input signals is routed accordingly to the phase relation between the population activity of the involved regions. **(a-b)** Full model. Each region in the model receives an independent input signal modeled as a gaussian random signal (see *Methods*). For visual clarity only that S_x and S_z are shown. **(c)** Left: Mutual information between the input signal to the source region S_x and the LFP activity of a target region Y as a function of the interaction delay (blue curve) is strongly enhanced in the associated phase configuration $\Delta\Phi_2^{xyz}$. This configuration has an effect similar to attention being directed towards the stimulus over the blue receptive field (RF). No significant information is present in the V4 site from the signal S_z, representing the non attended stimulus. Right: Phase configuration $\Delta\Phi_4^{zyx}$, analogous to attention being directed to the stimulus over the brown RF. Information of the competing stimulus again is non significant. Mutual information between the activity of V4 and the input signal S_y is systematically increased and reaches a maximum at an interaction delay. The state functional connectivity is indicated by motifs next to the graphs. **(d)** Complementary information to the shown in panel (c). Analogously to what is shown in Figure 2.24, when the downstream region Y lags in phase the activity of both regions X and Y ($\Delta\Phi_1, \Delta\Phi_3$), both input signals to X and Z can be simultaneously transmitted with different peak interaction latencies.

2.2.6 Controlling information routing

In the examples of all figures above, transients of the different phase-locking types — *Top* and *Bottom* for the two region model and $\Delta\Phi_1$ to $\Delta\Phi_6$ for tree region model — spontaneously arise with similar probabilities of occurrence.

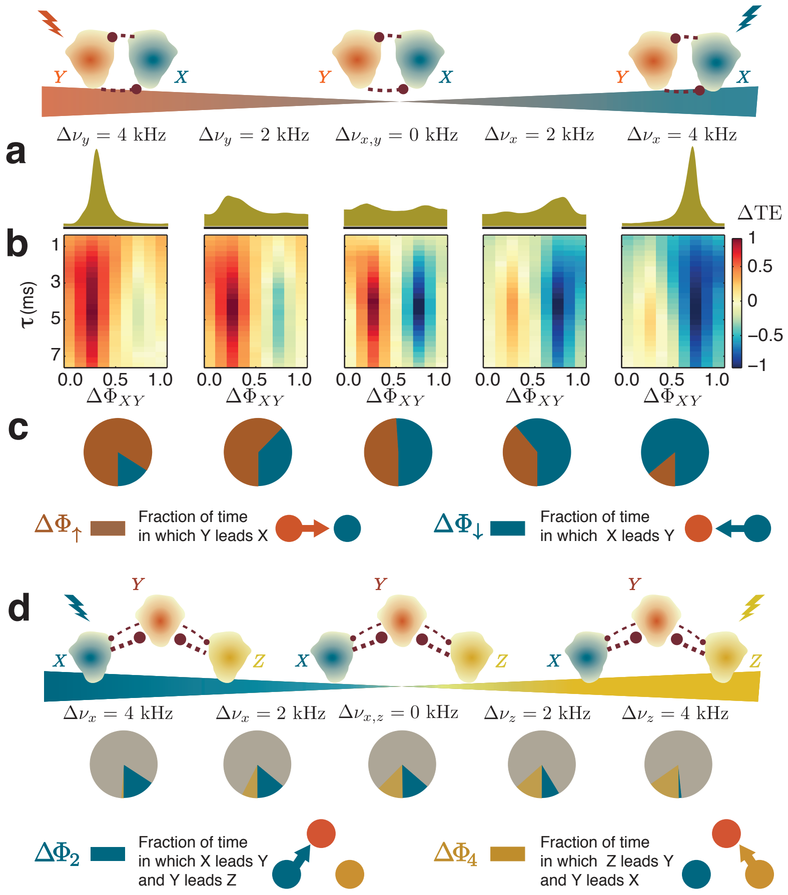

Figure 2.27: Biasing information transfer. (a) The application of a steady bias is modeled as a constant increasing $\Delta\nu$ of the background drive ν_{in} of only one of the two interconnected brain regions. **(b)** The predominant direction of information transfer is biased towards the region with lower background drive, as indicated by the maps of the Functional Anisotropy Index ΔTE. Middle column: no input bias. Extreme columns: strong background bias $\Delta\nu = +4$ kHz (on top of a baseline drive of $\nu = 3$ KHz) applied to population X (extreme right) or to Y (extreme left). Intermediate columns: weaker cases of $\Delta\nu = +2$ kHz. **(c)** Pie charts of the time the system spends in a *Top* or a *Bottom* state, matching the biased examples of panels **a–b**. The corresponding functional graph motifs are indicated below. For strong biases information can "leak" in the non-preferred direction (see also Fig. S11). **(d)** Center row: Without background bias, the dynamics of a three-area system spend the same fraction of time in a state $\Delta\Phi_2^{xyz}$ and a $\Delta\Phi_4^{zyx}$. When a mild bias perturbation is applied to population X (Z), to the left (right) columns, the fraction of time spent in a $\Delta\Phi_2^{xyz}$ ($\Delta\Phi_4^{zyx}$) increases, annihilating the fraction of time spent in the mirror configuration. Information is preferentially transmitted to the target downstream region Y from the region receiving the background bias.

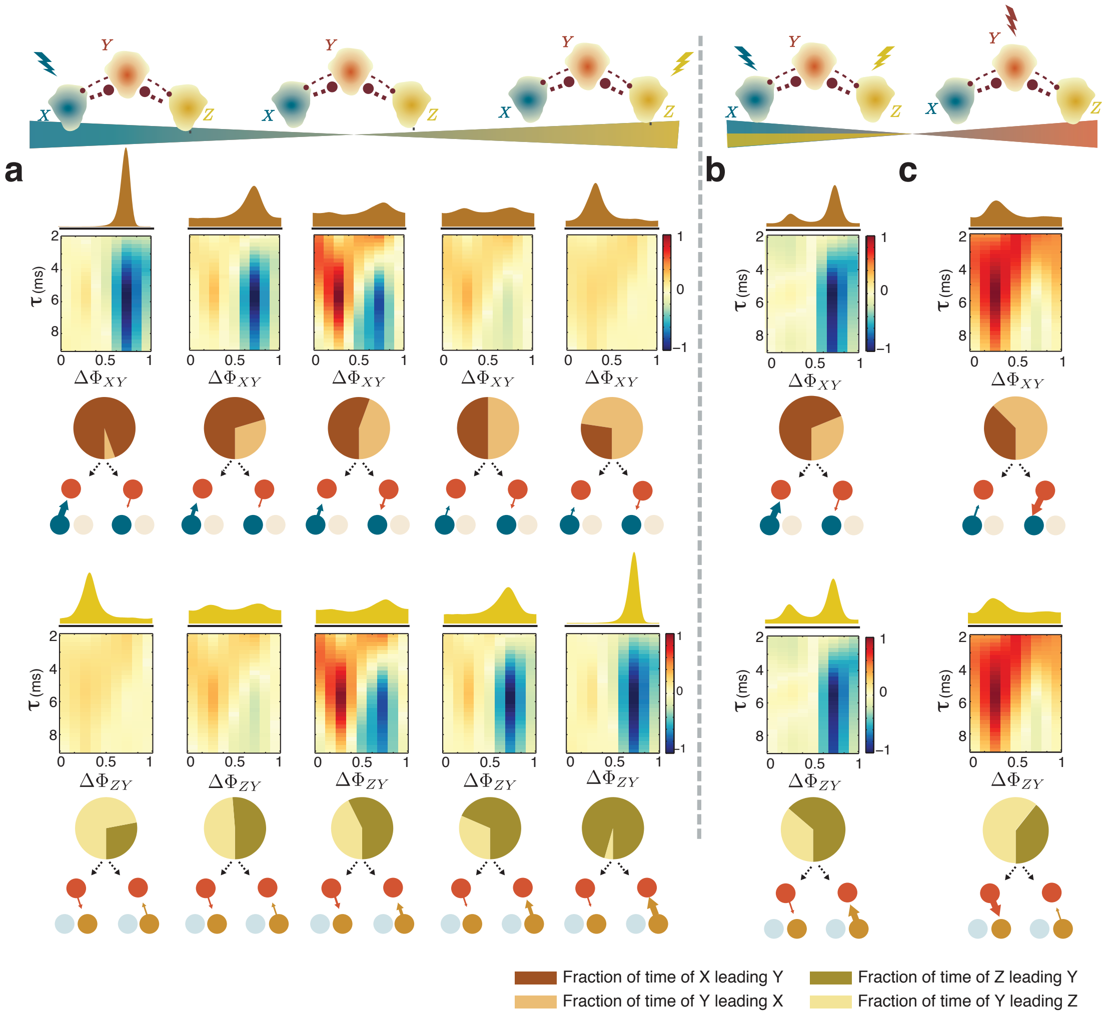

Figure 2.28: Controlling the direction of information flow in a asymmetric three population scheme. Simulation of the application to steady biases in each of the three populations. The resulting effect on the distributions of the pairwise phase relations,$\Delta\Phi_{XY}$ and $\Delta\Phi_{ZY}$ together with the phase resolved Asymmetry Index (see Methods) for the two pairs of signals are shown. **(a)** Analysis of the response of $\Delta\Phi_{XY}$ and the Anisotropy Index (AI) to lateral biases. *Top* row, center column: The phase relation between X and Y, $\Delta\Phi_{XY}$ is initially slightly distorted, given the asymmetry in the structural connectivity as detailed in Figure 2.24**(a)**. As a bias is applied to X (columns to the left), $\Delta\Phi_{XY}$ shows a an increase in its right peak, indicating predominance of X leading states. Correspondingly, the index of information anisotropy shows increasing predominance information flowing form X to Y. When a bias is applied to the Z population (right columns), the symmetry between X and Y is first restored and then switched to a predominantly Y leading states. Bottom row: Analysis of the response of $\Delta\Phi_{ZY}$. When a big external bias (extreme left) is applied to the region X, the relative information transmission between Z and Y compared to that between X and Y is severely diminished, as reflected by a near zero AI. Extreme bias to Z mutes the information channel coming from X. **(b)** A bias can also be applied to a downstream population Y, forcing states in which Y leads in phase. Information is then transmitted primarily from Y to both X and Z in a top-down manner, as clear from the predominant blob in the AI index for in Y leading states. **(c)** Alternatively, a bias with the same intensity can be applied two both populations, having equal strength information transmission from both regions in a bottom-up manner.

A given dominant direction of information transfer can nevertheless be enforced by applying a weak bias (Fig. 2.27) and making the bursts of a given type more likely to occur. Figure 2.27a–c refer to routing state control in the two region model of Figure 2.13. Figure 2.27d and 2.28 refer to the control in the three region model of Fig. 2.25. Raising the baseline input to either one of the two possible source regions by a certain amount $\Delta\nu$, increases the probability that the biased circuit becomes a transient phase leader, favoring the occurrence of specific routing states. As indicated by the pie charts of Fig. 2.27c, a bias to circuit X (or Y) increases the probability of occurrence of a *Bottom* (or *Top*) state , as seen in the rightmost (or leftmost) columns.

Equivalently, for the three region model a bias to the region X increases the probability of X leading Y and simultaneously of Y leading Z (Fig. 2.27c, left columns). Similarly, a bias to the region Z increases the probability of Z leading Y and simultaneously of Y leading X (right columns). As the relative phase distributions (Fig. 2.27d, Fig. 2.28) take on more asymmetric shapes, the maps of the Functional Anisotropy Index reveal a strong asymmetry in the direction of information transmission, showing that information flows preferentially from the biased region towards the target one. High applied bias (extreme right or left columns) eventually ends up muting the sub-dominant information transfer channels, with one of the two peaks of the relative phase distribution being flattened. For the three region model, this is further detailed in Figure 2.28. In panel a, the effects on the relative phase distributions and the anisotropy maps is shown when increasingly strong background inputs are added to the population X (left) or Z (right). Additionally, as shown in panel b, the simultaneous increase in a background bias to both populations X and Z traduces in an increase of the information transmitted to Z form both X and Z, enforcing the routing states $\Delta\Phi_1^{xyz}$, $\Delta\Phi_3^{xyz}$.

2.2.7 *Modulation of information transmission by spontaneous symmetry breaking*

The examples discussed above are associated to a distribution of inter-areal phase differences which is symmetric in the unbiased case (i.e. not spontaneously favored phase-locking configurations). However, and very much surprisingly, combined high levels of heterogeneity and local inhibition can spontaneously break the symmetry of the relative phase distribution. Some instances of the network, depending on specific realization of otherwise statistically identical variables, give rise to naturally asymmetric phase-difference distributions and hence, to an intrinsically more frequent functional state. For networks with no conductance heterogeneity although differences in the peaks might be observed, a bimodal phase distribution is generally obtained. The inclusion of large input conductance heterogeneity, can lead to asymmetric states. An example is shown in Figure 2.29 for a high synchrony working point. The initial asymmetry observed cannot be reverted even with large opposing biases. The asymmetric cases also occur in a lower synchrony regime. Nevertheless, they occur more seldomly and when they do, the effect is less drastic, given that the phase distribution is already spread out. This asymmetric feature of the networks hints at an interesting venue for phase locking control, in which tiny manipulations in the weight of the connectivity can lead to re-organizing effects at the network level with high impact in the information capabilities of the network.

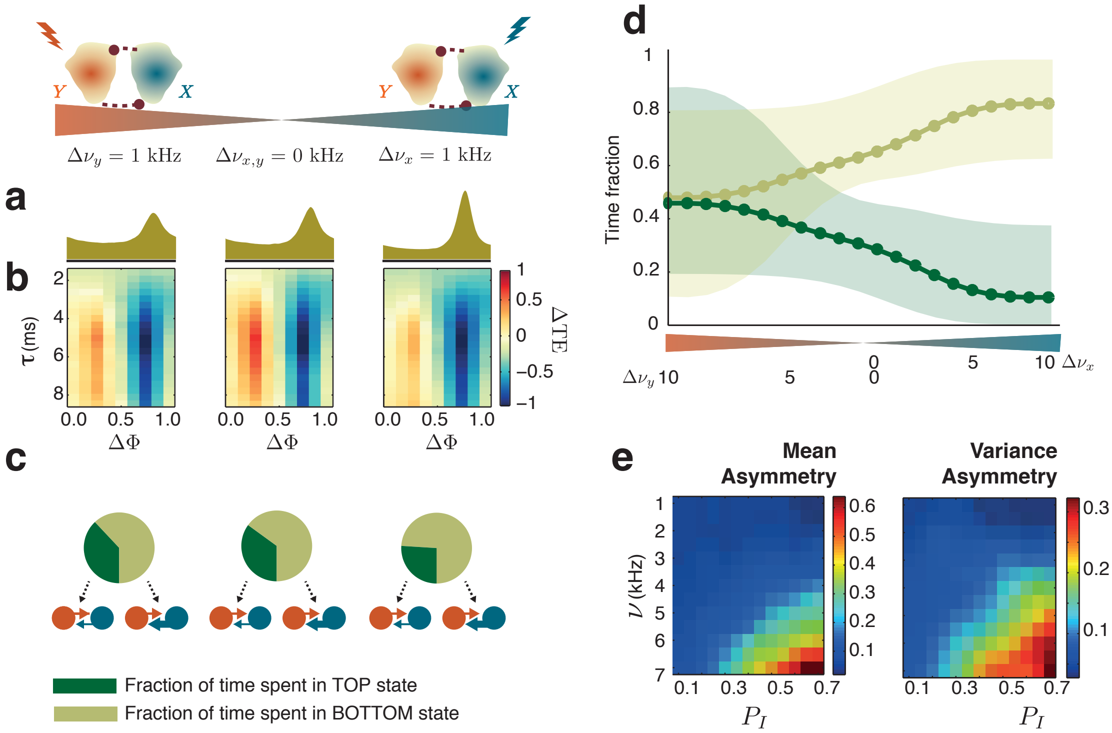

Figure 2.29: Asymmetric information transfer. Some instances of networks with heterogeneous input conductances give rise to distributions of the relative inter-areal phase difference which are not symmetric but display a marked asymmetry even in absence of external input bias. An example of the relative phase distribution of an asymmetric network is shown in panel **(a)** for the high synchrony working point. The application of external bias counteracting the network spontaneous asymmetry does not restore symmetry, even for stronger biases than the one depicted. The associated maps of information transfer anisotropy ΔTE (panel **(b)**) and the time spent in *Top*- or *Bottom*-like states (panel **(c)**) are as well shown. Note the significant leakage of information transfer occurring in the sub-dominant direction. **(d)** Mean and 95% c.i. of the time spent in a *Top* state (dark green) and *Bottom* (light green) as a continuous function of the applied bias for a network in a high synchrony working point and in an initially asymmetric state, aligned to be asymmetric in a X leader configuration, as in **(a)**. Note how on average the symmetry cannot be restored despite the application of a large bias. **(e)** Given the probability $P_\uparrow$ of having $\Delta\Phi$ in an interval [-0.1+$\Delta\Phi^*_\uparrow$, $\Delta\Phi^*_\uparrow + 0.1$] around the peak $\Delta\Phi^*_\uparrow$ and the analogously defined $P_\downarrow$, we define the asymmetry index as the normalized difference between them: AI= $\frac{P_\downarrow - P_\uparrow}{P_\uparrow + P_\downarrow}$. The mean (left) and the variance (right) of this asymmetry index over 40 network realizations per parameter combination is plotted as a function of the probability of local inhibitory connection P_I and the background drive rate ν_{in}.

2.2.8 Optogenetic control of phase relations, past and future

In networks where the level of synchronization is high, and the oscillation is periodic, an excitatory pulse to a single population can alter the phase relation in a long lasting way. We developed a protocol that would allow to perturb the ongoing phase relation between either spontaneously occurring or optogenetically induced gamma rhythms. A single strong excitatory pulse to a single population elicits a change in the relative phase, with a probability that depends on the phase at which the rhythms is perturbed. This protocol is suited to critically test the behavioral correlates of inter-areal phase relations between highly synchronous rhythms; the resulting work can be found in Appendix C. It remains a challenge to have a reliable perturbative method to set the rhythms of low and fluctuating level of synchronization in a desired phase configuration in a controlled manner. Possible avenues will be discussed in the next section.

2.3 Summary and Discussion

Our results show that, in coupled circuits at the edge of developing oscillatory synchrony, frequency-tracking and out-of-phase locking of oscillatory bursts are emergent features of the large scale circuits collective dynamics. Bursts are generated in coordinated sets of near simultaneous onset, and mediate transient phase locking between the region's activity. The transient patterns of inter-regional coherence define flexible routing states that determine the direction of information flow both of endogenously generated rate fluctuations and of externally supplied signals.

Our study sheds new light on several arguments against coherence mediated communication, introduced in detailed in section 1.1.6 of the Chapter 1. A first widespread concern has been the low and inconsistent power of gamma oscillations *in vivo*[44,286]. In our models, LFP oscillations show inconsistent power, fluctuating stochastically between 40 and 70 Hz and with a time-averaged LFP spectrum presenting broad-band gamma modulation (see Fig. 2.9), consistent with other models of neuronal activity with transient synchrony[171,15,56]. Despite this weak-average gamma power, TE analyses revealed that the transient power rise during oscillatory bursts is sufficient to impact on information transfer between areas and propagation of externally supplied information. A second issue relates to the low level of spiking correlations. While several studies identified marked and context-dependent oscillatory synchrony[146], others found only weaker spiking correlations[66]. In our simulations, spiking activity always remained highly irregular (Fig. 2.5). In particular, neuronal firing is poorly phase-concentrated, with the exception of bursting events, which are tightly localized in time (Fig. 2.9). These short epochs nevertheless convey the largest net contribution to directed information transfer (Fig. 2.14). A third obstacle may be the large variability of inter-areal conduction delays, impeding the phase-matched arrival of pre-synaptic spikes with respect to the oscillation in the target region. The regulation of information transfer, however, is the outcome of collective dynamics and not just of direct mono-synaptic interactions. In fact, observed inter-areal phase relations depend on a multitude of factors and don't seem to follow the inter-areal delay (see section 1.1.6 for details). As shown in Figure 2.11, different inter-areal phase-locking relations can be implemented with a fixed inter-areal delay, just by changing the level of local inhibition. It is thus plausible that the fine control of local inhibition exerted by specialized interneuron types[42] plays an active role in setting inter-areal phase relationships. A further impediment to the function of gamma oscillations as an internal coordination system may result from their sensitivity to external stimuli[203,134]. However, coupled oscillating local circuits coordinate the emergence of their own stochastic gamma bursting tracking each other's frequency and timing in a fully self-organized manner (Fig. 2.6), independently of their inputs (Fig. 2.20).

The out-of-phase relations we find may be potentially useful in establishing dynamic functional hierarchies of inter-areal communication[18], with information flowing preferentially from phase-leading toward phase-lagging regions. Since the structure of the phase patterns is not solely prescribed by connectivity, different regions can compete flexibly assuming the functional roles of sender or receiver of information, depending on the specific context and modulatory signals.

In the continuum of the reality of the world, in a remote era, a radical heterogeneity was established between any two things. A difference so irreducible that there was no term that could encompass both.

Varamo, by Cesar Aira

3

Chaos and synchrony in delayed neuronal networks

The dynamical stability of neuronal networks, and the possibility of chaotic dynamics in the brain pose profound questions to the mechanisms underlying perception. In a chaotic system, the exponential divergence of nearby trajectories implies an entropy production rate. On the one hand, the chaotic dynamics amplifies differences in initially undistinguishable states. When tracing backwards the diverging trajectories, we can increase the resolution of the initial condition. On the other hand, at a given point in time, the dynamics create new information that was not implicit in the initial conditions, necessarily measured to a finite precision[225], overwriting in a finite time any information that they could have encoded. Whether the rapid amplification of differences in the states and the finite-time dissolution of encoded information poses an advantage for brain processing or works in detriment to it, depends both on the resolution of the initial measurement, and on the time scales of integration needed to reunite the elements that compose perception.

In this chapter we are going to analyze the dynamical properties of delayed pulse-coupled neuronal networks. Rigorous approaches to study the stability and dimensionality of delayed dynamical systems, which have an infinite dimensional phase space, have generally remained elusive. While analytical approaches to calculate the full spectrum of delayed scalar equations have been successful in only few cases[155], numerical methods have provided some general intuitions about the dependence of the characteristics of the attractor on the delay[78,154,235]. In globally pulse coupled excitatory networks, in which the evolution of the units is continuous except at the reset point, the system has been shown to be reduced to a finite dimension whose upper bound depends on the dynamics of the network[12]. The existence of a finite spectrum of Lyapunov exponents characterizing the rate of divergence of nearby trajectories in the phase space, or the existence of a finite dimensional attractor is in principle not guaranteed in these systems.

Here we show that in pulse coupled neurons with delayed interactions the dependence on its history can be circumvented and mapped to a system with fixed and finite degrees of freedom. By introducing a postsynaptic single-compartment-axon (SCA) for every neuron, the effective transmission delays arise from the additional steps of input integration that is required by the delayer SCA to reach threshold. The dynamics of exactly solvable neuron models can be analyzed by the evolution of a map that propagates the activity from spike to spike in event-based simulations, which are only limited numerically by machine precision[174,173]. This approach can be equally extended to the study of delayed interactions by a suitable choice of a model for the SCA. The equivalent system, with a dimension that doubles that of the original, has a well defined map that iterates the state of the network from spike to spike. A Jacobian, through which the stability of the delayed system can be assessed is also defined.

We find that the inclusion of delays in inhibitory QIF networks in the balanced state[*] leads to a transition to a *slow* synchronous irregular state in which the frequency of the oscillation is only a few times larger than the mean firing rate of the neurons. The firing rate distributions remains broad, even in the absence of heterogeneity. At the critical delay where the oscillation develops, the exponential rate of divergence of nearby trajectories increases together with entropy production rate, indicating that chaos intensifies while departing from the asynchronous irregular state. Further increases in the delays mediate a transition to spike-spike synchronization. Nevertheless, even small amounts of heterogeneity in the single neuron parameters prevent this pathological state, working as counter-acting force to the delay, which tends to align the rhythm. After this new transition, the firing rate distributions become bimodal, with neurons locking to the rhythm and neurons with low firing rates acting independently of it, given the large amount of heterogeneity[121]. The entropy production rate and the attractor dimension decrease monotonically with increasing delay after this transition, as opposed to more standard delayed differential equations in which an increasingly large attractor dimension was reported[78,154]. The inclusion of excitation does not lead to a different dynamical behavior, and a transition to an irregular synchronous state with increasing delay is also observed, although the details of the transition depend on the details of the E-I loop. Finally, we explored the stability and synchronization properties of a neuronal model with tunable onset rapidness. For low values of heterogeneity, the increase of the synaptic delay in these networks leads to a sharp transition to spike-spike synchrony. Strikingly, for higher values of heterogeneity a *fast* synchronous irregular state emerges, that differently from the one described in the LIF neurons[29] is also chaotic.

This chapter is organized as follows: Section 3.1 will deal with the theoretical background on elements of ergodic theory of chaos and balanced state networks that will be later implemented and discussed. Section 3.2 will detail the mathematical methods, the spike to spike iteration map for different neuron classes, the mathematical definition of the SCA and the details of the numerical implementation and the definition of some network statistics. Section 3.3 will present the results briefly discussed above, that will be further summarized and discussed in section 3.4

---

[*] By balanced state networks in this context we refer to networks with random connectivity (i.e. given by a Erdős–Rényi graph) in which the synaptic weight J scales with the average amount of connections per neuron K like $J \propto 1/\sqrt{K}$, see 3.1

3.1 Theory

This section will deal with the theoretical background of both ergodic theory of chaos and balanced state networks, that together with section 1.2 in the introduction frame the work to be presented in the later sections.

3.1.1 Ergodic theory of chaos

Delta coupled neuronal networks are distinctly characterized by the independent evolution of the sub-threshold dynamics of each neuron between spikes. As the spike emission and reception are discrete events in time, the temporal evolution of a network of these characteristics can be analyzed like a discrete map, a procedure that will be detailed in the Methods section of this chapter. In a one dimensional system, a discrete map defined in an interval I, has the form:

$$x(n+1) = f(x(n)) \tag{3.1}$$

where $x \in I$, $f : I \to I$ is an invertible continuously differentiable map and $n \in \mathbb{Z}$. The above equation is equivalent to compose the function f n times: $x(n+1) = f \circ f ... \circ f(x(0))$. The right hand side for a trajectory with a slightly different initial condition will satisfy $(f \circ f ... \circ f(x(0) + \delta x(0)))$. Using the chain rule, the evolution of the distance between these two trajectories on the tangent space can be approximated by:

$$\delta x(n+1) = f'(x(n))f'(x(n-1))...f'(x(0))\delta x(0) = D_{x(0)}f^n \delta x(0) \tag{3.2}$$

With $f' = \frac{df}{dx}$. If the term on the right hand side evolves exponentially[67], an average growth rate λ of an infinitesimal perturbation can be defined as:

$$\lim_{n\to\infty} \frac{1}{n} \log |D_{x(0)}f^n| \delta x(0) = \lambda \tag{3.3}$$

This limit, in principle depends on the perturbation $\delta x(0)$ and the initial condition $x(0)$.

In the more general scenario, given the m dimensional dynamical system (M, f), $f : M \to M$ $M \subset \mathbb{R}^m$ such that $\boldsymbol{x}(n+1) = f(\boldsymbol{x}(n))$, the evolution of a perturbation $\delta\boldsymbol{x}$, will be given by

$$\delta\boldsymbol{x}(n+1) = \mathbb{L}(\boldsymbol{x}(n))\delta\boldsymbol{x}(n) = \prod_{i=0}^{n} \mathbb{L}(\boldsymbol{x}(i))\delta\boldsymbol{x}(0) \qquad \mathbb{P}_n[\boldsymbol{x}(0)] = \prod_{i=0}^{n} \mathbb{L}(\boldsymbol{x}(i)) \tag{3.4}$$

where $\mathbb{L}(\boldsymbol{x}(n))$ is the m-dimensional Jacobian evaluated in $\boldsymbol{x}(n)$, and $\mathbb{P}_n[\boldsymbol{x}(0)]$ dictates the evolution of perturbation in the tangent space after the nth iteration. The multiplicative theorem by V. Oseledets[67,190], states that the following limit exists:

$$\Lambda[\boldsymbol{x}(0)] = \lim_{n\to\infty} \frac{1}{n} \left[\mathbb{P}_n[\boldsymbol{x}(0)]^T \mathbb{P}_n[\boldsymbol{x}(0)]\right]^{\frac{1}{2n}} \tag{3.5}$$

The m eigenvalues of the Oseledets matrix, $\Lambda[x(0)]$, are the Lyapunov numbers ν_i[67] and their logarithm the Lyapunov exponents. The exponents are usually ordered as $\lambda_{\max} = \lambda_1 \geqslant \lambda_2 \geqslant ... \geqslant \lambda_s$, where $m \geqslant s$ is due to the possible degeneracy. The set of the Lyapunov exponents is usually referred as the Lyapunov spectrum. It is worth mentioning that the theorem was alternatively proven by Raghunathan[201] without the requirement of the matrices $\mathbb{L}(\boldsymbol{x}(n))$ to be invertible.

As an example, if the dynamics of the system have a stable fixed point, then the value of $\mathbb{L}(\boldsymbol{x}(n))$ stays constant and the Lyapunov numbers are the eigenvalues of such a matrix. Stability in a discrete setting means that those eigenvalues are smaller than one, and therefore the Lyapunov exponents are all negative.

The Oseledets theorem shows its full power when dealing with ergodic systems, as shown next. Generally, after a transient period, the orbits settle to a subset of M, $A \subset M$ that can be called the *attractor*. A probability density over A for the one dimensional case can be defined as:

$$\rho(x) = \lim_{n\to\infty} \sum_{i=1}^{n} \delta(x - x(i)) \tag{3.6}$$

A measure is related to the density of the orbits (under certain smoothness conditions) by $d\mu(x) = \rho(x)dx$, such that $\mu(A) = \int_A \rho(x)dx$. The measure μ of that set is said to be *invariant* if it does not change under the action of the dynamics, i.e. $\mu(f^{-t}(A))=\mu(A)$ for $t > 0$. The measure is said to be *ergodic* when it cannot be decomposed in other invariant measures. In that case, then the time and the spatial average can be used interchangeably. If μ is ergodic, for any continuous function Φ holds:

$$\bar{\Phi} = \lim_{n\to\infty} \frac{1}{n} \sum_{i=1}^{n} \Phi(\boldsymbol{x}(i)) = \int_A d\mu(\boldsymbol{x})\Phi(\boldsymbol{x}) = \langle \Phi \rangle \tag{3.7}$$

In that case, the Oseledets theorem states that the limits of Eqs. (3.3) and (3.5) not only exist, but are independent of the trajectory and a characteristic of the attractor. As discussed by Massimo et al.[169], in the one dimensional case, the Oseledets theorem as in (3.3), reduces to the law of large numbers. From Eq. (3.2)

$$\lambda = \lim_{n\to\infty} \frac{1}{n} \log \left(\prod_{i=0}^{n} |f'(x(i))| \right) = \langle \log |f'| \rangle \tag{3.8}$$

For the m dimensional case, the Lyapunov exponents measure the mean logarithmic growth rate with which perturbations in the direction of the eigenvectors of the Oseledets matrix, separate or converge to each other. The Oseledets theorem can equivalently be defined as[67]:

$$\lambda_i = \lim_{n\to\infty} \frac{1}{n} \log \|\mathbb{P}_n \delta\boldsymbol{x}\| \qquad \delta\boldsymbol{x} \in E^i \setminus E^{i+1} \tag{3.9}$$

Where the *linear* subspace E^i is defined as the one spanned by the eigenvectors with Lyapunov number such that $\nu < \nu_i$ (or equivalently that $\nu < \exp(\lambda_i)$). From that definition follows that the subspace E^1 includes the rest and the following holds: $E^1 \supset$

$E^2 \supset ... \supset E^m$. E^1 spans $\mathbb{R}^m$ and any perturbation will generally be aligned in the direction of the maximum Lyapunov exponent. This is known as Oseledets splitting, and holds even if the matrices $\mathbb{L}(\boldsymbol{x}(n))$ are non invertible as long as the underlying dynamical system is invertible[89].

Consider the k-dimensional parallelepiped spanned by k independent vectors w_j, $j = 1, ..., k$ in the m dimensional space tangent to the trajectory. The time evolution under the effect of the dynamics will expand the volume in some directions and contract it in others, such that after a long time, $V(t)$ is approximately $V(0)\exp(\lambda_1 t)... \exp(\lambda_k t)$. More formally, an initially normalized k-dimensional volume will then satisfy:

$$\Lambda_k = \sum_{i=1}^{k} \lambda_i = \lim_{n\to\infty} \frac{1}{n} \log\left(V_k(n)\right) \tag{3.10}$$

We note that from this equation, the Lyapunov exponents can be iteratively obtained by considering volumes of different dimensions, given that $\lambda_k = \Lambda_k - \Lambda_{k-1}$. The computation of the spectra via Eq. (3.10) is impractical numerically given that[22] i) the exponential growth of volumes leads to significant numerical errors for large times and that ii) the alignment of the vectors w_j with the direction of the maximum exponent make the angles between the vectors w_k very small, also introducing numerical error. For the calculation of the first exponent, only the first obstacle is relevant, and is overcome by a renormalization of the initially random vector w_1 . The further introduction of an orthonormalization step makes the calculation of the full spectrum possible[148,22,91,67]. In order to clarify this further, let W be the $m \times k$ matrix of the vectors w_j. If none of the vectors is parallel then the matrix W is invertible and has a unique QR decomposition, $W = QR$ where $Q = (q_1|...|q_j|...|q_k)$ is orthogonal and R is upper triangular. The parallelepiped spanned by the vectors $R_{jj}q_j$, where R_{jj} are the diagonal terms of R, has the same volume than that spanned by w_k, $V_k = \prod_{i=1}^{k} R_{ii}$ and then $\lambda_i = \lim_{n\to\infty} \frac{1}{n} \log\left(R_{ii}\right)$ holds. Keeping this in mind, given an initial volume spanned by vectors in the columns of $W(0)$, the evolution in the tangent space will be given by:

$$W^{n+1} = \mathbb{L}^n \mathbb{L}^{n-1} ... \mathbb{L}^1 \mathbb{L}^0 W^0 \tag{3.11}$$

Where $\mathbb{L}^n = \mathbb{L}(\boldsymbol{x}(n))$ and $W^n = W(n)$. In every step of iteration, the matrix $\mathbb{L}^n Q^n$ has a QR decomposition, so we can write[91,67] $\mathbb{L}^n Q^n = Q^{n+1} R^n$, where $W(0) = Q^0$, Q^j is orthonormal and R^j is upper triangular. Eq (3.11) then can be written as:

$$W^{n+1} = Q^{n+1} R^n ... R^0 = QR \tag{3.12}$$

From Eq. (3.10) the iterative algorithm[91,67] for obtaining the exponents is given by:

$$\lambda_i = \lim_{n\to\infty} \frac{1}{n} \sum_{i=0}^{m} \log\left(R_{ii}^n\right) \tag{3.13}$$

where in the case of a process with continuous time that is discretized for numerical integration, $n = \Delta t n$.

A positive Lyapunov exponent and the consequent sensitivity to initial conditions in compact sets is a signature of chaos. Chaotic dynamical systems in which volumes are preserved are said to be conservative, and are dissipative otherwise. Attractors of dissipative chaotic systems have a complex and self similar structure that emerges from the *stretching and folding* mechanisms natural to the coexistence of stable and unstable manifolds (see Fig 3.1). These attractors are called *strange* and have generally non-integer dimensions, forming *fractals* sets. The simplest measure of an attractor dimension is called Kolmogorov capacity or box-counting dimension[80]. It is a metric-based measure in the sense that it does not take into account the density of orbits on the attractor. Given a parallelepiped of side ϵ, the number $N(\epsilon)$ that is needed to cover the set of points conforming the attractor A is expected to satisfy $N(\epsilon) \approx \epsilon^{-d_c}$. The capacity of the set can then be defined as:

$$D_C = \lim_{\epsilon \to 0} -\frac{\log(N(\epsilon))}{\log(\epsilon)} \tag{3.14}$$

A different measure that incorporates the frequency with which orbits visit the different parts of the attractor can also be defined. If instead of considering the number of hypercubes of side ϵ to cover the attractor, we consider the number of hypercubes $N(\epsilon, \vartheta)$ needed to cover a fraction ϑ of the attractor, then the ϑ capacity can be defined as:

$$D_C(\vartheta) = \lim_{\epsilon \to 0} -\frac{\log(N(\epsilon, \vartheta))}{\log(\epsilon)} \tag{3.15}$$

This measure, which for $\vartheta = 1$ is directly the capacity and otherwise will be called D_μ, satisfies $D_\mu \leq D_C$. Finally, a pointwise dimension $D_p(x)$ can be as well defined by estimating the exponent with which the total probability within a ball of radius ϵ decreases as the radius vanishes[80]:

$$D_p(x) = \lim_{\epsilon \to 0} \frac{\log \mu(B_\epsilon(x))}{\log(\epsilon)} \tag{3.16}$$

For a definition of an attractor dimension that is related to the measure of the attractor, it is necessary to define a partition. Let $\mathcal{B} = \{B_i\}$ be a partition that covers the phase space. At each measurement, the trajectory of the system can be found in one B_i such that for sufficiently long times, a frequency of occurrence P_i can be assigned to each B_i. When the size of the elements of the partition tends to zero, P defines a probability density like that defined in Eq. (3.6), such that its sum over the attractor is equivalent to the measure on the attractor $\mu(A)$. Then, the frequency of occurrence can be written as $P_i = \mu(B_i) = \int_{B_i} \rho(x)dx$.

When observing the state of the dynamical system at a given point if time, the information that is gained about the state depends on the resolution of the instrument, the *diameter* of the partition used. This diameter is basically given by the largest size of the elements B_i of the chosen partition. If the partition has diameter ϵ, then the information gained by making a measurement is given by:

$$I(\mathcal{B}(\epsilon)) = -\sum_{i=1} \mu(B_i(\epsilon)) \log\left(\mu(B_i(\epsilon))\right) \tag{3.17}$$

If now, from all the possible partitions to be chosen, we choose that one that minimizes the above expression, $I(\epsilon) = \inf_{\mathcal{B}(\epsilon)} I(\mathcal{B}(\epsilon))$, then the information dimension D_I is defined as:

$$D_I = \lim_{\epsilon \to 0} \frac{I(\epsilon)}{-\log(\epsilon)} \tag{3.18}$$

The information gained in a snapshot measurement of the state of the system with an instrument of resolution ϵ can be approximated by $I \sim D_I * |\log(\epsilon)|$[79]. An interesting observation is that if instead of calculating $I(\epsilon)$, it is assumed that the probability distribution is homogeneous over the attractor, then $I(\epsilon) = -\frac{1}{n}\sum_{i=0}^{N(\epsilon)} \frac{1}{N(\epsilon)} \log(N(\epsilon)) = \log(N(\epsilon))$, and the information dimension reduces to the capacity. As the uniform distribution is the maximum entropy distribution in a bounded interval with no constraints on the moments, it follows that $D_I \leq D_C$.

If instead of estimating the information gained by a snapshot measurement, it is of interest to estimate the information acquisition rate, then a sequence of snapshots has to be considered. Roughly speaking, in the case of a system that can take n values, a sequence of k state measurements of the trajectory can be defined as $S^{k,n}$. The average information gained by knowing the actual trajectory will be given by the entropy of the distribution of k-long words with n possible symbols: $I_k = -\sum_i P(S_i^{k,n}) \log P(S_i^{k,n}))$. The average new information per symbol, the aaverage information we gain by making a new measurement in a sequence of measurements, is $\Delta I = \lim_{k\to\infty} I_k/k$[79]. The ratio $\Delta I/\Delta t$, with Δt the time interval between measurements, equal to one in maps, will then be the average information rate per symbol gained.

In the context of a dynamical system, a different approach to the calculation of I can be made. Given an invariant measure μ over an attractor A and a partition $\mathcal{B}^0 = \{B_i^0\}$, the set of points contained in B_i^0 will be evolved by the map. If the system initially is in B_i^0, and after an iteration can be located in B_j^1 the initial condition will be located within $f^{-1}(B_j^1) \cap B_i^0$. If by $\mathcal{C} \vee \mathcal{D}$ we mean all the possible intersections of the components of the partitions, i.e. $\mathcal{C} \vee \mathcal{D} = \{C_i \cap D_j\}$, then after the kth iteration the initial condition can be then located in:

$$\mathcal{B}^k = \mathcal{B}^0 \vee \mathcal{B}^1 ... \vee \mathcal{B}^{k-1} = \mathcal{B}^0 f^{-1}\mathcal{B}^0 ... \vee f^{-(k-1)}\mathcal{B}^0 \tag{3.19}$$

The partition $\mathcal{B}^k$ is a k refinement of $\mathcal{B}^0$. The information contained after the kth measurement can be then written as $I_k = I(\mathcal{B}^k)$, which is defined as in Eq. (3.17). The *metric entropy*, an upper bound to the information rate is defined as:

$$h_\mu = \sup_{\mathcal{B}} \lim_{k\to\infty} I(\mathcal{B}^k)/k \tag{3.20}$$

Similarly as before, the topological entropy can be defined by instead of calculating $I(\mathcal{B}^k)$, assuming that I is that of a uniform distribution. Then, $h_t = \sup_{\mathcal{B}} \lim_{k\to\infty} \log N_k/k$. Where N_k is the amount of elements in the k refined partition $\mathcal{B}^k$.

Although the calculation of the above defined attractor dimensions and the metric entropy can be done analytically for some low dimensional maps, in the general case for

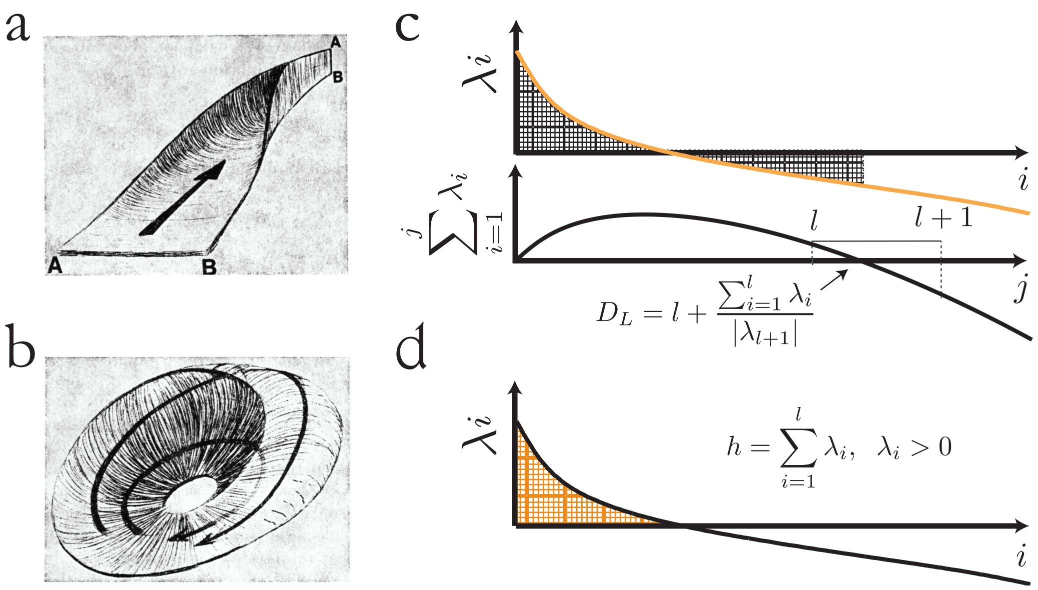

Figure 3.1: Features of chaos (a-b) Drawing (from Shaw[226]) illustrating how trajectories can exponentially diverge while remaining bounded. AB is expanded to twice its width, folded and sutured together. **(c)** Lyapunov dimension. In the upper panel, a Lyapunov spectra is shown. The shaded area in black is the Lyapunov dimension D_L. This is obtained by the linear extrapolation of the point where the cumulative sum of the Lyapunov exponents changes sign, as shown in the bottom panel. **(d)** Metric entropy, the sum of the positive Lyapunov exponents (shaded in orange).

complex high dimensional nonlinear systems the estimation of these measures presents a numerical challenge. Kaplan & Yorke[140], defined a measure of an attractor, the Lyapunov dimension, as a function of the Lyapunov exponents:

$$D_L = l + \frac{\sum_{i=1}^{l} \lambda_i}{|\lambda_{l+1}|} \tag{3.21}$$

Where l is such that $\sum_{i=1}^{l} \lambda_i > 0$ and $\sum_{i=1}^{l+1} \lambda_i < 0$. A graphic illustration of this formula can be found in Figure 3.1. Kaplan & Yorke[140] conjectured initially that the Lyapunov dimension D_L was generally equal to the fractal (box counting) dimension, or a lower bound to it[80]. This form of the Kaplan-York conjecture can be found in the literature[88,140] and in text books[169,222]. In further work by both Kaplan and York[84] and York and colleagues[80], this conjecture was updated to a form which includes information of the density of orbits over the attractor. They specifically conjecture that

$$D_L = D_C(\vartheta) \tag{3.22}$$

Farmer et al.[80] further conjectured that this equality and the original Kaplan York conjecture all hold. Rigorous results show that $D_P = D_I = \lim_{\vartheta \to 1} D_C(\vartheta) \leq D_L$ for invertible smooth maps (as reviewed in Eckmann & Ruelle[67], Farmer et al.[80]). The conjecture has been shown to hold whenever a Sinai-Ruelle-Bowen (SRB) measure (defined as a measure that is absolutely continuos along the unstable manifolds) exists.

Regarding the relation of the metric entropy with the Lyapunov exponents, Ruelle proved[67] that :

$$h_\mu \leq \sum_{i=1}^{l} \lambda_i, \quad \lambda_i > 0 \tag{3.23}$$

The equality, known as the Pesin identity, was shown to hold true for SRB measures. In the general case, and in particular in the work that will be shown in this chapter, finding an SRB measure is not a simple task. One possible way is to investigate whether the system is hyperbolic. In this case, the tangent space to the trajectory can be decomposed in the direct sum of its linear stable and unstable subspaces [*]. Hyperbolicity implies the existence of an SRB measure, and that the Pesin identity and the Kaplan York conjecture hold. Nevertheless, ruling out the hyperbolicity of the system allows for no statement regarding the existence of an SRB measure. Investigations of the angle between the stable and the unstable manifolds of delta coupled networks as the one that will be studied in this chapter, have shown numerically that it is unlikely that the system is hyperbolic[156]. Keeping in mind that the measures derived from the Lyapunov spectrum are upper bounds and that no rigorous statement can be made in favor of the equalities, we will nevertheless refer to them as the entropy production rate and the Lyapunov attraction dimension.

3.1.2 The balanced state equations

Most of this chapter will deal with transitions from asynchronous irregular states towards states exhibiting different types of rhythms at the population level. The theoretical framework developed by van Vreeswijk & Sompolinsky[264] and generally called *balanced-state networks* has as main mechanism to produce irregular and asynchronous activity the mean cancellation of large inhibitory and excitatory inputs. The *balanced-state model*, requires that the inputs to each neuron in the network have non-vanishing variance. This requirement translates into a *balanced state scaling*, in which the weights J of the synaptic connections between randomly connected neurons scales as $1/\sqrt{K}$, where K is the average number of connections per cell. In order to illustrate this fact, a short motivational example is shown in what follows[264,266,173]:

Consider a neuron σ_i, whose purely stochastic time evolution is given by:

$$\sigma_i = \begin{cases} 1 & \text{With probability m} \\ 0 & \end{cases}$$

The temporal average value of the variable is given by $\langle \sigma_i \rangle = m$. Consider now a postsynaptic test neuron that receives on average K inputs from neurons whose dynamics are as described above. The net input I will be a weighted sum of the activity of its K

---

[*] This means that the tangent spaces are never collinear, there is a finite angle between them, and the tangent space can be written as $TM = E^u \bigoplus E^s$

presynaptic neurons. If we call S the sum of the activities and J the synaptic weight, then the input I satisfies $I = JS$. The mean and variance of the input are:

$$S = \sum_{i=1}^{K} \sigma_i \qquad \Rightarrow \qquad \langle S \rangle = \sum_{i=1}^{K} m = Km \tag{3.24}$$

$$\begin{aligned} \langle S^2 \rangle - \langle S \rangle^2 =& \langle \sum_{i=1}^{K} \sum_{j=1}^{K} \sigma_i \sigma_j \rangle - \langle S \rangle^2 & (3.25) \\ =& \sum_{i=1}^{K} \sum_{i \neq j}^{K} m^2 + \sum_{i=1}^{K} m - \langle S \rangle^2 & (3.26) \\ =& (Km)^2 + K(m - Km^2) = Km & (3.27) \end{aligned}$$

where $\langle \sigma_i \sigma_j \rangle = \langle \sigma_i \rangle \langle \sigma_j \rangle$ for $i \neq j$ (and used $\sigma_i \sigma_j = \sigma_i$ when $i = j$). This is exact for stochastic uncorrelated variables, and is in the more general case of neurons in a network justified by the asynchronous, irregular and weakly correlated activity of the neurons. The input to the test neuron has mean and variance:

$$\langle I \rangle = J \langle S \rangle = JKm \qquad \mathrm{Var}_I = J^2 Km \tag{3.28}$$

In order to study the evolution of the test neuron in the limit in which the amount of inputs is large ($\lim_K \to \infty$), a relation between the weights J and the average amount of inputs K has to be given. A possible choice, $J = \frac{J_0}{K}$ seems reasonable given that it leads to a finite mean. In that case, the variance vanishes for large amount of incoming connections. Another choice, given by $J = \frac{J_0}{\sqrt{K}}$, allows for order one fluctuations in the large K limit, while the mean inputs are large.

The balanced state equations

The intuition developed above for stochastic neurons firing with probability m can be formalized to a mean field theory of binary neurons that linearly integrate their inputs and define its state variable by comparing it with a threshold θ^x, where x is excitatory or inhibitory. In this case, the state variable σ_i^x, is given by:

$$\sigma_i^x = \Theta(I_i^x) \tag{3.29}$$

The time dependent input current is given by:

$$I_i^x(t) = I_{\mathrm{Ext}}^x + \frac{J_{xE}}{\sqrt{K}} \sum_{j=1}^{N} A_{ij}^{xE} \sigma_i^E(t) - \frac{J_{xI}}{\sqrt{K}} \sum_{j=1}^{N} A_{ij}^{xI} \sigma_i^I(t) - \theta^x \tag{3.30}$$

I_{Ext}^x is the excitatory external input to the excitatory neurons, A_{ij}^{xE} is a matrix of ones and zeros indicating that there is a connection or not from an excitatory neuron j to i, and equivalently for an inhibitory neuron j to i in the case of A_{ij}^{xI}. J_{xE} is the weight of the excitatory input to the population of type x. The mean input to a neuron of type x is:

$$
\begin{aligned}
\langle I_i^x \rangle =& I_{\text{Ext}}^x + \frac{J_{xE}}{\sqrt{K}} K m^E - \frac{J_{xI}}{\sqrt{K}} K m^I && (3.31) \\
=& \sqrt{K} \left(\frac{I_{Ext}^x}{\sqrt{K}} + J_{EE} m^E - J_{EI} m^I \right) && (3.32) \\
& && (3.33)
\end{aligned}
$$

where $m^x = \frac{1}{N^x} \sum_i^{N^x} \sigma_i^x$. We see from this equation that for the external input to make a non-zero contribution in the large K limit, it should also be large, proportional to $\sqrt{K}$. Writing $I_{Ext}^E = \sqrt{K} E_0$ and $I_{Ext}^I = \sqrt{K} I_0$, we obtain equations for the mean input currents to the inhibitory and excitatory neurons:

$$
\begin{pmatrix} I^E \\ I^I \end{pmatrix} = \sqrt{K} \left(\begin{pmatrix} E_0 \\ I_0 \end{pmatrix} + \begin{pmatrix} J_{EE} & -J_{EI} \\ J_{IE} & -J_{II} \end{pmatrix} \begin{pmatrix} m_E \\ m_I \end{pmatrix} \right) \tag{3.34}
$$

For the large K limit to exist, the parenthesis should be $\mathcal{O}(1/\sqrt{K})$. In the limit:

$$
\begin{aligned}
E_0 + J_{EE} m_E - J_{EI} m_I &= 0 && (3.35) \\
I_0 + J_{IE} m_E - J_{II} m_I &= 0 && (3.36)
\end{aligned}
$$

In compact form, $\boldsymbol{X} + \boldsymbol{J}\boldsymbol{m} = 0$, $\boldsymbol{X} = \begin{pmatrix} E_0 \\ I_0 \end{pmatrix}$. A first and important observation, is that given that E_0 and I_0 are positive, $J_{EE} m_E < J_{EI} m_I$, as well as $J_{IE} m_E < J_{II} m_I$. To guarantee that the variables remain finite, we can explicitly request:

$$
J_{EE} < J_{EI} \qquad\qquad J_{IE} < J_{II} \tag{3.37}
$$

Summarizing, $\frac{J_{EE}}{J_{EI}} < \min(\frac{m_I}{m_E}, 1)$ and $\frac{J_{IE}}{J_{II}} < \min(\frac{m_I}{m_E}, 1)$. The solution to equation (3.35), is given by $\boldsymbol{m} = -\boldsymbol{J}^{-1}\boldsymbol{X}$, where $\boldsymbol{J}^{-1} = \frac{1}{|\boldsymbol{J}|} \begin{pmatrix} -J_{II} & J_{EI} \\ -J_{IE} & J_{EE} \end{pmatrix}$ and $|\boldsymbol{J}|$ is the determinant of the matrix.

The mean field variables have the form:

$$
\begin{aligned}
m_E &= -\frac{J_{EI} I_0 - J_{II} E_0}{|\boldsymbol{J}|} && (3.38) \\
m_I &= -\frac{J_{EE} I_0 - J_{IE} E_0}{|\boldsymbol{J}|} && (3.39)
\end{aligned}
$$

Requesting that both numerators are negative and the determinant positive, leads to inequalities that are compatible with the condition in (3.37).

$$
\frac{J_{EE}}{J_{IE}} < \frac{J_{EI}}{J_{II}} < \frac{E_0}{I_0} \qquad\qquad \frac{J_{IE}}{J_{II}} < \min\left(\frac{m_I}{m_E}, 1 \right) \tag{3.40}
$$

3.2 Methods

The following subsections will first review how to construct a map that allows for analytical state propagation between spikes for different neuron models. Later, a model for the delayer SCA will be specified, which allows to preserve the analytical treatment of simplified neuronal circuit models while introducing interaction delays. These elements together allow for deriving an expression for the Jacobian $\mathbb{L}(\boldsymbol{x}(n))$ of the delayed system (as in Eq. (3.4)). In the last subsections, details about the numerical methods, the definition of some network statistics, and parameter sets will be specified.

3.2.1 Non-delayed pulse coupled neural networks

For generic one-dimensional neuronal models, the voltage dynamics of neurons in a network can be described by:

$$\tau_i^m \dot{V}_i = F(V_i) + I_i^{\text{tot}} \tag{3.41}$$

where τ_i^m is the membrane time constant of the neuron i, and the total input current I_i^{tot}, is usually decomposed in an external component I_i, in principle different and independent for each neuron, and a synaptic input I_i^{syn} arising from the activity of presynaptically connected neurons. Every time a neuron j^* spikes, each of the postsynaptic neighbors i^*, K on average, receive a synaptic current that is modeled by a delta pulse. The input current to neuron i^*, is a weighted sum of the contributions of its neighbors, with the weight, $J_{i^*j^*}$, defined by the neuron pair. The equation for the evolution of the network is given by:

$$\tau_i^m \dot{V}_i = F(V_i) + I_i + \tau_i^m \sum_{j \in pre(i)} \sum_s J_{ij} \delta(t - t_j^s) \tag{3.42}$$

The last term is the synaptic current I_i^{syn} that a neuron i receives at time t given that its pre-synaptic neighbors j emitted spikes in the times t_j^s. This pulse induces an *instantaneous* and constant change in the voltage, that can easily be obtained by integrating Eq. (3.42) in a small window of time ϵ, and equals the summed weight of the connections. If the rates of the individual neurons is low enough for two spikes not to occur simultaneously, each spiking event of a neuron j will induce a change in the voltage postsynaptic to the neuron i equal to J_{ij}.

3.2.2 Event based simulations

Numerical simulation of networks of the type of defined in Eq. (3.42) can be made by means of standard integration schemes. By discretizing time, simulations of this type yield a numerical precision in the spike times given by the chosen step size used, dt. Alternatively, when the single neuron dynamics can be solved analytically, numerical calculations are only needed to link the episodes of neuronal interaction, which are discrete in time. This type of event based simulation requires a map that propagates the state of the network between spikes. The link between such a map and Eq. (3.42) is detailed below for specific single neuron models.

Simplified neuron models like the ones that will be used in this chapter have a defined threshold x_t that defines the spike event, and a reset value x_r, to which the voltage, or the equivalent dynamical variable x to which the voltage is mapped to, is reset afterwards. The evolution between these two points in absence of recurrent input, as well as between any pair of consecutive spiking events from the network, is given by the solution of Eq. (3.41) or its variable-transformed form. Following the notation introduced in[173], closely related to that widely used in networks of coupled oscillators[252,249,250,76,172] we define the inter-spike neuronal propagator function f as:

$$x_i(t_{s+1}^-) = f(x_i(t_s^+), t_{s+1}^- - t_s^+) \tag{3.43}$$

The function f evolves the state of the neuron i after the last spike in the network, $x_i(t_s^+)$, to the state just before the next spike at t_{s+1}. If the neuron i is not postsynaptic to the neuron j^* that produces an spike at t_{s+1}, the state variable will be left unaffected, and then $x_i(t_{s+1}) = x_i(t_{s+1}^-)$. On the contrary, if the neuron i^* is postsynaptic to j^*, then its state variable has to be further updated:

$$x_{i^*}(t_{s+1}^+) = g(x_{i^*}(t_{s+1}^-)) \tag{3.44}$$

Eqs, (3.43) and (3.44), form the basis of the iterative evolution of the network from spike to spike. Its precise form will depend on the neuron model considered, as will the expression for the time to the next spike.

Phase reduction for supra-threshold regime models

Neuron models working in a regime in which in absence of any recurrent input have active and periodic spiking activity can be mapped to a phase variable that linearly evolves in time. This variable, ϕ, has a propagator function $f(\phi)$ that is a linear function of the inter-spike times. All the information about the particular neuron model considered next will then be condensed in the form of the update function g, which is transformed from a simple step increase in the voltage representation to more complex forms.

1) Leaky integrate and fire neuron model[33,1] (LIF)

The dynamics of LIF neuron model with threshold and reset values given by V_t and V_r respectively, are given by:

$$\tau_i^m \dot{V}_i = -V_i(t) + I_i(t) \tag{3.45}$$

The solution for this equation gives the time evolution of the voltage, in the range $V \in (-\infty, V_t)$, and defines the propagator function for the voltage between the network spike times t_s and t_{s+1}:

$$f(V_i(t_s^+), t_{s+1}^- - t_s^+) = I_i - (I_i - V_i(t_s^+)) \exp\left(-\frac{t_{s+1}^- - t_s^+}{\tau_i^m}\right) \tag{3.46}$$

The update function of a postsynaptic neuron i^* of a spiking neuron j^* in the voltage representation is always, independently of the neuron model:

$$g(V_{i^*}(t_s^+)) = V_{i^*}(t_s^-) + J_{i^*j^*} \tag{3.47}$$

In the phase representation, the LIF evolves linearly with time : $\phi(t) = \phi(t_0) + \frac{\omega_i}{\tau_i^m}(t - t_0)$, where $\phi \in (-\infty, 1)$. The value of the variable ω_i can be found by calculating the free period (time from reset to threshold in the absence of recurrent input, $\omega_i = \tau_i^m / T_i^{\text{free}}$), by direct integration of Eq. (3.45) we obtain that $\frac{\tau_i^m}{\omega_i} = T_i^{\text{free}} = -\tau_i^m \log\left(\frac{I_i - V_t}{I_i - V_r}\right)$. Choosing the value of the phase at the reset equal to zero, we obtain the desired mapping from the voltage to the phase representation.

$$\phi_i(t) = -\omega_i \log\left(\frac{I_i - V}{I_i - V_r}\right) \tag{3.48}$$

Finally, the propagator function f and the update function g in the phase representation are given by the following expressions:

$$f(\phi_i(t_s^+), t_{s+1}^- - t_s^+) = \phi_i(t_{s+1}^-) = \phi_i(t_s^+) + \frac{\omega_i}{\tau_i^m}(t_{s+1}^- - t_s^+) \tag{3.49}$$

$$g(\phi_{i^*}(t_{s+1}^-)) = \phi_{i^*}(t_{s+1}^+) = \omega_{i^*} \log\left(\frac{J_{i^*j^*}}{I_{i^*} - V_r} + \exp\left(-\phi_{i^*}(t_{s+1}^-)/\omega_{i^*}\right)\right) \tag{3.50}$$

The update function g in the phase representation, for the LIF and all the neurons in the following that allow for a phase representation, is equivalent to the phase transition curve (PTC). The phase response (or resetting[73]) curve, is defined by:

$$Z(\phi) = g(\phi) - \phi \tag{3.51}$$

and defines both the synchronization properties of the network as well as its stability properties of the network.

2) Quadratic integrate and fire model (QIF)

The quadratic integrate and fire neuron model is the canonical model for type I excitability:

$$\tau_i^m \dot{V}_i = V_i^2(t) + I_i(t) \tag{3.52}$$

Although it is also possible to define reset and threshold values in this model, the QIF, in contrast to the LIF, diverges in finite time and thus has an active mechanism for spike generation. Eq. (3.52) together with the after-spike resetting is the normal form of a saddle node on an invariant circle bifurcation[126]. When the current I changes sign, the two fixed points at $\pm\sqrt{I}$ collide and the neuron spikes periodically with a frequency that scales as $\sqrt{I}$ as in class I excitable systems. The transformation to a phase variable can be done via $\theta = 2\arctan(V)$ for any value of I, arriving to a closed form equation for the evolution of the phase θ, and is known as the theta neuron[74]. Nevertheless, this model is not solvable analytically, limiting its usage for iterative simulations and for the formalism that will be detailed later. Different solutions of Eq. (3.52) can be obtained depending on the sign of I. In the supra-threshold regime ($I > 0$) the solution to Eq. (3.52) is:

$$V_i(t) = \sqrt{I_i}\tan\left(\arctan\left(\frac{V_0}{\sqrt{I_i}}\right) + \sqrt{I_i}\left(\frac{t-t_0}{\tau_i^m}\right)\right) \tag{3.53}$$

The propagator function f and the update function g in the voltage representation for the supra-threshold QIF are then:

$$f(V_i(t_s^+), t_{s+1}^- - t_s^+) = \sqrt{I_i}\tan\left(\arctan\left(\frac{V_i(t_s^+)}{\sqrt{I_i}}\right) + \sqrt{I_i}\left(\frac{t_{s+1}^- - t_s^+}{\tau_i^m}\right)\right) \tag{3.54}$$

$$g(V_{i^*}(t_s^+)) = V_{i^*}(t_s^-) + J_{i^*j^*} \tag{3.55}$$

We see that from Eq. (3.53), that the variable change $\phi = 2\arctan\left(\frac{V}{\sqrt{I}}\right)$ strongly reduces the complexity of the voltage dynamics, and reduces it to a linearly evolving phase. Differently from the definition of the LIF, the phase equation that has reset and threshold values given by $\phi_r = -\pi$ and $\phi_t = \pi$ respectively, satisfies $\phi \in (-\pi, \pi)$. The free period can be now obtained as for the LIF, but requesting that $V_t = +\infty$ and $V_r = -\infty$: $T_i^{\text{free}} = \tau_i^m \pi/\sqrt{I_i}$. This yields a value for the frequency $\omega_i = \tau_i^m \frac{2\pi}{T_i^{\text{free}}} = 2\sqrt{I_i}$. We obtain in this case:

$$f(\phi_i(t_s^+), t_{s+1}^- - t_s^+) = \phi_{i^*}(t_{s+1}^-) = \phi_i(t_s^+) + \frac{\omega_i}{\tau_i^m}(t_{s+1}^- - t_s^+) \tag{3.56}$$

$$g(\phi_{i^*}(t_{s+1}^-)) = \phi_{i^*}(t_{s-1}^+) = 2\arctan\left(\tan\left(\frac{\phi_{i^*}(t_{s+1}^-)}{2} + \frac{J_{i^*j^*}}{\omega_{i^*}/2}\right)\right) \tag{3.57}$$

3) Quadratic integrate and fire model with tunable onset rapidness (rQIF)[72,173]

The rQIF model is a neuronal model developed in Monteforte[173] that, while keeping the analytical tractability of the QIF, allows to incorporate further complexity in the dynamics of the action potential initiation. As shown in Figure 3.2, rQIF is a piecewise quadratic function, in which the parameter r modulates the speed of the action potential initiation. In phase space, this is equivalent to a change of the slope at the unstable fixed point.

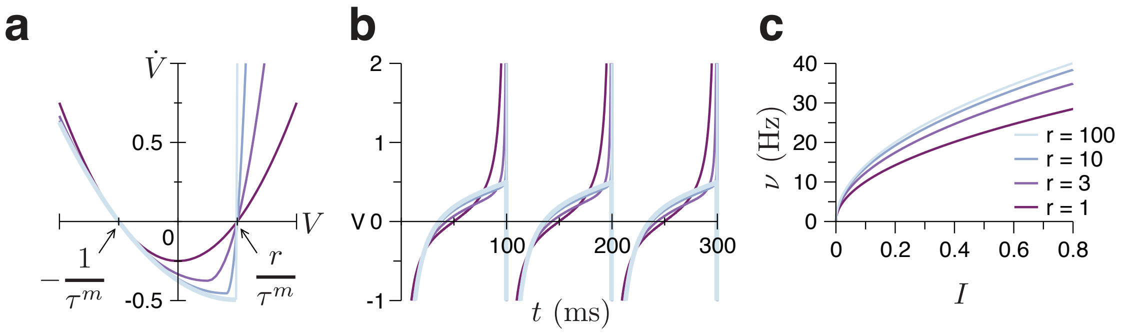

Figure 3.2: (a) Phase portrait for different values of the onset rapidness r. The symmetric parabola in purple corresponding to $r = 1$ illustrates the case of the QIF. **(b)** Voltage traces for different rapidness values. **(c)** F-I curve for the rQIF. Modified from Monteforte[173]

The temporal evolution of the rQIF neuron in voltage representation is given by:

$$\tau_i^m \frac{dV_i}{dt} = \begin{cases} a_s(V_i - V_G)^2 + I(t) - I_T & V_i \le V_G \\ a_u(V_i - V_G)^2 + I(t) - I_T & V_i > V_G \end{cases} \tag{3.58}$$

The conditions for the left branch, $\left.\frac{\partial \dot{V}}{\partial V}\right|_{V_s} = -1$ and $\left.\dot{V}\right|_{V_s} = 0$ and for the right branch $\left.\frac{\partial \dot{V}}{\partial V}\right|_{V_u} = r$ and $\left.\dot{V}\right|_{V_u} = 0$ define a system with four equations and four unknowns:

$$V_G = \frac{1}{2}\frac{r-1}{r+1} \tag{3.59a}$$

$$I_T = \frac{1}{2}\frac{r}{r+1} \tag{3.59b}$$

$$a_s = \frac{1}{2}\frac{r+1}{r} \tag{3.59c}$$

$$u_s = \frac{1}{2}r(r+1) \tag{3.59d}$$

Similarly as for the above cases, a transformation can be made such that the dynamics between spikes is described by a phase that unwraps linearly in time. Integrating for each branch of equation (3.58) the time spent in each branch, its sum (the total period), the phase velocity and the phase value of the glue point can be obtained:

$$\phi_G = \pi \frac{r-1}{r+1} \tag{3.60a}$$

$$T_{\text{free}} = \frac{\pi \tau^m}{\sqrt{I}} \sqrt{\frac{r+1}{2r}} \tag{3.60b}$$

$$\omega = \frac{2\pi}{T_{\text{free}}} \tag{3.60c}$$

Solving for each branch independently the transformation between the neuron models is:

$$\phi_i = \phi_G + \begin{cases} \frac{2}{a_s} \arctan\left(\frac{V_i - V_G}{\sqrt{I/a_s}}\right) & V_i \leq V_G \\ \frac{2}{r a_s} \arctan\left(r \frac{V_i - V_G}{\sqrt{I/a_s}}\right) & V_i > V_G \end{cases} \qquad V_i = V_G + \begin{cases} \sqrt{I/a_s} \tan\left(a_s \frac{\phi_i - \phi_G}{2}\right) & \phi_i \leq \phi_G \\ \sqrt{I/r^2 a_s} \tan\left(r a_s \frac{\phi_i - \phi_G}{2}\right) & \phi_i > \phi_G \end{cases} \tag{3.61}$$

In order to calculate the phase response of the neuron, analogously as before, the jump in the voltage given by $g(V_{i^*}(t_s^+)) = V_{i^*}(t_s^-) + J_{i^* j^*}$ in the ϕ representation has to be calculated. Although for jumps within each branch the calculation is identical to the QIF, the special case when an incoming spike is such that $V_{i^*}(t_s^+)$ and $V_{i^*}(t_s^-)$ belong to different branches has to be considered separately. If a neuron receives an incoming inhibitory spike, the smallest voltage that *stays* in the same branch is $V_{i^*}(t_s^-) = V_G + J$. Inserting this condition in (3.61), gives the value above ϕ_G below which a change of branch would occur, $\phi_- = \phi_G + \frac{2}{r a_s} \arctan\left(r \frac{J_{i^* j^*}}{\sqrt{I/a_s}}\right)$.

$$g(\phi_{i^*}(t_{s+1}^-)) = \phi_G + \begin{cases} \frac{2}{a_s} \arctan\left(\tan\left(a_s \frac{\phi_{i^*}(t_{s+1}^-) - \phi_G}{2} + \sqrt{a_s} \frac{J_{i^* j^*}}{\sqrt{I}}\right)\right) & -\pi < \phi_{i^*}(t_{s+1}^-) \leq \phi_G \\ \frac{2}{a_s} \arctan\left(\frac{1}{r} \tan\left(r a_s \frac{\phi_{i^*}(t_{s+1}^-) - \phi_G}{2} + \sqrt{a_s} \frac{J_{i^* j^*}}{\sqrt{I}}\right)\right) & \phi_G < \phi_{i^*}(t_{s+1}^-) \leq \phi_- \\ \frac{2}{r a_s} \arctan\left(\tan\left(r a_s \frac{\phi_{i^*}(t_{s+1}^-) - \phi_G}{2}\right) + r \sqrt{a_s} \frac{J_{i^* j^*}}{\sqrt{I}}\right) & \phi_- \leq \phi_{i^*}(t_{s+1}^-) \leq \pi \end{cases} \tag{3.62}$$

3.2.3 Delayer single-compartment-axon

Synaptic and axonic delays consistent with the framework above specified can be incorporated to the network defined in Eq. 3.42 by means of the introduction of *delayer* variables. The implementation at the network level of such variables will be detailed in the subsection 3.3.1. Here, we will only give a mathematical definition of these variables, the single compartment axons.

Mapping QIF in the excitable regime to an exponentially decaying variable

To analyze the dynamics of the excitable (non-periodically spiking) regime of the QIF neuron we focus on the solutions of :

$$\tau_l^m \dot{V}_l = V_l^2 - I_l \qquad I_l > 0 \tag{3.63}$$

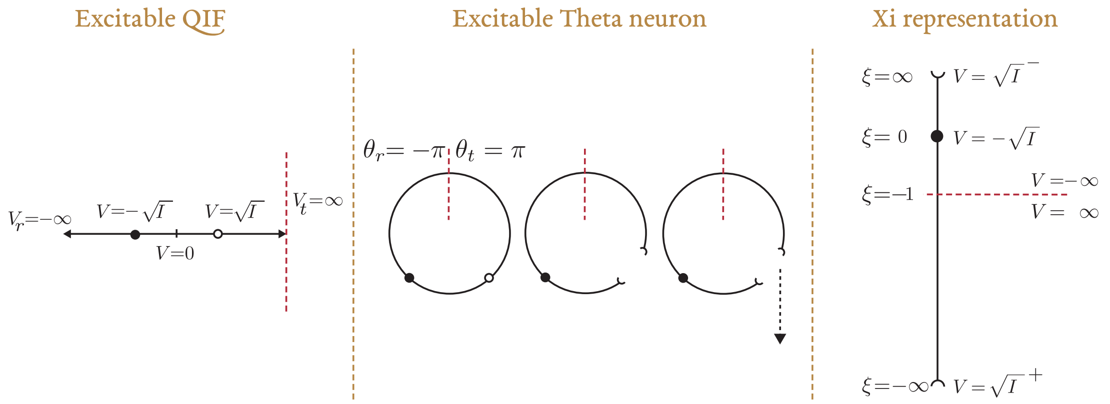

Figure 3.3: QIF in the excitable regime Three possible representation for the dynamics of the QIF neuron in the excitable regime. In the left, in the voltage representation given by Eq. (3.63), in the middle the theta neuron as conceived by Ermentrout & Kopell [74], and the ξ representation in the right. In this last scenario, the neuron at rest in $\xi = 0$ is pulled towards $-\infty$ when receiving a spike, and evolves towards zero, emitting a spike at $\xi = -1$.

The solution of Eq. (3.63) for all three cases (i) $V_l > \sqrt{I_l}$, (ii) $|V_l| < \sqrt{I_l}$, (iii) $V_l < -\sqrt{I_l}$) can be written in the following compact form:

$$\frac{t - t_0}{\tau_l^m} = \frac{-1}{2\sqrt{I_l}} \ln \left(\frac{(\sqrt{I_l} + V_l)(\sqrt{I_l} - V_0)}{(\sqrt{I_l} - V_l)(\sqrt{I_l} + V_0)} \right) \tag{3.64}$$

The transition betweens the regimes (i),(ii),(iii) is dynamically forbidden. We can define a change of variables

$$\xi = \frac{\sqrt{I} + V}{\sqrt{I} - V} \implies \qquad V = \sqrt{I}\frac{(\xi - 1)}{(\xi + 1)} \tag{3.65}$$

that simplifies the expression. Eq. (3.64) then reads:

$$\xi_l = \xi_o e^{\frac{-2\sqrt{I_l}(t - t_0)}{\tau_l^m}} \tag{3.66}$$

The three possible representations of this regime, are shown in Figure 3.3. Note that the variable ξ can in principle take any real value, like its voltage representation. Given that the time evolution given by Eq. (3.66) is sign preserving, the isolated ξ variable will hit the threshold value $\xi_t = -1$ and spike if it was initially negative, and will just relax to zero otherwise. Depending on the value of the reset ξ_r, three different dynamical regimes can be identified. By setting a reset value such that $\xi_r < -1$, a periodically spiking regime is re-obtained. If the reset is set equal to the threshold $\xi_t = \xi_r = -1$, after spiking the variable will exponentially relax to zero. A third possibility, is to set the reset to the value of its stable fixed point, i.e. $\xi_r = 0$, which is illustrated in Figure 3.4.

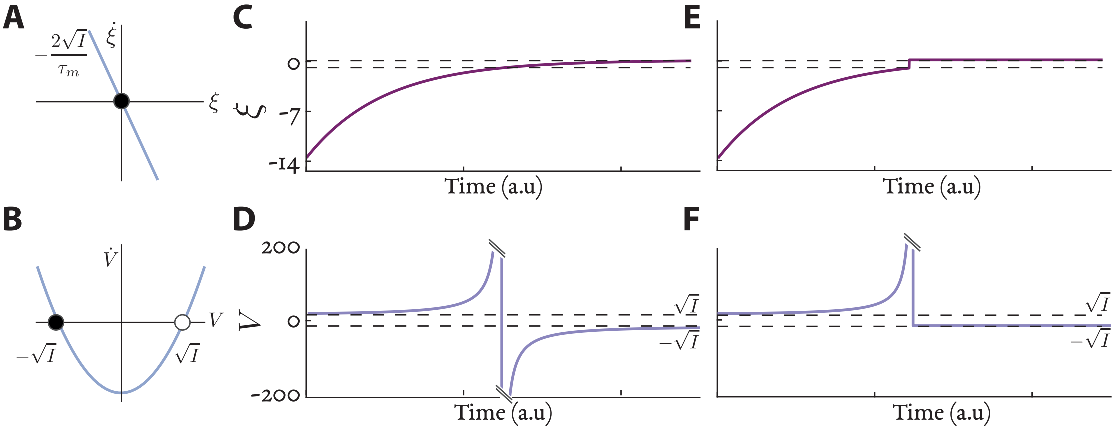

Figure 3.4: (a) Phase portrait of the delayer neuron in the ξ representation **(b)** Phase portrait in its usual QIF form. **(c-d)** Time evolution with no reset, i.e. $\xi_r = \xi_t = -1$. When the ξ variable crosses -1, in the voltage representation the voltage diverges. **(e-f)** Time evolution with reset in the stable fix point, i.e. $\xi_r = 0$.

In this representation a propagator function η and an update function γ, analogous to f and g of section 3.2.2 for the neuron models that allow for a phase representation, can as well be defined:

$$\eta(\xi_l(t_s^+), t_{s+1}^- - t_s^+) = \xi_{l^*}(t_{s+1}^-) = \xi_l(t_s^+)e^{\frac{-2\sqrt{I_l}(t_{s+1}^- - t_s^+)}{\tau_l^m}} \tag{3.67}$$

$$\gamma(\xi_{l^*}(t_{s+1}^-)) = \xi_{l^*}(t_{s+1}^+) = \frac{\xi_{l^*}(t_{s+1}^-)(1 + \frac{2\sqrt{I_{l^*}}}{J_{l^*j^*}}) + 1}{\frac{2\sqrt{I_{l^*}}}{J_{l^*j^*}} - 1 - \xi_{l^*}(t_{s+1}^-)} \tag{3.68}$$

The γ function is obtained analogously to the previous cases, by introducing Eq. (3.65) in $V_{l^*}(t_{s+1}^+) = V_{l^*}(t_{s+1}^-) + J_{l^*j^*}$.

Delayer single-compartment-axon from a excitable QIF in ξ representation

The ξ variable, when initially at $\xi_0 < -1$ takes a finite time to spike given by $\delta_l = \frac{\tau_l^m}{2\sqrt{I_l}} \ln(-\xi_0)$. If the reset value is set to $\xi_r = 0$, there will be no dynamics after the spiking event. If while in its resting state, an incoming spike from neuron j^* is received, then its state will be modified according to $\gamma(0)$ and will depend only on the parameters of the system:

$$\gamma(0) = \frac{J_{l^*j^*}}{2\sqrt{I_{l^*}} - J_{l^*j^*}} \tag{3.69}$$

If the incoming spike has a weight that was *strong enough* then the ξ variable will be pushed beyond its unstable fixed point and emit an spike after a fraction of time given by:

$$\delta_{l^*j^*} = \frac{\tau^m_{l^*}}{2\sqrt{I_{l^*}}} \ln\left(\frac{J_{l^*j^*}}{J_{l^*j^*} - 2\sqrt{I_{l^*}}}\right) \tag{3.70}$$

before relaying it to the next neuron. Note that in Eq. (3.70) the value of $J_{l^*j^*}$ has to be bigger than $2\sqrt{I_{l^*}}$, the distance between the fixed points in equation (3.63), formalizing the initial intuition of “strong enough” kick in the voltage. For the case in which $J_{l^*j^*}$ is independent of the neuronal pair, the delay introduced by the SCA will only depend on its own parameters, and then $\delta_{l^*j^*} = \delta_{l^*}$. The single-compartment-axon (SCA), is then defined by Eqs. (3.68), with a reset value $\xi_r = 0$ for the “exact delay” framework.

If the SCA has a reset value that is equal to any value between the threshold $\xi_T = -1$ and zero, the delay will depend on the dynamics of the network and change from spike to spike. The delay in that case will be :

$$\delta_{l^*j^*} = \frac{\tau^m_{l^*}}{2\sqrt{I_{l^*}}} \ln\left(-\frac{\xi_{l^*}(t^-_{s+1})(1 + \frac{2\sqrt{I_{l^*}}}{J_{l^*j^*}}) + 1}{\frac{2\sqrt{I_{l^*}}}{J_{l^*j^*}} - 1 - \xi_{l^*}(t^-_{s+1})}\right) \tag{3.71}$$

For $J > 0$, this equation has solutions for $\xi > \frac{2\sqrt{I_{l^*}}}{J_{l^*j^*}} - 1$. The smaller the value of $\frac{2\sqrt{I_{l^*}}}{J_{l^*j^*}}$, the larger the range of ξ to which it can be reset, and the faster the function in the logarithm reaches a value that is only weakly dependent on ξ. This configuration, is what will can call “dynamic delay” framework.

In both cases, when the SCA is arranged post-synaptically to each neuron in a network, it will delay the transmission of the spike by an amount given by Eq. (3.70) or (3.71), while preserving the desirable features of iterable maps.

3.2.4 Balanced state

In the introduction, the balanced state framework for networks presenting asynchronous and irregular dynamics was shown in the language of its original formulation, with binary neurons. Equivalently, we could think of the mean activity as m_l (with l excitatory or inhibitory) as the mean firing rate in the units of the membrane time constant. In this case the firing rates satisfy:

$$\nu_E = -\frac{J_{EI}I_0 - J_{II}E_0}{\tau^m|\boldsymbol{J}|} \tag{3.72}$$

$$\nu_I = -\frac{J_{EE}I_0 - J_{IE}E_0}{\tau^m|\boldsymbol{J}|} \tag{3.73}$$

and identical conditions to those in Eq. (3.40) on the weights are obtained. The input currents, in this case have a mean given by:

$$\langle I^x \rangle = \sqrt{K}(X_0 + \tau^m J_{xE}\nu^E - \tau^m J_{xI}\nu^I) \tag{3.74}$$

where X_0, the excitatory input to the population x is E_0 for the excitatory population and I_0 for the inhibitory one.The variance of the input currents are given by [*]:

$$\sigma^2_{I_x} = \langle (I^x)^2 \rangle - (\langle I^x \rangle)^2 = \tau^m (J^2_{xE}\nu^E + J^2_{xI}\nu^I) \tag{3.75}$$

For the particular case of only inhibitory neurons, the condition of a finite mean imposes that $I_0 - \tau^m J_{II}\nu$ has to be $\mathcal{O}(1/\sqrt{K})$. In the limit of large K the firing rate must then satisfy:

$$\nu = \frac{I_0}{\tau^m J_{II}} + \mathcal{O}(1/\sqrt{K}) \tag{3.76}$$

In the case of inhibitory and excitatory networks, conditions need to be imposed if the statistics of these neuron types are to be indistinguishable. We request that the first moment of the firing rates distributions are the same $\nu_E = \nu_I$, and that the variances of the input currents are also equal: $\sigma^2_{I_E} = \sigma^2_{I_I}$. Together, these conditions impose further constraints on the synaptic weights: $J^2_{EE}+J^2_{EI} = J^2_{IE}+J^2_{II} = J^2_0$. In order to incorporate these to those obtained in Eqs. (3.40), the weight matrix is written as a function of three parameters: J_0, $\eta = J_{EE}/J_{EI} < 1$ and $\epsilon = J_{IE}/J_0$. The synaptic weights then have the form:

$$J = \frac{J_0}{\sqrt{K}} \begin{pmatrix} \epsilon\eta & -\sqrt{1-\epsilon^2\eta^2} \\ \epsilon & -\sqrt{1-\epsilon^2} \end{pmatrix} \tag{3.77}$$

The inequalities of Eq. (3.40) then constrain the values of η and ϵ to fulfill: $\eta\epsilon < \epsilon < \sqrt{1/2}$.

Equations (3.76) and (3.72) define the mean firing rate of the network as a function of the input current to each neuron. For simulations in the *fix rate* configuration, a mean firing rate will be chosen, and a guess on the current will be made. This guess, from Eq. (3.76), is for the purely inhibitory network given by:

$$I_0 = \tau^m J_{II}\nu \tag{3.78}$$

---

[*] As in [30,29], the variance of the input current is defined in units of the membrane time constant, and therefore has a τ^m "less" than it would be obtained by the straight forward calculation.

3.2.5 Numerical Methods

High performance parallel simulations of the network were written in C++, originally by Monteforte[173] and later developed to deal with interaction delays. Smaller simulations and comparison with delayed networks via standard integration schemes were made in Python with custom code while the analysis was performed with custom code in Matlab. The simulations are event based as described in the previous subsections. For each simulation, random topologies (Erdős–Rényi) for the neuronal block (See Eq. (3.83) for detail of the complete connectivity) and random initial conditions are generated, and an over all firing rate is calculated. In the networks labeled as *fixed rate*, the mean firing was kept fixed at a target value. By means of root finding algorithms (Regula Falsi and Ridders method)[197], a guess on the input current I needed to have a target firing rate was made from Eq. (3.78). After a simulation lasting $\mathrm{S_R}$ spikes per neuron, the rate was calculated and a new guess on the currents is made. This procedure is then iterated until the target mean firing rate is found with 1% precision. The multiplying factor that measures the distance to the balance condition is defined by $Is = I/I_0$. Once the appropriate value of the current I is found, the network can be warmed up to disregard transients, which can be large in delayed systems by a time equivalent to $\mathrm{S_W}$ spikes per neuron. Finally, a random orthonormal matrix Q is chosen and the QR algorithm described in the theory section was left to warm up for a time duration equivalent to $\mathrm{S_{WONS}}$ spikes. This guarantees some degree of alignment of the first Lyapunov vector to the first vector of the orthonormal system. The simulation runs for a time equivalent to $\mathrm{S_C}$ spikes per neuron (see subsection 3.2.7 for parameters).

The direct method for the estimation of the first LE

Numerical corroboration of the equations derived in the subsection 3.3.2 of the Results can be done by direct perturbation of the trajectory of the network. After a long warm-up, the state of the network is perturbed by adding a random vector of norm ϵ. After a short simulation of $T = 100$ ms the norm η between the perturbed and the unperturbed final states, simulated separately is stored. The iteration of this procedure N times, leads to the estimation of the first Lyapunov exponent via the following formula:

$$\lambda_1 = \sum_{i}^{N} \frac{1}{NT} \log(\eta(i)/\epsilon) \tag{3.79}$$

Where ϵ was chosen to be 10^{-10} and N=5000.

3.2.6 Characterization of network activity

Rates, coefficient of variation, and silent percentages

The firing rates of each neuron ν_i were calculated by summing all the spikes and dividing by the time spanned between the first and the last spike. The mean population rate is then ν. The coefficient of variation is the square root of the squared inter-spike-interval times the squared rate, i.e.

$$CV = \sqrt{\sigma^2_{\mathrm{ISI}} \nu^2} = \frac{\sigma_{ISI}}{\mu_{ISI}} \tag{3.80}$$

If a neuron did not spike during the whole simulation, its CV and its rate are not considered to build the respective distributions. Instead, they contributed to the measure $\%S$, defined as percentage of silent neurons respect to the total amount of neurons N_x of its type, where x can be inhibitory or excitatory.

Oscillatory activity related quantities

The level of synchrony of the network was assessed by the synchronization index χ^2 (see also Chapter 2), defined as

$$\chi^2 = \frac{\sigma^2_{\phi(t)}}{\sum_{i=1}^{N} \sigma^2_{\phi_i(t)}/N} \tag{3.81}$$

Where, $\phi(t) = \sum_{i=1}^{N} \phi_i(t)/N$ is the mean activity in the phase representation. The variables $\sigma_{\phi(t)}$ and $\sigma_{\phi_i(t)}$ are the standard deviation of the mean phase over time or, respectively, of the phase trace $V_i(t)$ of each individual neuron i. The χ coefficient is bounded to the unit interval $0 < \chi < 1$, with vanishing values indicating asynchronous dynamics.

The amplitude A (Hz) and the frequency f (Hz) of the population activity was calculated by making a binning histogram of a 1 ms bin of the spikes of the entire network. This quantity normalized by the bin size and the number of neurons defines a Multi-Unit like signal (glsMUA). The mean peak high defines the amplitude A (Hz). The frequency of the MUA was obtained as the inverse of the first autocorrelation peak. In the Results section the normalized value $\frac{f\ (\mathrm{Hz})}{\nu\ (\mathrm{Hz})}$ is usually shown, given that facilitates the identification of different types of oscillatory synchrony.

Heterogeneities

Heterogeneities in the network were introduced by setting either the individual time constants to different values, or by setting the input currents of each neuron to different values. The level of heterogeneity is quantified by the standard deviation of τ_i^m, σ_{τ^m}, or the standard deviation of I_i, σ_I. Gaussian and uniform distributions yielded similar results for adequate σ values, specified in the Results.

3.2.7 Parameters of the simulations

Type of neuron		QIF
Number of neurons	N	10000
Average connections per neuron	K	100
Mean firing rate in *fixed rate* configurations	ν	5 Hz
Input current in the *non fixed rate* configurations	I_0	Eq. 3.78
Standard deviation of the input current distribution	σ_I	0
Standard deviation of the membrane time constant distribution	σ_{τ^m}	0.5
Inhibitory to excitatory ratio in EI networks	N_I/N_E	0.2N/0.8N
Strength of the Inhibitory-Excitatory loop in EI networks	ϵ	0.1
Ratio of excitatory weights $\eta = J_{EE}/J_{EI}$ in EI networks	η	0.9
Spikes per neuron in firing rate search	$\mathrm{S_R}$	200
Spikes per neuron in warm up	$\mathrm{S_W}$	200
Spikes per neuron in warm up or orthonormal system	$\mathrm{S_{WONS}}$	200
Spikes per neuron in simulation	$\mathrm{S_C}$	300

Table 3.1: List of default network parameters.

The table 3.1 shows a list of default simulation parameters. Deviations from the default are as follows: In Figures 3.8,3.10, 3.26 and 3.27, there was no fixed rate. In Figure 3.14, the heterogeneity was in the input current (threshold heterogeneity), with the value indicated in the Figure, while no heterogeneity in the membrane time constant was included. In Figure 3.15(a-c),(e-f), and Figures 3.20,3.21,3.22 in panels (f-h) and 3.25(c-d) N was 2000, while in 3.17 N=400 and in all those cases $\mathrm{S_R}$=$\mathrm{S_Q}$=$\mathrm{S_{WONS}}$=600. In Figure 3.12 no heterogeneity of any kind was present. Figures 3.23,3.24,3.25 had only current heterogeneity and no membrane time constant heterogeneity. In the Figures 3.28, 3.29, N=20000, the membrane time constant heterogeneity was $\sigma_{\tau^m} = 1.5$ and the threshold heterogeneity was σ_I =0.05.

3.3 Results

3.3.1 Network of delayed phase neurons

The system we are interested in analyzing is of the generic form:

$$\tau_i^m \dot{V}_i(t) = F(V_i) + I_i + \tau_i^m \sum_{j \in pre(i)} \sum_s J_{ij} \delta(t - t_j^s - \delta_j) \tag{3.82}$$

$F(V_i)$ contains the dynamics of a one dimensional neuronal model, τ_i^m is the membrane time constant of the neuron, V is the neuron's membrane voltage, I_i is an external input current that is independent for every neuron. The last term represents the recurrent input to the neuron i from its neighbors j, which consist of a pulse of amplitude J_{ij}. The pulse is emitted at time t_j^s, and reaches its post-synaptic target at $t_j^s + \delta_j$; with δ_j a delay that depends only on the pre-synaptic neuron. The study of the dynamics and the ergodic properties of such a system without sacrificing the possibility of an analytical solution between spikes, can be done by the introduction of a *delayer* single-compartment axon, SCA. When located post-synaptically to each neuron in a network, the SCA (see Sec. 3.2.3) introduces a delay due to the extra integration steps needed to reach threshold. Afterwards, it is reset to a X_R value, that can also be a fixed point. In this last case, a new incoming spike will depolarize the SCA to a precise value such that it takes a time δ_j, given by Eq. (3.70), until the spike is transmitted to the postsynaptic neighbors of neuron j.

A diagram of the network architecture of a delayed network with balanced state properties is shown in Fig. 3.5. A spiking neuron j^* (in blue, left), described by its phase variable ϕ_{j^*} receives independent and large inputs proportional to the square root of the average amount of connections per neuron K. Its spike is instantaneously transmitted to the SCA, of variable ξ_{l^*} in black. The parameters of the SCA define the time it will take for the spike to be transmitted, from the SCA to the postsynaptic neurons of j^*, whose phase variable is ϕ_{i^*}.

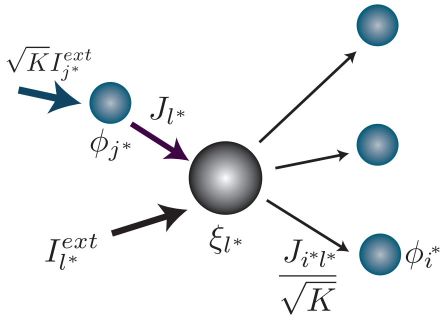

Figure 3.5: Network connectivity of the delayed system. Every neuron is uniquely connected to a *delayer* SCA, that later distributes the spike from neuron j^* to its pot-synaptic neurons i^*. See details in text.

The connectivity matrix, $\mathbb{J}$ has then the form in Eq. (3.83). For ease of notation, indexes i and j (from 1 to N) will be reserved for phase neurons and l and m (from N+1 to M = 2N) for the SCA. The connectivity matrix is a block matrix describing an Erdős–Rényi random graph on the upper right block, with weights proportional to $1/\sqrt{K}$ and a diagonal matrix in the bottom left:

$$J = \begin{pmatrix} & & & & & J_{1,N+1} & \cdots & J_{1,l} & \cdots & J_{1,M} \\ & & & & & \vdots & \ddots & \vdots & \ddots & \vdots \\ & & & & & J_{j,N+1} & \cdots & J_{j,l} & \cdots & J_{j,M} \\ & & & & & \vdots & \ddots & \vdots & \ddots & \vdots \\ & & & & & J_{N,N+1} & \cdots & J_{N,l} & \cdots & J_{N,M} \\ J_{N+1,1} & & & & & & & & & \\ & \ddots & & & & & & & & \\ & & J_{l,j} & & & & & & & \\ & & & \ddots & & & & & & \\ & & & & J_{M,N} & & & & & \end{pmatrix} \tag{3.83}$$

3.3.2 Derivation of the single spike Jacobian

Given a neuronal model $F(V_i)$ and a model for the SCA that allow for an analytical solution, the network can be propagated between spikes by Eq. (3.43) and updated by (3.44). Also, a Jacobian $\mathbb{L}(\boldsymbol{x}(n))$ at each spike time can be obtained. This expression enables the estimation of the Lyapunov dimension D_L (Eq.(3.21)) and the metric entropy production rate H_μ (Eq.(3.23)) via QR decomposition as in Eq. (3.13).

In the following, we will focus on the derivation of $\mathbb{L}(\boldsymbol{x}(n))$ for the delayed system of neuronal types that allow for a phase representation, although it is not restricted to it. For these neuronal models, the Jacobian elements can be written in terms of the phase response curve (PRC) defined in Eq. (3.51).

Four cases will have to be distinguished. First, we consider the situation in which a SCA, with associated variable ξ_{m^*}, spikes at τ_{s+1} between two other time events, $\tau_{s+1} \in [t_s, t_{s+1}]$. The neurons that are not postsynaptic to it will evolve independently of when the spike is exactly, following $f(\phi_{i^0}(t_s), t_{s+1} - t_s)$ (see Methods section 3.2.2 for the definition of f for different neuron models). The ones that are postsynaptic to it will follow the scheme presented in Fig. 3.6. Its temporal evolution through the spike is given by $f(g(f(\phi_i(t_s), \tau_{s+1}^- - t_s)), t_{s+1} - \tau_{s+1}^+)$.

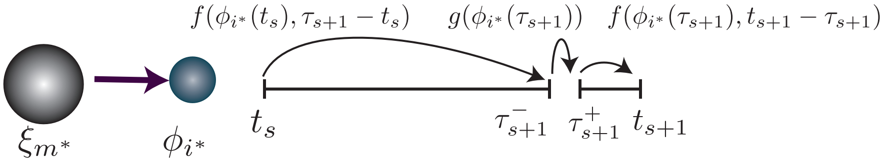

Figure 3.6: Evolution of a neuron with dynamics described by ϕ_{i^*}, when receiving a spike from a SCA described by ξ_{m^*}

Equivalently, when a spike is emitted by a neuron, it will be received only by its own associated SCA. The effect of the incoming spike on the dynamics of the SCA will then be $\eta(\gamma(\eta(\xi_l^*(t_s), \tau_{s+1}^- - t_s)), t_{s+1} - \tau_{s+1}^+)$. SCA that are not post-synaptic to the spiking neuron will evolve with $\eta(\xi_{i^0}(t_s), t_{s+1} - t_s)$.

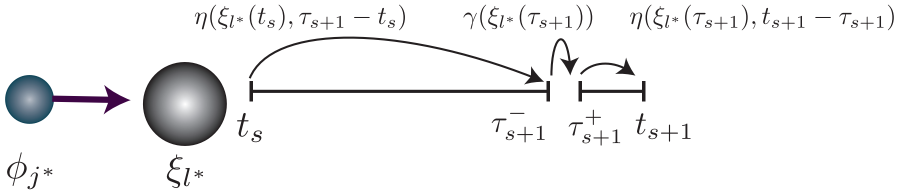

Figure 3.7: Evolving a SCA with dynamics described by ξ_{l^*} after receiving a spike from ϕ_{j^*}

In order to calculate the single spike Jacobian, we first summarize the equations for the phase neuron and the SCA, as derived in the Methods. We define:

$$T_l = \frac{\tau_l^{m,\xi}}{2\sqrt{I_l^\xi}} \qquad\qquad A_{lj} = \frac{2\sqrt{I_l^\xi}}{J_{lj}} \tag{3.84}$$

Where the supra-index ξ was added to emphasize that those constants are only meaningful for SCA. The propagation and update functions for the neurons f and g, and for the SCA, η and γ, are:

Phase Neuron

$$f(\phi_i(t_0), \Delta t) = \phi_i(t_0) + \omega_i \frac{\Delta t}{\tau_i^m} \tag{3.85}$$

With derivatives

$$\partial_x f(\phi_i(t_0), \Delta t) = 1 \qquad\qquad \partial_t f(\phi_i(t_0), \Delta t) = \frac{\omega_i}{\tau_i^m} \tag{3.86}$$

$$g(\phi_i(t_0)) = \phi_i(t_0) + \mathrm{PRC}(\phi_i) \tag{3.87}$$

With derivatives

$$\partial_x g(\phi_i(t_0)) = 1 + \mathrm{PRC}'(\phi_i(t_0)) \tag{3.88}$$

SCA

$$\eta(\xi_l(t_0), \Delta t) = \xi_l(t_0) e^{-\frac{\Delta t}{T_l}} \tag{3.89}$$

With derivatives

$$\partial_x \eta(\xi_l(t_0), t) = e^{-\frac{\Delta t}{T_l}} \qquad \partial_t \eta(\xi_l(t_0), t) = -\frac{\xi_l(t_0)}{T_l} e^{-\frac{\Delta t}{T_l}} \tag{3.90}$$

$$\gamma(\xi_l(t_0)) = \frac{\xi_i(t_0)(1 + A_{lj}) + 1}{A_{lj} - 1 - \xi_i(t_0)} \tag{3.91}$$

With derivatives

$$\partial_x \gamma(\xi_l(t_0)) = \frac{A_{lj}^2}{(A_{lj} - 1 - \xi_l(t_0))^2} \tag{3.92}$$

For a generic neuron model with state variable x, that evolves with function f and updates with function g, the derivative with respect to some other neuron variable (possibly defined by a different neuron model) y can be written as:

$$\frac{dx_i(t_s + 1)}{dy_j(t_s)} = \tag{3.93a}$$

$$\partial_x f(x_i(t_s), t_{s+1} - t_s) \frac{\partial x_i(t_s)}{\partial y_j(t_s)} \delta_{ii^0} + \tag{3.93b}$$

$$\partial_x f(x_i(\tau_{s+1}^+), t_{s+1} - \tau_{s+1}^+) \partial_x g(x_i(\tau_{s+1}^-)) \partial_x f(x_i(t_s), \tau_{s+1}^- - t_s) \frac{\partial x_i(t_s)}{\partial y_j(t_s)} \delta_{ii^*} \tag{3.93c}$$

$$\partial_x f(x_i(\tau_{s+1}^+), t_{s+1} - \tau_{s+1}^+) \partial_x g(x_i(\tau_{s+1}^-)) \partial_t f(x_i(t_s), \tau_{s+1} - t_s) \frac{\partial \tau_{s+1}}{\partial y_j(t_s)} \delta_{ii^*} \tag{3.93d}$$

$$- \partial_t f(x_i(\tau_{s+1}^+), t_{s+1} - \tau_{s+1}^+) \frac{\partial \tau_{s+1}}{\partial y_j(t_s)} \delta_{ii^*} \tag{3.93e}$$

Where i^0 is the index corresponding to the non-postsynaptic neurons, i^* for the postsynaptic ones and the spiking neuron j^*. Note that if the spiking neuron is reset, then only the last term (Eq. (3.93e)) survives given that $g(x_i(\tau_{s+1}^-)) = X_R$ and therefore has null derivative. The term $\frac{\partial x_i(t_s)}{\partial y_j(t_s)} = \delta_{xy}\delta_{ij}$ and $\frac{\partial \tau_{s+1}}{\partial y_j(t_s)}$ can be extracted from the fact that $f(y_{j^*}(t_s), \tau_{s+1} - t_s)) = X_T$ and therefore:

$$\frac{\partial \tau_{s+1}}{\partial y_j(t_s)} = -\frac{\partial_x f(y_j(t_s), \tau_{s+1} - t_s)}{\partial_t f(y_j(t_s), \tau_{s+1} - t_s)} \delta_{jj^*} \tag{3.94}$$

In the case we are analyzing here,

$$\frac{\partial \tau_{s+1}}{\partial \phi_{j^*}(t_s)} = -\frac{\tau_{j^*}^m}{\omega_{j^*}} \qquad \frac{\partial \tau_{s+1}}{\partial \xi_{m^*}(t_s)} = \frac{\tau_{m^*}^{m,\xi}}{2\sqrt{I_{m^*}^{\xi} \xi_{m^*}(t_s)}} = \frac{T_{m^*}}{\xi_{m^*}(t_s)} \tag{3.95}$$

The terms of the Jacobian for the delayed system can be summarized as follows:

Non-postsynaptic neurons $\phi_{i^0}(t_{s+1}) = f(\phi_{i^0}(t_s), t_{s+1} - t_s)$

- Contribute to the Jacobian only with diagonal terms from Eq. (3.93b)

$$\frac{d\phi_{i^0}(t_{s+1})}{d\phi_j(t_s)} = \delta_{ji^0} \tag{3.96}$$

Postsynaptic neurons $\phi_{i^*}(t_{s+1}) = f(g(f(\phi_{i^*}(t_s), \tau^-_{s+1} - t_s)), t_{s+1} - \tau^+_{s+1})$

- From Eq. (3.93c) contribute with diagonal terms

$$\frac{d\phi_{i^*}(t_{s+1})}{d\phi_j(t_s)} = 1 + \underset{i^*j^*}{\mathrm{PRC}}'(\phi_{i^*}(t^-_{s+1}))\delta_{ji^*} \tag{3.97}$$

- Contribute with non diagonal terms (when receiving a spike from a neuron ϕ_{j^*}) from Eq. (3.93d) and (3.93e)

$$\frac{d\phi_{i^*}(t_{s+1})}{d\phi_j(t_s)} = -\underset{i^*j^*}{\mathrm{PRC}}'(\phi_{i^*}(t^-_{s+1}))\frac{\omega_{i^*}}{\tau^\phi_{i^*}}\frac{\tau^\phi_j}{\omega_j}\delta_{jj^*} \tag{3.98}$$

- Contribute with non diagonal terms (when receiving a spike from a delayer SCA ξ_{m^*}, from Eq. (3.93d) and (3.93e)

$$\frac{d\phi_{i^*}(t_{s+1})}{d\xi_m(t_s)} = \underset{i^*m^*}{\mathrm{PRC}}'(\phi_{i^*}(t^-_{s+1}))\frac{\omega_{i^*}}{\tau^\phi_{i^*}}\frac{T_m}{\xi_m(t_s)}\delta_{mm^*} \tag{3.99}$$

Spiking neuron $\phi_{j^*}(t_{s+1}) = f(g(f(\phi_{j^*}(t_s), \tau^-_{s+1} - t_s)), t_{s+1} - \tau^+_{s+1})$

- Only one term in the Jacobian, from Eq. (3.93e), Eq. (3.93c) and (3.93d) vanish

$$\frac{d\phi_{j^*}(t_{s+1})}{d\phi_j(t_s)} = \delta_{jj^*} \tag{3.100}$$

Non-postsynaptic SCA $\xi_{l^0}(t_{s+1}) = \eta(\xi_{l^0}(t_s), t_{s+1} - t_s)$

- Contribute with diagonal terms from Eq. (3.93b)

$$\frac{d\xi_{l^0}(t_{s+1})}{d\xi_m(t_s)} = \exp\left(-\frac{(t_{s+1} - t_s)}{T_{l^0}}\right)\delta_{ml^0} \tag{3.101}$$

Postsynaptic SCA $\xi_{l^*} = \eta(\gamma(\eta(\xi_{l^*}(t_s), \tau^-_{s+1} - t_s)), t_{s+1} - \tau^+_{s+1})$

- Contribute with diagonal terms from Eq. (3.93c)

$$\frac{d\xi_{l^*}(t_{s+1})}{d\xi_l(t_s)} = \frac{A^2_{l^*j^*}}{\left(A_{l^*j^*} - 1 - \xi_{l^*}(t^-_{s+1})\right)^2} \exp\left(-\frac{(t_{s+1} - t_s)}{T_{l^*}}\right)\delta_{l^*l} \tag{3.102}$$

- Contribute with non-diagonal terms (when receiving a spike from a neuron ϕ_{j^*}) from Eq. (3.93d) and (3.93e)

$$\frac{d\xi_{l^*}(t_{s+1})}{d\phi_j(t_s)} = \frac{\tau^\phi_j}{w_j}\frac{1}{T_{l^*}}\left(\frac{A^2_{l^*j}}{\left(A_{l^*j^*} - 1 - \xi_{l^*}(t^-_{s+1})\right)^2}\xi_{l^*}(t_s)\exp\left(-\frac{(t_{s+1} - t_s)}{T_{l^*}}\right) - \xi_{l^*}(t^+_{s+1})\right)\delta_{j^*j} \tag{3.103}$$

- Contribute with non-diagonal terms (when receiving a spike from a neuron a spiking SCA ξ_{m^*}) from Eq. (3.93d) and (3.93e)

$$\frac{d\xi_{l^*}(t_{s+1})}{d\xi_m(t_s)} = \frac{-T_m}{T^*_l\xi_m(t_s)}\left(\frac{A^2_{l^*m}}{\left(A_{l^*m} - 1 - \xi_{l^*}(t^-_{s+1})\right)^2}\xi_{l^*}(t_s)\exp\left(-\frac{(t_{s+1} - t_s)}{T_{l^*}}\right) - \xi_{l^*}(t^+_{s+1})\right)\delta_{m^*m} \tag{3.104}$$

Spiking SCA $\xi_{m^*}(t_{s+1}) = \eta(\gamma(\eta(\xi_{m^*}(t_s), \tau^-_{s+1} - t_s)), t_{s+1} - \tau^+_{s+1})$

- Only one term in the Jacobian, from Eq. (3.93e). Eq. (3.93c) and (3.93d) cancel one each other

$$\frac{d\xi_{m^*}(t_{s+1})}{d\xi_m(t_s)} = \frac{\xi_{m^*}(t^+_{s+1})}{\xi_m(t_s)}\delta_{mm^*} = \frac{\xi_R}{\xi_m(t_s)} \tag{3.105}$$

  If one chooses $\xi_R = 0$, then the delay introduced in the network is exact, and the equation vanishes $\xi_{m^*}(t^+_{s+1}) = X_R = 0$ for the *delayer* SCA. In this case, the Jacobian is going to be singular. If the reset value is small but nonzero, an invertible Jacobian is obtained. In this last case, is necessary to ensure that the reset value is passed by the singularity at $\xi_l = 1 - A_{lj}$ (see 3.91), so an incoming spike takes finite time to drive the SCA to threshold (i.e. that there is a solution for Eq. (3.71)). Then it is necessary that $\xi_R > 1 - A_{lj}$.

We note that although here the Jacobian was derived for the more generic case in which phase neurons and the SCAs can interact directly with each other, those terms will be unnecessary in the following, given the block-structure of the connectivity matrix.

3.3.3 Network of delayed inhibitory QIF neurons

Non-delayed networks in the balanced state, as described in the Methods section 3.2.4, exhibit asynchronous and irregular activity[207,266,265,174,173,175]. The introduction of moderate delays, does not disrupt the irregularity and the asynchronicity of the dynamics in the initial transient in LIF neurons[129]. Here we show that in the case of QIF neurons a small delay δ preserves the irregularity and asynchronicity of the dynamics. Given a set of network parameters, a large enough delay will eventually induce a transition to collective rhythmicity. Figure 3.8 illustrates the effect of increasing synaptic delays in a balanced network of QIF neurons, for two values of the membrane time constant heterogeneity (see Methods 3.2.6). Independently of the level of heterogeneity, the inclusion of moderate delays leads to oscillatory collective behavior that preserves variability ($\delta \approx 2$ ms), where the collective activity is rhythmic while single neurons fire irregularly. Larger delays induce a transition to sharp synchrony in the homogeneous case ($\sigma_{\tau^m} = 0$), while in the heterogeneous case, although increasingly synchronized, presents still irregularity: The CV and the firing rate distribution (Fig. 3.8(c-d)) are spread out.

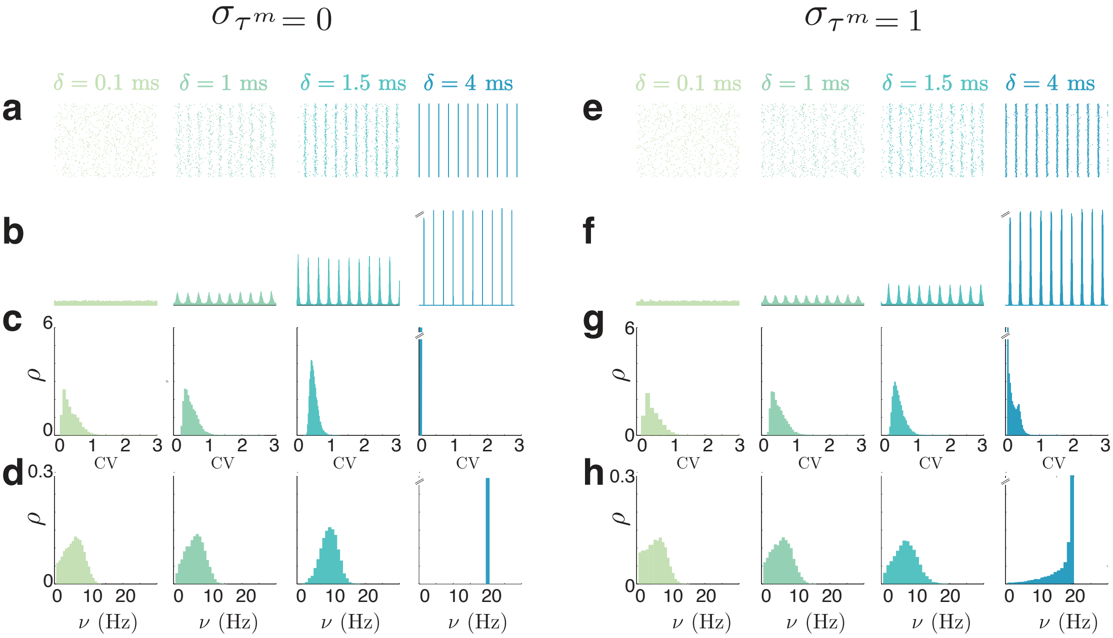

Figure 3.8: Network of QIF neurons with interaction delays Left panels: No heterogeneity. Right Panels: Large Heterogeneity. **(a,e)** Raster plots of 500 neurons for 1 s of simulation. **(b,f)** Multi-Unit Activity like signal (time dependent population rate) for 0.5 s of simulation. **(c,g)** Distribution of the neuron's coefficient of variation. **(d,h)** Distribution of the neuronal firing rates. Note that the firing rate distributions in panel (h) are skewed toward lower values, as is characteristic of heterogeneous networks[121]. Parameters: Default parameters in table 3.1.

The effect of the heterogeneity can be better understood in Figure 3.9. The Figure shows the joint distribution of membrane time constants and firing rates of the individual neurons, in a *fixed rate* configuration (see Methods 3.2.5). For low delays in the heterogeneous cases the distribution spreads along a line with negative slope. Contrary to the scenario in which all neurons are identical, the inclusion of heterogeneity avoids the collapse of the firing rate distribution to a delta function and the corresponding transition to spike-spike synchronization. Neurons with small time constant (which tend to spike faster) align with the population rhythm, while those with large time constant contribute to spreading out the firing rate distribution. The smaller the heterogeneity, the faster the system eventually reaches spike-spike synchrony.

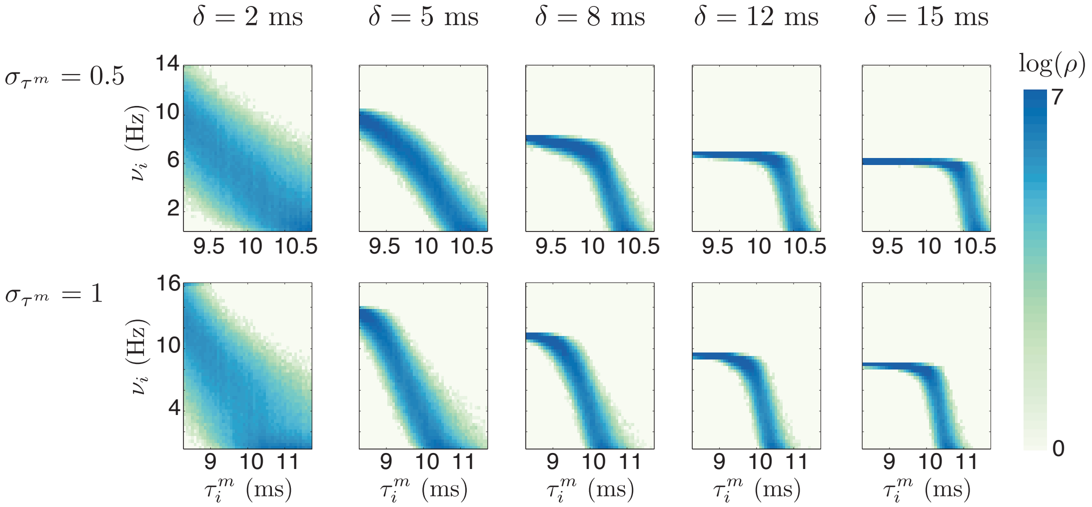

Figure 3.9: Effects of delay and heterogeneity in the firing rate distribution of a network of inhibitory QIF neurons Joint rate and membrane time constant distribution for two levels of heterogeneity in the membrane time constant and various delays. Note the different axes ranges. Parameters: Default parameters in table 3.1.

These results are summarized in Figure 3.10. The cases analyzed in Figure 3.8 are shown in yellow and dark orange, together with two other levels of heterogeneity. In the homogeneous case (yellow curve) the synchrony index (see Methods section 3.2.6), exhibits a step jump to one, the fully synchronized state, together with a jump in the mean firing rate, as seen in panel b. This jump can also be clearly seen in the amplitude of the MUA signal, A in panel c. The heterogeneous cases still maintain a coexistence between some degree of synchrony among neurons and variability. The ratio between the population frequency f and the mean firing rate of the neurons ν approaches one asymptotically and in a continuous manner (panel d). At the transition the network oscillates at a frequency several times higher than the mean firing rate, while the neurons fire in an irregular manner bearing some parallels from the case of the synchronous irregular state SI described for the LIF neuron[31,35,30,29]. Unlike the LIF neuron, the QIF neuron exhibits oscillation frequencies of around 20 Hz. Using the terms coined in[29], we refer to this state as the *slow* SI state. Finally, the coefficient of variation CV (panel e), and the standard deviation of the firing rate distribution σ_ν (panel f), also evident the lack of complete synchrony. We note that increasing heterogeneity skews the firing rate distribution to lower values, as theoretically described in Hiemeyer[121] for integrate and fire neurons with no reset.

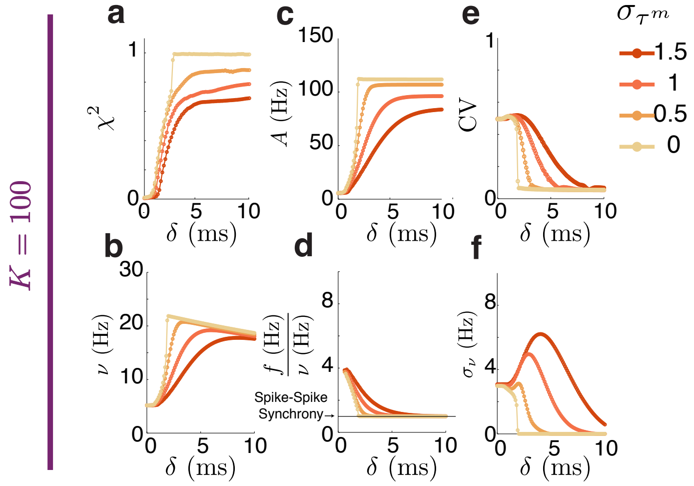

Figure 3.10: Characterization of a network of inhibitory QIF neurons with *no fixed rate* with membrane time constant heterogeneity (a) χ index. **(b)** Mean firing rate ν. **(c)** Amplitude of the MUA-like signal. **(d)** Population frequency f normalized by the mean rate ν. **(e)** Coefficient of variation **(f)** Standard deviation of the firing rate distribution. Parameters: Default parameters in table 3.1 , except explicitly indicated in the figure.

In order to analyze the impact of delayed interactions on the ergodic measures described in the theory section 3.1, is necessary to control independently the variables that characterize the stability properties of the network in the large N limit. Gicen that the lyapunov spectrum depends stronglyon the mean firing rate, we analyze the network properties together with the first Lyapunov exponent in a fixed rate configuration (see Methods 3.2.5).

The first row of Figure 3.11, corresponds to the fixed rate configuration of Figure 3.10. In this case, corresponding to a large average indegree K, the amplitude of the MUA signal increases smoothly, for all levels of heterogeneity, including the homogeneous case. The network oscillates at a frequency that is a few times larger than the neuronal firing rate, in the *slow* SI state. When decreasing K, the transition to collective oscillations is postponed to larger delays and for values of K low enough, the smooth transition seen for large K is abolished. A transition to spike-spike synchronization occurs for all analyzed values of K and heterogeneities provided a delay that is large enough.

A calculation of the mean squared deviation (MSD) of the MUA activity for the homogeneous case is shown in Figure 3.12. A vanishing MSD indicates an asynchronous state, while any degree of synchronization will have a non vanishing value for large N.

The asynchronous irregular state loses stability to oscillatory population activity through Hopf bifurcation at a critical delay δ_0. If the dependence of the oscillation amplitude A on the bifurcation parameter δ follows $A - A_0 \propto \sqrt{\delta - \delta_0}$ as expected from a Hopf bifurcation, then the dependence of the MSD of the MUA signal should be piece-

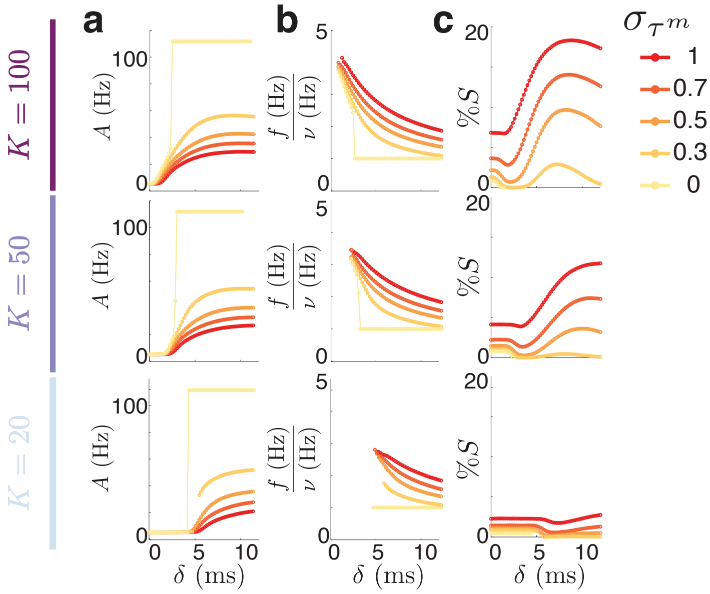

Figure 3.11: Characterization of a network of inhibitory QIF neurons with *fixed rate* and membrane time constant heterogeneity (a) χ index. **(b)** Mean firing rate. **(c)** Amplitude of the MUA-like signal. **(d)** Population frequency f normalized by the mean rate ν. **(e)** Coefficient of variation **(f)** Standard deviation of the firing rate distribution. Parameters: Default parameters in table 3.1, except explicitly indicated in the figure.

wise linear with respect to the delay. In Figure 3.12a, the dependence of the MSD is shown for various values of the average in-degree K as a function of the delay for the homogeneous case for N=10000. The dashed color lines indicate the transition to full synchrony. For low values of K, the MSD detaches from zero to directly reach a dashed line, indicating that the transition is to full synchronization. For values of K larger than $K \approx 40$, MSD takes finite and non zero values indicating some degree of synchrony, and corresponds to the *slow* SI state. In Figure 3.12c, a similar figure shows the case in which heterogeneity is present. The dashed black guiding lines show the possible intersection between the two arms of the piecewise linear function. A zoom of an example case is presented for the homogeneous case in Figure 3.12c and the heterogeneous case in Figure 3.12d for several network sizes. It is apparent that for larger networks sizes, the system departs from the asynchronous state, characterized by a vanishing MSD, with a MSD that is linear with the delay.

The value of the critical delay after which a collective rhythm develops depends on the level of heterogeneities, the average amount of connection per neuron K, the firing rate of the network and the weight of the synaptic conductances. A further increase in the delay mediates a transition to perfect synchrony. This transition occurs at increasingly large delays the largest the level of heterogeneity and the smaller the value of the average connections K.

The maximum Lyapunov exponent of the system characterized in 3.11 in shown in Figure 3.13 as a function of the delay, for different levels of heterogeneity and average amount of connections per neuron. Whenever the amplitude takes non-vanishing values,

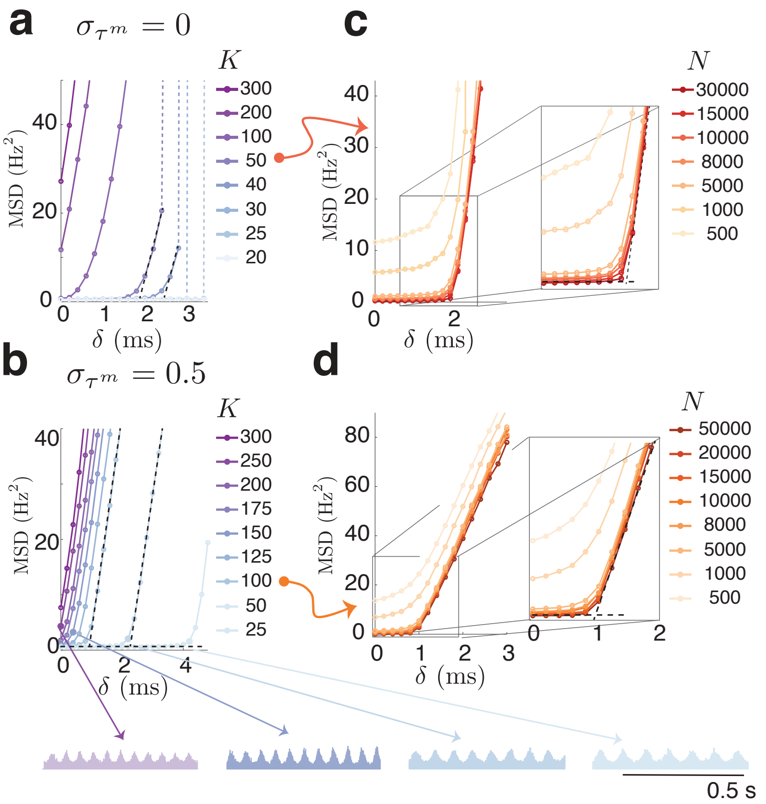

Figure 3.12: Characterization of the transition to collective oscillations for a network of inhibitory QIF neurons **(a)** Mean Squared Deviation of the MUA signal for an homogeneous network and different levels K. Black dashed lines are guides to point out the points falling out the piecewise function. **(b)** Same as panel a for the heterogeneous case. The MUA signal in the first point departing from a vanishing MSD is shown for K=250, 100, 50 and 25 **(c-d)** Dependence of N of the homogeneous case for $K = 50$ (panel **(c)**) and the heterogeneous case for $K = 100$ (panel **(d)**). Mind the different color codes in all panels. Parameters: Default parameters in table 3.1, except explicitly indicated in the figure.

indicating the emergence of a synchronous irregular state, the maximum Lyapunov exponent exhibits a sharp increase. The system not only remains chaotic after the inclusion of delayed interactions, but in the regime in which sparse oscillations are observed, nearby trajectories separate exponentially faster than in the asynchronous case. This increase, is accompanied by an increase in the CV of the neurons (panel b). For low values of K (3.13,third row), the sharp transition to synchrony is accompanied by a transition to dynamical stability. Nevertheless, moderate amounts of heterogeneity restore the irregular oscillation seen for higher valued of K as indicated by the peak in the CV and in the maximum Lyapunov exponent. Figure 3.13c, shows the measure I_s quantifying the deviation from the balanced state equation in (3.78), that departs from one as the oscillation develops.

Given that in the phase representation the phase velocity of the QIF neuron is a ratio between the external input current I_i and the membrane time constant, the inclusion of heterogeneity in any of these parameters is expected to yield similar results. As the

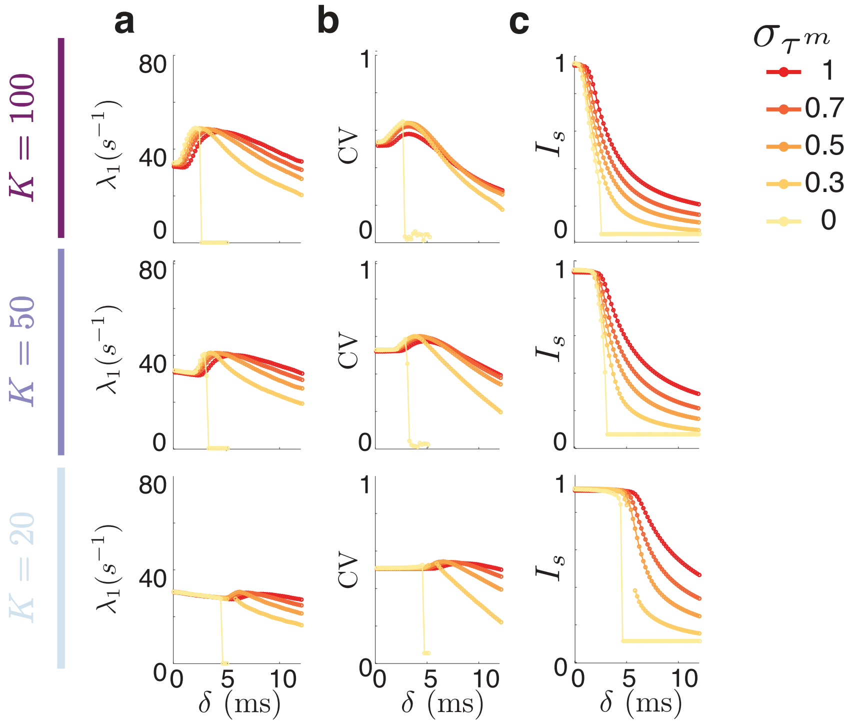

Figure 3.13: Chaos in a network of inhibitory QIF neurons with membrane time constant heterogeneity (a) Maximum Lyapunov exponent for three values of average in-degree K. **(b)** CV. **(c)** I_s. Parameters as in Figure 3.11: Default parameters in table 3.1, except explicitly indicated in the figure.

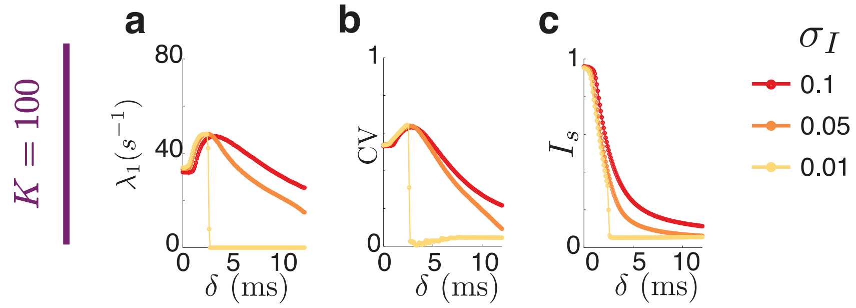

Figure 3.14: Chaos in a network of inhibitory QIF neurons with threshold heterogeneity (a) Maximum Lyapunov exponent for three values of average in-degree K. **(b)** CV. **(c)** I_s. Parameters: Default parameters as in table 3.1, with no membrane time constant heterogeneity but threshold heterogeneity instead, as indicated in the figure.

fixed points of the QIF are only dependent on I_i, heterogeneity in this parameter can also be called threshold heterogeneity. As shown in Figure 3.14, an identical smearing out of the transition to spike-spike synchrony and the concomitant prolongation of the chaotic regime is also obtained in this case.

Figure 3.15a shows a comparison between the maximum Lyapunov exponent shown in Figure 3.13a ($\sigma_{\tau^m} = 0.5$) as obtained via the calculation of the Jacobian, and that obtained via the direct method described in the Methods section 3.2.5, showing good

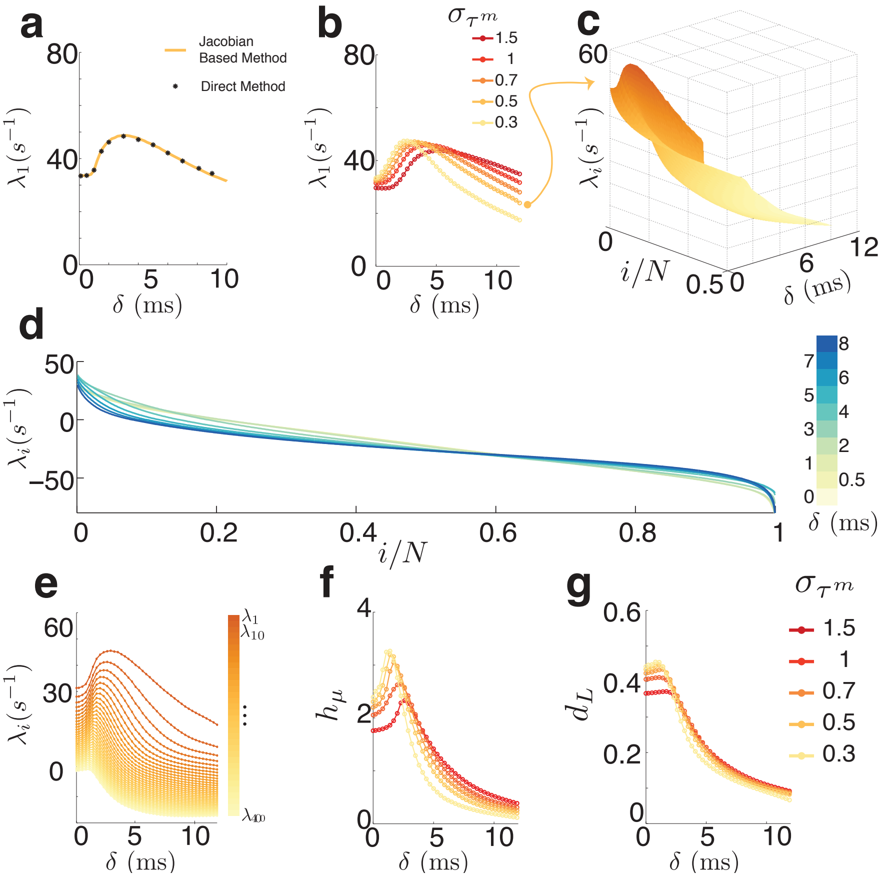

Figure 3.15: Ergodic measures of a network of heterogeneous inhibitory QIF neurons (a) Comparison between the maximum Lyapunov exponent obtained through the calculation of the single spike Jacobian as in section 3.3.2 (full line) and that obtained by direct the direct method described in the Methods section 3.2.5 (starts) **(b)** Maximum exponent for different values of heterogeneity, as in the first row of Figure 3.13, for N=2000. **(c)** N/2 Lyapunov exponents for different delays, shown as a 2D sheet. **(d)** Spectrum of the delayed network. Although the full spectrum is composed of 2N exponents, only N are shown here. **(e)** Overlaid cross sections of panel **c**, showing the dependence of selected Lyapunov exponents as a function of the synaptic delay. **(f)** Entropy production rate per neuron ($h_\mu = H_\mu/N$) as a function of the delay for different levels of membrane time constant heterogeneity. **(g)** Lyapunov dimension per neuron ($d_L = D_L/N$). Parameters: Default parameters as in table 3.1, except in panels b-g, where N=2000.

agreement. To explore the properties of the system beyond the first exponent, we focus on a mild level of heterogeneity, orange in panel b. All positive Lyapunov exponents peak at a certain delay (Fig. 3.15 c-e), but are not necessarily aligned. As a consequence, the entropy production rate per neuron h_μ (Fig. 3.15f) exhibits a peak at a delay that is generally between the onset of the oscillation and the peak of the maximum exponent. The Lyapunov dimension on the other hand (Fig. 3.15g), has a mild linear increase to later decay with increasing delay. This results, should be seen in the light of what is observed in some scalar delayed systems, in which the spectrum decays as $1/\delta$, the entropy production rate is independent of the delay and the attractor dimension grows

Figure 3.16: Poincare section of a 3 neurons network for various delays. Left: Small delay $\delta = 0.1$ ms, $\lambda_1 = 0.29$ s^{-1}, D_L is 2.90. Right: When increasing the delay to 0.9 ms, λ_1 decreases to 0.10 s^{-1} and the dimension D_L to 2.72. Visually, the area occupied by the strange attractor appears smaller, although this is only a zero volume section of the attractor. Axis go from π to π. Parameters: $\nu = 2$ Hz, $J_0 = 0.1, K = 2, \sigma_{\tau^m} = 0.5$. See Methods.

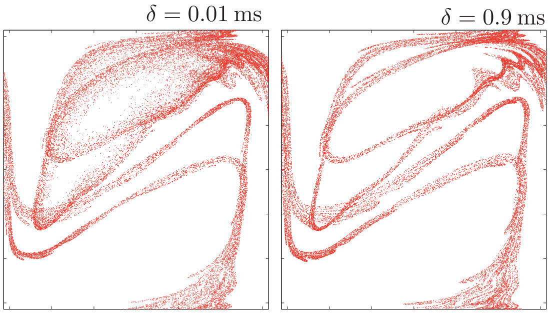

linearly with increasing δ[78,153,154]. In the spiking networks studied here, the shrinkage of the chaotic attractor with the delay is characteristic, given that beyond the oscillatory bifurcation neurons can only align tighter to the rhythm with increasing delay. It might be nevertheless, that for small delays, before the oscillatory transition develops, these classical dependences are observed (see also Fig. 3.20) but no in depth investigation was made. A toy example of the shrinkage of the attractor with increasing delay in shown in the Poincaré section of a three-neuron network in Figure 3.16.

As discussed in the Methods section 3.2.3 and in the first part of the Results (Eq. 3.3.2), depending on the value of the reset of the *delayer* SCA, the Jacobian of the system will or not be singular. When the reset is chosen to be zero, the delay can be controlled exactly. In this case, the Jacobian will be singular, with N singular columns and the corresponding exponents will be $-\infty$, denoting infinitely fast response. When the reset is nonzero ($-1 < \xi_R < 0$), the SCA will continue to evolve towards the stable fixpoint at zero after reset. In that case, the delay we calculate via formula 3.70 will be an approximation. Given the low firing rates of the neurons in the network, and depending on the choice of the three free parameters defining the temporal evolution of the SCA (Eq.(3.84)), the axon will relax back to the fixpoint before receiving another spike. Figure 3.17a shows a comparison of the entropy production rate and the attractor dimension as a function of the reset value of the SCA. Virtually no change in the ergodic measures is observed when changing the reset value (Fig. 3.17a). The full Lyapunov spectrum of the delayed system is shown in 3.17b-d for different values of the reset. For this value of the delay ($\delta = 2$ ms) and for reset values larger than 0.1, the second part of the spectrum lies on the negative inverse of the membrane time constant, $-1/\tau^{\xi}$, indicated with a dashed line. The first N components of the spectrum remain unaltered despite the non-invertibility of the Jacobian with zero reset.

When considering smaller networks, the finite size effects can hinder the identification of transition points, both in the network measures and those aiming to quantify the characteristics of the strange attractor of the delayed system. An analysis of the dependence of the first Lyapunov exponent as on the network size is shown in Figure 3.18. Small networks fail to reveal the onset of collective oscillations as revealed by the monotonous increase in the maximum Lyapunov exponent (panel a). Larger system sizes on the other hand, present a plateau corresponding to the still stable asynchronous state for short delays. The maximum exponent approaches a fixed value for increasing

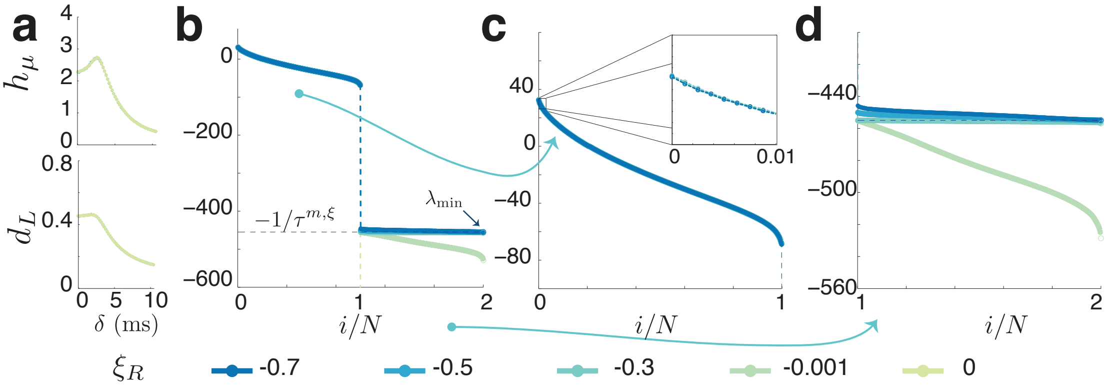

Figure 3.17: Comparison between reset values (a) The entropy production rate per neuron and the Lyapunov dimension remain unaltered after a change in the reset value. **(b)** Full Lyapunov spectrum of the delayed system. The amount of Lyapunov exponents is 2N, where N is the amount of neurons in the network. **(c)** Zoom of the first half of the spectrum, the inset shows the first few exponents. **(d)** Zoom of the last half of the spectrum. For small absolute value of the reset, the single compartment axon responds increasingly faster. Nevertheless the precise values depend on the parameters of the SCA. For larger absolute values of the reset (i.e. more negative), the second part of the spectrum lies basically on the negative inverse of the time constant of the SCA, in dashed line. Parameters: Default parameters as in table 3.1, except N=400, K=50 and those indicated int the figure.

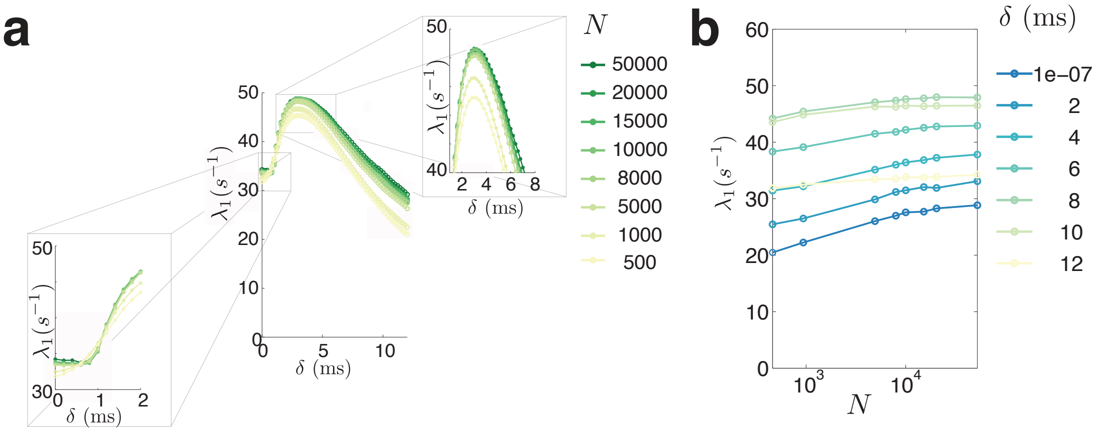

Figure 3.18: Maximum Lyapunov exponent for different system sizes. (a) Maximum Lyapunov exponent as a function of the interaction delay for different system sizes. The inset to the left show the plateau clearly seen for large networks, for which the asynchronous irregular state is still stable. Th inset on the right, shows the apparent convergence to a value in the peak. **(b)** Maximum Lyapunov exponent as a function of system size N for different values of the delay. Parameters: Default parameters as in table 3.1 except those indicated in the figure.

network size, hinting at extensive chaos similar to that observed for non delayed systems. Generally, it is also observed that not only the transition to synchrony is smoothed by small system sizes but also the tail for larger delays is strongly underestimated. The system remains chaotic for moderate amounts of heterogeneity for large delays.

The convergence of some example Lyapunov exponents is shown in Figure 3.19. Figure 3.19a shows the value of some positive exponents as a function of simulation time (i.e the value of Eq. (3.13)), for 10 different network realizations. In Figure 3.19b, the absolute difference between any of the trajectories and the final mean value is shown. This plots illustrate the rather slow convergence of the delayed system, to a precision of 10^{-2}

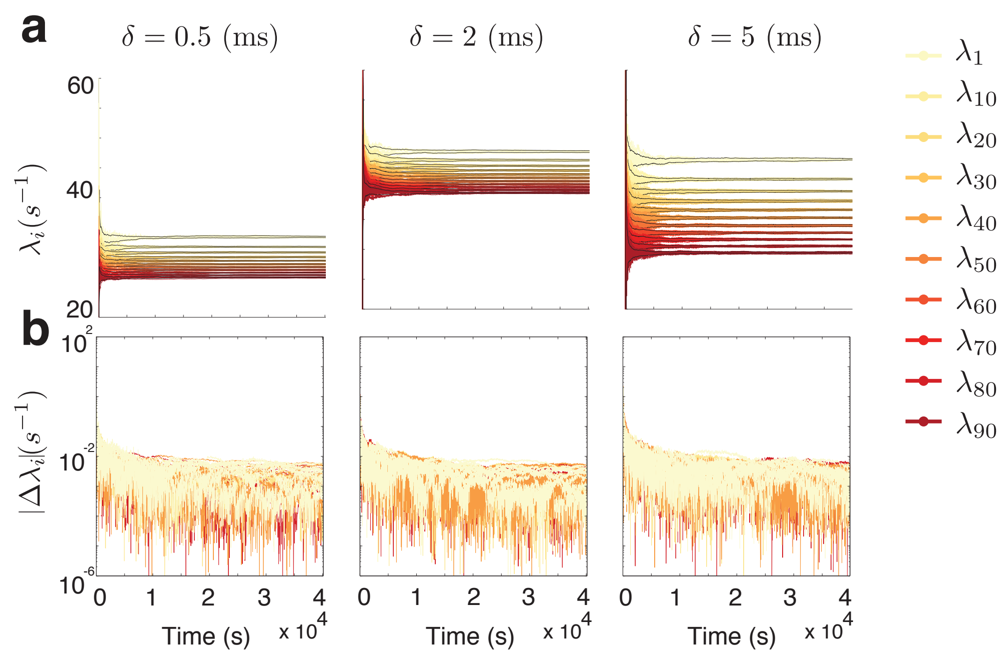

Figure 3.19: Convergence of the Lyapunov Exponents (a) Convergence of 10 selected Lyapunov Exponents as a function of simulation time, for three different values of interaction delay. Each color represents a different exponent, the color lines are 10 different trials (randomization of both connectivity and initial conditions), wile the black enclosing line is the standard deviation. **(b)** Absolute value of the distance to the mean for each realization. At the end of the simulation all traces differ from the mean only in the second decimal. Parameters: Default parameters as in table 3.1.

Figure 3.12, together with Figure 3.20 show that a transition to collective oscillations in the QIF can also be obtained by increasing the average connectivity K. This transition in one dimension, together with that introduced by the delay in the other, are independent mechanisms to generate collective rhythms. In Figure 3.1, the dependence of the network characteristics and the ergodic properties on K is shown for a network with mild heterogeneity. For values of K above ≈ 200 oscillatory activity emerges without the need of a delay (see 3.20a and[173]). For decreasing values of K, increasingly larger delays are needed to force the transition to synchrony. The frequency at the onset of the oscillation increases approximately logarithmically with K, as seen in the inset of panel b. The frequency as a function of the delay, for a fixed value of K, decreases approximately as $1/\delta$, as indicated by the dashed lines. It is important to note that there is currently no mathematical theory to describe this dependences for QIF networks, and that these observations and future ones of this kind are simple numerical fits. Future work, could use semi-analytical approaches to study the transitions to synchrony in similar networks to the ones used here, by profiting from the framework developed by Richardson[208?] .

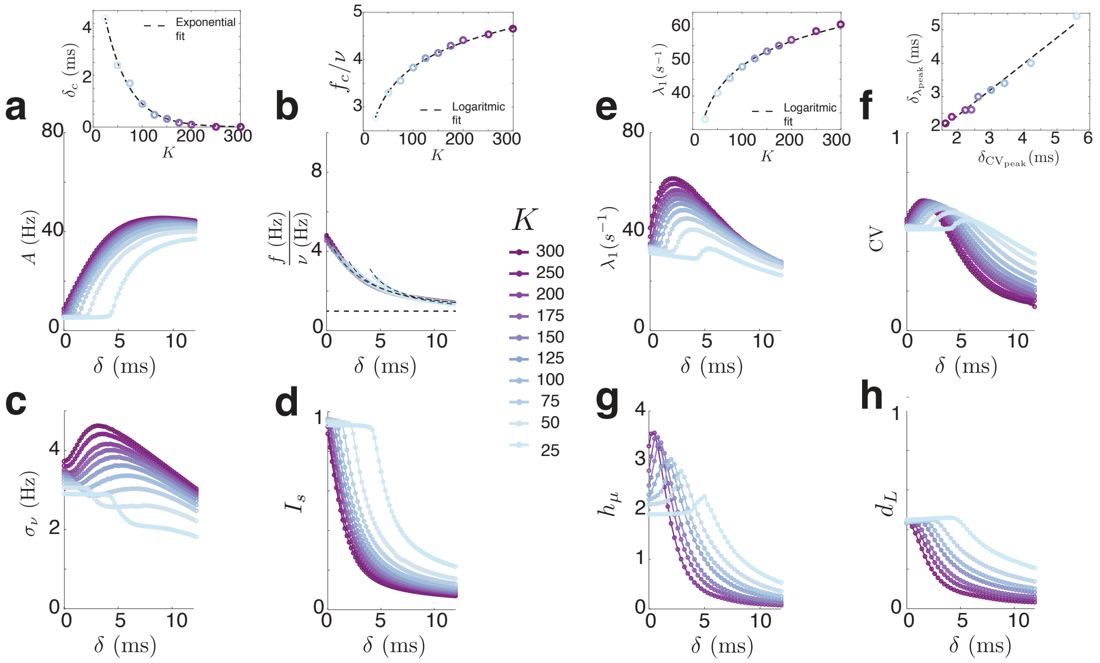

Figure 3.20: Chaos in inhibitory QIF networks, dependence on average in-degree K (a) Amplitude of the MUA signal. The inset shows the dependence of the critical delay (the delay at which the dynamics depart from asynchronous irregular state) on K. **(b)** Frequency of the oscillation. The values depicted are shown only when the MUA amplitude departed from baseline. The inset shows the value of the frequency at the critical delay. **(c)** Standard deviation of the firing rate distribution. **(d)** Departure from the balanced state equation. **(e)** Maximum Lyapunov Exponent. The inset shows the dependence of the value of the exponent at the peak on K. **(f)** Coefficient of Variation. The inset shows the dependence of the location of the peak maximum Lyapunov exponent and the location of the peak CV. **(g)** Entropy production rate under the assumption of the Pesin identity. **(h)** Lyapunov Dimension. Parameters: Default parameters as in table 3.1 with panel (g,h) N=2000.

The peak value of the first Lyapunov exponent, which is not located at the onset of oscillations but where the oscillations would collapse to a limit cycle in the homogeneous case, also increases logarithmically with the average amount of connections (Fig. 3.20e). The dependence of the first exponent and the coefficient of variation on the delay seem to bear some parallels. The inset of Figure 3.20f shows that the peak exponent and the peak CV value are approximately linearly related. After the critical delay, the heterogeneity opposes the synchronizing effect of delayed inhibition, effectively broadening the firing rate distribution and introducing opposing mechanisms that act on each neuron, increasing their variability compared to the asynchronous state. For larger delays, regularity is progressively reached by increasing the fraction of neurons that are aligned to the rhythm. Figure 3.20g–h show the dependence of the entropy production rate and the Lyapunov dimension with the delay for different values of K. It is interesting to note, that for low values of K, the entropy production rate exhibits a large plateau, while the attractor dimension grows linearly, although very slowly, with the delay. The Lyapunov exponent in this case decays with δ.

The dependences of the network measures on the mean firing rate are shown in Figure

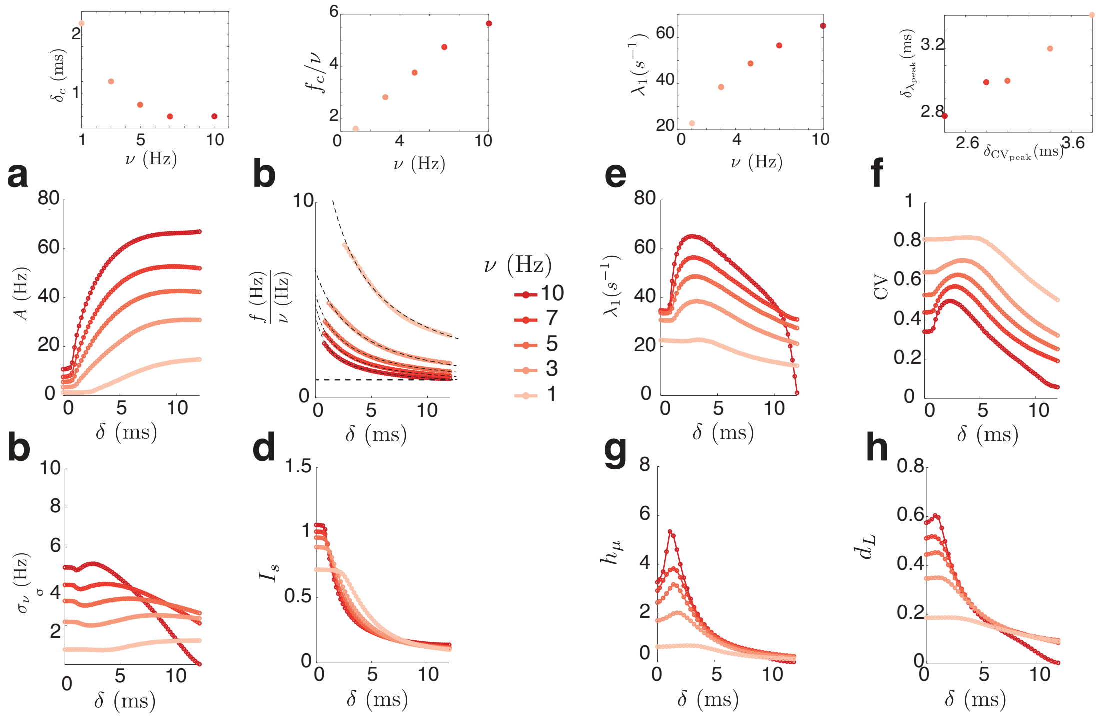

Figure 3.21: Chaos in inhibitory QIF networks, dependence on mean firing rate ν **(a)** Amplitude of the MUA signal . The inset shows the dependence of the critical delay (the delay at which the dynamics depart from asynchronous irregular state) with the mean rate ν. **(b)** Frequency of the oscillation. The values depicted are shown only when the MUA amplitude departed from baseline; the inset shows the dependence of the frequency at the onset with the mean rate ν. **(c)** Standard deviation of the firing rate distribution. **(d)** Departure from the balanced state equation. **(e)** Maximum Lyapunov Exponent. The inset shows the dependence of the value at the peak with the mean rate ν. **(f)** Coefficient of Variation. Inset shows the relation between the location of the peak of the CV and the maximum exponent. **(g)** Entropy production rate under the assumption of the Pesin identity. **(h)** Lyapunov Dimension. Parameters: Default parameters as in table 3.1, except for panels **(g-h)** where N=2000 and the changes indicated in the figure.

3.21. For increasing mean firing rate ν, the transition to oscillations occurs for smaller delays (Fig. 3.21a). We have not observed a transition to oscillations in the non-delayed case. The balanced-state equations are guaranteed for any rate, given that the weights satisfy the inequalities in Eq.(3.40). Nevertheless, those are derived for the infinitely large networks, and for finite sizes it is conceivable that even small delays force a transition to collective oscillations. Given the lack of clear tendency, we have not attempted to fit functions to he dependences shown in the insets. The frequency at the transition increases as a function of the delay. The maximum Lyapunov exponent, increases with the firing rate, and so does its peak. The larger the delays, the faster the transition to full synchrony occurs, and larger heterogeneities would be needed to prevent the synchronous collapse. Notably the entropy production rate per neuron increases drastically with increasing rate.

Finally, a characterization of the network as a function of increasing synaptic weights

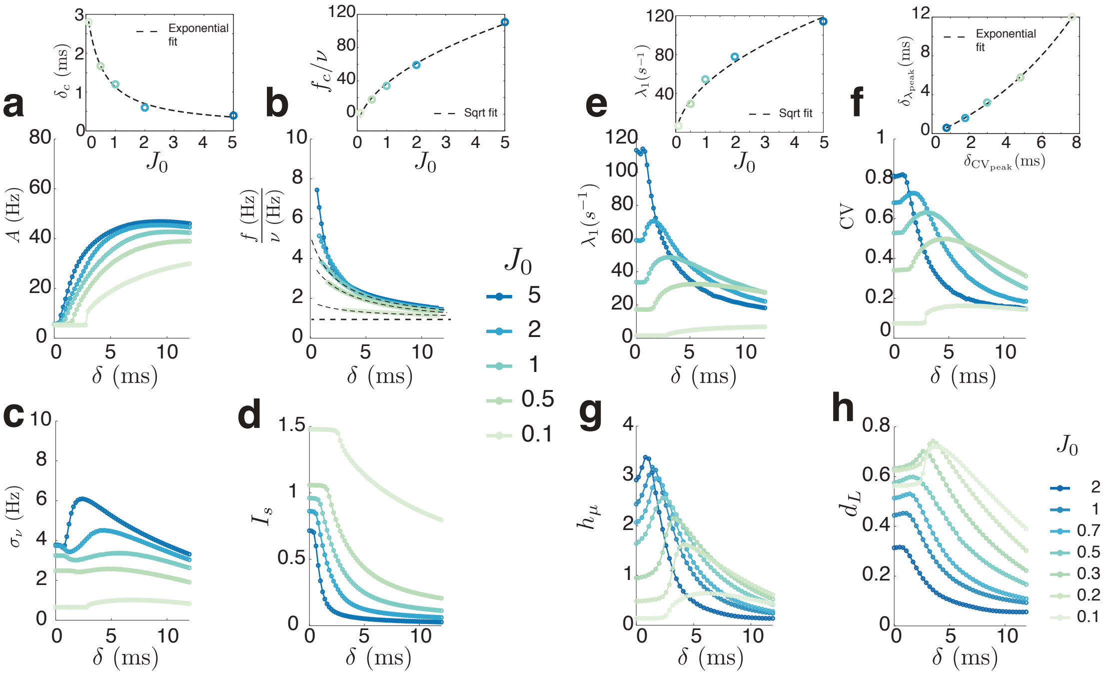

Figure 3.22: Chaos in inhibitory QIF networks, dependence on synaptic weight (a) Amplitude of the MUA signal. The inset shows the dependence of the critical delay on the synaptic weight J_0. **(b)** Frequency of the oscillation. The values depicted are shown only when the MUA amplitude departed from baseline; the inset shows the dependence of the frequency at the onset with the synaptic weight J_0. **(c)** Standard deviation of the firing rate distribution. **(d)** Departure from the balanced state equation. **(e)** Maximum Lyapunov Exponent. The inset shows the dependence of the value at the peak with the synaptic weight J **(f)** Coefficient of Variation. Inset shows the relation between the location of the peak of the CV and the maximum exponent. **(g)** Entropy production rate under the assumption of the Pesin identity. **(h)** Lyapunov Dimension. Parameters: Default parameters as in table 3.1, except for panels **(g-h)** where N=2000 and the changes indicated in the figure.

is shown in Figure 3.22. As a reminder, the connections between neurons have a weight $J = -\frac{J_0}{\sqrt{K}}$. Here, we characterize the dependence of the network activity on J_0. As can be expected, large weights contribute to transition faster to the oscillatory regime. The critical delay to the collective rhythms scales exponentially (with an offset) with the connection weight. In the absence of heterogeneity, for very strong coupling (J_0>25), a transition to oscillations is as well seen for very small delay (10^{-4}), but this was not studied systematically. Interestingly, for low $J_0 < 0.1$, the transition to collective oscillations has a sharp jump, not to perfect synchrony but to a oscillatory state that remains irregular and chaotic. This state that possibly corresponds to the weak coupling limit has, judging from the firing rate distribution and the CV, a very low irregularity, as opposed to that seen in balanced state networks. In this case, the frequency of the oscillations has a very weak dependence on the delay.

The frequency dependence at the onset of the oscillation increases as the square root of the synaptic coupling, as does the value of the maximum Lyapunov exponent. The position of the peak of the maximum exponent, continues to be monotonically related to the maximum variability (the peak of the mean CV), but not linearly. Surprisingly, as seen in Figure 3.22g, the attractor dimension depends non-monotonically on the coupling J_0. Previous work has shown[173], that networks in the balanced state with low (≈ 1 Hz) firing rates, the attractor dimension decreases exponentially with J_0. Here, at higher rates, we see that for very low values of J_0, the dimension depends non monotonically with J_0. The higher the firing rates, and the lower the coupling, the more pronounced this effect is (not shown).

3.3.4 Network of delayed excitatory and inhibitory QIF neurons

Much like in the analytically tractable case of LIF neurons[29], the inclusion of excitation in our networks does not contribute with novel dynamical behaviors. Its inclusion exhibits parallel transitions to those observed in networks in which excitation is only present in the form of an external current. In Figure 3.23 a characterization of the EI network with 80% of excitatory neurons, $\eta = J_{EE}/J_{IE} = 0.9$ and $\epsilon = J_{IE}/J_0 = 0.1$ (see Eq. (3.77)) is shown for two different synaptic delays and various levels of heterogeneity. As indicated in the Methods section 3.2.4, ϵ regulates the amount of feedback excitation to the network. Non-delayed networks with $\epsilon < 1/\sqrt{2}$ leads to asynchronous irregular activity.

Figure 3.23a–d shows how the oscillatory dynamics are affected by increasing levels of threshold heterogeneity. Both type of neurons, excitatory and inhibitory, show similar behavior. The coefficient of variation for each E or I networks have overlapping distributions as can be seen in panel b. The larger the heterogeneity, the CV distribution takes an increasingly exponential shape. The firing rate distributions are shown in panel c. Inhibitory neurons appear more susceptible to the effects of the heterogeneity, whose distribution is shifted leftwards. We note that as in the purely inhibitory network, increasing heterogeneity at a fixed delay effectively increases the frequency of the population rhythm (see panel d). This can as well be understood by a shift of the oscillatory transition toward higher delays, after which the frequency decays with approximately $1/\delta$. In panels e-h, a higher synaptic delay is chosen. For low levels of heterogeneity the network is in a fully synchronized state. Increasing the heterogeneity reduces the amplitude of the oscillation as seen for inhibitory networks.

An analysis and summary of the measures presented in the screenshot of Figure 3.23 can be found in Figure 3.24. The amplitude of the MUA like signal, when separated in its excitatory and inhibitory components, shows that the relative amplitude of the inhibitory neurons is smaller than of the excitatory ones. This difference, can be understood as a consequence of the distribution of firing rates. For intermediate levels of heterogeneity, (Fig. 3.24c), the inhibitory firing rates have a broader distribution. This increased variability leads to a reduced contribution to the amplitude of the rhythm. The frequency of the oscillation, on the contrary, is indistinguishable between E and I neurons. The effects of the heterogeneity can also be seen in Figure 3.24d, showing the percentage of suppressed neurons, being always higher for the inhibitory ones. Finally, the coefficient of variation in Figure 3.24d, are also higher valued for the inhibitory neurons.

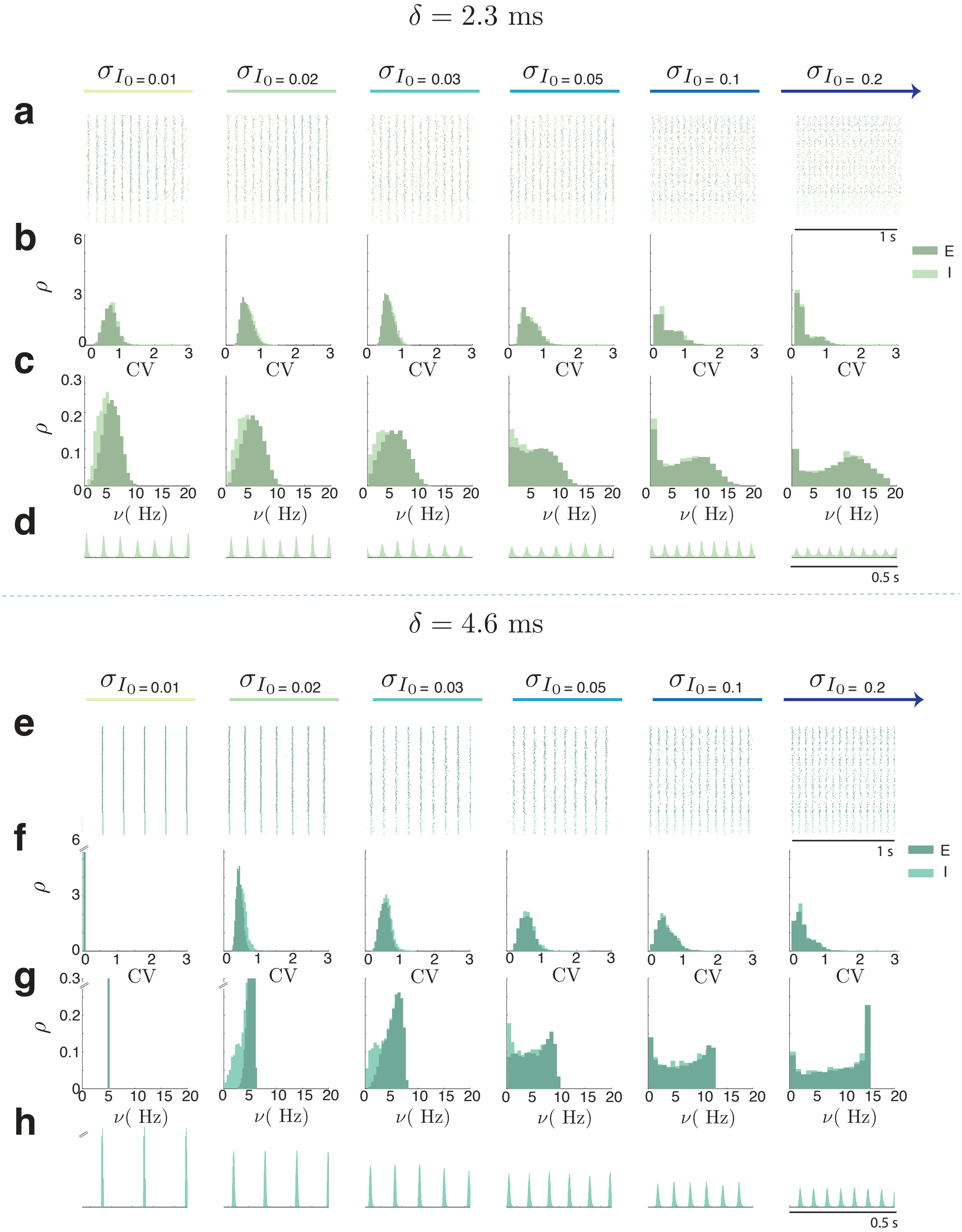

Figure 3.23: Networks of excitatory and inhibitory QIF neurons, for various levels of threshold heterogeneity (a-d) Small delay **(e-h)** Large delay. **(a,e)** Raster plots for various levels of threshold heterogeneity. Excitatory neurons are in dark green. **(b,f)** Distribution of CV. **(c,g)** Distribution of firing rates. **(d,h)** MUA signal of both populations. Parameters: Default parameters as in table 3.1, except for $\sigma_{\tau^m} = 0$ and the changes indicated in the figure.

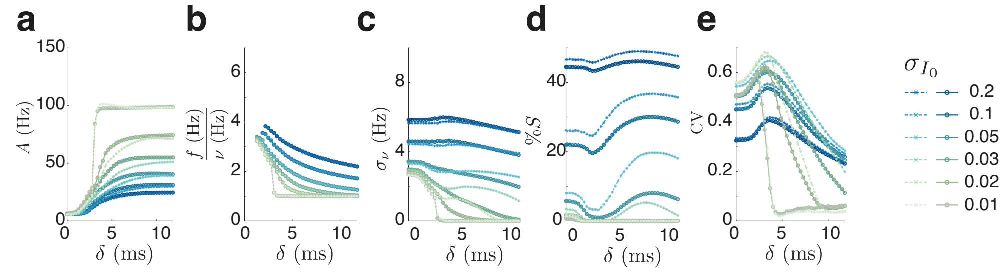

Figure 3.24: Characterization of a network of excitatory-inhibitory QIF neurons with threshold heterogeneity (a) Amplitude A of the MUA signal. **(b)** Population frequency f normalized by the mean rate ν. **(c)** Standard deviation of the firing rate distribution. **(d)** Percentage of silent neurons for separately inhibitory and excitatory neurons. **(e)** Coefficient of variation. Parameters: Default parameters in table 3.1 except for $\sigma_{\tau^m} = 0$ and the changes indicated in the figure.

The dependence of the first Lyapunov exponent on the delay for EI networks with $\eta = J_{EE}/J_{IE} = 0.9$ and $\epsilon = 0.1$ is shown in Figure 3.25a. As with inhibitory neurons, large values of heterogeneity trivially reduce the maximum exponent by effectively reducing the K of the network. As before, highly heterogeneous networks bypass the transition to sharp synchrony through the irregular firing that broadens the MUA signal. The degrees of freedom that contribute to the chaotic dynamics are those associated to the neurons that are not phase locked to the rhythm. Figure 3.25b shows the dependence of the first exponent on the excitation-to-excitation/excitation-to-inhibition ratio η. We see that mild modifications of this parameter do not result in a change of the maximum exponent, or the ergodic measures (comparison not shown). This ratio is required to be smaller than one for the balanced solution to be stable in the absence of delays. For each level of η, the changes introduced in the maximum exponent are analyzed as a function of the strength of the excitatory feedback loop variable ϵ in panels (b_1-b_3). Larger ϵ (increased active excitation) postpones the transition to collective oscillations towards larger delays, and therefore the peak in the maximum Lyapunov exponent. Panels c–d show the entropy production rate and the Lyapunov dimension.

3.3.5 Network of delayed inhibitory QIF neurons with tunable onset rapidness

Neurons *in vivo* and *in vitro* have a rapid and variable action potential onset, as revealed in somatic measurements[179]. For various different neuron classifications, cortical areas and animals, the onset of the action potential is several times faster than the ones that can be obtained by conductance based neurons[179]. This property, has at least two consequences for population coding. First, high onset rapidness enlarges the encoding bandwidth, as reported in studies analyzing the frequency response to fluctuating inputs[72,83,178,180]. Secondly, as shown in this Chapter and elsewhere[173,72], balanced state networks of neurons with a relatively *slow* action potential onset have chaotic dynamics. Differently from LIF neurons with infinitely fast spike onset, QIF neurons have different synchronization properties. The transition to synchrony for increasing delay is charac-

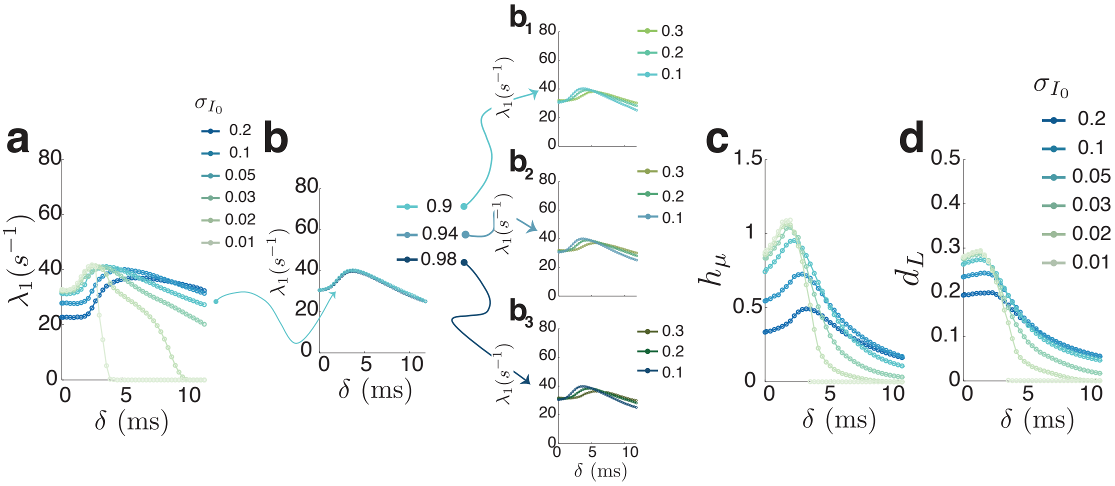

Figure 3.25: Chaos in a network of excitatory-inhibitory QIF neurons with threshold heterogeneity (a) Maximum Lyapunov exponent as a function of the delay for the values of heterogeneity shown in 3.23. **(b)**The maximum exponent is invariant under small changes in the excitation ratio parameter η. **(c)** Different values of the feedback loop ϵ delay the transition to collective rhythms and push the peak of the exponent towards larger delays. **(c)** Entropy production rate per neuron h_μ. Lyapunov dimension per neuron d_L. Parameters: Default parameters in table 3.1 except for $\sigma_{\tau^m} = 0$, N=5000 in panel (b) and N=2000 in panel (c-d), as well as the changes indicated in the figure.

terized by *slow* collective oscillations that are only a few times faster than the mean firing rate. The population oscillation is evident from the raster plots, as opposed to the seemingly irregular rasters observed in the *fast* synchronous irregular state (SI) seen with the LIF[30,31,35,90,29].

Here we profit from one particular model with tunable onset rapidness that is analytically solvable and can be studied under the framework of event based simulations. This model[173], is a variation from the QIF, in the sense that its phase portrait is composed of two connected parabolas. As shown in the Methods section 3.2.2, the rapidness of the action potential initiation in this model can be controlled by a single parameter r. Figure 3.26, shows the behavior of a network of rapid QIF neurons (rQIF) as a function of the delay, for different values of rapidness and of heterogeneity. Rapidness greater than $r = 2$ leads to a sharp transition to spike-spike synchrony, even in the heterogeneous case (upper row) while $r = 2$ has a similar dependence to that described for the QIF network (corresponding to $r = 1$).

The inclusion of heterogeneity in networks of rQIF stabilizes the asynchronous irregular state for larger delays but, unlike the QIF case, it does not smooth the transition to full synchrony (panels g–l). Interestingly, before the sharp transition, there is an increase in the synchronization index χ. Although the increase is modest, it hints at a change in the dynamical behavior of the network. This change is not appreciated in the CV (panel h), the mean firing rate (panel i) or in the variance of the firing rate distribution (panel l), but it can be appreciated from the amplitude of the MUA signal and its frequency (panel j–k). The frequencies of the population oscillation for low rapidness follows a behavior similar to that of the QIF neurons. Networks of neurons with high rapidness,

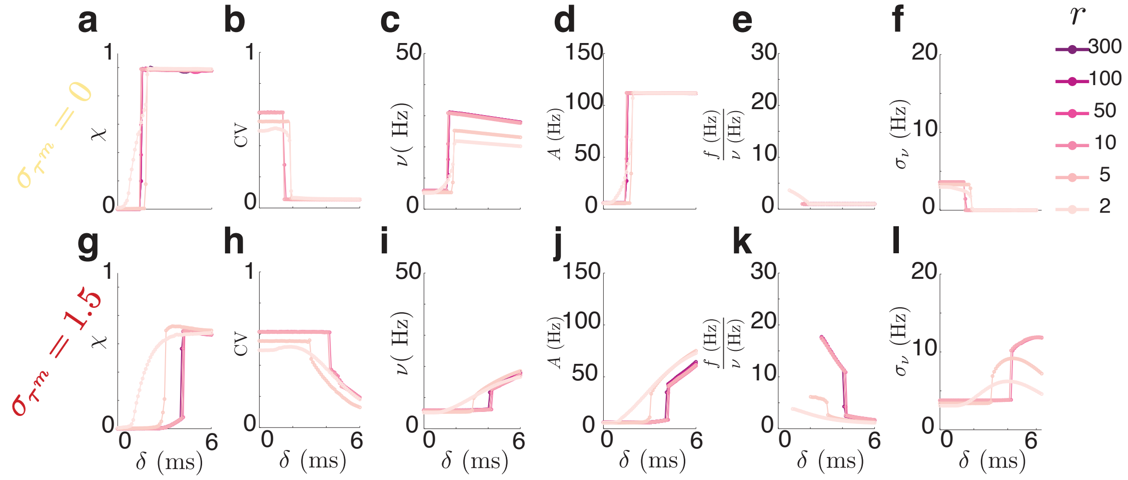

Figure 3.26: Network of delayed inhibitory neurons with tunable onset rapidness with no fixed rate Upper row: no heterogeneity. Bottom row: large heterogeneity in the membrane time constant. **(a,g)** Synchronization index χ as a function of the delay for different values of the rapidness r. Notice how for the homogeneous case high rapidness have a sharp transition to spike-spike synchrony. For high heterogeneity, at $\approx \delta = 5$ ms the χ index hints a transition to other than the AI state. **(b,h)** Coefficient of variation. **(c,i)** Mean firing rate. **(d,j)** Amplitude of the MUA signal. **(e,k)** Frequency of the MUA signal relative to the mean firing rate. **(f,l)** Standard deviation of the firing rate distribution. Parameters: Default parameters in table 3.1 except for $\sigma_{\tau^m} = 1.5$ and the changes indicated in the figure.

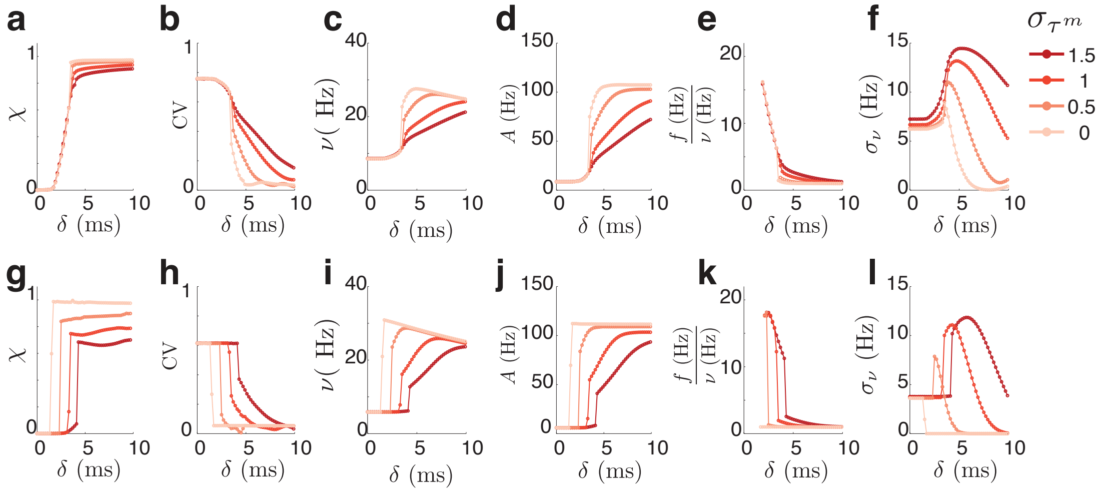

Figure 3.27: Comparison between LIF and rQIF networks for various degrees of heterogeneity Upper row: LIF neurons. Bottom row: Rapid neurons with $r = 100$. **(a,g)** Synchronization index χ as a function of the delay for different values of the heterogeneity σ_{τ^m}. **(b,h)** Coefficient of variation. **(c,i)** Mean firing rate. **(d,j)** Amplitude of the MUA signal. **(e,k)** Frequency of the MUA signal relative to the mean firing rate. **(f,l)** Standard deviation of the firing rate distribution. Parameters: Default parameters in table 3.1 except for the changes indicated in the figure.

exhibit population rhythms with frequencies 20 times faster than the mean firing rates, and that are well within the gamma band. We notice that the transition to stronger synchrony, occurring at larger delays, is not a transition to spike-spike synchrony. Similarly to what was observed for the heterogeneous QIF, the network oscillates with frequencies that are of the order of the firing rate, with large spread in the firing rate distribution (panel i).

An explicit comparison between the delayed networks composed of LIF or rQIF neurons is shown in Figure 3.27 for various degrees of heterogeneity in otherwise identical networks. The SI state is robust in the LIF networks. The effect of heterogeneity is only noticeable for larger delays, where a transition to stronger synchrony also occurs. On the contrary, rapid neurons are highly sensitive to the effects of heterogeneity, developing a SI state only in the highly heterogeneous case. This state is facilitated by large values of the average in-degree K, although such dependences are not shown here.

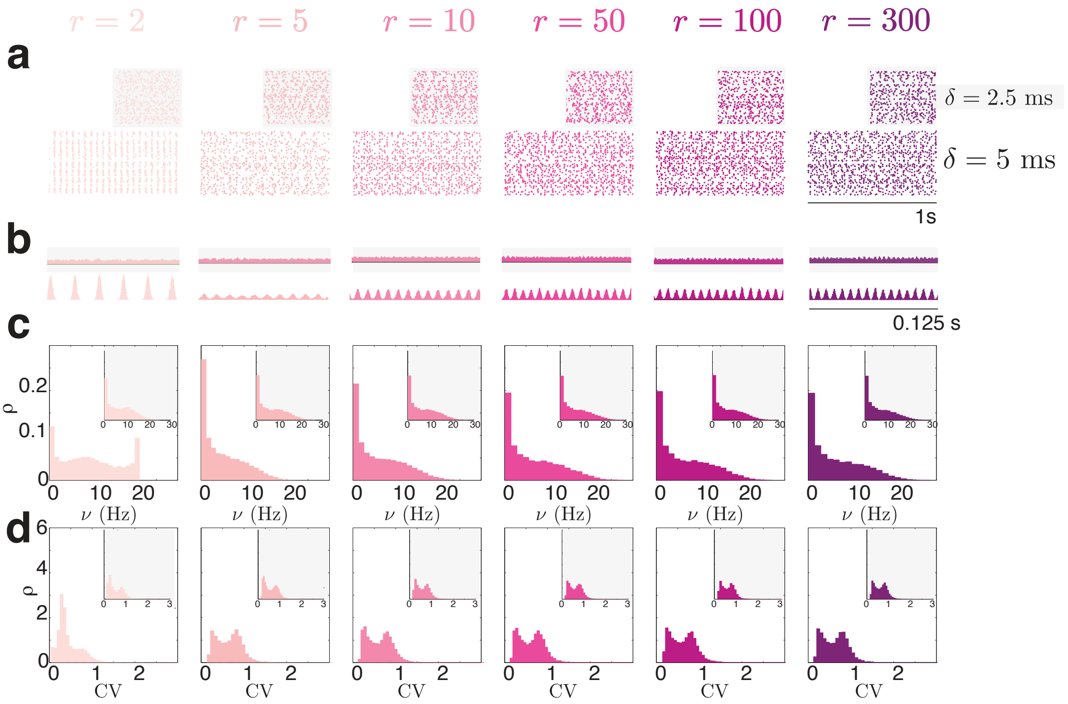

Figure 3.28: Networks of rapid QIF neurons before and after the transition to the synchronous irregular state. Insets with light grey background indicate a network with synaptic delay $\delta = 2.5$ ms, while the larger principal panels have a synaptic delay of $\delta = 5$ ms. **(a)** Raster plots for different values of spike onset rapidness and a high level of heterogeneity. Panels have the same temporal scale. **(b)** MUA signal. The signal before the transition exhibits small transient oscillations that are visible by eye. **(c)** Firing rate distributions. Notice the difference in the fire rate distribution between the small rapidness, where the rhythm is evident in the raster plot, and the high rapidness. In this last case, there are no neurons fully locked to the fast rhythm. **(d)** Coefficient of variation. Parameters: Default parameters in table 3.1 except for $\sigma_{\tau^m} = 1.5$,$\sigma_I = 0.05$, N=20000 and the changes indicated in the Figure.

A example characterization of the heterogeneous case described above is shown in Figure 3.28 for a *fixed rate* configuration. For various onset rapidness r, we compare the network response for two values of the interaction delay: one below (insets with shaded background) and one above the transition to the synchronous irregular state. We can see that for large rapidness there is virtually no change in the raster plots. The firing rate distributions and the CV after the oscillatory transition (central panels) are identical to those before the oscillatory transition (shown in the insets with a gray background). On the other hand, a change in the rhythmicity of the MUA signal is apparent.

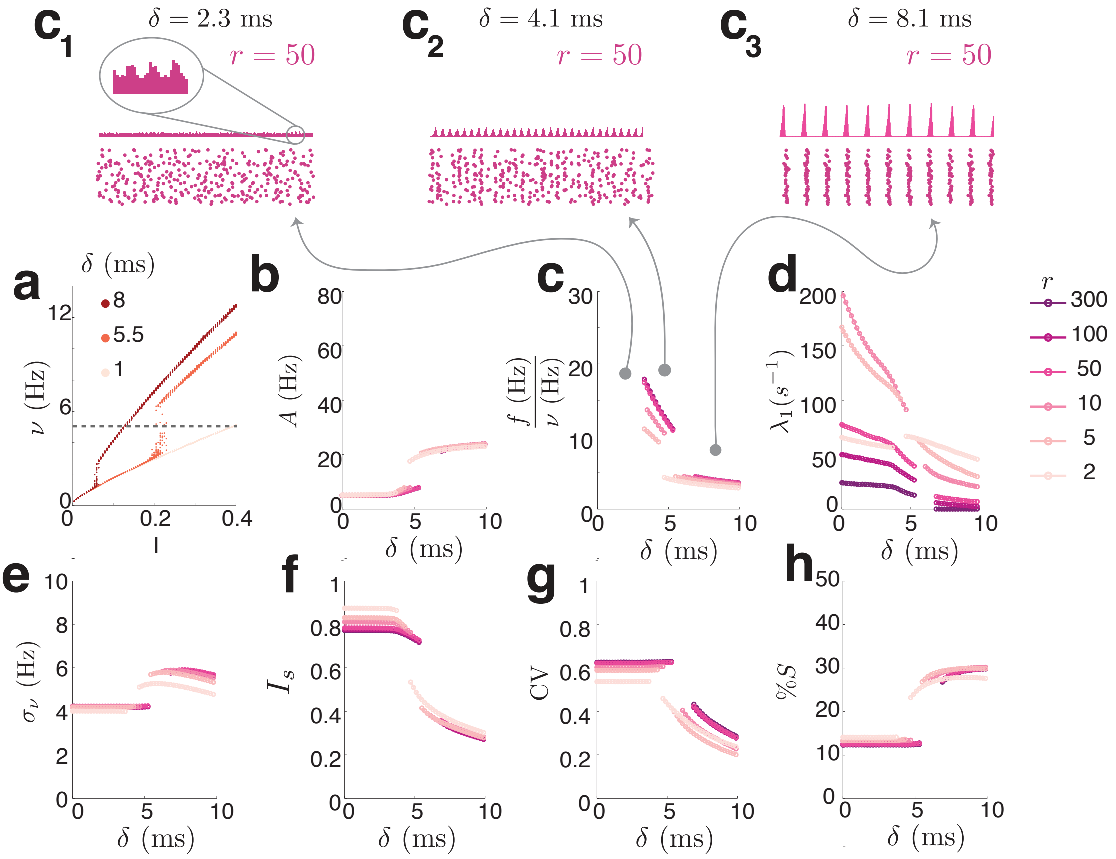

Figure 3.29: Network of rapid QIF neurons. (a) Mean firing rate as a function of the input current for a network with $r = 100$ for three values of interaction delay δ. Unlike the QIF, the rQIF has a discontinuity in its f-I curve, making it for some values of the delay impossible to fix the mean rate at the desired value. Fixing the rate at 5 Hz is possible for low ($\delta = 1$ ms) or high delay ($\delta = 8$ ms), but not for $\delta = 5.5$ ms. **(b)** Amplitude as a function of the delay. The missing values correspond to those in which the rate could not be stabilized. **(c)** Frequency of the population oscillation normalized by the mean firing rate (5 Hz). Values are only displayed when both the rate was stabilized and there was a modulation of the amplitude. Three regimes can be distinguished, in **(c$_1$)** before the oscillatory transition, the asynchronous irregular state. Even in large networks (N=20000), collective oscillations are evident close to the bifurcation. **(c$_2$)** Immediately after the transition to the asynchronous irregular state. **(c$_3$)** After the transition to stronger synchrony. Population oscillations are clearly noticeable from the raster-gram. **(d)** Maximum exponent as a function of the synaptic delay. All three regimes in panel **(c)** are chaotic, But the maximum Lyapunov exponent seems to only decrease with the delay. **(e)** Standard deviation of the firing rate distribution. **(f)** Departure from the balanced state equation. **(g)** Coefficient of variation. No change is visible in this measure regarding the transition to SI state. **(g)** Percentage of silent neurons.

Networks of rQIF neurons have a discontinuity in their *f*-*I* curve (Fig. 3.29a). When increasing the value of the input current I to every neuron in the network, the mean firing rate of the network ν does not increase continuously. When analyzing the response of the network at a *fixed rate* configuration for given a delay, not all values of the mean firing rate are available: For a small delay (pink curve), the curve is continuous and the desired mean firing rate of 5 Hz is successfully found. For a delay of 5 ms (red curve), there is a discontinuity in the curve and the network cannot be settled to a fixed rate. For even larger delays, the discontinuity is far from the desired mean firing rate value, and the network can be set to the desired rate again. In the following panels, the missing values in the curve correspond to those configurations in which the desired mean firing rate could not be achieved. Figure 3.29b–c show the amplitude and the frequency of the population oscillation for the mean firing rate fixed at 5 Hz. High onset rapidness leads to collective rhythms well within the gamma range. In panel d, the maximum Lyapunov exponent is shown as a function of the delay for different values of onset rapidness. As previously described in networks of non delayed neurons[173], the maximum exponent peaks for intermediate values of rapidness. After the transition to stronger synchrony, this peak exponent is flattened and the maximum Lyapunov exponent is smaller the larger the rapidness. From this panel, it can also be seen that for a rapidness of $r = 300$, the transition to stronger synchrony is accompanied by a further transition to dynamical stability, although spike-spike synchronization has not yet occurred. This transition to stable dynamics with higher rapidness is of a different nature than that observed for the QIF, and is related to the fact that after a critical rapidness, non-delayed networks of rQIF neurons present a transition to dynamical stability at a critical rapidness, that scales as $r_c \approx N^{0.6} K^{0.4} \nu^{-0.8}$[173].

3.4 Summary and Discussion

In this chapter we studied the impact of the delayed interactions and heterogeneities on the stability properties of pulse-coupled neuronal networks. We showed that in networks of exactly solvable mathematical neuronal models, delays can be introduced without sacrificing their semi-analytical tractability. By introducing a postsynaptic single-compartment-axon (SCA) to every neuron, transmission delays between neurons constitute the extra steps of integration required for the SCA to reach threshold, while the interaction between neurons and the SCA remains instantaneous. This framework allows to compute the dynamics of the network exactly and to asses its stability through the numerical evaluation of the network's Jacobian, which is calculated analytically.

We have shown that delayed QIF neurons of very *diluted* networks in the balanced state are unaffected by the presence of relatively small delays. After a critical value of the delay, the chaotic asynchronous irregular state loses stability to a perfectly synchronous and dynamically stable one (Fig. 3.11 and 3.13, bottom row). For larger values of the average amount of connections per neuron K, an intermediate transition develops for increasing delay, with all the characteristics of a supercritical Hopf bifurcation (Fig. 3.11 and 3.13, top row, Fig. 3.12). In this state, collective regular oscillations at the population level coexist with unimodal firing rate distributions and high dimensional chaos (Figs. 3.8 and 3.13, bottom row). The firing patterns show a sparse synchronization with a population frequency that is *higher* than the single neuron firing rate. Nevertheless, as this oscillation is only a few times higher than the mean firing rate, and slow compared to the synchronous irregular state that we described in the Introduction section 1.2.6, we term it *slow* SI state. The transition to collective rhythms marks an increase of the maximum Lyapunov exponent and of the entropy production rate of the network (Fig. 3.15). The intensification of the chaotic measures does not rely on the level of heterogeneity (Fig. 3.15), or on the presence of excitation (Fig. 3.25), whose inclusion modulate but does not alter the qualitative characteristics of this transition. Increasing the mean firing rate, the average amount of connections per neuron, or the weight of the connections contribute to accelerating the oscillatory transition and to intensity chaos (Figs. 3.22,3.21,3.20). The increase in the entropy production rate and in the maximum Lyapunov exponent is particular the case studied here, and differs to what is found in scalar delayed differential equations, and in which the entropy production rate is largely independent of the delay[78,154].

Networks in the balanced state are unaffected by a moderate amount of heterogeneity. In delayed systems, the inclusion of heterogeneity is a counter-acting force that pushes the oscillatory transition towards larger delays and enlarges the stability region of the asynchronous irregular state (Figs, 3.8, 3.23, 3.28). When heterogeneities are present, further increase of the delay after the first oscillatory transition does not lead to spike-spike synchrony, but to a partial synchrony state characterized by a broad firing rate distribution. This is due to the opposite effects of delays and heterogeneity in these networks. The heterogeneity biases the distribution of rates towards lower values (Fig. 3.9), while the delay tends to align the neurons to the rhythm. The fraction of neurons phase locked to the rhythm increases with the delay until the full synchrony state together with dynamical stability is reached.

Finally, we analyzed the delay-induced transitions in networks composed of neurons with fast action potential onset. The increase of the synaptic delay in diluted networks leads to a sharp transition to spike-spike synchrony in the absence of heterogeneity (Figs. 3.26, 3.27). For the heterogeneous case, a synchronous irregular state emerges (Fig. 3.28), with strong similarities to the SI obtained for LIF neurons[30,31,35,90,29]. The larger the average connection per neuron and the wider the single neuron parameter distributions, the bigger is the fraction of delay values that leads to this *fast* SI state. In contrast to the LIF, whose transition to the SI state is independent of the heterogeneity (Fig. 3.27), the one obtained for the rQIF neuron is chaotic (Fig. 3.29).

4

Discussion and Outlook

4.1 Summary

In this thesis we have explored the encoding and transmission capabilities associated with oscillatory network dynamics. For this purpose, we have taken a twofold approach. First, we investigated a class of models that emulates the dynamical behavior of population activity in the mammalian cortex. Instead of aiming to exactly match specific network parameters, we have rather studied landscapes in parameter space leading to a stereotypical dynamical behavior of fluctuating synchrony, resembling the one reported experimentally. We found that within this class of models, coupled networks give rise to uni-directional information transmission that can be flexibly gated by the phase relation between the rhythms and modulated by the level of fluctuating synchrony. In a second part, we have taken a different approach. We have focused on models with reduced complexity and developed a framework to study the dynamics of delayed heterogeneous pulse-coupled neuronal networks of exactly solvable neuronal models. We found that these networks, which in general have an infinite dimensional phase space, can be studied in equivalent systems of finite and fixed degrees of freedom. Large synaptic delays between the coupled units can destabilize the initially irregular and asynchronous dynamics and generate a transition to collective population rhythms. The onset of collective oscillations leads to an increase in the exponential rate of divergence of nearby trajectories and of the entropy production rate of the chaotic dynamics. Together, these approaches not only show that a high encoding capability of chaotic dynamics is compatible with regular behavior at the population level, but that this oscillatory behavior is suitable for for the flexible routing of high dimensional patterns of complex activity.

4.2 Information routing at the edge of synchrony: Discussion and Outlook

Gamma oscillations are ubiquitous across brain areas and species[48,50,52,274], yet their functional role remains controversial[132,204,134,43]. The wide variety of studies that link enhanced gamma synchrony with disparate behaviors[258,36,284,195], rather than narrowing its potential function to specific tasks, have lead to the hypothesis of a more central role[99,216,86,18]. In particular, the proposal of oscillatory coherence as a mechanism for information routing[86,18] has found both a large amount of supportive evidence[105,103,261] and a wide range of criticisms[57,133,135,132,134,204,205,286].

Arguments against the potential use of gamma coherence in communication generally stress the large power and frequency variability found in population-based neuronal recordings[44,43,286,203], whose labile nature is furthermore strongly sensitive to the balance of inhibition and excitation[13]. In the class of models analyzed in Chapter 2, fluctuations of frequency and power arise spontaneously as a consequence of the complex dynamics emerging from random, strongly-coupled delayed networks. Instead of fitting parameters to experimentally reported values (as done in various degrees of detail[118,127]) we focused on a region in parameter space where these fundamental dynamical features arise spontaneously and are characteristic. We hypothesize that refined models leading to similar population dynamics can only affect quantitatively but not qualitatively the nature of the analysis.

The firing patterns of models with transient synchrony are on average irregular 2.2 and exhibit low degrees of oscillatory synchronization. When coupled, their degree of synchrony is only weakly modulated by the incoming long-range excitatory inputs from distant areas (Figs. 2.6,2.7,2.9). Furthermore, the frequency fluctuations characteristic of single population dynamics are coordinated between connected areas, while the rhythms transiently phase-lock. These phase-locking patterns observed in our model are reminiscent of those found at higher levels of synchrony[20] and described mathematically in rate models[19]. Nevertheless, in contrast to its synchronous counterparts, gamma burst in our models are fast enough to conciliate transient locking with a rapid dissolution of oscillatory synchrony after a few cycles (Fig. 2.9). This coordination, while so far unexplored in biologically plausible models, was reported experimentally[209]. In our models, fast dynamic frequency matching is a robust emergent feature of interacting oscillating neuronal populations and does not require an external controller.

The low degree of synchronization and phase coordination, far from hindering its usage in communication, provides a flexible scheme for information transmission. The hierarchies imposed by the meta-stable phase relations translate to uni-directional information flow from the population leading in phase to the lagging one (Fig. 2.13). The level of fluctuating synchrony boosts information flow when high, or decreases it when low, working as a gain parameter on top of the anisotropy imposed by the phase relation (Figs. 2.14, 2.17). The preferred relative phases, prominent within the gamma bursts (Fig. 2.8), define the optimal inter-areal lag of information transmission (Figs. 2.13,2.14).

This lag is not prescribed by the synaptic delay only (Fig 2.11) and is determined by the phase response properties of the coupled circuits[282,248]. In fact, the experimentally reported values o f inter-areal lag largely deviate from the inter-areal synaptic delay (see section 1.1.6 for details), and strongly depend on the behavioral state[65]. As shown in Figure 2.11, different inter-areal phase-locking relations can be implemented with a fixed inter-areal delay, just by changing the level of local inhibition. Therefore, the regulation of information transfer defined by the routing patterns is the outcome of collective dynamics and not just of direct mono-synaptic interactions.

The routing patterns defined by the analysis of spontaneous activity constrain the routes of information of externally supplied input signals. Smooth inputs are selectively gated through the routing states, despite the coarseness of the defined phase relations and the fluctuating level of power (Figs. 2.21, 2.22). Higher order motifs can rely either on the combinatorial amount of phase locking patterns (Fig. 2.23) or on a combined phase-fluctuating synchronization machinery (Fig. 2.25) to achieve targeted uni-directional information transmission. We hypothesize that a combination of those are exploited by the brain.

The high order motifs exhibit a large variety of routing patterns. Convergent information from lower order areas to those of higher order exists independently of the feedback projections and allow for temporally segregated information transmission from multiple areas to a single target area (Fig. 2.24). Alternatively, the existence of effectively disconnected areas depends on the strength of the feedback projections (Fig.2.24, compare $\Delta\Phi_2^{\mathrm{xyz}}$ and $\Delta\Phi_4^{\mathrm{zyx}}$). In symmetric configurations, the disconnected scheme is replaced by a top down signal to the non leading area, of a possible suppressive nature. Further advancements on the precise quantification of the macaque's structural connectome[58,167,166] will allow to further constraint the current models.

Transitions between alternative routing states, multiplexed within a fixed structural circuit[20], are paralleled by switching patterns of inter-areal phase differences. Such a scheme is compatible with both a rate coding as well as more complex representations relying on finer organization of the spiking patterns. Future studies could explore whether the simultaneous emergence of synchronized bursts can modulate the propagation of stimuls-dependent cell assemblies[116,49], or whether the information to be decoded in a target area over specific spike words[219] could be selectively gated by inter-areal phase coordination[20]. We speculate that the inclusion of plasticity in our models could result in the formation of stimulus-grouped neuronal assemblies. Gamma oscillations modulate neuronal excitability in a a score of ms, which overlap with the time scale of synaptic plasticity[50,48]. It seems plausible that in models of networks including Hebbian plasticity, oscillating patterns of activity would form assembly-like neuronal groups coding for a particular stimulus, carrying specific information. A possible avenue for further studies is to elucidate whether the flexibility of routing patterns could transmit information about a particular input (e.g. orientation) to be read out with other tools than the ones proposed here.

The information theoretic measures implemented in Chapter 2, as with those generally used in neuroscience[260,268,98,37] are based on densities estimated over a certain time of simulated data. Given the highly fluctuating nature of our signals, we also aimed to explore possible avenues of time dependent information theoretic analysis. We have made attempts (not reported in this thesis) to develop time-dependent state filters over which transfer entropy could operate in a trial based manner. Unlike circuits in highly synchronous states[282,20,142], homogeneous and weak pulse-like perturbations to all neurons in the network fail to switch the phase pattern. Possible avenues for more efficient and robust perturbation methods would need to be developed to unveil the time dependent structure of information transmission. One so far unexplored possibility, lies in the observed asymmetry of the phase distribution, arising as a product of the strong heterogeneity and the randomness of the connections. Disentangling the specific mechanisms of this broken symmetry is part of the current research agenda, given the advantageous insights that targeted stimulation can have into the control of information flow. In particular, it would be interesting to analyze and profit from the possible restructuring of routing patterns by the introduction of time dependent conductances.

Lastly, for simplicity, our model was designed to generate transient oscillations within a single gamma band. This specification, however, is not inherent to our approach and can be relaxed to reproduce multifrequency oscillations. Inter-areal interactions have also been shown to be mediated by coherence in the beta band. Future studies should examine more complex models including multifrequency interactions or multi-area networks of greater complexity. Our study follows a methodology that can be used to asses their dynamic routing properties and to design future experimental studies. It reveals that features which may at first sight appear dysfunctional with respect to information routing may in fact provide the brain with a particularly flexible routing mechanism.

4.3 Chaos and synchrony in delayed neuronal networks: Discussion and Outlook

Reduced models in neuroscience allow the dissection of the mechanisms giving rise to complex dynamics, and to relate them to known classes of systems of similar dynamical properties. Contrary to the detailed descriptions used in the first part of this thesis, which are useful for understanding the *consequences* for information transmission of a certain type of dynamics, in the second part we studied the *properties and mechanisms* underlying the complex dynamical behavior of delayed neuronal networks. Delayed dynamical systems require for their initialization the definition of a history *function* and thus even scalar differential equations are infinite dimensional when delayed. Although under some assumptions ergodic theorems analogous to those known for finite-dimensional systems exist[67,217], this is in fact not known for the general case and a finite spectrum of Lyapunov exponents acting on well defined subspaces is not guaranteed. In delayed maps, where the system is finite dimensional for finite delay, the spectrum can be obtained in only few cases[155] without the aid of numerical methods based on approximations. Generally, the calculation of the Lyapunov spectrum of delayed systems, or even only of the maximum Lyapunov exponent has been relegated to numerical estimations. Methods rank from direct discretization[78,154], methods involving chaotic synchronization[235] to simple small delay approximations to numerically estimate the stability properties of the system.

Pulse-coupled neuronal networks with interaction delays modeling cortical circuits have in principle infinite degrees of freedom. In globally pulse-coupled excitatory networks it has been shown that the system reduces to a finite dimension, where an upper bound can be calculated as a function of the maximum amount of spikes in the delay interval. However, for the general case, no general approach to the study of the effective dimension of the attractor has been developed. In Chapter 3 we introduce a framework that allows to study the stability and ergodic properties of large networks of coupled oscillators with interaction delays in an exact manner. The strategy consists in introducing a dynamical variable to account for the time delay between neuronal interactions, and allows to study the dynamics of these infinite dimensional systems on the same footing with systems of fixed and finite degrees of freedom. This is possible due to the pulse coupled nature of synaptic connections, which are discrete events in time. Although phase coupling between phase oscillators[149,241,4], or models with simple variable coupling[113,211] would not profit from this approach, analogous extensions could be performed in more complex pulse coupled systems.

The inclusion of delays in non-linear systems can have a strong impact on their dynamics. The inclusion of a delay can lead to changes as drastic as a chaotic transitions[78,163], or to synchronization in coupled chaotic maps[14]. In the context of networks of spiking neurons, the inclusion of synaptic delays favors the emergence of collective rhythms. In particular cases,[288,183,76,249], the inclusion of interaction delays leads the dynamics from an initially asynchronous state to a fully synchronous one. Although synaptic delays could also mediate more complex transitions[251,77], it is widely acknowledged that they are a fundamental component mediating the emergence of collective rhythms[31,29,30,211] as well as their locking properties[19,150].

Delayed-induced transitions to collective oscillations, from initially asynchronous and irregular dynamics of large networks in the balanced state were studied in Chapter 3. We found that while a transition to collective rhythms occurs inexorably for increasing delays (Fig. 3.12), the characteristics of the emergent oscillation and the magnitude of the critical delay depend on the action potential onset rapidness and the level of heterogeneity (compare Figs 3.8 and 3.28). In networks of delayed QIF neurons with slow action potential onset, the lost of stability of the asynchronous irregular state to a slow SI state leads to an increase of the chaotic measures (Fig. 3.15). The entropy production rate and the first Lyapunov exponent peak after the transition, while the attractor dimension is either unaffected or exhibits a mild linear increase, depending on the network parameters (Figs. 3.22,3.21,3.20). On the contrary, when the action potential onset is fast, increasing delays in these heterogeneous networks leads to two different types of oscillatory transitions (Fig. 3.29): the first to a *fast* SI state, and the second to a slower, more regular oscillatory one, where the rhythms can be observed from the raster plots and look similar to those obtained for QIF neurons for large delays. In this case, the first Lyapunov exponent decreases monotonically with the delay. Larger delays, independently of the onset rapidness and the heterogeneity, will lead to increasingly synchronized dynamics. Therefore, in the limit of large delays, both the entropy production rate and the attractor dimension vanish. This is to be contrasted with the classic work on delayed differential equations. In those cases, the limit of large delays leads to either a constant maximum Lyapunov exponent in the *strong chaos* case[117,138,155], or to a maximum exponent that scales like $\lambda_{\max} \propto 1/\tau$ in the *weak chaos* case[78,117,138]. Furthermore, numerical studies of the full Lyapunov spectrum have shown that in some cases, notably in, but not restricted to, the Mackay-Glass model, the attractor dimension grows linearly with the delay while the entropy production rate remains constant[78,153,154]. Similar results are obtained in a very simple small delay approximation of a network of rate units with gaussian distributed weights, which lead to conjecture that the effects of delays in systems that are variable coupled [*] are very different from those that have a finite temporal extension.

The inclusion of delays in balanced state like networks of QIF or rQIF neurons revealed a state where high dimensional chaos coexists with interesting collective dynamics. This coexistence was rarely reported: Some studies have pointed out how complex chaotic dynamics at the population level arises in networks in which the units are themselves chaotic[161,114,113]. Others, in networks of more conventional LIF neurons with temporally extended excitatory interactions, found asymptotically stable dynamics (in fully or densely connected networks)[187] or extensive chaos (in diluted networks)[161], while the network is in a partially synchronous state[262]. In the partially synchronous state, neurons fire quasi-periodically at rates slightly *higher* than the oscillation period. In contrast, in our networks, after the oscillatory transition, neurons fire irregularly, with a broad firing rate distribution characteristic of balanced state networks which is compatible to what it is observed experimentally[231]. An analogous transition can be obtained for the QIF network in the non delayed case, by means of increasing the average amount of connections per neuron (see Fig. 3.20 and Monteforte[173]), that relates to the minimal connectedness reported in early work of spiking networks[95,285]. In the fully coupled case, where the dynamical equation of the order parameter can be obtained analytically for arbitrary amount of coupled populations (see Appendix B), similar dynamics can be obtained with yet a different type of coupling.

Large delays force a transition to spike-spike synchronization in the homogenous case for both QIF and rQIF. Nevertheless, any type of heterogeneity can break the fully synchronized state, replacing that transition with a partially locked one (Figs. 3.13 3.26 and 3.29). The larger the delay, the larger the fraction of neurons locked to the rhythm, and the smaller the dimension of the attractor, which remains nonzero until the network reaches full synchrony. The role of the neurons locked to the rhythm and those that function seemingly independent from it, can be analyzed in the light of the recent findings by Okun et al.[186]. Neurons in somatosensory cortices have a different attachment to the population activity, and can be broadly classified by their population coupling (how much

---

[*] By variable coupling we mean that the differential equation of a variable x depends on y, and not only on the time of its spike

they follow the mean). They find that the population coupling is an adequate measure to predict the underlying connectivity and the response to sensory stimuli. Although in these experiments population coupling is thought to arise from diversity in the mean input[186], we hypothesize that in cortical dynamics where population rhythms exist, the heterogeneity of the neuronal properties can also create the same kind of diversity in the population coupling as that observed here.

From a neuronal networks perspective, a possible avenue of future research is the self consistent calculation of the critical delay at the oscillatory transition. Mean field theories of neuronal networks have made use of the so called diffusion approximation, to study the transitions from the asynchronous irregular to synchronous irregular states. In particular **?**[208] has proposed a method to self consistently find the frequency and phase of the oscillation at the oscillatory bifurcation as a function of network parameters for rather general neuronal models. Given the remarkably different synchronization properties that the QIF and the rQIF neurons have with increasing rapidness, a proper quantification of the nature of this transition is desirable. In particular, it would directly link the rapidness of the action potential (related to a higher bandwidth capacity[72]) with the frequency of the population oscillation, which we have only observed numerically.

Finally, the perfect rhythmicity of the oscillations observed in our networks is different from that seen in experiments. The frequency and power fluctuations that are observed and reproduced in the first part of this thesis are not present in these simplified models. The challenge of developing biologically realistic models that describe these basic statistics and further allow for exact mathematical treatment remains open (see also next section). One avenue of possible exploration is the inclusion of multi-frequency oscillations, as discussed in the previous section. In detailed bifurcation analyses by Brunel[29], in networks similar to ours, parameter ranges in which rhythms coexist were found. Furthermore, the approach taken here can be extended to exponentially decaying synapses. It would be interesting to see whether the temporal extent of the interaction, that in the non delayed case can lead a transition from stability to extensive chaos with LIF neurons[199], leads to different population dynamics than the simple oscillations observed here.

4.4 General Discussion and Outlook

We have explored the capacity for complex high dimensional dynamics and their impact on information transmission in heterogeneous delayed neuronal networks. In the following, we delineate future directions of research at the interface of the aforementioned approaches: to investigate the role of action potential onset rapidness in information transmission on the one hand, and the role of inter-areal phase relations in shaping the ergodic properties of connected areas on the other.

In Chapter 3, we have found that the action potential onset has profound impact on the type of oscillatory rhythms that develop after the delay-induced transition. In particular, we find that the chaotic measures have a different behavior depending on this parameter. The neurons that composed the networks studied in Chapter 2 were of the Wang-Buzsaki type[285], where the action potential onset has a rather small slope as can be seen in Figure 4.1a. This is in strong contrast to the rapid action potential onset observed in cortical neurons[179]. A possible avenue of future research is to understand not only the synchronization properties of rapid neurons, but the impact that they have on their information transmission capabilities.

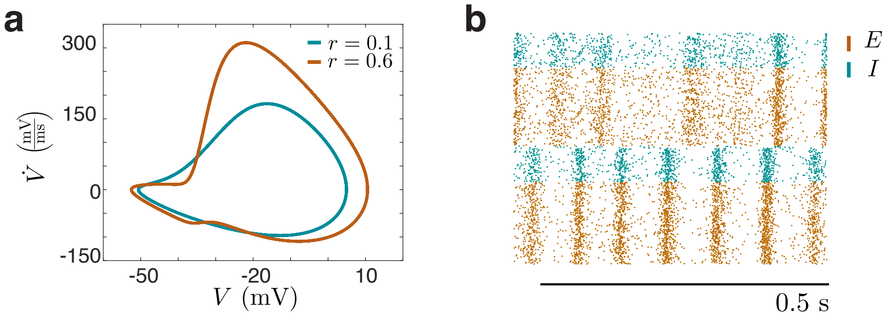

Figure 4.1: Projects Crossover. (a) Phase portrait of the *rapid* Wang Buzsaki Neuron model with different rapidness. The parameter r changes the steepness of the fast sodium activation by manipulating the sodium channel opening rate $\alpha_m = x/(1 - \exp(-x))$ with $x = r(V + 35)$. In blue in its original parameters (r=0.1), in brown $r = 0.6$ **(b)** Two populations of E-I QIF neurons connected by long range excitation. Parameters: Default parameters as in table 3.1 for each population with a local and inter areal delay of 2 ms. The membrane time constant heterogeneity is 0.5 and a threshold heterogeneity of 0.05. The inter-areal value of K is 50.

Lastly, a possible future exploration is the reduction of the complexity of the models used in 2 to find the minimal components that give rise to reasonably similar dynamics, and study the effect of the rhythms relative phase from an ergodic theory perspective. Figure 4.1b shows an implementation of networks of heterogeneous QIF neurons similar to those described in Chapter 3, connected by delayed long range excitation. Although each population in isolation exhibits regular dynamics, the coupled case shown in Figure 3.8e–h exhibits transients of desynchronized activity and reveals frequency and locking irregularities. Time dependent measures like the fraction of positive local Lyapunov exponents, could aid in understanding the dependence of the micro state of these coupled networks on the phase relation.

A

Ergodic properties of a network of delayed rate units

This appendix contains a small side project also studying chaos in delayed networks, from a coarser level of description. Part of it (section A.2.1) has been independently published by Bimbard et al.[24].

A.1 The classic SCS network

In a seminal work by Sompolinsky et al.[234], the study of networks that with further restrictions in the coupling matrix J would relate to spin glasses, was translated to the language of neuroscience. They describe the behavior of continuous units or *neurons* that obey the equation:

$$\dot{h}_i = -h_i + \sum_{j}^{N} J_{ij}\phi(h_j) \qquad \phi(x) = g\,\mathrm{tanh}(x) \tag{A.1}$$

The variable h can be thought as a rate unit that integrates inputs from other sets of units, with a nonlinear transfer function given by ϕ. For this model to achieve one of the many basic requirements that a rate network should accomplish, the function ϕ shouldn't take negative values. Further, the connectivity matrix J_{ij}, whose components are drawn independently from a normal distribution with variance J^2/N (without loss of generality we take J=1), in this setting doesn't accomplish dales law. Extensions of this model in these directions exist[139,170], but won't be analyzed here.

Analytical treatment of the network defined by Eq. (A.1) is possible in many flavors, as summarized in section 1.5 of the introduction. In its original form, the Eq. A.1 can be reduced to an equation for a single neuron given by:

$$\dot{h}_i(t) = -h_i(t) + \eta(t) \tag{A.2}$$

where η is a noise term whose autocorrelation can be found self-consistently. This procedure, called dynamic mean field theory, allows also for a calculation of the maximum Lyapunov exponent. A remarkable transition from full stability to chaos is observed at g=1. The linear stability of the fixed point at $h_i = 0$ can be studied by solving the linearized version of A.1, given by :

$$\dot{\boldsymbol{h}} = -\boldsymbol{h} + \boldsymbol{h}\boldsymbol{J}^{\mathrm{T}} \tag{A.3}$$

By writing $J = E\Lambda E^{-1}$, where Λ is a diagonal matrix, and proposing solutions of the form $h_i = u_i \exp(\nu\tau)$, we obtain the following condition:

$$\nu + 1 = \lambda \tag{A.4}$$

For the proposed solutions to be stable, $\Re(\nu) < 0$ and then $a = \Re(\lambda) < 1$. This means that the eigenvalue distribution of J, which is necessarily centered in zero, has to have a radius, given by g, that is smaller than one.

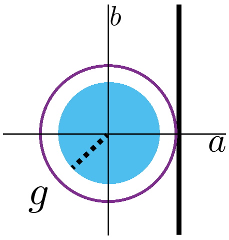

A.2 The delayed SCS network

A.2.1 Estimation of the frequency of the first unstable mode

We are interested in a system similar to that defined above, but in which the rate coupling is not instantaneous in time:

$$\dot{h}_i(t) = -h_i(t) + \sum_{j}^{N} J_{ij}\phi(h_j(t-\tau)) \qquad \phi(x) = g\tanh(x) \tag{A.5}$$

This system is what we can call the delayed SCS. Identically as in the non-delayed case, and as published before[81,136], an equation for the instability boundary can as well be found.

$$\nu + 1 = \lambda\exp(\nu\tau) \tag{A.6}$$

Looking for a Hopf bifurcation, we can replace $\nu = i\omega$. The resulting equation is a parametric form of the Archimedean spirals[81]. Surprisingly, the intersection between the distribution of eigenvalues of J, given by the circle of radius g, and the spirals does not occur before g is larger than one. Thus, the stability boundary of a network with random gaussian connections is independent of the delay. Graphically nevertheless, and indicated in the figure on the right, by modifying the distribution of eigenvalues we

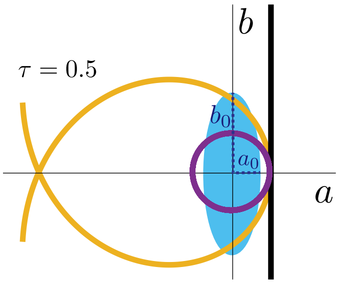

might be able to see other transition beyond the one previously observed. For that, we look at asymmetric matrices of the form[233]:

$$J = g\left(\frac{(1+\alpha)}{2}(J+J^T) + \frac{(1-\alpha)}{2}(J-J^T)\right) \tag{A.7}$$

The axis of the eigenvalue distribution of this matrix are[233]:

$$a_0 = g^2\frac{(1+\alpha)^2}{\sqrt{1+\alpha^2}} \qquad b_0 = g^2\frac{(1-\alpha)^2}{\sqrt{1+\alpha^2}} \tag{A.8}$$

For a given delay τ an intersection (i.e. a value for ω) between the instability boundary given by Eq. (A.6) and the ellipse defined by the axis in Eq. (A.7) can be found. The value of ω, is the frequency of the unstable mode. By direct numerical integration (Fig. A.1a), the numerical estimation of the frequency of the first observed unstable mode at the chosen value of the delay can be obtained(Fig. A.1c). The frequencies obtained via this two methods are in good agreement (Fig. A.1d).

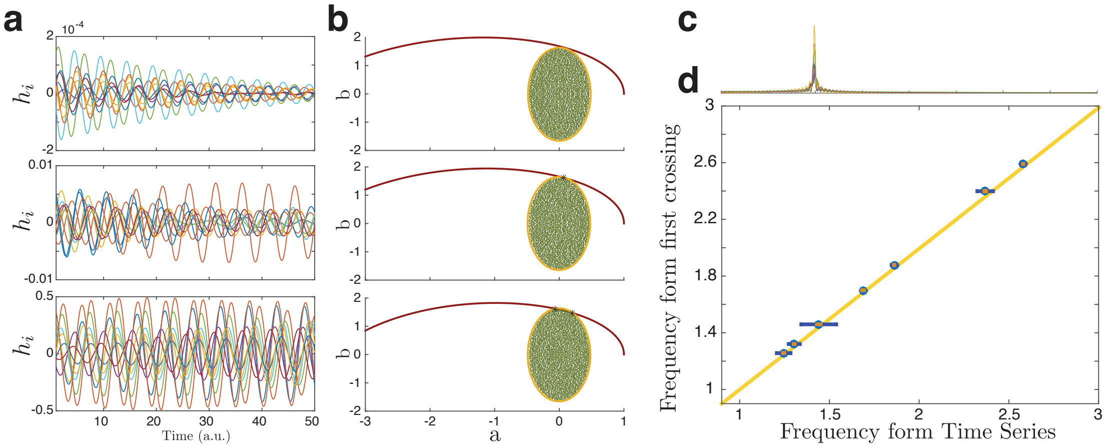

Figure A.1: Predicting the value of the frequency of the first unstable mode. **a** Traces of the rate units for three different delays. Parameters: N=5000,α=-0.3, τ=47 (top), τ=49 (middle), τ=55 (bottom) **b** Intersection of the spiral with the eigenvalue distribution boundary given by Eq. A.8. Parameters as in (a). **c** Example power spectrum at the boundary. **d** Frequency predicted by intersection and the one obtained numerically making a FFT of the unstable mode.

B

Mean field theory of M populations of fully coupled networks of QIF neurons

This appendix contains another side project, of a particular case in which a dynamical equation for the order parameter can be obtained analytically. This is an straightforward extension of the one population case analyzed in So et al.[230].

B.1 M populations of fully coupled networks of Theta neurons

We are going to consider a network of fully coupled θ neurons[74]:

$$\dot{\theta} = (1 - \cos(\theta)) + (1 + \cos(\theta))(\eta + I_{syn}) \tag{B.1}$$

where $I_{syn}(t)$ is a coupling function. To follow the approach originally proposed by Ott & Antonsen[191] and later extended by So et al.[230], we are going to use a coupling function that can be written as a function of the variable θ. This coupling emulates the pulse like connections between units for large N, but counts on the advantage of being differentiable.

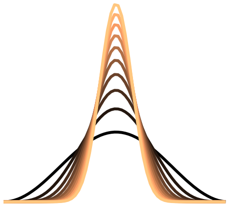

$$I_{syn} = \frac{K}{N} \sum_{i=1}^{n} a_n (1 - \cos(\theta_i))^n \tag{B.2}$$

The parameter n, controls the sharpness of the coupling function. For infinitely large n, a delta-like pulse is obtained at $\theta = \pi$, corresponding to the threshold used in Chapter

3. Two populations of theta neurons coupled by the current above described

$$\dot{\theta_i^1} = (1-\cos(\theta_i^1)+(1+\cos(\theta_i^1)\left(\eta^1 + \frac{K^{11}}{N_1}\sum_{j=1}^{N_1} a_{n_1}(1-\cos(\theta_j^1))^{n_1} + \frac{K^{12}}{N_2}\sum_{j=1}^{N_2} a_{n_2}(1-\cos(\theta_j^2))^{n_2}\right) \tag{B.3}$$

$$\dot{\theta_i^2} = (1-\cos(\theta_i^2)+(1+\cos(\theta_i^2)\left(\eta^2 + \frac{K^{21}}{N_1}\sum_{j=1}^{N_1} a_{n_1}(1-\cos(\theta_j^1))^{n_1} + \frac{K^{22}}{N_2}\sum_{j=1}^{N_2} a_{n_2}(1-\cos(\theta_j^2))^{n_2}\right) \tag{B.4}$$

This can be written, for M populations as

$$\dot{\theta_i^\sigma} = (1-\cos(\theta_i^\sigma)) + (1+\cos(\theta_i^\sigma))\left(\eta^\sigma + \sum_{\sigma'=1}^{M}\frac{K^{\sigma\sigma'}}{N_{\sigma'}}\sum_{j=1}^{N^{\sigma'}} a_{n^{\sigma'}}(1-\cos(\theta_j^{\sigma'}))^{n_{\sigma'}}\right) \tag{B.5}$$

The problem as formulated in its original form Ott & Antonsen[191] can be expressed, in the thermodynamic limit, as a function of the probability density $\rho(\theta,\omega,t)$. $\rho(\theta,\omega,t)$ dθ dω is the probability that the phase of an oscillatory belongs to the interval $[\theta,\theta+d\theta]$ while its frequency belongs to $[\omega,\omega+d\omega]$. In the case of theta neurons and in the absence of synaptic input, the neuron starts to fire tonically with a frequency that scales as the square root of the DC input. For this reason the thermodynamic limit in the case of the theta neuron can be equivalently treated as a function of the mean external input $\bar{\eta}$. The probability density will have to satisfy the continuity equation:

$$\frac{\partial\rho^\sigma(\theta,\bar{\eta},t)}{\partial t} + \frac{\partial}{\partial\theta}(\rho^\sigma(\theta,\bar{\eta},t)v_\theta^\sigma) = 0 \tag{B.6}$$

Assuming that the frequency distribution is stationary the probability density will have to satisfy, besides the normalization condition (left), that given a point in time the integral over all active phases equals the initial frequency distribution $g^{\sigma'}(\bar{\eta})$ (right):

$$\int_{-\infty}^{\infty}\int_0^{2\pi}\rho^\sigma(\theta,\bar{\eta},t)d\theta d\bar{\eta} = 1 \qquad \int_0^{2\pi}\rho^\sigma(\theta,\bar{\eta},t)d\theta = g^{\sigma'}(\bar{\eta}) \tag{B.7}$$

In the case of the M populations of theta neurons, the velocity term of Eq. (B.8) will be given by the continuum equivalent of Eq. (B.5):

$$v_\theta^\sigma = (1-\cos(\theta))+(1+\cos(\theta))\left(\eta^\sigma(t) + \sum_{\sigma'=1}^{M} K^{\sigma\sigma'}a_{n^{\sigma'}}\int_{-\infty}^{\infty}\int_0^{2\pi}\rho^{\sigma'}(\theta',\bar{\eta}',t)(1-\cos(\theta'))^{n_{\sigma'}}d\theta' d\bar{\eta}'\right) \tag{B.8}$$

The order parameter of the system, r^σ will be the weighted sum of the mean of the phasors for each population, z^σ, also called the mean field variable.

$$r^\sigma = \sum_{\sigma'=1}^{M} K^{\sigma\sigma'} z^{\sigma'} \qquad z^{\sigma'}(t) = \int_{-\infty}^{\infty}\int_0^{2\pi} \rho^{\sigma'}(\theta,\bar{\eta},t)d\theta d\bar{\eta} \tag{B.9}$$

Replacing equation (B.8) into (B.6), gives us a differential equation for the probability density. Analytical treatment for this type of equations was opened after what is now known as the Ott-Antonsen ansatz: Given the Fourier expansion of the probability density

$$\rho^{\sigma'}(\theta,\bar{\eta},t) = \frac{g^{\sigma'}(\bar{\eta})}{2\pi}\left(1 + \sum_{k=1}^{\infty} \alpha_k^{*\sigma'}(\bar{\eta},t)e^{ik\theta} + \sum_{k=1}^{\infty} \alpha_k^{\sigma'}(\bar{\eta},t)e^{-ik\theta}\right) \tag{B.10}$$

and that the velocity can be written in the form $v_\theta^{\sigma'} = h(\bar{\eta},t) + f(\bar{\eta},t)e^{i\theta} + f^*(\bar{\eta},t)e^{-i\theta}$, they showed choosing $\alpha(\bar{\eta},t)_k = \alpha(\bar{\eta},t)^k$ leads to a differential equation for the coefficients $\alpha(\bar{\eta},t)$ whose solutions are an invariant manifold of the system, given that certain condition over the coefficients are imposed. The equation of the coefficients can be further linked to equations for the mean field variables by means of residue theory.

$$\dot{\alpha}^\sigma(\bar{\eta},t) = i(f\alpha^\sigma(\bar{\eta},t)^2 + h\alpha^\sigma(\bar{\eta},t) + f^*) \tag{B.11}$$

B.2 The derivation of a mean field variable

For obtaining a differential equation for the mean field variable z^σ the following steps will be taken:

Step 1): Writing the synaptic coupling term in equation (B.8) in the form of the Daido moments

Step 2): Write the Daido moments in terms of the Fourier coefficients of $\alpha_k^{\sigma'}(\bar{\eta},t)$

Step 3): Writing the velocity in the form $v_\theta^{\sigma'} = h^{\sigma'}(\bar{\eta},t) + f^{\sigma'}(\bar{\eta},t)e^{i\theta} + f^{*\sigma'}(\bar{\eta},t)e^{-i\theta}$

Step 4): Give an explicit form for the frequency distribution $g^{\sigma'}(\bar{\eta})$ and use equation (B.9) to obtain a dynamical equation for z^σ

Step 1)

We focus on the term $H(z^{\sigma'}, n_{\sigma'}) = \int_{-\infty}^{\infty}\int_0^{2\pi} \rho^{\sigma'}(\theta', \bar{\eta}', t)(1-\cos(\theta'))^{n_{\sigma'}} d\theta' d\bar{\eta}'$. We can show that:

$$(1-\cos(\theta))^n = c_0 + \sum_{q=1}^{n} c_q(e^{iq\theta} + e^{-iq\theta}) \tag{B.12}$$

Which leads to a synaptic coupling term of the form:

$$H(z^{\sigma'}, n_{\sigma'}) = c_0 + \sum_{q=1}^{n} c_q \left(\int_{-\infty}^{\infty}\int_0^{2\pi} \rho^{\sigma'}(\theta', \bar{\eta}', t) e^{iq\theta'} d\theta' d\bar{\eta}' + \int_{-\infty}^{\infty}\int_0^{2\pi} \rho^{\sigma'}(\theta', \bar{\eta}', t) e^{-iq\theta'} d\theta' d\bar{\eta}' \right) \tag{B.13}$$

$$H(z^{\sigma'}, n_{\sigma'}) = c_0 + \sum_{q=1}^{n} c_q \left(z_q^{\sigma'} + z_{-q}^{\sigma'} \right) \tag{B.14}$$

Where $z_q^{\sigma'}$ are the Daido moments, defined as:

$$z_q^{\sigma'} = \int_{-\infty}^{\infty}\int_0^{2\pi} \rho^{\sigma'}(\theta', \bar{\eta}', t) e^{iq\theta'} d\theta' d\bar{\eta}' \tag{B.15}$$

Step 2)

Including Fourier expansion of the probability density in this last definition we obtain

$$z_q^{\sigma'} = \int_{-\infty}^{\infty}\int_0^{2\pi} \frac{g^{\sigma'}(\bar{\eta'})}{2\pi} \left(1 + \sum_{k=1}^{\infty} \alpha_k^{*\sigma'}(\bar{\eta}', t) e^{ik\theta'} + \sum_{k=1}^{\infty} \alpha_k^{\sigma'}(\bar{\eta}', t) e^{-ik\theta'} \right) e^{iq\theta'} d\theta' d\bar{\eta}' \tag{B.16}$$

Using that $\int_0^{2\pi} e^{i(q-k)\theta'} d\theta' = 2\pi\delta_{qk}$, and that q and k are positive integers we obtain the moment as a function of the Fourier coefficient (left), that takes the form in the right after including the OA ansatz. The equations are analogous for the conjugated variable.

$$z_q^{\sigma'} = \int_{-\infty}^{\infty} g^{\sigma'}(\bar{\eta'}) \alpha_q^{\sigma'}(\bar{\eta}', t) d\bar{\eta}' \qquad z_q^{\sigma'} = \int_{-\infty}^{\infty} g^{\sigma'}(\bar{\eta'}) (\alpha^{\sigma'}(\bar{\eta}', t))^q d\bar{\eta}' \tag{B.17}$$

Extending α to complex values of $\bar{\eta}$ and asking for it to be analytical in the upper part of the plane, its only needed to define the probability distribution for the excitability parameter

$$g^{\sigma'}(\bar{\eta'}) = \frac{\Delta/\pi}{(\bar{\eta}-\eta_0)^2+\Delta^2} = \frac{1}{2\pi i}\left(\frac{1}{\bar{\eta}-(\eta_0+i\Delta)} - \frac{1}{\bar{\eta}-\eta_0-i\Delta}\right) \tag{B.18}$$

Integrating in a semi-circle in the upper half of the plane,

$$z_q^{\sigma'} = 2\pi i Res(g^{\sigma'}\alpha^{\sigma' q}, \eta_0+i\Delta) = \alpha^{\sigma'}(\eta_0+i\Delta,t)^q \tag{B.19}$$

which therefore means that:

$$z_q^{\sigma'} = \alpha^{\sigma'}(\eta_0+i\Delta,t)^q = (z^{\sigma'})^q \tag{B.20}$$

And therefore,

$$H(z^{\sigma'},n_{\sigma'}) = c_0 + \sum_{q=1}^{n} c_q\left((z^{\sigma'})^q + (z^{*\sigma'})^q\right) \tag{B.21}$$

Step 3)

The velocity is then

$$v_\theta^\sigma = (1-\cos(\theta)) + (1+\cos(\theta))\left(\eta^\sigma(t) + \sum_{\sigma'=1}^{M} K^{\sigma\sigma'} a_{n_{\sigma'}} H(z^{\sigma'},n_{\sigma'})\right) \tag{B.22}$$

$$W^\sigma(\vec{z},\vec{n},M) = \sum_{\sigma'=1}^{M} K^{\sigma\sigma'} a_{n_{\sigma'}} H(z^{\sigma'},n_{\sigma'}) \tag{B.23}$$

Noticing that W is also real, we can the write:

$$v_\theta^\sigma = 1+\eta^\sigma(t)+W^\sigma(\vec{z},\vec{n},M) - \frac{1}{2}(1-\eta^\sigma(t)-W^\sigma(\vec{z},\vec{n},M))e^{i\theta} - \frac{1}{2}(1-\eta^\sigma(t)-W^\sigma(\vec{z},\vec{n},M))e^{-i\theta} \tag{B.24}$$

$$v_\theta^{\sigma'} = h^{\sigma'}(\bar{\eta},t) + f^{\sigma'}(\bar{\eta},t)e^{i\theta} + f^{*\sigma'}(\bar{\eta},t)e^{-i\theta}$$

Step 4)

Given that the velocity can therefore be written in the "sinusoidal" form, the equation (B.11) holds, and in our case, writing $W^\sigma(\vec{z},\vec{n},M)$ as $W^\sigma(t)$:

$$\dot{\alpha}^\sigma(\bar{\eta},t) = -\frac{i}{2}\left(1-\eta^\sigma(t)-W^\sigma(t)\right)\alpha^\sigma(\bar{\eta},t)^2 + i(1+\eta^\sigma(t)+W^\sigma(t))\alpha^\sigma(\bar{\eta},t) - \frac{i}{2}(1-\eta^\sigma(t)-W^\sigma(t)) \tag{B.25}$$

Multiplying both sides by $g^{\sigma'}(\bar{\eta'})$, integrating in the upper part of the complex plane, we obtain for each term:

a) $\int_{-\infty}^{\infty} g^{\sigma}(\bar{\eta'})\dot{\alpha}^{\sigma}(\bar{\eta}', t)d\bar{\eta}' = \dot{z}^{\sigma}(t)$

b) $\int_{-\infty}^{\infty} \frac{-i}{2} g^{\sigma}(\bar{\eta'})(\alpha^{\sigma}(\bar{\eta}', t))^2(1-\eta^{\sigma}(t)-W^{\sigma}(t))d\bar{\eta}' = \frac{-i}{2} z^{\sigma}(t)(1-\eta_0(t)-i\Delta-W^{\sigma}(t))$

c) $\int_{-\infty}^{\infty} ig^{\sigma}(\bar{\eta'})\alpha^{\sigma}(\bar{\eta}', t)(1+\eta^{\sigma}(t)+W^{\sigma}(t))d\bar{\eta}' = iz^{\sigma}(t)(1+\eta_0(t)+i\Delta+W^{\sigma}(t))$

d) $\int_{-\infty}^{\infty} \frac{-i}{2} g^{\sigma}(\bar{\eta'})(1-\eta^{\sigma}(t)-W^{\sigma}(t))d\bar{\eta}' = \frac{-i}{2} z^{\sigma}(t)(1-\eta_0(t)-i\Delta-W^{\sigma}(t))$

$$\dot{z}^{\sigma} = \frac{-i}{2}(z^{\sigma}-1)^2 - \frac{1}{2}(z^{\sigma}+1)^2 \left(\Delta - i\eta_0(t) - \sum_{\sigma'=1}^{M} K^{\sigma\sigma'} a_{n\sigma'} \left(c_0 + \sum_{q=1}^{n} c_q \left((z^{\sigma'})^q + (z^{*\sigma'})^q\right)\right)\right) \tag{B.26}$$

This equation can be re-written if we take $z^{\sigma} = \rho^{\sigma} e^{\phi^{\sigma}}$

$$\dot{\rho^{\sigma}} = \frac{1}{2}\sin(\phi^{\sigma})(\rho^{\sigma 2}-1)(1-\eta_0(t)-I^{\sigma}_{syn}) - \frac{\Delta}{2}\cos(\phi^{\sigma})(\rho^{\sigma 2}+1) - \Delta\rho^{\sigma} \tag{B.27}$$

$$\dot{\phi^{\sigma}} = (1+\eta_0(t)+I^{\sigma}_{syn}) - \frac{1}{2}\cos(\phi^{\sigma})(\rho^{\sigma}+\frac{1}{\rho^{\sigma}})(1-\eta_0(t)-I^{\sigma}_{syn}) - \frac{\Delta}{2}(\rho^{\sigma}-\frac{1}{\rho^{\sigma}})\sin(\phi^{\sigma}) \tag{B.28}$$

$$I^{\sigma}_{syn} = \sum_{\sigma'=1}^{M} K^{\sigma\sigma'} a^{\sigma'}_{n}(c_0 + 2\sum_{q=1}^{n} c_q (\rho^{\sigma'})^q \cos(q\phi^{\sigma'})) \tag{B.29}$$

B.3 First case study: One population

In the single population case we obtain[230] the following equations for the order parameter:

$$\dot{\rho} = \frac{1}{2}\sin(\phi)(\rho^2-1)(1-\eta_0(t)-I_{syn}) - \frac{\Delta}{2}\cos(\phi)(\rho^2+1) - \Delta\rho \tag{B.30}$$

$$\dot{\phi} = (1+\eta_0(t)+I_{syn}) - \frac{1}{2}\cos(\phi)(\rho+\frac{1}{\rho})(1-\eta_0(t)-I_{syn}) - \frac{\Delta}{2}(\rho-\frac{1}{\rho})\sin(\phi) \tag{B.31}$$

$$I_{syn} = Ka_2\left(c_0 + 2c_1\rho\cos(\phi) + 2c_2\rho^2\cos(2\phi)\right) \tag{B.32}$$

Where c_q are the double binomial coefficients given by:

$$c_q = \sum_{j.m=0}^{n} \delta_{j-2m,q} Q_{jm} \qquad Q_{jm} = \frac{(-1)^j n!}{2^j m!(n-j)!(j-m)!} \tag{B.33}$$

For n=2 then we have

$$c_0 = \frac{3}{2} \qquad c_1 = -1 \qquad c_2 = 1/4 \tag{B.34}$$

Following equation B.2, a_n is chosen such $a_n \int_0^{2\pi} (1-\cos(\theta_i))^n d\theta = 2\pi$. In the case of n=2, the integral is equal to 3π and therefore $a_n = \frac{2}{3}$.

$$I_{syn} = \frac{2K}{3} \left(\frac{3}{2} - 2\rho\cos(\phi) + \frac{1}{2}\rho^2 \cos(2\phi) \right) \tag{B.35}$$

To compare with simulations, networks of fully coupled networks of a few thousand In the network simulation the same term, written as a function of the N discrete phases, would be

$$I_{syn} = \frac{K}{N} \sum_{i=1}^{n} \frac{2}{3} (1-\cos(\theta_i))^2 \tag{B.36}$$

B.4 Second case study: Comparison with numerical simulations for the E-I case

Similarly, using equations Eq.(B.30),(B.31),(B.32), the two population cases is obtained. The current terms will have identical contributions from the local population and from the distant one, each one satisfying, for $n = 2$, Eq (B.35) with the corresponding $K_{\sigma\sigma'}$. The sign of $K_{\sigma\sigma'}$ determines the nature, inhibitory of excitatory, of the connections. In the two population case, four different coupling strengths can be defined, K_{ee},K_{ii},K_{ei},K_{ie}. The notation of choice is that K_{ij} is the coupling from j to i.

Figure B.1 shows in panel a, color coded the absolute value of the order parameter at the fixed point. Lighter colors code for a higher absolute value, meaning that the network is more synchronized. Black areas shows point in which no fixed point was found: The order parameter oscillates indicating that the network behavior undergoes periodic changes in the level of synchronization. An example for this regime can be found for $K_{ee} = 5$, $K_{ei} = -3.85$, $K_{ie} = 3.85$, $K_{ii} = -5$, $\eta_0 = 5$ In Figure B.1 b. The analytical results are compared with direct numerical simulations of N=10000, whose coupling is given by B.36. A snapshot of the spiking activity of the networks, is shown in Figure B.1 c. The oscillation is irregular with a degree of irregularity similar to that of delayed balanced networks of Chapter 3.

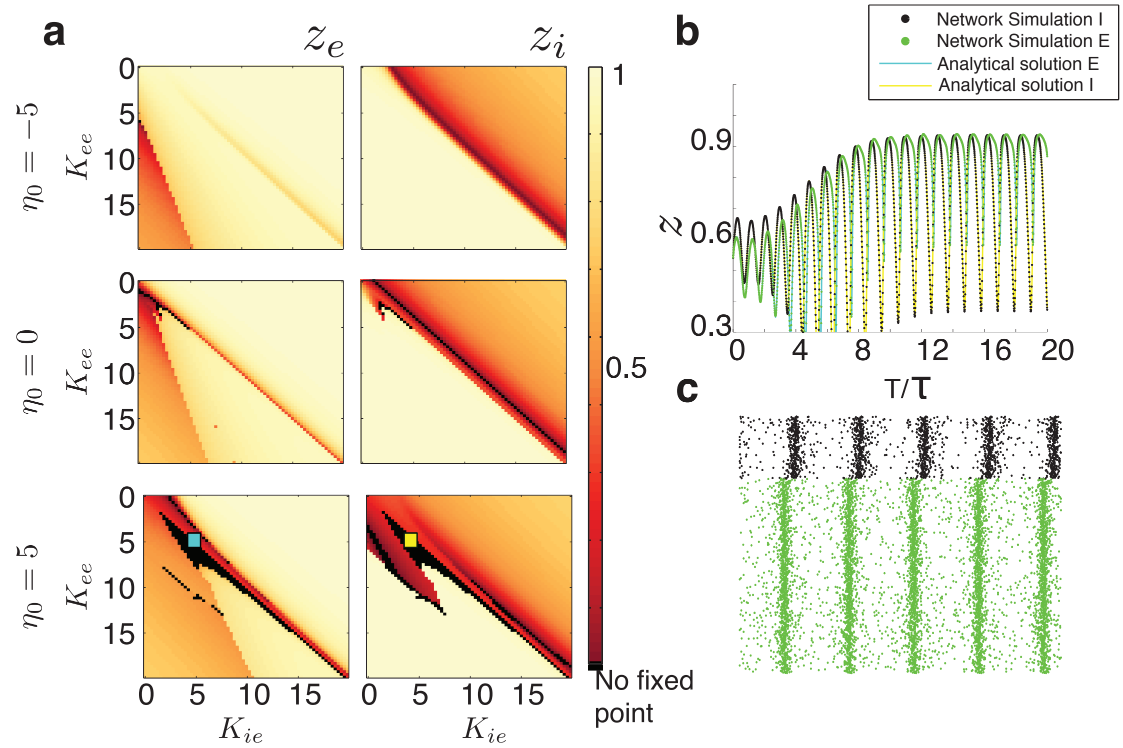

Figure B.1: Mean field of two fully coupled E and I networks. Comparison with direct numerical Simulations. a) As a function of the parameters K_{ee} and K_{ie} (with $K_{ii} = -K_{ee}$ and $K_{ei} = -K_{ie}$), the fixed points of the absolute value of z_e (left) and z_i (right) are shown for three values of the mean frequency distribution, η_0. In black, points were no fixed points were found are indicated. **b)** Parameters as indicated like a red and a blue squares in panel a, are chosen. The absolute value of the order parameter of the excitatory population z_e (blue) and inhibitory population z_i (red) are shown together with their estimation via direct numerical simulation, showing good agreement. **c)** Raster plot showing the underlying network behavior.

C

Optogenetic control of inter-areal phase relations

frontiers in
NEURAL CIRCUITS

ORIGINAL RESEARCH ARTICLE
published: 17 April 2013
doi: 10.3389/fncir.2013.00049

Controlling the oscillation phase through precisely timed closed-loop optogenetic stimulation: a computational study

Annette Witt[1], Agostina Palmigiano[2], Andreas Neef[3], Ahmed El Hady[3], Fred Wolf[3]* and Demian Battaglia[2]*

[1] *Cognitive Neuroscience Department, German Primate Center, Bernstein Center for Computational Neuroscience, Max Planck Institute for Dynamics and Self-Organization, Göttingen, Germany*
[2] *Bernstein Center for Computational Neuroscience, Max Planck Institute for Dynamics and Self-Organization, Göttingen, Germany*
[3] *Max Planck Institute for Dynamics and Self-Organization, Bernstein Center for Computational Neuroscience and Bernstein Focus Neurotechnology, CRC-889 Cellular Basis of Sensory Processing, Göttingen, Germany*

Edited by:
Steve M. Potter, Georgia Institute of Technology, USA

Reviewed by:
Carmen Canavier, LSU Health Sciences Center, USA
Nathan Urban, Carnegie Mellon University, USA
Robert J. Butera, Butera Lab, Georgia Institute of Technology (Georgia Tech), USA

***Correspondence:**
Fred Wolf and Demian Battaglia, Max Planck Institute for Dynamics and Self-Organization, Am Faßberg 17, D-37077 Göttingen, Germany.
e-mail: fred@nld.ds.mpg.de; demian@nld.ds.mpg.de

Dynamic oscillatory coherence is believed to play a central role in flexible communication between brain circuits. To test this communication-through-coherence hypothesis, experimental protocols that allow a reliable control of phase-relations between neuronal populations are needed. In this modeling study, we explore the potential of closed-loop optogenetic stimulation for the control of functional interactions mediated by oscillatory coherence. The theory of non-linear oscillators predicts that the efficacy of local stimulation will depend not only on the stimulation intensity but also on its timing relative to the ongoing oscillation in the target area. Induced phase-shifts are expected to be stronger when the stimulation is applied within specific narrow phase intervals. Conversely, stimulations with the same or even stronger intensity are less effective when timed randomly. Stimulation should thus be properly phased with respect to ongoing oscillations (in order to optimally perturb them) and the timing of the stimulation onset must be determined by a real-time phase analysis of simultaneously recorded local field potentials (LFPs). Here, we introduce an electrophysiologically calibrated model of Channelrhodopsin 2 (ChR2)-induced photocurrents, based on fits holding over two decades of light intensity. Through simulations of a neural population which undergoes coherent gamma oscillations—either spontaneously or as an effect of continuous optogenetic driving—we show that precisely-timed photostimulation pulses can be used to shift the phase of oscillation, even at transduction rates smaller than 25%. We consider then a canonic circuit with two inter-connected neural populations oscillating with gamma frequency in a phase-locked manner. We demonstrate that photostimulation pulses applied locally to a single population can induce, if precisely phased, a lasting reorganization of the phase-locking pattern and hence modify functional interactions between the two populations.

Keywords: oscillations, functional connectivity, modeling, closed-loop systems, optogenetic stimulation, phase response

INTRODUCTION

Neural activity of brain circuits at many scales has often been reported to display oscillatory components at different frequencies (Eckhorn et al., 1988; Gray et al., 1989; Kreiter and Singer, 1996; Tallon-Baudry et al., 1996; Roelfsema et al., 1997; Varela et al., 2001; Brovelli et al., 2004; Samonds and Bonds, 2004; Melloni et al., 2007; Buffalo et al., 2011). In particular, the *communication-through-coherence* hypothesis (Fries, 2005) suggests that oscillatory coherence between different neural circuits could control functional interactions between them with a high degree of flexibility (Womelsdorf et al., 2007). In particular, evidence for a role of enhanced inter-areal oscillatory coherence in attentional modulation is rapidly accumulating (Fries et al., 2001; Gregoriou et al., 2009; Rotermund et al., 2009; Bosman et al., 2012; Gregoriou et al., 2012; Grothe et al., 2012).

The circuit mechanisms underlying the local generation of oscillations, specifically in the gamma range of frequencies (30–100 Hz) have been explored in studies *in vitro* (Whittington et al., 1995; Bartos et al., 2007) and *in silico* (Brunel and Hakim, 1999; Whittington et al., 2000; Brunel and Hansel, 2006; Wang, 2010). All of these contributions have highlighted the crucial role played by the interplay of GABAergic interneurons in creating time-windows in which excitatory and inhibitory neurons can fire in a sparsely synchronized manner, before being counteracted by strong and delayed feedback inhibition. More recently, the functional involvement of local inhibitory networks could be causally verified *in vivo* by targeted selective optogenetic stimulation of Parvalbumine-positive basket cells in a cortical circuit (Cardin et al., 2006; Sohal et al., 2009).

In an analogous way, optogenetic techniques might be used for direct tests of the communication-through-coherence hypothesis and other suggested functional roles of brain oscillations, like their implication in phase coding (Lisman, 2005; Koepsell et al., 2010; Nadasdy, 2010; Kayser et al., 2012). For such applications, however, improved optogenetic stimulation protocols are needed that allow for precise control of the phase relations between different neuronal populations or assemblies, rather than a pure enhancement of oscillatory power.

Theoretical investigations suggest that, due to non-trivial phase response properties (Pikovsky et al., 2001) of oscillating neuronal populations (Akam et al., 2012), stimulation pulses might have a strong influence on local and long-range phase-relations, but only if properly timed with respect to the ongoing oscillatory dynamics (Tiesinga and Sejnowski, 2010; Battaglia et al., 2012). Application of phase-timed stimuli requires a real-time estimate of the phase from continuously recorded local field potential (LFP) data.

Optogenetic stimulation conditional on recorded activity constitutes a closed-loop setup. The advantage of closed-loop stimulation compared to open-loop stimulation is the possibility to program an artificial feedback with defined rules and constraints dependent on the target system's dynamical history. Closed loop electrical stimulation has been successfully used to clamp network activity (Wallach et al., 2011), to control the firing rate of neurons (Miranda-Dominguez et al., 2010), to control bursting activity (Wagenaar et al., 2005), and to train cultured neuronal networks (Marom and Shahaf, 2002). Closing the loop between living neurons and robotics has also been used to realize embodiment—by using representations generated by network activity either to control a robotic arm (Bakkum et al., 2007) or control autonomous systems (Bandyopadhyay, 2005)—or to study neuronal plasticity (Novellino et al., 2007).

In this study, we explore through a modeling approach the feasibility of closed-loop optogenetic control of the phase of a local oscillation and of inter-areal phase synchronization. To this end, we simulated the activity of populations of excitatory and inhibitory conductance-based neurons with random connectivity. To investigate the case where a sparse transduction with Channelrhodopsin 2 (ChR2) is achieved *in vitro* or *in vivo*, small fractions of these neurons were endowed with a newly developed and data-constrained conductance-based model of a light-activated channel. This case is of particular interest, since it has been shown that low transduction rates achieved through either particle mediated gene transfer or via lipid reagents (Takahashi et al., 2012) can increase the spatial specificity of light stimulation (Schoenenberger et al., 2008). Our model, however, applies robustly also to the case of higher ChR2 transduction rates, as the ones that can be achieved using viral transfection (Adamantidis et al., 2007; Aravanis et al., 2007), in utero electroporation (Petreanu et al., 2007) or in T helper type 1 (Thy1) transgenic mice (Wang et al., 2007).

Demonstrating the reliability of our model, we first simulated phase shifting of LFP oscillations with open-loop optogenetic stimulation, quantitatively reproducing and generalizing experimental results *in vitro* (Akam et al., 2012). We moved then to the analysis of a canonical cortical circuit with two interacting areas. Here, we simulated a realistic closed-loop stimulation protocol which was suited to trigger lasting changes of inter-areal phase relations and, correspondingly, to affect communication-through-coherence. Thus, we intend our modeling exploration to foster the implementation of a new generation of closed-loop optogenetic experiments *in vitro* and *in vivo* aiming at inducing distributed reorganization of functional interactions at the system level.

MATERIALS AND METHODS

ChR2 PHOTOCURRENT EXPERIMENTAL CHARACTERIZATION

Human embryonic kidney cells were transfected with a plasmid encoding a ChR2-YFP fusion protein. The pcDNA 3.1-ChR2-YFP construct was kindly provided by Ernst Bamberg, (MPI for Biophysics, Frankfurt, Germany). After two–four days, successfully transfected cells were identified by their YFP fluorescence. In the whole-cell configuration, the membrane voltage was clamped to −60 mV. Channelrhodopsin's conductance was changed by 500 ms long light pulses. The conductance change was monitored as a time and light-intensity dependent current change (**Figure 1B**). In the case of cultured hippocampal neurons, cell were transfected at 7 DIV with AAV1/2-CAG-ChR2-YFP virus. After 1 week, successfully transduced cells could be identified by their YFP fluorescence.

Whole-field illumination was provided by an extended laser beam (488 nm). Light intensity was controlled by neutral density filters (optical density 1 and 2, respectively) and by means of the software provided for the laser. A comparison of the light-induced current waveforms for 90% attenuation by software and a neutral density filter with an optical density of 1.0 showed excellent agreement, indicating that the software produced the intended attenuation. The laser was switched using a built-in mechanical shutter with a response time in the μs range, achieved through the minute spatial extent of the beam.

BIOPHYSICALLY CALIBRATED MODEL OF ChR2 PHOTOCONDUCTANCE

Based on the results of the previously described experiment, we modeled the evoked photocurrents as the product of activation and inactivation functions. The current activation could be described by a single exponential function and the current inactivation by the sum of two exponential functions (see also **Figure 1B**). This light-induced conductance change could be well described by the functional form:

$$F_{ChR2}(t) = A_{\text{act}}\left(1 - e^{-\frac{t-t_{\text{ON}}-d}{\tau_{\text{act}}}}\right) \cdot \left(A_{\text{persist}} + A_{\text{inact}}^{(1)} e^{-\frac{t-t_{\text{ON}}-d}{\tau_{\text{inact}}^{(1)}}} + A_{\text{inact}}^{(2)} e^{-\frac{t-t_{\text{ON}}-d}{\tau_{\text{inact}}^{(2)}}}\right) \quad (1)$$

Here d represents a latency observed between the times t_{ON} of light onset and the actual start of the conductance rise and A_{persist} is set to $A_{\text{persist}} = 1 - A_{\text{inact}}^{(1)} - A_{\text{inact}}^{(2)}$ in order to prevent the inactivation conductance factor from becoming negative. Note that Equation 1 holds true only as long as the light is switched on. After switching off the light, the response returns to baseline with a single exponential time course with time constant τ_{OFF}. When individual current responses were fitted, the latency d, the amplitude A_{act}, the inactivating fractions $A_{\text{inact}}^{(1)}$ and $A_{\text{inact}}^{(2)}$, and

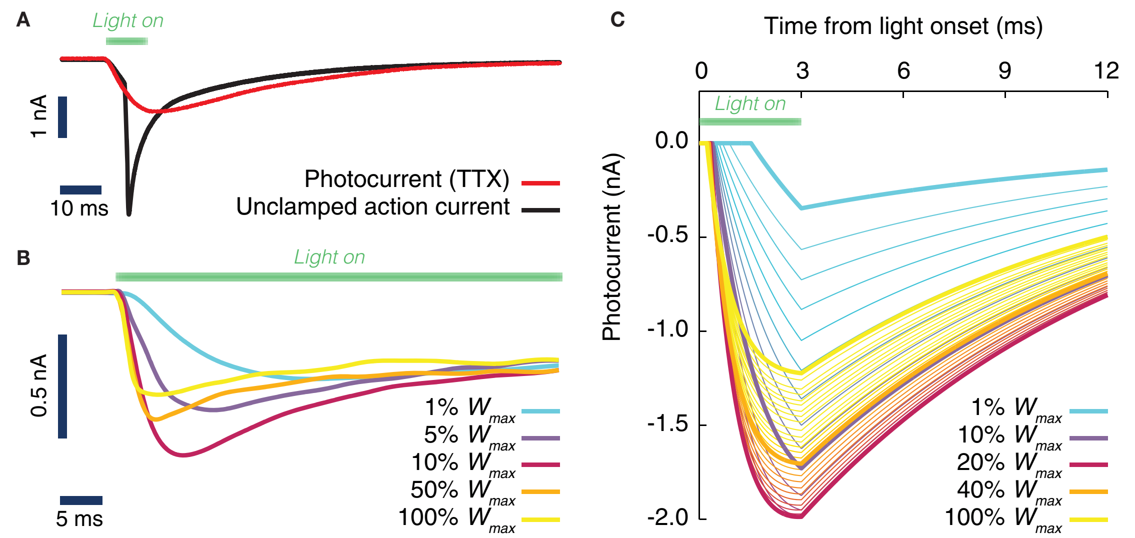

FIGURE 1 | Evoked ChR2 photocurrent: conductance-based model. **(A)** Whole cell voltage clamp recording of a cultured neuron, transduced with Channelrhodopsine 2 (ChR2) and illuminated with LED light (during the time interval shown by a green horizontal bar). Two current intensity recordings have been performed, the first in a physiological solution, i.e., with all channels active (black curve), the second with TTX in the bath, i.e., with blocked Na-channels (red curve). When the Na channels are still active (black curve), even the voltage clamp (−70 mV) at the soma cannot prevent the cell from spiking. **(B)** Activation kinetics of the photo-induced conductance in human embryonic kidney cells (HEK-293) that are transfected with ChR2. For increasing light power density (100% $W_{\max}$ corresponds approximately to 130 mW/mm^2) the activation becomes faster. Peak conductance increases from 0 to ∼10% of the maximal intensity and decreases for higher light intensities. Note the different scale of evoked currents in neurons and HEK cells. **(C)** Simulated photocurrents generated by the conductance-based model described by Equation (1), for different light intensities (expressed relatively to maximum illumination intensity) and for a rectangular shaped light pulse stimulation with a duration of 3 ms. Model parameters and their dependence on light intensity (see **Table 2**) are obtained from fits to photoconductance recordings analogous to the one shown in panel **(B)**, performed for different light intensities. For short light pulses as used here, the experiments indicate that the largest conductances are obtained for light intensities between 10% and 50% (interpolation of the simulated photocurrent results in an optimal value of 18% of the maximum light intensity).

the activation time constant τ_{act} were found to be dependent on the light-intensity W_{light} when individual current responses were fitted. However, the time constants related to inactivation were almost unchanged for different light intensities. Therefore, for simultaneously fitting current responses evoked by different light intensities (ranging over two orders of magnitude), two global (i.e., light-independent) parameters $\tau^{(1)}_{\text{inact}}$ and $\tau^{(2)}_{\text{inact}}$were used. In order to model the dependence on the light intensity of the other parameters (d, τ_{act}, A_{act}, $A^{(1)}_{\text{inact}}$, and $A^{(2)}_{\text{inact}}$) we fitted the following functions to the recorded data:

$$d = d_A + d_B W_{\text{light}} + \frac{d_C}{W_{\text{light}}} \tag{2}$$

$$\tau_{\text{act}} = \tau^{(0)}_{\text{act}} + c_{\text{act}} e^{-k_{\text{act}} W_{\text{light}}} \tag{3}$$

$$A_{\text{act}} = a_0 + \frac{a_{\min} - 1}{1 + \left(W_{0.5}/W_{\text{light}}\right)^2} \tag{4}$$

$$A^{(1)}_{\text{inact}} = b_0 + \frac{b_1}{b_2 + \left(W_{\text{light}} - W_{\text{inact}}\right)^2} \tag{5}$$

$$A^{(2)}_{\text{inact}} = c_{\text{inact}} e^{-k_{\text{inact}} W_{\text{light}}} \tag{6}$$

All the parameters of Equations (2–5) are the result of least-squared fits. For Equation (6) k_{inact} has been set manually to assure convergence of the fitting procedure. All fitted parameters of the ChR2 conductance model, together with their standard deviations, are summarized in **Table 1**. Light intensity is measured relatively to the maximum intensity $W_{\max}$ that can be achieved in our setup. A precise calibration of the absolute power density at the maximal intensity was not performed. We have estimated it to be approx. $W_{\max} = 130\,\text{mW/mm}^2$ for a continuous illumination, which is rather high if compared to 5–6 mW/mm^2 used by Ishizuka et al. (2006) and Ernst et al. (2008) and the maximum (around 20 mW/mm^2) used in Nikolic et al. (2009).

ChR2-TRANSDUCED NEURONAL POPULATIONS MODEL

A local neuronal population was modeled as a random network of $N_E = 4000$ excitatory and $N_I = N_E/4 = 1000$ inhibitory conductance-based model neurons of the Wang-Buzsáki (WB) type (Wang and Buzsáki, 1996). The WB model describes a single compartment neuron endowed with sodium and potassium currents. The membrane potential follows the equation:

$$C\frac{dV}{dt} = -I_L - I_{Na} - I_K + I_{\text{syn}} + I_{\text{noise}} + \kappa I_{ChR2} \tag{7}$$

where C is the capacitance of the neuron, $I_L = g_L(V - V_L)$ is the leakage current, I_{syn} reflects recurrent interactions with other neurons in the network, I_{noise} models the driving exerted by background noise and I_{ChR2} is the photocurrent-induced by external light stimulation. Sodium and potassium currents are

Table 1 | Parameters of the ChR2 conductance model.

Type of parameter	Parameter	Value ± *SD* l.sq fit (unit)
Latency	d_A	$0.27 \pm 0.04\,(ms)$
	d_B	$-0.05 \pm 0.06\,(ms/[W_{\text{light}}])$
	d_C	$0.0126 \pm 0.0006\,(ms \times [W_{\text{light}}])$
Activation	$\tau_{\text{act}}^{(0)}$	$0.74 \pm 0.20\,(ms)$
	c_{act}	$12.0 \pm 0.4\,(ms)$
	k_{act}	$25 \pm 2\ (1/[W_{\text{light}}])$
	a_0	1.00 ± 0.04
	$a_{\min}$	0.4 ± 0.1
	$W_{0.5}$	$0.38 \pm 0.15\ ([W_{\text{light}}])$
Inactivation (first component)	$\tau_{\text{inact}}^{(1)}$	$9.06\,(ms)$
	b_0	0.16 ± 0.01
	b_1	$0.013 \pm 0.004\ ([W_{\text{light}}]^2)$
	b_2	$0.027 \pm 0.007\ ([W_{\text{light}}]^2)$
	W_{inact}	$0.11 \pm 0.01\ ([W_{\text{light}}])$
Inactivation (second component)	$\tau_{\text{inact}}^{(2)}$	$59.6\ (ms)$
	c_{inact}	0.29
	k_{inact}	$2.4\ (1/[W_{\text{light}}])$
Deactivation	τ_{off}	10 (ms)
Coupling prefactor	g_{ChR2}	$0.007\ (\mu S)$

Parameters to simulate time and light-intensity dependent conductance changes mediated by channelrhodopsin 2. Errors are sample standard deviations. Parameters returned from the global fit procedure do not have a measure of uncertainty. See section Materials and methods for the model description.

voltage-dependent and given by $I_{Na} = g_{Na} m_\infty^3 h(V - V_{Na})$ and $I_K = g_K n^4 (V - V_K)$. The activation of the sodium current was modeled as instantaneous. We used sodium and potassium current voltage-dependent activation and inactivation functions as given in Wang and Buzsáki (1996).

The synaptic current evoked by a single presynaptic action potential was given by $I_{\text{spike}}(t) = -g_\alpha s_{\text{spike}}(t)(V - V_\alpha)$, where the reversal potential V_α of the synapse is 0 mV for excitatory AMPA synapses ($\alpha = E$) and −80 mV for inhibitory GABA synapses ($\alpha = I$). The time-course of the postsynaptic conductance was described as a difference of exponentials:

$$s_{\text{spike}}(t) \propto \left(e^{-(t + d_{\text{syn}} - t_{\text{spike}})/\tau_{\text{rise}}} - e^{-(t + d_{\text{syn}} - t_{\text{spike}})\tau_{\text{decay}}}\right) \quad (8)$$

for $t > t_{\text{spike}}$, 0 otherwise, where t_{spike} is the time of the presynaptic spike, d_{syn} is a combined conduction and synaptic delay, and τ_{rise} and τ_{decay} are respectively the rise- and decay time constants. The normalization constant of $s_{\text{spike}}(t)$ was chosen such that its peak value is equal to 1. The peak conductances of all excitatory and inhibitory synapses were set to g_E and g_I, respectively. The total recurrent current $I_{\text{syn}}(t)$ was then given by the sum of the contributions $I_{\text{spike}}(t)$ from all presynaptic spikes fired before time t.

The background noise input I_{noise} to each neuron was modeled as an additional synaptic current-induced by statistically independent Poisson trains of excitatory spikes with a common firing rate ν_{noise} and a peak conductance g_{noise}.

Excitatory and inhibitory neurons in the populations were transduced by ChR2 with a same probability, given by the transduction rate P_{ChR2}. The photocurrent prefactor κ was set to 1 and 0 respectively for transduced and non-transduced neurons. The induced photocurrent was given by $I_{ChR2}(t) = -g_{ChR2} F_{ChR2}\left[W_{\text{light}}(t)\right](V - V_{ChR2})$. The conductance waveform $F_{ChR2}(t)$ given by Equation (1)—that depends on the applied waveform $W_{\text{light}}(t)$ of the optical stimulation—was multiplied by a prefactor g_{ChR2}, such that the peak photocurrent evoked by a pulse with optimal light intensity in the used model neurons (simulated at resting potential) was 2 nA . The reversal potential was $V_{ChR2} \cong 0$.

Excitatory neurons established synapses with other excitatory or inhibitory neurons within the same local circuit with probability P_E, inhibitory neurons with probability P_I. In addition, when considering multiple interconnected local areas, excitatory neurons within a local circuit established long-range connections with excitatory or inhibitory neurons in a remote local area with a probability $P_E^{(lr)}$.

ADOPTED PARAMETERS AND OSCILLATORY SYNCHRONY

The neuronal population model described in the previous section can generate two qualitatively different dynamical regimes, characterized by different degrees of oscillatory coherence. The network resides in one or the other regime depending both on the drive to the network, controlled in this study by varying the background firing rate ν_{noise}, and on the strength of local inhibitory interactions, controlled in this study by varying the probability of inhibitory connection P_I.

The single neuron and network parameters used for all simulations are summarized in **Table 2**. However, we note that qualitatively similar dynamical features, in particular the existence of a smooth transition between a weakly and a strongly synchronous oscillatory regime, would be obtained for a broad range of parameters, with the frequency of the collective oscillation primarily determined by the synaptic time constants, τ_{rise} and τ_{decay}, (Brunel and Wang, 2003). We also find that the transition toward strong synchrony tends to get sharper with increasing network size [not shown, but see as well (Brunel and Hakim, 1999)].

Synchronization of the population activity was quantified through the synchronization index χ (Golomb and Hansel, 2000):

$$\chi = \frac{\sigma_{\text{LFP}}^2}{\langle \sigma_{V_i}^2 \rangle} \quad (9)$$

given by the ratio between the variance of the average membrane potential of all excitatory and inhibitory neurons in the local population—here briefly defined conventionally as the "LFP" signal—and the average variance of the membrane potentials

Table 2 | Parameters of the spiking neuronal network model.

Type of parameter	Parameter	Value (unit)
Single neuron	g_L	0.01 (μS)
	V_L	−65 (mV)
	C	100 (pF)
	g_{Na}	3.5 (μS)
	V_{Na}	55 (mV)
	g_k	0.9 (μS)
	V_k	−90 (mV)
	m_∞, h, n	See Wang and Buzsáki (1996)
Population size	N_E	4000
	N_I	1000
Excitatory synapses	τ_{rise}	1 (ms)
	τ_{decay}	3 (ms)
	g_E	0.5 (μS)
Inhibitory synapses	τ_{rise}	1 (ms)
	τ_{decay}	4 (ms)
	g_I	18 (μS)
Synaptic latencies	d_{syn} (local)	1.5 (ms)
	d_{syn} (long-range)	1.0 (ms)
Connection probabilities	P_I	0.3
	P_E	0.12
	$P_E^{(lr)}$	0.06
Background noise	ν_{noise}	3 (kHz)
	g_{noise}	0.5 (μS)

Parameters to simulate the activity of transduced neuronal populations (see section Materials and methods for the model description).

V_i of individual neurons in the population. The synchronization index χ is bounded in the unit range, $\chi = 0$ meaning asynchronous and $\chi = 1$ fully synchronous dynamics.

The dependency of firing rate of excitatory and inhibitory neurons, of the collective oscillation frequency and of the synchrony level χ was studied by systematically varying the parameters ν_{noise} in the range between 2 and 6 kHz and P_I between 0.2 and 0.6 (the reference values, tabulated in **Table 2**, being $\nu_{\text{noise}} = 3$ kHz and $P_I = 0.3$). All the quantities were evaluated over simulated time-series lasting 20 s of real time.

ANALYSIS OF PHASE RESPONSE

Although the simulation generates spike trains for all neurons, we focus here on alterations of the ongoing collective activity and, therefore, on the oscillating LFP signal. A single rectangular-shaped light pulse with a given intensity W_{light} and duration T_{light} was applied to the considered network at a specific time of application t_{ON}. For different values of W_{light} and T_{light}, we tested the effects of overall 1500 different light onset times t_{ON}, distributed uniformly over a time interval of approximately 50 oscillation periods. Indeed, averaging over multiple periods was required, because of stochastic fluctuations of the period length. For each stimulation pulse, the activity of the network was further simulated over 60 oscillation cycles following the perturbation.

In every simulation run, the initial conditions, the network topology and the background noise were kept identical, in order to exclusively study the dependence of the induced perturbation on the parameters of the light stimulation and its application time. Pairs of LFP time series were thus generated consisting of a time series after the application of a photostimulation and a time series of the corresponding unperturbed neural dynamics. For every such pair of time series, instantaneous phase values were extracted using a Hilbert transform (Gabor, 1946), an approach extensively used for investigating phase dynamics and synchronization of non-linear oscillators (Pikovsky et al., 2001). The induced phase shift was then measured by averaging the phase difference $\Delta\phi$ between the perturbed and the unperturbed LFPs over the last 50 recorded oscillation cycles. A transient of 10 oscillation cycles immediately following t_{ON} was discarded to ignore transient effects caused by the applied light pulse. The times of perturbation application t_{ON} were translated into phases and binned into 30 equally sized phase bins. The observed phase shifts $\Delta\phi$ were averaged over each bin and plotted as a function of the phase of perturbation application $\phi(t_{\text{ON}})$ for different light intensities W_{light} and perturbation pulse duration T_{light}, and also for networks with different transfection rates P_{ChR2}.

The dependency of phase responses on varying values of light intensity, pulse duration and timing of the perturbation were investigated for a specific realization of the network random connectivity. We have repeated our analysis for three different random realizations of connectivity (with the same homogeneous probabilities of connection, P_I and P_E). The corresponding phase responses to light stimuli were qualitatively and quantitatively very similar (not shown). In particular, differences between random network instances were of the same order of magnitude as the error bars shown in **Figure 4**, corresponding to fluctuations of the phase response over time for a same connectivity realization. These similarities are not surprising and match theoretical expectations, since dynamical effects arising from fluctuations due to finite-size connectivity are small for the large network size adopted here (Golomb and Hansel, 2000). Therefore, we can conclude that our results hold in general for random networks with the same (in a probabilistic sense) connectivity features.

ANALYSIS OF PHASE LOCKING CHANGES

If two coupled neuronal populations are simulated with the parameters given in **Table 2**, the oscillations of the two LFPs self-organize in a phase-locked configuration. The temporarily stable relative phase difference, $\Delta\phi$, can have two different values: $\Delta\phi_{\text{locked}}$ or $1 - \Delta\phi_{\text{locked}}$ (phases are measured over the cyclic unit interval $0 \leq \phi \leq 1$). Both phase-locking values correspond to out-of-phase configurations in which either of the two populations leads in phase over the other.

In our simulations, only one of the two local neuronal populations was transduced with ChR2. We applied light stimulation pulses to this transduced population, with a light intensity $W_{\text{light}} = 20\%$ (expressed as the percentage of the maximum possible light intensity of our setup W_{max}) and a pulse duration of $T_{\text{light}} = 3$ ms. Similar to the protocol used for the phase response analysis of a single population, 1500 different pulse onset times, t_{ON}, were used, which were uniformly distributed over 50 oscillation cycles. Starting from random initial conditions, no perturbation was applied for the first 100 oscillation cycles, to ensure complete convergence to a stable phase-locked attractor. Without loss of generality, we considered the configuration in which the phase of the transduced population leads over that of the not transduced population (i.e., in which the stable inter-circuit phase difference is close to $\Delta\phi_{\mathrm{locked}}$ before the perturbation).

Variations of the phase-difference between the two populations were measured in two different time-windows. We first studied the short-term effects of the light stimulation, by averaging the instantaneous Hilbert phase difference over the first 5 oscillation cycles after the perturbation. Binning different onset times according to the corresponding phase of application of the perturbation (as done for the estimation of single population phase response), we quantified the probability $P_{\mathrm{shifting}}(\phi)$, that a light pulse induces a relative variation of more than 10% (reduction or increase) of the inter-population phase-difference. For each application phase bin, $P_{\mathrm{shifting}}(\phi)$ was compared with the probability of observing similarly large spontaneous fluctuations of $\Delta\phi$ in the unperturbed activity of the same network.

We then studied longer term effects of the light stimulation by averaging the difference of the instantaneous Hilbert phases over the 50 cycles that follow the ten omitted oscillation cycles directly after stimulation. The aim of this long-term analysis was to assess the occurrence of a switching from the phase-locking pattern with phase-difference close to $\Delta\phi_{\mathrm{locked}}$ toward the other phase-locking pattern with phase difference close to 1-$\Delta\phi_{\mathrm{locked}}$. Once again binning onset times according to the corresponding phase of perturbation application, we quantified the probability $P_{\mathrm{switching}}(\phi)$ that the long-term averaged phase difference was within a tolerance interval of $1 - \Delta\phi_{\mathrm{locked}} \pm \delta$, with $\delta = 0.05$ (i.e., the transduced population switched steadily from the role of phase leader to phase laggard). For each phase bin, $P_{\mathrm{switching}}(\phi)$ was compared to the probability of observing a spontaneous switching of the phase locking (from $\Delta\phi_{\mathrm{locked}}$ to 1-$\Delta\phi_{\mathrm{locked}}$) over an equivalent time span of 50 cycles, based on time-series of the unperturbed dynamics of the same network.

The probabilities $P_{\mathrm{shifting}}(\phi)$ and $P_{\mathrm{switching}}(\phi)$ were finally plotted as polar histograms with ten equally-spaced bins for the phase of the onset of the light stimulation $\phi(t_{\mathrm{ON}})$, in which the corresponding probabilities of spontaneous shifting or switching were also reported in order to identify phase bins in which the effects induced by the perturbation pulse were significantly low or high (**Figure 5**).

ONLINE PHASE PREDICTION

A closed-loop approach (**Figure 6**) is necessary to estimate a time t_{ON} which corresponds to a future occurrence of a given target phase ϕ_{target}, leading to the largest possible probability of switching of the inter-areal locking (**Figure 5**).

To study the feasibility of such an approach, we modeled its implementation, considering the same bi-areal network used to characterize induced switching between phase-locked states (see previous section and **Figure 5**). Simulated LFPs were recorded from both the stimulation target area and a second coupled area. However, the calculations performed online involved only the LFP time-series $V(t)$ recorded in the target area. The time-series $\tilde{V}(t)$ of the second area were recorded and analyzed offline to determine phase-locking patterns before and after the stimulation.

We approximated the "true" Hilbert phase $\phi_H(t)$ associated to $V(t)$ by a linearly interpolated phase. This approximation could be simply done by interpolating a variable $\phi_L(t)$that was linearly growing in the unit interval $0 \leq \phi_L < 1$ between any two times t_k and t_{k+1} delimiting an oscillation cycle. As shown by **Figure 7B**, the phase variables $\phi_H(t)$ and $\phi_L(t)$ are related by a mildly non-linear map, described as a static non-linearity $\phi_H = f_{LH}(\phi_L)$. However, we systematically ignored this non-linearity in the following by approximating $\phi_H(t)$ directly by $\phi_L(t)$.

The workflow for the prediction of the perturbation onset time t_{ON} is split up into multiple stages (**Figure 6**). First of all, it was necessary, during a *testing stage*, to detect the presence of sufficiently strong local oscillations and to measure their average frequency f_{peak}. It was important to monitor the characteristics of LFP oscillations (band-passed around f_{peak}) in the stimulation target area (*monitoring stage*) and to extract, based on observations of past activity, a model able to approximately predict future phase evolution (*prediction stage*).

Even in the ideal case of an elevated synchrony index χ and sustained oscillations, the duration of oscillation periods T_i fluctuated from cycle-to-cycle around their average $\bar{T}$(cf. **Figure 7A**). Let us suppose that the last oscillation period recorded in the monitoring stage was $T_k = t_k - t_{k-1}$ and that the prediction stage lasts (less than) s oscillation cycles. Neglecting correlations between period lengths of consecutive cycles, the time of beginning of the next cycle after the end of the prediction stage could be estimated via a simple *linear extrapolation*:

$$t^{(0)}_{k+s} = t_k + s\bar{T} \tag{10}$$

However, for our network model, the temporal autocorrelation function of period lengths T_i, $i = 1, \ldots, k$ displayed a fast but not instantaneous decay for increasing lags (measured in oscillation cycles). These weak, positive correlations between consecutive cycle durations could be well captured by a *first order autoregressive process* [AR(1)], $T_i = \bar{T} + a(T_{i-1} - \bar{T}) + \epsilon_i$, with $\bar{T}$ the average oscillation period over the monitoring time-window, a the AR(1) coefficient and $_i$ an i.i.d. Gaussian distributed residual noise term (Brockwell and Davis, 1996). With this AR(1) model, the beginning of the next cycle was estimated as:

$$t^{(1)}_{k+s} = t_k + s\bar{T} + \left(\frac{a^{s+1} - a}{a-1}\right) \cdot T_k \tag{11}$$

The AR(1) coefficient was derived as:

$$a = \frac{k}{k-1} \frac{\sum_{i=1}^{k-1}\left(T_i - \bar{T}\right)\left(T_{i+1} - \bar{T}\right)}{\sum_{i=1}^{k}\left(T_i - \bar{T}\right)^2} \tag{12}$$

based on the periods T_i, $i = 1, \ldots, k$, measured during the monitoring stage and on their average duration $\bar{T}$.

Spectral analysis of LFPs recorded in the stimulation target area and in a second coupled area was performed during the testing stage. A windowed Fast Fourier Transform (FFT) was applied to demeaned chunks of the LFP signal, to extract a rough estimate of the instantaneous power spectrum. When the power at some frequency f_{peak} in the gamma range exceeded a determined threshold in both recorded areas, the monitoring stage started.

During the monitoring stage, a computationally efficient low-order recursive time domain filter (Percival and Walden, 1993) was applied to clean the oscillating LFP signals. The filtered time-series was computed online as:

$$V_{\text{filtered}}(t) = V(t) + \alpha_1 V_{\text{filtered}}(t-1) + \alpha_2 V_{\text{filtered}}(t-2) \quad (13)$$

Filter coefficients were chosen as $\alpha_2 = -0.99$ and $\alpha_1 = 4\alpha_2 \cos(2\pi(1-f_{\text{peak}}))/(1-\alpha_2)$ (assuming a sampling rate of 1 kHz). The pass frequency was then equal to f_{peak} and the main frequency of the activity of recorded areas was maintained. The LFP time-series $V(t)$ and $\tilde{V}(t)$ recorded during the monitoring stage were stored. An analysis of the inter-areal phase-locking pattern before stimulation was then performed offline, while the closed-loop experiment was continuing. A monitoring stage including approximately 20 oscillation cycles was found to be sufficiently long to achieve accurate model estimation.

The limited amount of fast computations to be performed during the prediction stage is summarized as follows:

1. Subtract the mean value from the band-passed LFP time series $V_{\text{filtered}}(t)$ measured during the monitoring window in the stimulation target area.
2. Calculate the timings $t_0, t_1, \ldots, t_k$ at which the LFP $V_{\text{filtered}}(t)$ crosses zero. Their differences $T_i = t_i - t_{i-1}, i = 1, \ldots, k$ are the estimated period lengths of the observed oscillations.
3. Calculate the average period length $\bar{T}$ from the series of T_i.
4. If the AR(1) approach is used, then compute the a coefficient based on equation (12) and compute the perturbation onset time as $t_{\text{ON}}^{(1)} = t_{k+s}^{(1)} + \phi_{\text{target}}\bar{T}$, where $t_{k+s}^{(1)}$ is given by Equation (11).
5. If a simpler linear extrapolation is used, compute the perturbation onset time directly as $t_{\text{ON}}^{(0)} = t_{k+s}^{(0)} + \phi_{\text{target}}\bar{T}$, where $t_{k+s}^{(0)}$ is given by Equation (10).

After the application of the perturbation pulse, the LFPs of both areas were recorded and stored. An analysis of the inter-areal phase-locking pattern after stimulation was then performed offline and compared to the phase-locking assessed before stimulation. In case of failed switching, either the same linear model was used to extrapolate directly the time t_{ON} of a further stimulation pulse, or a new testing stage was initiated, verifying that oscillations were still ongoing or waiting for the next oscillatory epoch to begin.

The decision between a prediction scheme based on the AR(1) model and a simpler linear extrapolation scheme depends ultimately on the correlation statistics of the series of period lengths. It can be shown that the prediction error of the estimated phase is reduced by the AR(1) prediction scheme compared to linear extrapolation by a maximal amount of $100\%/\sqrt{1-a^2}$ (and by exactly this amount for Gaussian distributed samples). If the AR(1) parameter a estimated from the recordings during the monitoring window is small (as a rule of thumb, $a < 0.3$), then the performance improvement is negligible and advantage can be taken from the faster computation of the simpler linear extrapolation. Unfortunately, this criterion requires the evaluation of a. Nevertheless, the analysis of **Figure 7E** indirectly suggests that the AR(1) coefficient depends non-monotonically on the synchrony level, and that it increases going from low to intermediate synchrony indices χ, but drops again going toward higher χ. The choice of a high power threshold during the testing stage guarantees a high level of synchrony and, therefore, small values of a during the monitoring stage. This allows one to adopt the computationally faster step (5) instead of (4). However, a tradeoff should be made between the need of a fast prediction and the probability to detect a number of oscillatory epochs sufficient for meeting the testing stage criteria.

RESULTS

DATA-CONSTRAINED MODEL OF ChR2-PHOTOCURRENT

In order to assess from *in silico* experiments the efficacy of optogenetic stimulation in inducing changes of local phase or of inter-areal phase relations, we first derived a realistic and fully data-constrained model of the evoked ChR2 conductance. To do so, we first performed an experimental characterization of photocurrents evoked in living cells *in vitro* by light stimulation over a broad range of light intensities spanning two decades of power (see section Materials and Methods). Then, based on this systematic set of measurements, we fitted to the whole dataset a unique conductance-based model that describes the evoked time-dependent photocurrent, and hence the conductance, as the product of activation and inactivation factors.

The light-activated ChR2 ion channel mediates a current that is carried mostly by Na^+, K^+, and H^+ with contributions of Ca^{2+}. Its reversal potential is typically around 0 mV and therefore it is depolarizing at neuronal resting potential. We found that upon illumination onset, a current built up with a nearly exponential time course with a time constant τ_{act} ranging from 10 ms, for very weak light intensities that barely evoked any current response, to below 1 ms for high intensities. For a large range of intensities the current displayed a transient behavior and its amplitude, after reaching a peak, decayed over tens of milliseconds to reach a plateau. This inactivation behavior was biphasic and its time constants were not dependent on light intensity, unlike the activation time constant. Finally, when the light was switched off, the current decayed back to baseline with a time course that was well described by a single exponential with a 10 ms time constant.

Figure 1A depicts inward currents induced by a light pulse of moderate intensity (approximately 3 mW/mm^2 for 10 ms) in a cultured hippocampal neuron transduced with ChR2. Even such a weak light pulse was able to elicit an action current, as the axon escaped the voltage-clamp (**Figure 1A**, black line). The ChR2 photocurrent could be isolated, by blocking Na-channels with tetrodotoxin (**Figure 1A**, red line).

To achieve an improved characterization of the photocurrent time-course, we systematically analyzed recordings over (non-spiking) transfected kidney cells (**Figure 1B**) using a very large range of light power densities for the characterization of ChR2 activation and inactivation kinetics. We found that the peak and steady state photocurrent do not increase monotonically with light power density. A maximal peak current is achieved around 10–20% of the maximum power density (see section Discussion). For applications, where such power densities can be attained, for instance with a laser or a strongly focused LED, a careful tuning of the applied light intensity could thus potentially reduce the minimum transduction rate needed to efficiently drive the local oscillations in a target area.

As detailed in section Materials and Methods, it was possible to capture the time-course of the evoked ChR2 current with a single conductance-based model with light-dependent parameters. The simulated photocurrents generated by the model in response to a single square pulse of light lasting 3 ms are shown in **Figure 1C** for various light intensities (corresponding to the typical short pulse length used in the simulations of next sections). As evident from **Figure 1C**, our data-constrained model was able to capture the non-monotonic dependence of peak photocurrent on the light intensity, leading to the largest peak photocurrent for a light intensity of approximately 18% the largest deliverable intensity $W_{\max}$.

SPIKING NETWORK MODELS OF TRANSDUCED OSCILLATING AREAS

To study the response to light stimulation of systems involving transfected neuronal areas, we simulated the activity of simple canonic circuits composed of just one local area or of two local areas mutually coupled with equal strength. Each area was modeled as a large network of randomly interconnected excitatory and inhibitory neurons. As shown in **Figure 2A**, a fraction of these excitatory and inhibitory model neurons were equipped with ChR2 photoconductances, inducing depolarization in response to simulated light stimulation.

For most of the analyses reported in this study, we adopted within each local area strong and delayed inhibition and a sufficiently strong background drive (see **Table 2**). With such a choice of parameters, local circuits underwent—through an "ING"-type (i.e., "interneuron-generated") mechanism (Whittington et al., 2000; Brunel and Wang, 2003; Brunel and Hansel, 2006; Tiesinga and Sejnowski, 2009) a marked and persistent oscillatory activity, well visible in the traces of a LFP-like signal. The collective frequency of oscillation was in the gamma range. Since driving was provided by background Poisson noise, the spiking activity of individual neurons was very irregular and characterized by a weaker firing rate (cf. **Figure 2B**). Weak pairwise correlations between spike trains coexisted thus with stronger pairwise correlations between membrane potential fluctuations (Yu and Ferster, 2010; Battaglia and Hansel, 2011). While inhibitory connections were confined within each local area, excitatory neurons could additionally establish long-range connections between distant local areas (**Figure 5A**). In this case, the gamma oscillations generated by each local circuit were set into one of many possible multistable phase-locked states (**Figure 5B**).

The dynamical features of the simulated neural activity, including in particular its degree of oscillatory synchrony, depended sensibly on the noisy drive to the network and on the strength of local inhibition. For increased drive intensity and/or stronger inhibitory interactions, a smooth transition occurred toward a dynamic regime characterized by elevated collective synchronization (**Figure 3A**). In this synchronous regime, the frequencies of the network oscillation were in the gamma range, varying between 40 and 70 Hz (**Figure 3B**), while the average firing rate of individual excitatory neurons varied between 1 and 3 Hz (**Figure 3C**) and of inhibitory neurons between 2 and 7 Hz (**Figure 3D**).

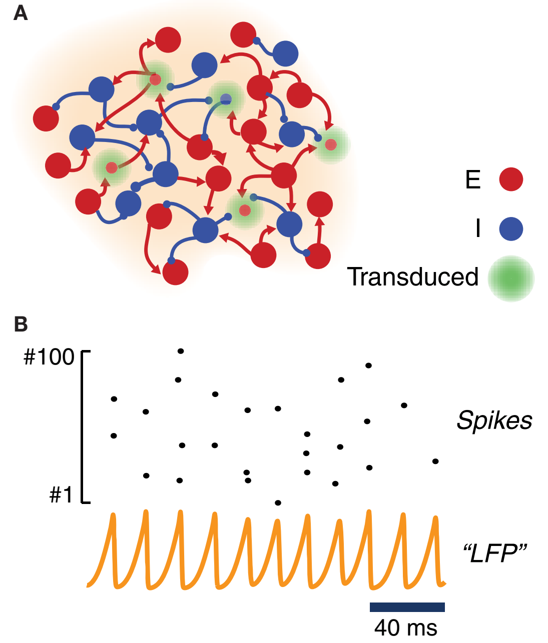

FIGURE 2 | Model of a ChR2-transduced population. (A) Graphic cartoon of a randomly-connected network of inhibitory and excitatory spiking neurons. In order to model the effects of local ChR2 transduction a variable fraction of the neurons is endowed with a ChR2 photoconductance. **(B)** Sample activity from the local circuit model of panel **(A)**. Due to strong and delayed recurrent mutual inhibition, the network undergoes a collective oscillatory activity with a frequency in the gamma range. Even when oscillations at the population level are very regular (see an example "LFP"—i.e., average membrane potential—time series), individual neurons spike very irregularly with a much lower firing rate (see raster plot of the activity of 100 excitatory neurons).

Starting from a very wide range of parameters including the probability of inhibitory connections and the strength of the external driving force (**Figure 3**), oscillatory synchrony can be robustly boosted by enhancing the external drive to the network. Qualitatively reproducing existing experimental findings (Adesnik and Scanziani, 2010; Akam et al., 2012), our simulations showed that slowly ramping or constant low-intensity optogenetic stimulation can be used to "switch on" a markedly oscillatory behavior. As shown by **Figure 3E** a network with poorly synchronous activity can be optogenetically driven toward higher oscillatory synchrony, as evident not only from LFP spectrograms but also visually from LFP traces.

In the following, we will mainly consider model networks tuned to generate strong LFP gamma oscillations. However, such

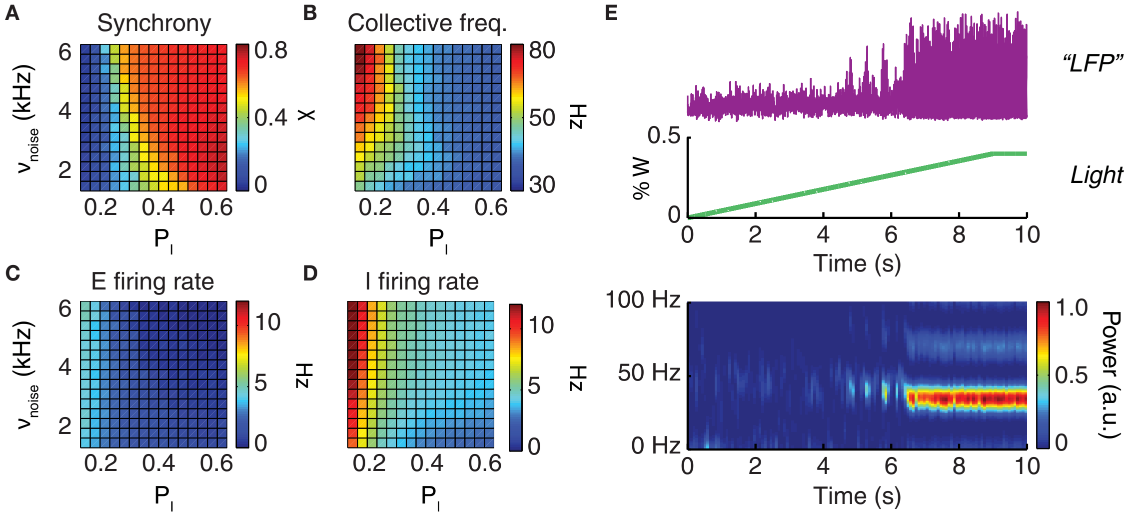

FIGURE 3 | Driving the network toward coherent oscillations. The dynamical regime of a neuronal population depends on the strength of local inhibition (parameterized by the probability p_I of inhibitory connections) and on the strength of an external driving force (parameterized by the rate ν_{noise} of background inputs). Shown are the synchronization index **(A)** which has values in the unit interval (0 corresponds to asynchronous and 1 to perfectly synchronous dynamics); the oscillation frequency of collective activity **(B)**; and the average firing rates of excitatory **(C)** and inhibitory **(D)** neurons. All four quantities are presented in their dependence on the probability of inhibitory connections, P_I, and the rate of background noise input, ν_{noise}. **(E)** Constant or slowly ramping optogenetic stimulation increases the external drive to a neuronal population. This results in intensified collective oscillations and enhanced synchronization at the population level. From top to bottom: LFP time-series (purple) observed during a slowly ramping photostimulation (green); the associated spectrogram (graph at the bottom) indicates the development of highly coherent gamma oscillations as an effect of continuous photostimulation.

a choice is not an arbitrary restriction. Indeed, high synchrony regimes—either spontaneously emergent or induced artificially by continuous photostimulation—are particularly suited for analyses of phase shifting and locking.

SHIFTING THE PHASE OF AN ONGOING LOCAL OSCILLATION

It is well known that the effect of a perturbation to an oscillating system depends on the phase at which the perturbation is applied (Pikovsky et al., 2001). To explore the phase dependency of light stimulation, we applied simulated stimulation pulses with different durations T_{light} to local populations with different transduction rates P_{ChR2} (**Figure 4**). Light intensity was always set to the optimum value of $W_{light} = 18\%\ W_{max}$, which led to maximum evoked peak photocurrents.

For all the explored conditions, we always found strongest effects on the phase of an ongoing oscillation when the perturbation was applied at a phase half-way between the trough and the peak of the collective population oscillation (**Figure 4B**). In this case the phase of the perturbed oscillation was advanced with respect to the unperturbed case (**Figures 4C,D**). Short pulses lasting 1 or 3 ms led only to phase advance effects. As shown in **Figure 4C**, phase advances of the order of one quarter of a cycle could be achieved using such short pulses, over a very wide range of transduction rates, going from very high (100%) down to moderate (25%). Noticeable phase advance effects (although reduced to just one tenth of a cycle) could even be detected for transduction rates as low as 5%.

As displayed by **Figure 4D**, longer stimulation durations also led to phase lagging effects. These effects occurred in different ranges of perturbation application phases than for phase advancing effects. However, phase lagging effects were always weaker than phase advancing effects. For instance, for a transduction rate of 25%, pulses lasting 10 ms could induce phase advances of over a quarter of cycle, but only phase laggings of less than one tenth of cycle.

The positive peaks of the *phase response curves* (PRCs) plotted in **Figures 4C,D** were aligned across all conditions. The strongest phase shifting effects were always observed when the perturbation was applied in proximity of the phase $\phi = 0.17$. We also mention that for the short stimulation duration used, the evoked photocurrent was dominated by the fast activation time-course. Inactivation played no role in determining the response. As a matter of fact, the effect of the fast initial rise of the photocurrent was to evoke a spike in the transduced neurons, as in panel 1A, and additional synchronous spikes evoked in a subpopulation of cells were the dynamic cause of the induced phase shift, as in Battaglia et al. (2012).

PERTURBING PHASE RELATIONS BETWEEN DIFFERENT OSCILLATING POPULATIONS

After the controlled shifting of the phase of a local oscillation, we explored whether precisely phased stimulation could be used to manipulate phase relations between different local oscillating circuits. To do so, we considered a canonic circuit of two coupled oscillating areas, interconnected by long-range random excitatory projections (**Figure 5A**). In general, when driven into a synchronous regime, motifs of a few local areas mutually connected with equal strength can give rise to different phase-locked states.

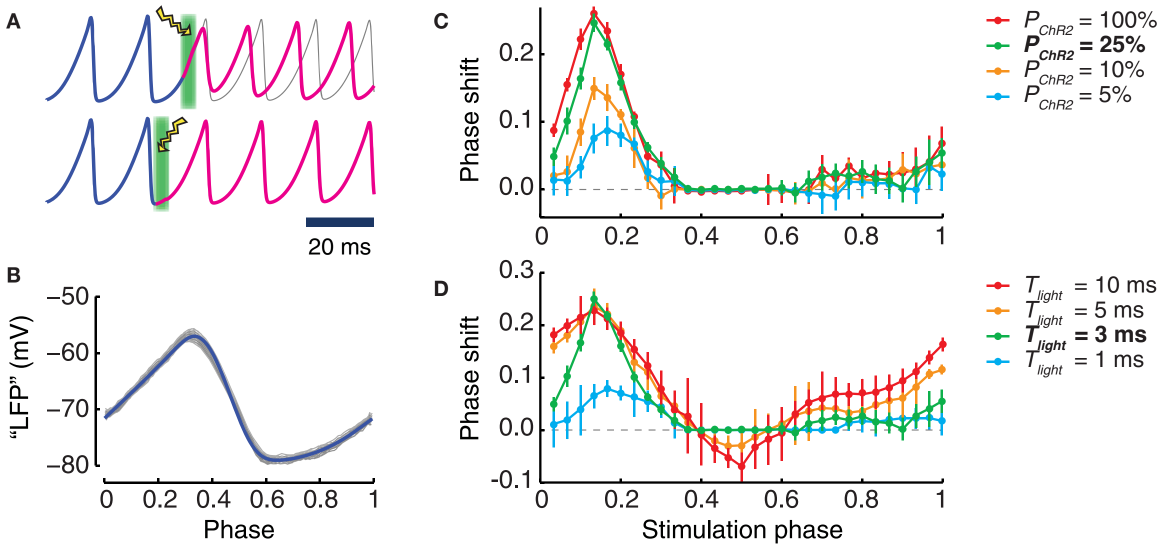

FIGURE 4 | Phase shifts induced by photostimulation. (A) Examples of phase shifts induced by a single light pulse. Top: the phase (blue curve) of the oscillation of the transduced population is shifted by light perturbation (illustrated as a lightning symbol with green background) and, afterwards (magenta curve), remains advanced with respect to the unperturbed oscillation (gray curve). Bottom: such a phase shift cannot be seen when the timing of the light perturbation corresponds to other differently chosen oscillation phases. **(B)** Waveform of the oscillating LFP in dependence on the Hilbert phase. Shown are 500 oscillation cycles (gray) of a LFP and their average waveform (blue). By our conventions, the phase ranges in the unit interval. The maximum of the LFP is obtained for (Hilbert) phase values close to 0.3 while the minimum occurs for phase values close to 0.6. **(C,D)** phase shifts caused by light pulses applied at different (Hilbert) phases of the ongoing LFP oscillation. An optimal light intensity of 18% $W_{\max}$ is used. **(C)** Dependence of the phase shift on the transduction rate P_{ChR2} of the population (for a stimulus duration $T_{\text{light}} = 3$ ms). **(D)** Dependence of the phase shift on the stimulus duration T_{light} (for a fixed transduction rate of $P_{ChR2} = 25\%$). Bold characters in the legend denote the "reference" phase shift, i.e., $P_{ChR2} = 25\%$ and $T_{\text{light}} = 3$ ms of stimulus duration (green curves). In panels **(C)** and **(D)**, error bars are standard deviation of the phase shifts obtained for different perturbations applied in a same time-bin.

These states are associated to different patterns of inter-areal phase relations, which are maintained in a relatively stable manner over long time intervals (Battaglia et al., 2007, 2012).

The specific bi-areal network of **Figure 5A** generated two multi-stable phase-locked states. In the unperturbed system, background noise caused spontaneous switching between these two states (i.e., from one configuration of inter-areal phase relations to another). The result of these stochastic fluctuations was a clearly bimodal distribution of the instantaneous phase difference between the two areas (**Figure 5B**). The actual phase relations in the phase-locked modes depend ultimately on the PRC of the coupled populations. As discussed in Battaglia et al. (2007, 2012), the PRCs associated to our network model are such that they lead to *out-of-phase* locking for sufficiently strong inhibition (unless long-range synaptic delays are tuned *ad-hoc* within narrow intervals associated to in- or anti-phase configurations). Out-of-phase locking is found also in more general systems of pulse-coupled neurons (or neuronal masses) under certain conditions on synaptic delays (Woodman and Canavier, 2011; Wang et al., 2012).

In out-of-phase locked modes, it is always possible to identify one area (leader) whose oscillations lead in phase over the oscillations of the other area (laggard). This leads to anisotropic directed functional influences between local circuits (Battaglia et al., 2012), in agreement with the communication-through-coherence hypothesis (Fries, 2005), despite the fact that inter-areal connections are reciprocal and of equal strength in both directions. Switching between alternative phase-locking configurations would thus correspond to changes in the dominant direction of inter-areal functional influences. Spontaneous switching was a relatively rare event in the high synchrony regime explored here (the average waiting time for spontaneous switching was over 60 periods). Nevertheless, optogenetic stimulation could be used to actively trigger switching events (**Figure 5C**).

Inter-areal phase relations after the application of a single perturbation pulse were compared to the average locked phase difference before the pulse itself. We studied how both transient short-term and persistent long-term effects depend on the phase of perturbation onset. **Figure 5D** shows the probability that the average inter-areal phase difference for the five cycles directly following the perturbation has increased or reduced by at least 10% relative to the average phase difference prior to the perturbation. For a wide range of phases of stimulation onset, such probability was larger than 50% and remarkably larger than the level accounted for by spontaneous fluctuations of the inter-areal phase difference.

The dependency on the perturbation phase was more pronounced for long-term effects. **Figure 5E** shows the probability of a switch in phase locking, i.e., that the average inter-areal phase difference over a long time window beginning ten cycles after the perturbation has changed its sign (note, indeed, that the two phase-locked configurations of the simulated bi-areal motif are characterized by average phase-differences of $\Delta\phi = \pm\Delta\phi_{\text{locked}}$,

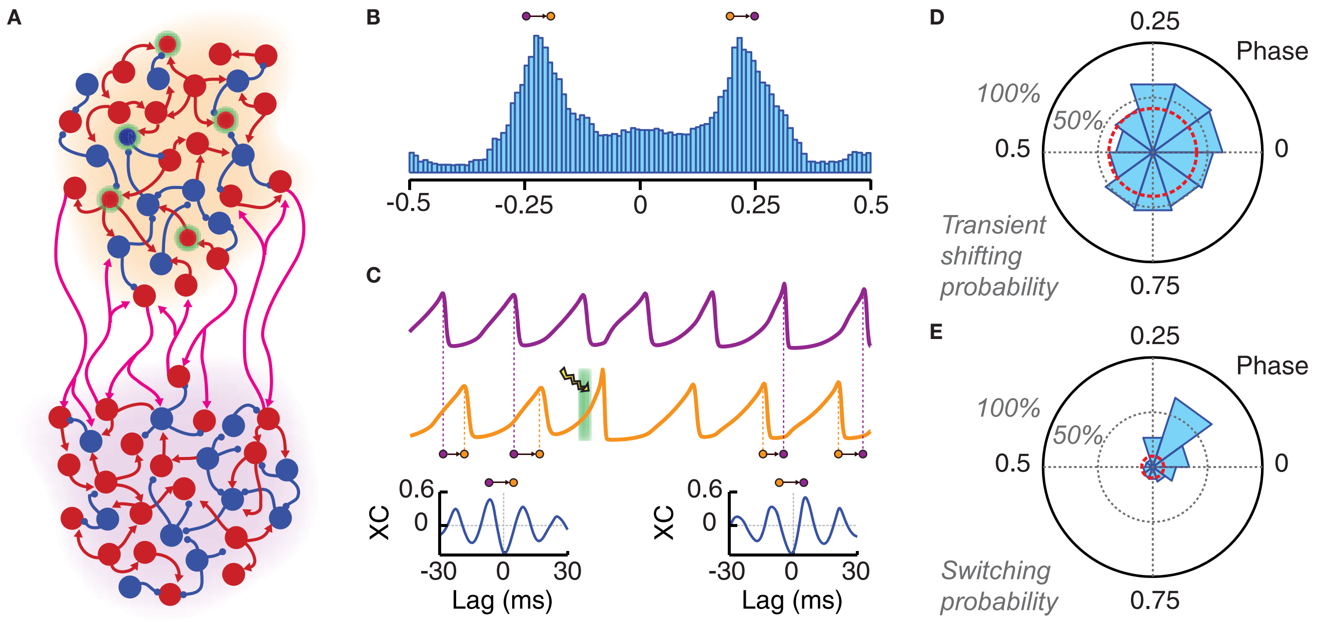

FIGURE 5 | Local photostimulation can reorganize long-range phase-locking patterns. (A) Cartoon of two local populations (each of them with an individual background color: orange and violet) coupled by long-range excitatory connections. **(B)** Both populations oscillate in a non-regular way but with the same main frequency. A histogram of the instantaneous phase difference is shown for a pair of very long LFP time series (over 50,000 oscillation cycles). This distribution is clearly bimodal, indicating the existence of two favorite modes of approximate out-of-phase locking (with the orange population leading in phase over the violet, or the other way around). **(C)** LFP traces of two phase-locked populations. The application of a light pulse stimulation (denoted by a green background and a lightning symbol) can induce switching to another phase-locked mode. This is shown by the qualitative changes between the crosscorrelogram (XC, computed over 500 ms) of the two LFPs before (left) and after (right) light stimulation. Note the changed sign of the lag of the highest XC peak, which corresponds to an inversion of the direction of functional connectivity. **(D)** Probability of changing the average inter-population phase difference of more than 10% during five oscillation cycles after light stimulation ($P_{ChR2} = 25\%$, $T_{\text{light}} = 3$ ms). This probability is presented by a polar histogram in dependence on the phase of the onset of the light stimulation (with respect to the leader population). The red circle indicates the probability of similarly large spontaneous phase shifts (i.e., without photostimulation). **(E)** Phase difference averaged over 50 cycles starting 10 cycles after the light pulse. A switching is considered as successful if the sign of this average phase difference has changed (see panel **B**). The probability of successful phase switching is given by a polar histogram, as in panel **(D)**. The red circle indicates the probability of spontaneous switching in the case of non-stimulated activity. Ignoring transient effects, switching can be induced with high probability only if the perturbation is applied within a specific narrow phase range.

cf. **Figure 5B**). In contrast to short-term shifting, the probability of actual switching was concentrated in a narrow phase interval centered on the peak of the single-area PRC, as expected from theory (Battaglia et al., 2012). The switching probability for other phase bins dropped quickly to the level of spontaneous switching.

Our simulations show that the peak probability of optogenetically-induced switching could rise above 60% even for small transduction rates of 25%. However, this happened only if the phase of the perturbation onset was precisely selected. Indeed, the comparison of **Figures 5D,E** shows that many of the short-term shifting effects observed for randomly phased perturbations did not develop into lasting changes in phase-locking. To conclude, we would like to mention that a similar pulse-induced reorganization of inter-areal phase relations could be achieved even when the perturbation was applied to the laggard rather than to the leader area [not shown, but see (Battaglia et al., 2012)].

CLOSING THE LOOP

As discussed in the last section, the controlled switching of inter-areal phase-locking—and, hence, of functional connectivity—required perturbations optimally phased with respect to ongoing oscillations. To increase the probability to induce switching, the timing of perturbation must thus be determined based on phase information extracted from recordings of the recent population activity. We suggest here a possible closed-loop protocol for the online prediction of the timing of stimulation achieving an optimal switching rate. The workflow of the proposed idealized experiment is outlined by a schematic time bar (**Figure 6A**) and a corresponding flow chart (**Figure 6B**). The potential performance of such protocol was studied by simulating the induction of switching in the bi-areal network of **Figure 5A**.

In contrast to this well behaved *in silico* model, oscillatory coherence *in vivo* or *in vitro* recordings is usually transient and confined to specific epochs. There is nevertheless experimental evidence that epochs of phase synchronization at fast gamma frequencies can persist over several hundreds of ms *in vivo* (Varela et al., 2001; Pesaran et al., 2002; Gregoriou et al., 2009; Bosman et al., 2012; Grothe et al., 2012). Detecting the onset of one of such oscillatory epochs was precisely the aim of the *testing stage*, in which LFPs in both areas of the bi-areal motif were recorded and their spectral characteristics extracted in real-time to verify that LFP power and inter-areal coherence with respect to a common

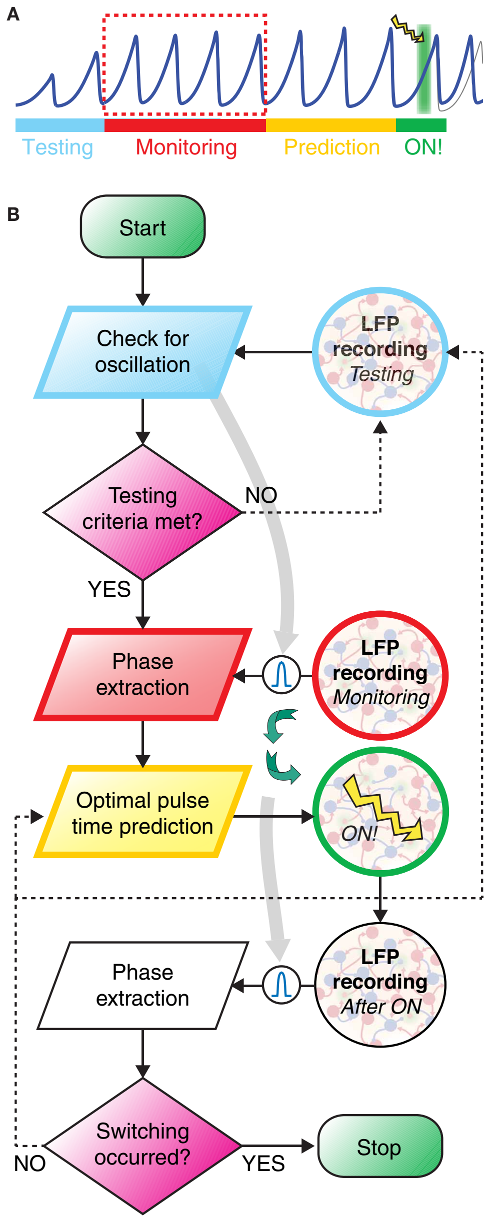

FIGURE 6 | Closed loop strategy for precisely phased photostimulation. (A) Schematic illustration of the proposed experimental protocol. During the *testing stage* (light blue) the LFP is recorded and tested for sufficiently strong power in the gamma-range. If the gamma band power is high enough, then a bandpass-filter is tailored to its peak frequency (light gray arrow). In the *monitoring* stage (red), phases are extracted from the band-passed LFP. Based on these observations, during the *prediction stage* (yellow), lasting only a very few oscillation periods, a linear model of phase evolution is extrapolated to predict the time at which the target phase of the oscillation will occur next. A light pulse is then delivered at this predicted time (green background with lightning symbol). **(B)** The workflow of the closed loop experiment is presented as a flow chart, with the left swim lane presenting computation and decision steps and the right swim lane showing recording and stimulation of the transfected neuronal population. Curved green arrows highlight the closed-loop nature of the workflow, i.e., the light pulse stimulation delivered at a time depending on the phase evolution of LFP oscillations during the monitoring window.

frequency (band) rose above a minimum threshold (see section Materials and Methods).

The *monitoring stage* was entered immediately after the detection of an epoch of reliable inter-areal coherence. During this monitoring stage, LFP signals were recorded, filtered in real time through a low-order band-pass filter with a pass frequency optimized during the testing window and, finally, stored.

A fast online analysis of the phase dynamics of the stored LFP of only the target area was then performed during the following *prediction stage*. Its aim was to predict the timing of one of the next occurrences of the target phase, solely from the phase information acquired during the monitoring stage. To keep the prediction window as short as possible, we propose to use computationally cheap and consequently linear techniques for phase extrapolation. Indeed, the “real” phase values (given by Hilbert Transform of the LFP signal, see section Materials and Methods) and a simple linear descriptor of the phase are strongly correlated (**Figure 7B**) and non-linear effects can be neglected in a first-order approximation.

The phase-locking between LFPs recorded after the stimulation application was finally compared with the locking existing before the stimulation to verify the successful induction of state switching.

Figure 7 analyzes the simulated performance of the proposed protocol, when applied to *in silico* recordings from the bi-areal network motif of **Figure 5**. **Figure 7C** shows how the predicted onset phases of light stimulation concentrate around the actual target phase given by the peak PRC value of $\phi_{\text{target}} = 0.18$. The scattering of predicted phases is computed by hypothesizing prediction stages with different possible (short) durations. This estimate was done with two prediction schemes which both have fast implementations: a simple linear extrapolation based on the average period length and a first-order autoregressive model [AR(1)] (see section Materials and Methods), accounting for correlations between the durations of successive oscillation cycles, at least approximately. For increasing lengths of the prediction window, the median and the average value of the predicted Hilbert phase remained very close to the target (**Figure 7C**). However, the distribution of extrapolated phase values broadened, as indicated by their increasing dispersion. Nevertheless, for a prediction window lasting three oscillation cycles—a sufficiently long time to perform the fast computation required for linear extrapolation (see section Discussion)—the interquartile range of predicted phase values was still contained in the width of the reference PRC. Consequently, we still expect an enhanced effectiveness of light stimulation pulses applied at the inferred time t_{ON}, compared to randomly timed pulses.

The error made in predicting a target phase depends necessarily on the quality of the recorded oscillation. The dynamical regime of the simulations in **Figures 5** and **7C** was strongly synchronous. As previously discussed, the degree of synchrony of the collective response depends on the external driving force to the network and on the strength of local inhibition (**Figure 3A**). We performed phase prediction based on recordings of simulated dynamics with different degrees of synchrony. As shown in **Figure 7D**, stronger synchrony was associated to smaller prediction errors. Interestingly, prediction errors remained moderate

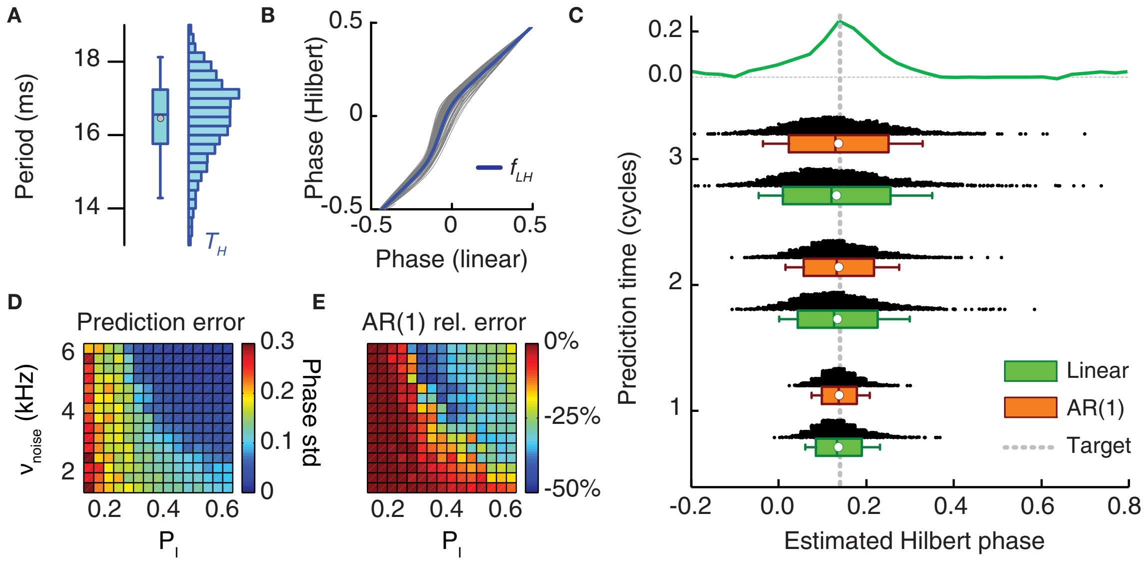

FIGURE 7 | Online prediction of the phase of stimulation onset. (A) The period length of LFP oscillations fluctuates from cycle to cycle and has a broad-range uni-modal distribution (here shown for period lengths as estimated from the Hilbert phases). **(B)** Hilbert phase versus linear phase for a sample LFP time series. To speed-up the computation of t_{ON} in the prediction stage, the Hilbert phase can be approximated by a linear phase, since, as here shown, they are strongly correlated and the mild static non-linearity f_{LH} linking them can be neglected. **(C)** Distribution of the phase of t_{ON} predicted by two different methods and for different lengths of the prediction window (measured in oscillation cycles). Shown are histograms and box plots (box giving median and interquartile range, white circle the mean value and whiskers the 5-th and 95-th percentiles) of the predicted phase of light stimulation $\phi(t_{ON})$ for two prediction methods—pure linear extrapolation based on the average period length (green) and first order autoregressive [AR(1)] models (orange)—applied to period lengths recorded during the monitoring stage. Both the median and the mean of predicted Hilbert phase are in good agreement with the exact target phase (leading with highest probability to a phase shift) with a dispersion not larger than the width of the positive part of the reference phase-shift response curve (reproduced from **Figures 4C,D** on the top of the panel). **(D)** The prediction error (i.e., the standard deviation of the inferred phase $\phi(t_{ON})$ of photostimulation onset) depends on the synchronization level of the neuronal population activity (cf. **Figure 3A**). The prediction error based on linear extrapolation (measured in units of average oscillation period lengths) is shown for different probabilities of local inhibitory connection p_I and background noise rates ν_{noise}. Larger synchronization leads to better prediction. **(E)** The ratio of the prediction error based on the AR(1) model and the prediction error based on linear extrapolation in dependence on the same parameters. For intermediate synchrony levels, the prediction error can be consistently reduced by the use of an AR(1) model.

even when considering regimes "at the edge of synchrony." Furthermore adopting a more elaborate AR(1) approach yielded the strongest performance improvement with respect to simpler linear extrapolation precisely for these intermediate synchrony values (**Figure 7E**).

In contrast, prediction errors associated to weak synchronous dynamics were larger and even the AR(1) approach failed to improve over linear extrapolation in these cases. However, in these regimes, the dynamics rarely displayed long-lasting oscillatory epochs and the probability of spontaneous switching was comparable to the one of induced switching, thus invalidating our analysis protocol. In these cases, therefore, continuous photostimulation should be used to enhance the degree of coherence of the coupled populations activity (analogously to **Figure 3E**).

DISCUSSION

FROM POWER BOOSTING TO RELIABLE PHASE CONTROL

Optogenetic stimulation has been successfully applied to boost the power of fast neural oscillations *in vivo* and *in vitro*. In Cardin et al. (2006), pulsed optogenetic stimulation *in vivo* was used to highlight the existence of a resonance at gamma range frequencies of local inhibitory cortical microcircuits. Adesnik and Scanziani (Adesnik and Scanziani, 2010) and Akam et al. (2012) experimented with ramped light stimulation to induce long-lasting oscillatory episodes in slices.

Beyond controlling oscillation power, the experiments by Akam et al. (2012) are closely related to the first part of our model study. They used 5 ms-long light stimulation pulses to shift local oscillation phases and quantify the phase response curves (PRCs) of oscillations in hippocampal slices, analogously to the simulated experiment of **Figure 4**. The hippocampal PRC measured by Akam et al. (2012) was distinctly biphasic, leading to phase advancement or phase delaying, depending on the phase of application of the stimulation. Such biphasic PRC shape is in qualitative and approximately in quantitative agreement with the PRCs extracted from our local population model for stimulation pulses of comparable lengths (cf. **Figure 4D**, orange curve for 5 ms-long pulses and red curve for 10 ms-long pulses).

Interestingly, however, the PRCs extracted from our model for shorter stimulation durations lacked phase-delaying regions and displayed only a narrow phase range leading to consistent phase advancement. Furthermore, they were characterized by a relatively broad range of application phases for which light stimulation was completely ineffective. These features of the PRC shapes are robustly obtained if the circuit mechanism for the generation of oscillations dominantly relies on delayed mutual interactions within interneuronal networks (Battaglia et al., 2007, 2012). One can actually use very different neuronal models to obtain oscillatory and phase-locking behaviors that qualitatively match those observed. For instance, spatially structured networks of integrate-and-fire neurons (Battaglia and Hansel, 2011) have dynamical regimes that tightly correspond to those of homogeneous networks of the conductance-based neurons (Battaglia et al., 2007) that we adopt here. We predict therefore that similarly looking PRCs could be obtained in the case of Kainate-induced *in vitro* oscillations in slices, in which excitatory neurons are entrained by a coherently oscillating interneuronal population but are not actively involved in the generation of the local rhythm (Fisahn et al., 2004; Bartos et al., 2007; Andersson et al., 2012).

Narrow phase ranges associated to large PRC values reduce the probability of inducing stable phase shifting by applying stimulation at arbitrary times. However such narrow intervals become a desirable resource when optogenetic stimulation is precisely phased conditional to ongoing oscillations, as executable in perspective with a closed-loop setup. Indeed, PRC shapes like the reference PRC discussed in **Figure 3** (green curve for $P_{ChR2} = 25\%$, and $T_{\text{light}} = 3\,\text{ms}$ light-pulses) could allow an "all-or-none" control of phase shifting, in which strong effects are obtained only if the stimulation is applied within a specific target range of phases, but in which undesired switching triggered by noise or by a misapplied input is largely suppressed.

A SIMPLE ChR2 MODEL CAPTURES NON MONOTONIC PHOTORESPONSE

The light-activated cation channel ChR2 activates more rapidly and supports larger peak current amplitudes for increasing light intensities. Therefore, we speculated that brief, high intensity light pulses would provide the optimal stimulation for our purposes. To our knowledge there were no studies that systematically documented ChR2 current responses for stimuli with light intensities above 20 mW/mm^2 (Ishizuka et al., 2006; Ernst et al., 2008; Lin et al., 2009). At this intensity the activation rate is still light sensitive and we aimed to increase it even more using light intensities as high as approximately 130 mW/mm^2. While the activation rate did indeed decrease further, the fact that the peak current amplitude *decreased* for intensities above approximately 20 mW/mm^2 came to us as a surprise (**Figures 1B,C**). This behavior has not been reported before, to the best of our knowledge, though the measurements published in Lin et al. (2009) hint at a decreasing peak amplitude for the highest intensity applied there, which was approximately 19.8 mW/mm^2.

Such phenomenon might be reminiscent of the photoreactive P480b intermediate state, which can be converted by blue light to the early P500 intermediate state. This transition was proposed as a shortcut of the photocycle from a spectroscopic study of ChR2 channels (Ritter et al., 2008). Since previously published models of ChR2 currents (Nikolic et al., 2006, 2009) could not account for this non-monotonic light response, it was necessary to deploy a novel model. Our simple conductance-based model correctly captures the existence of an optimal light intensity for photostimulation, without need to incorporate elaborate details about the ChR2 molecular structure and dynamics. Note that the application of our model is not limited to brief light pulses, but can also predict light-induced conductance in response to ramps of light (cf. **Figure 3E**).

Our model is also accurately data-constrained. To calibrate model parameters, light induced changes of ChR2 conductance were measured in voltage clamp. If the voltage can be clamped throughout a cell, any changes in the whole-cell current can be attributed to ChR2 conductances. In differentiated neurons, however, this perfect voltage control cannot be attained. This is obvious from the recording in **Figure 1A** (black trace), where the activation of ChR2 depolarized the axon sufficiently to activate voltage-dependent sodium channels, which created an unclamped spike. Even when sodium channels are blocked, the conditions are not optimal for a precise biophysical characterization. Using essentially passive and electrotonically compact cells, such as HEK-293 cells (Nikolic et al., 2009), provided optimal recording conditions (**Figure 1B**). The smaller amplitude of the photocurrents in these cells reflected differences in cell surface and expression levels, while the biophysical properties of ChR2 were most likely identical to those expressed in neurons.

TECHNICAL FEASIBILITY

As discussed above, the extraction of PRCs describing the collective response of a transduced neuronal population to light stimulation was already achieved *in vitro* (Akam et al., 2012). Our modeling study suggests that a similar approach could be successfully applied *in vivo*, since phase-shifting effects can be robustly obtained with high and low transduction rates, covering the wide range achievable with different experimental techniques (Adamantidis et al., 2007; Petreanu et al., 2007; Wang et al., 2007; Takahashi et al., 2012). The success rate will depend on a suitably tuned light intensity and on the ability to select the phase of the stimulation onset conditional on ongoing oscillation dynamics. Another factor that might enhance the controllability of phases is the use of faster variants of Chr2, such as ChETA (Gunaydin et al., 2010) and the E123T/T159C (Berndt et al., 2011) mutants.

A closed-loop approach is required for determining the optimal timing of pulse stimulations. **Figure 7C** shows that if the time required for the prediction stage is of the order of a few oscillation cycles, then the discrepancy between the target and the actual perturbation phase is comparable to the width of the peak of the PRC. Consequently the resulting phase shifting should remain close to the optimum. The prediction strategy that we propose (**Figure 6**) is based uniquely on a small number of linear computations, which are particularly suited for ultrafast (millisecond scale) implementation on reconfigurable hardware chips (Zhuo and Prasanna, 2008; Sadrozinski and Wu, 2011) or on GPU architectures (Owens et al., 2008; Volkov and Demmel, 2008) on which FFT algorithms can be efficiently implemented (Bhattacharyya et al., 2010). As a matter of fact, hardware implementations of period extraction (Waskito et al., 2010) and autoregressive modeling of biologic signals (Marinkovic et al., 2005; Kim and Rosen, 2010) have already proven to be order(s) of magnitude faster than on conventional CPUs. Taking into account these high levels of performance and the approximations we propose to implement, a length of the prediction window of ∼50 ms that corresponds to approximately three cycles of a 40–70 Hz rhythm appears completely realistic.

Our simulated oscillations constitute an idealized model for neuronal rhythms measured *in vivo* or *in vitro*. In our model, especially when the synchronization index is very high, cycle-to-cycle period length fluctuations are positively correlated with weak to intermediate correlation strength. In real neuronal oscillations, however, adaptation or other phenomena might introduce more complex correlation patterns between the lengths of different periods. Nevertheless, such correlations might still be captured by AR(1) modeling, as hinted to by the better performance of AR(1) in dynamic regimes at the “edge of synchrony” (**Figure 7E**), in which period length fluctuations are more strongly correlated.

Under specific experimental conditions, long-lasting oscillatory epochs might be a rare event. It would then become difficult to meet the conditions for the applicability of our protocol (i.e., the testing stage of **Figure 6** might never be passed). In this case, continuous optogenetic stimulation could be used to stabilize and boost oscillations, as simulated in **Figure 3E**. Then, similarly to the approach of Akam et al. (2012), precisely timed “kicks,” superposed on this continuous light stimulation, could be used to perturb the instantaneous phase. In this sense, optogenetic stimulation is more promising than electric micro-stimulation. First, it allows combining continuous and pulsed stimulation within a single setup. Second, it can control with high selectivity the degree of synchronization, not only by providing an unspecific drive to the entire network, but also enhancing the drive to specific neuronal subpopulations, like for instance FS-PV cells which provide the phasic inhibition crucial for rhythm generation (Cardin et al., 2006; Sohal et al., 2009).

Finally, we are optimistic that the network models of transduced neural populations that were pioneered by Talathi et al. (2011) and further developed in this study are powerful tools, which will be increasingly adopted to conduct, optimize and accelerate the design and the calibration of closed-loop optogenetic experimental protocols.

PROBING PHASE-CODING AND COMMUNICATION-THROUGH-COHERENCE

Reliable optogenetic manipulation of the phase dynamics of oscillating neuronal populations would open the way to an interventional exploration of phase coding schemes. In the phase coding framework, it is argued that the phase of spikes relative to a “reference clock”—paced either by a stimulus-locked (De Charms and Merzenich, 1996; Arabzadeh et al., 2006) or an internally-generated oscillation (O’Keefe and Recce, 1993; Siegel et al., 2009)—carry information, which is independent from and multiplexed with the one conveyed by rate fluctuations (Montemurro et al., 2008). Anticipating or delaying the ticks of such a “reference clock,” as the one putatively framed by slow cortical oscillations (Kayser et al., 2012), should perturb the decoding of phase-based representations.

Beyond the control of the phase of a local oscillation, inter-areal phase correlations could be disrupted transiently by unspecific optogenetic stimulation (**Figure 5D**). Furthermore, precisely-phased perturbations determined within a closed-loop system could induce persistent switching between alternative phase-locked dynamic patterns (Tiesinga and Sejnowski, 2010; Battaglia et al., 2012). In this sense, the realization of an experiment inspired by the idealized analysis of **Figure 4**, would provide a direct testing of the communication-through-coherence hypothesis (Fries, 2005). More specifically, it would allow experimental testing of whether different sets of inter-areal phase relations lead to different inter-areal functional interactions and to an altered balance between bottom-up and top-down information flows, as predicted by theory (Battaglia et al., 2012).

A reorganization of phase relations between distant neuronal populations might have perceptual or behavioral consequences. Selective alteration of inter-population phase relations, for instance between areas FEF and V4 (Gregoriou et al., 2009) or areas V1 and V4 (Grothe et al., 2012), might be used to suppress or boost attentional effects or even to emulate reorienting of attention. Furthermore, our theoretical investigations suggest that stimulation applied locally to a single area might induce distributed reorganization of phase relations between other more distant areas (Battaglia et al., 2012). Closed-loop optogenetic stimulation might then in perspective be used to trigger system-level switching between global brain states (Deco et al., 2009; Freyer et al., 2011).

AUTHOR CONTRIBUTIONS

Agostina Palmigiano and Demian Battaglia performed the simulations. Annette Witt, Agostina Palmigiano, and Demian Battaglia analyzed the simulations. Andreas Neef and Ahmed El Hady performed and analyzed the experiments. Annette Witt, Andreas Neef, Fred Wolf, and Demian Battaglia designed the models and the study. Annette Witt, Agostina Palmigiano, Andreas Neef, Ahmed El Hady, Fred Wolf, and Demian Battaglia wrote the manuscript.

ACKNOWLEDGMENTS

The authors thank Pascal Fries, Alexander Gail, Theo Geisel, Andreas Kreiter, Shy Shoham, and Walter Stühmer for inspiring discussions. Annette Witt was supported by the Stifterverband für die deutsche Wissenschaft and by the Claussen-Simon-Stiftung. We all acknowledge financial support by the German Federal Ministry of Education and Research (BMBF) via the Bernstein Center for Computational Neuroscience—Göttingen (01GQ1005B, 01GQ0430, 01GQ07113), the Bernstein Focus Neurotechnology—Göttingen (01GQ0811) and the Bernstein Focus Visual Learning (01GQ0921, 01GQ0922), the German Israel Research Foundation and the VolkswagenStiftung (ZN2632) and the Deutsche Forschungsgemeinschaft through CRC-889 (906-17.1/2006).

REFERENCES

Adamantidis, A. R., Zhang, F., Aravanis, A. M., Deisseroth, K., and de Lecea, L. (2007). Neural substrates of awakening probed with optogenetic control of hypocretin neurons. *Nature* 450, 420–424.

Adesnik, H., and Scanziani, M. (2010). Lateral competition for cortical space by layer-specific horizontal circuits. *Nature* 464, 1155–1160.

Akam, T., Oren, I., Mantoan, L., Ferenczi, E., and Kullmann, D. M. (2012). Oscillatory dynamics in the hippocampus support dentate gyrus-CA3 coupling. *Nat. Neurosci.* 15, 763–768.

Andersson, R., Johnston, A., and Fisahn, A. (2012). Dopamine D4 receptor activation increases hippocampal gamma oscillations by enhancing synchronization of fast-spiking interneurons. *PLoS ONE* 7:e40906. doi: 10.1371/journal.pone.0040906

Arabzadeh, E., Panzeri, S., and Diamond, M. E. (2006). Deciphering the spike train of a sensory neuron: counts and temporal patterns in the rat whisker pathway. *J. Neurosci.* 26, 9216–9226.

Aravanis, A. M., Wang, L. P., Zhang, F., Meltzer, L. A., Mogri, M. Z., Schneider, M. B., et al. (2007). An optical neural interface: *in vivo* control of rodent motor cortex with integrated fibreoptic and optogenetic technology. *J. Neural Eng.* 4, S143–S156.

Bakkum, D. J., Gamblen, P. M., Ben-Ary, G., Chao, Z. C., and Potter, S. M. (2007). MEART: the semi-living artist. *Front. Neurorobot.* 1:5. doi: 10.3389/neuro.12.005.2007

Bandyopadhyay, P. R. (2005). Trends in biorobotic autonomous undersea vehicles. *IEEE J. Oceanic Eng.* 30, 109–139.

Bartos, M., Vida, I., and Jonas, P. (2007). Synaptic mechanisms of synchronized gamma oscillations in inhibitory interneuron networks. *Nat. Rev. Neurosci.* 8, 45–56.

Battaglia, D., Brunel, N., and Hansel, D. (2007). Temporal decorrelation of collective oscillations in neural networks with local inhibition and long-range excitation. *Phys. Rev. Lett.* 99:238106. doi: 10.1103/PhysRevLett.99.238106

Battaglia, D., and Hansel, D. (2011). Synchronous chaos and broad band gamma rhythm in a minimal multilayer model of primary visual cortex. *PLoS Comp. Biol.* 7:e1002176. doi: 10.1371/journal.pcbi.1002176

Battaglia, D., Witt, A., Wolf, F., and Geisel, T. (2012). Dynamic effective connectivity of inter-areal brain circuits. *PLoS Comp. Biol.* 8:e1002438. doi: 10.1371/journal.pcbi.1002438

Berndt, A., Schoenenberger, P., Mattis, J., Tye, K. M., Deisseroth, K., Hegemann, P., et al. (2011). High-efficiency channelrhodopsins for fast neuronal stimulation at low light levels. *Proc. Natl. Acad. Sci. U.S.A.* 108, 7595–7600.

Bhattacharyya, K., Hazra, A., Hatai, I., and Banerjee, S. (2010). Architectural design of a radix-4 CORDIC-based Radix-4 IFFT algorithm and its FGGA implementation. *Int. J. Sig. Imaging Syst. Eng.* 2, 201–215.

Bosman, C. A., Schoffelen, J.-M., Brunet, N., Oostenveld, R., Bastos, A. M., Womelsdorf, T., et al. (2012). Attentional stimulus selection through selective synchronization between monkey visual areas. *Neuron* 75, 875–888.

Brockwell, P. J., and Davis, R. A. (1996). *Introduction to Time Series and Forecasting*. New York, NY: Springer.

Brovelli, A., Ding, M., Ledberg, A., Chen, Y., Nakamura, R., and Bressler, S. L. (2004). Beta oscillations in a large-scale sensorimotor cortical network: directional influences revealed by Granger causality. *Proc. Natl. Acad. Sci. U.S.A.* 101, 9849–9854.

Brunel, N., and Hakim, V. (1999). Fast global oscillations in networks of integrate-and-fire neurons with low firing rates. *Neural Comput.* 11, 1621–1671.

Brunel, N., and Hansel, D. (2006). How noise affects the synchronization properties of recurrent networks of inhibitory neurons. *Neural Comput.* 18, 1066–1110.

Brunel, N., and Wang, X.-J. (2003). What determines the frequency of fast network oscillations with irregular neural discharges? I. Synaptic dynamics and excitation-inhibition balance. *J. Neurophysiol.* 90, 415–430.

Buffalo, E. A., Fries, P., Landman, R., Buschman, T. J., and Desimone, R. (2011). Laminar differences in gamma and alpha coherence in the ventral stream. *Proc. Natl. Acad. Sci. U.S.A.* 108, 11262–11267.

Cardin, J. A., Carlén, M., Meletis, K., Knoblich, U., Zhang, F., Deisseroth, K., et al. (2006). Driving fast-spiking cells induces gamma rhythm and controls sensory responses. *Nature* 459, 663–667.

De Charms, R. C., and Merzenich, M. M. (1996). Primary cortical representations of sounds by the coordination of action-potential timing. *Nature* 381, 610–613.

Deco, G., Jirsa, V., McIntosh, A. R., Sporns, O., and Kötter, R. (2009). Key role of coupling, delay, and noise in resting brain fluctuations. *Proc. Natl. Acad. Sci. U.S.A.* 106, 10302–10307.

Eckhorn, R., Bauer, R., Jordan, W., Brosch, M., Kruse, W., Munk, M., et al. (1988). Coherent oscillations: a mechanism of feature linking in the visual cortex? Multiple electrode and correlation analyses in the cat. *Biol. Cybern.* 60, 121–130.

Ernst, O. P., Sánchez Murcia, P. A., Daldrop, P., Tsunoda, S. P., Kateriya, S., and Hegemann, P. (2008). Photoactivation of channelrhodopsin. *J. Biol. Chem.* 283, 1637–1643.

Fisahn, A., Contractor, A., Traub, R. D., Buhl, E. H., Heinemann, S. F., and McBain, C. J. (2004). Distinct roles for the kainate receptor subunits GluR5 and GluR6 in kainate-induced hippocampal gamma oscillations. *J. Neurosci.* 24, 9658–9668.

Freyer, F., Roberts, J. A., Becker, R., Robinson, P. A., Ritter, P., and Breakspear, M. (2011). Biophysical mechanisms of multistability in resting-state cortical rhythms. *J. Neurosci.* 31, 6353–6361.

Fries, P. (2005). A mechanism for cognitive dynamics: neuronal communication through neuronal coherence. *Trends Cogn. Sci.* 9, 474–480.

Fries, P., Reynolds, J. H., Rorie, A. E., and Desimone, R. (2001). Modulation of oscillatory neuronal synchronization by selective visual attention. *Science* 291, 1560–1563.

Gabor, V. D. (1946). Theory of communication. *J. IEE* 93, 429–457.

Golomb, D., and Hansel, D. (2000). The number of synaptic inputs and the synchrony of large, sparse neuronal networks. *Neural Comp.* 12, 1095–1139.

Gray, C. M., König, P., Engel, A. K., and Singer, W. (1989). Oscillatory responses in cat visual cortex exhibit inter-columnar synchronization which reflects global stimulus properties. *Nature* 338, 334–337.

Gregoriou, G. G., Gotts, S. J., and Desimone, R. (2012). Cell-type-specific synchronization of neural activity in FEF with V4 during attention. *Neuron* 73, 581–594.

Gregoriou, G. G., Gotts, S. J., Zhou, H., and Desimone, R. (2009). High-frequency, long-range coupling between prefrontal and visual cortex during attention. *Science* 324, 1207–1210.

Grothe, I., Neitzel, S. D., Mandon, S., and Kreiter, A. K. (2012). Switching neuronal inputs by differential modulations of gamma-band phase-coherence. *J. Neurosci.* 32, 16172–16180.

Gunaydin, L. A., Yizhar, O., Berndt, A., Sohal, V. S., Deisseroth, K., and Hegemann, P. (2010). Ultrafast optogenetic control. *Nat. Neurosci.* 13, 387–392.

Ishizuka, T., Kakuda, M., Araki, R., and Yawo, H. (2006). Kinetic evaluation of photosensitivity in genetically engineered neurons expressing green algae light-gated channels. *Neurosci. Res.* 54, 85–94.

Kayser, C., Ince, R. A. A., and Panzeri, S. (2012). Analysis of slow (theta) oscillations as a potential temporal reference frame for information coding in sensory cortices. *PLoS Comp. Biol.* 8:e1002717. doi: 10.1371/journal.pcbi.1002717

Kim, H., and Rosen, J. (2010). Epileptic seizure detection – an AR model based algorithm for implantable device. *Conf. Proc. IEEE Eng. Med. Biol. Soc.* 2010, 5541–5544.

Koepsell, K., Wang, X., Hirsch, J. A., and Sommer, F. T. (2010). Exploring the function of neural oscillations in early sensory systems. *Front. Neurosci.* 4:53. doi: 10.3389/neuro.01.010.2010

Kreiter, A. K., and Singer, W. (1996). Stimulus-dependent synchronization of neuronal responses in the visual cortex of the awake macaque monkey. *J. Neurosci.* 16, 2381–2396.

Lin, J. Y., Lin, M. Z., Steinbach, P., and Tsien, R. Y. (2009). Characterization of engineered channelrhodopsin variants with improved properties and kinetics. *Biophys. J.* 96, 1803–1814.

Lisman, J. (2005). The theta/gamma discrete phase code occuring during the hippocampal phase precession may be a more general brain coding scheme. *Hippocampus* 15, 913–922.

Marinkovic, B., Gillette, M., and Ning, T. (2005). "FPGA implementation of respiration signal classification using a soft-core processor," in *Proceedings of the 31st Annual Northeast Bioengineering IEEE Conference* (New York, NY), 54–55.

Marom, S., and Shahaf, G. (2002). Development, learning and memory in large random networks of cortical neurons: lessons beyond anatomy. *Rev. Biophys.* 35, 63–87.

Melloni, L., Molina, C., Pena, M., Torres, D., Singer, W., and Rodriguez, E. (2007). Synchronization of neural activity across cortical areas correlates with conscious perception. *J. Neurosci.* 27, 2858–2865.

Miranda-Dominguez, O., Gonia, J., and Netoff, T. I. (2010). Firing rate control of a neuron using a linear proportional-integral controller. *J. Neural Eng.* 7:066004. doi: 10.1088/1741-2560/7/6/066004

Montemurro, M. A., Rasch, M. J., Murayama, Y., Logothetis, N. K., and Panzeri, S. (2008). Phase-of-firing coding of natural visual stimuli in primary visual cortex. *Curr. Biol.* 18, 375–380.

Nadasdy, Z. (2010). Binding by asynchrony: the neuronal phase code. *Front. Neurosci.* 4:51. doi: 10.3389/fnins.2010.00051

Nikolic, K., Degenaar, P., and Toumazou, C. (2006). Modeling and engineering aspects of channelrhodopsin-2 system for neural photostimulation. *Conf. Proc. IEEE Eng. Med. Biol. Soc.* 1, 1626–1629.

Nikolic, K., Grossman, N., Grubb, M. S., Burrone, J., Toumazou, C., and Degenaar, P. (2009). Photocycles of channelrhodopsin-2. *Photochem. Photobiol.* 85, 400–411.

Novellino, A., D'Angelo, P., Cozzi, L., Chiappalone, M., Sanguineti, V., and Martinoia, S. (2007). Connecting neurons to a mobile robot: an *in vitro* bidirectional neural interface. *Comput. Intell. Neurosci.* 2007, 1–14.

O'Keefe, J., and Recce, M. L. (1993). Phase relationship between hippocampal place units and the EEG theta rhythm. *Hippocampus* 3, 317–330.

Owens, J. D., Houston, M., Luebke, D., Green, S., Stone, J. E., and Phillips, J. C. (2008). GPU computing. *IEEE Proc.* 96, 879–899.

Percival, D. B., and Walden, A. T. (1993). *Spectral Analysis for Physical Applications.* Cambridge: Cambridge University Press.

Pesaran, B., Pezaris, J. S., Sahani, M., Mitra, P. P., and Andersen, R. A. (2002). Temporal structure in neuronal activity during working memory in macaque parietal cortex. *Nat. Neurosci.* 5, 805–811.

Petreanu, L., Huber, D., Sobczyk, A., and Svoboda, K. (2007). Channelrhodopsin-2-assisted circuit mapping of long range callosal projections. *Nat. Neurosci.* 10, 663–668.

Pikovsky, A. S., Rosenblum, M., and Kurths, J. (2001). *Synchronization – A Universal Concept in Nonlinear Sciences*. Cambridge: Cambridge University Press.

Ritter, E., Stehfest, K., Berndt, A., Hegemann, P., and Bartl, F. J. (2008). Monitoring light-induced structural changes of Channelrhodopsin-2 by UV-visible and Fourier transform infrared spectroscopy. *J. Biol. Chem.* 283, 35033–35041.

Roelfsema, P. R., Engel, A. K., König, P., and Singer, W. (1997). Visuomotor integration is associated with zero time-lag synchronization among cortical areas. *Nature* 385, 157–161.

Rotermund, D., Taylor, K., Ernst, U. A., Kreiter, A. K., and Pawelzik, K. R. (2009). Attention improves object representation in visual cortical field potentials. *J. Neurosci.* 29, 10120–10130.

Sadrozinski, H. F. W., and Wu, J. (2011). *Applications of Field-Programmable Gate Arrays in Scientific Research*. Boca Raton, FL: Taylor and Francis.

Samonds, J. M., and Bonds, A. B. (2004). Gamma oscillation maintains stimulus structure-dependent synchronization in cat visual cortex. *J. Neurophysiol.* 93, 223–236.

Schoenenberger, P., Grunditz, A., Rose, T., and Oertner, T. (2008). Optimizing the spatial resolution of channelrhodopsin-2 activation. *Brain Cell Biol.* 36, 119–127.

Siegel, M., Warden, M. R., and Miller, E. K. (2009). Phase-dependent neuronal coding of objects in short-term memory. *Proc. Natl. Acad. Sci. U.S.A.* 106, 21341–21346.

Sohal, V. S., Zhang, F., Yizhar, O., and Deisseroth, K. (2009). Parvalbumin neurons and gamma rhythms enhance cortical circuit performance. *Nature* 459, 698–702.

Takahashi, H., Sakurai, T., Sakai, H., Bakkum, D. J., Suzurikawa, J., and Kanzaki, R. (2012). Light-addressed single-neuron stimulation in dissociated neuronal cultures with sparse expression of ChR2. *Biosystems* 107, 106–112.

Talathi, S. S., Carney, P. R., and Khargonekar, P. P. (2011). Control of neural synchrony using channelrhodopsin-2: a computational study. *J. Comput. Neurosci.* 31, 87–103.

Tallon-Baudry, C., Bertrand, O., Delpuech, C., and Pernier, J. (1996). Stimulus specificity of phase-locked and non-phase-locked 40 Hz visual responses in human. *J. Neurosci.* 16, 4240–4249.

Tiesinga, P., and Sejnowski, T. J. (2009). Cortical enlightenment: are attentional gamma oscillations driven by ING or PING? *Neuron* 63, 727–732.

Tiesinga, P. H., and Sejnowski, T. J. (2010). Mechanisms for phase shifting in cortical networks and their role in communication through coherence. *Front. Hum. Neurosci.* 4:196. doi: 10.3389/fnhum.2010.00196

Varela, F., Lachaux, J. P., Rodriguez, E., and Martinerie, J. (2001). The brainweb: phase synchronization and large-scale integration. *Nat. Rev. Neurosci.* 2, 229–239.

Volkov, V., and Demmel, J. W. (2008). "Benchmarking GPUs to tune dense linear algebra," in *The International Conference for High Performance Computing, Networking, Storage, and Analysis (SC 2008)* (Piscataway, NJ), 1–11.

Wagenaar, D. A., Madhavan, R., Pine, J., and Potter, S. M. (2005). Controlling bursting in cortical cultures with closed-loop multi-electrode stimulation. *J. Neurosci.* 25, 680–688.

Wallach, A., Eytan, D., Gal, A., Zrenner, C., and Marom, S. (2011). Neuronal response clamp. *Front. Neuroeng.* 4:3. doi: 10.3389/fneng.2011.00003

Wang, H., Peca, J., Matsuzaki, M., Matsuzaki, K., Noguchi, J., Qiu, L., et al. (2007). High-speed mapping of synaptic connectivity using photostimulation in channelrhodopsin-2 transgenic mice. *Proc. Natl. Acad. Sci. U.S.A.* 104, 8143–8148.

Wang, S., Chandrasekaran, L., Fernandez, F. R., White, J. A., and Canavier, C. C. (2012). Short conduction delays cause inhibition rather than excitation to favor synchrony in hybrid neuronal networks of the entorhinal cortex. *PLoS Comp. Biol.* 8:e1002306. doi: 10.1371/journal.pcbi.1002306

Wang, X. J. (2010). Neurophysiological and computational principles of cortical rhythms in cognition. *Physiol. Rev.* 90, 1195–1268.

Wang, X. J., and Buzsáki, G. (1996). Gamma oscillation by synaptic inhibition in a hippocampal interneuronal network model. *J. Neurosci.* 16, 6402–6413.

Waskito, P., Miwa, S., Mitsukura, Y., and Nakajo, H. (2010). "Parallelizing Hilbert-Huang Transform on a GPU," in *Proceedings of the 2010 First International Conference on Networking and Computing (ICNC 2010)* (Washington, DC), 184–190.

Whittington, M. A., Traub, R. D., and Jefferys, J. G. (1995). Synchronized oscillations in interneuron networks driven by metabotropic glutamate receptor activation. *Nature* 373, 612–615.

Whittington, M. A., Traub, R. D., Kopell, N., Ermentrout, G. B., and Buhl, E. H. (2000). Inhibition-based rhythms: experimental and mathematical observation on network dynamics. *Int. J. Psychophysiol.* 38, 315–336.

Womelsdorf, T., Schoffelen, J.-M., Oostenveld, R., Singer, W., Desimone, R., Engel, A. K., et al. (2007). Modulation of neuronal interactions through neuronal synchronization. *Science* 316, 1609–1612.

Woodman, M. M., and Canavier, C. C. (2011). Effects of conduction delays on the existence and stability of one to one phase locking between two pulse-coupled oscillators. *J. Comput. Neurosci.* 31, 401–418.

Yu, J., and Ferster, D. (2010). Membrane potential synchrony in primary visual cortex during sensory stimulation. *Neuron* 68, 1187–1201.

Zhuo, L., and Prasanna, V. K. (2008). High-performance designs for linear algebra operations on reconfigurable hardware. *IEEE Trans. Comput.* 57, 1057–1071.

Conflict of Interest Statement: Ahmed El Hady is also appointed editor of the present special research topic issue. The other authors declare that the research was conducted in the absence of any commercial or financial relationships that could be construed as a potential conflict of interest.

Received: 01 November 2012; accepted: 07 March 2013; published online: 17 April 2013.

Citation: Witt A, Palmigiano A, Neef A, El Hady A, Wolf F and Battaglia D (2013) Controlling the oscillation phase through precisely timed closed-loop optogenetic stimulation: a computational study. Front. Neural Circuits ***7****:49. doi: 10.3389/fncir.2013.00049*

Acknowledgments

First and foremost, I would like to thank Theo Geisel, for the opportunity to work in this marvelous department and for the support, advice and consideration he has offered me all these years. Thank you Theo, for creating this enjoyable and incredibly diverse working environment and keeping it filled with music.

I want to most sincerely thank Fred Wolf, for that I have learned from him the most fundamental things in science. How to look at problems, where their complexity lies, how to critically test an idea. I am most grateful for his supervision, his constant encouragement and positive criticism which have largely contributed to the final form that this thesis has reached.

I would like to thank Demian Battaglia, who introduced me to the fascinating world of oscillatory networks. His constant optimism and creativity have been an invaluable source of enthusiasm at all stages of my PhD. I also want to thank Demian for his openness and kindness when inviting me to the sunny part of Europe, especially for the extended visits in Marseille.

I am grateful to the cluster team, Denny Fliegner, and Hecke Schrobsdorff, for keeping the clusters up and running in such a remarkable way. I also want to thank them for the incomparable patience they have had with me, and for their generous help. I am grateful to Yorck-Fabian Beensen for his invaluable help and his constant good mood when I came back for the tenth time asking for something. I would like to thank Ayse Bolik, for helping me to find my way in Germany in the early days, and for her help with many personal issues. I am grateful to Ayse, Viktoryia Novak, Regina Wunderlich and Zrinka Gattin for their constant help and patience with my lack of paperwork skills.

I want to thank Rainer, Joscha, and Manuel for very valuable discussions, nice dinners, entertaining random moments and for the fun of organizing the summer school together. I also want to thank Alex and Nico for the always funny and interesting chats, and to Nico particularly for his office-mate patience these last weeks. I want to especially thank Max Puelma Touzel, part of the Latin-Rhythms team, for his cheerful enthusiasm and for guiding me through the first stages of the chaos project. I would like to thank Manuel, Demian, Fred, Tureiti and Jakob for carefully reading this thesis.

CarMax, David, Bernhard, Lukas, Mirko, Flor, Eli and Fran, thanks for all the great times inside and outside work, for the nice dinners and for some nice holidays trips, future and past. I also want to thank to my very dear friends Aqui, Andy, Chuse, Marce, Martin y Pablo from *El Equipo ++*, for the magic of growing up together scientifically, first in Buenos Aires, and later via WhatsApp.

Very special thanks go to my dear mother Nora Palmigiano, who trusts in me more than I trust in myself, and who convincingly taught me that everything was possible. For your strength, support and never-ending optimism, gracias ma.

Bibliography

[1] Abbott, L. (1999). Lapicque's introduction of the integrate-and-fire model neuron (1907). *Brain Research Bulletin*, 50(5-6), 303–304.

[2] Abbott, L. & Van Vreeswijk, C. (1993). Asynchronous states in networks of pulse-coupled oscillators. *Physical Review E*, 48(2), 1483–1490.

[3] Abeles, M., Hayon, G., & Lehmann, D. (2004). Modeling compositionality by dynamic binding of synfire chains. *Journal of Computational Neuroscience*, 17(2), 179–201.

[4] Acebron, J. A., Bonilla, L. L., Vicente, C. J. P., Ritort, F., & Spigler, R. (2005). The Kuramoto model: A simple paradigm for synchronization phenomena. *Reviews of Modern Physics*, 77(1), 137–185.

[5] Adrian, E. D. (1942). Olfactory reactions in the brain of the hedgehog. *The Journal of Physiology*, 100(4), 459–473.

[6] Adrian, E. D. & Matthews, B. H. C. (1934). The interpretation of potential waves in the cortex. *The Journal of physiology*, 81(4), 440–471.

[7] Akam, T. E. & Kullmann, D. M. (2010). Oscillations and filtering networks support flexible routing of information. *Neuron*, 67(2), 308–320.

[8] Akam, T. E. & Kullmann, D. M. (2012). Efficient Communication through Coherence Requires Oscillations Structured to Minimize Interference between Signals. *PLoS Computational Biology*, 8(11), e1002760.

[9] Alonso, J.-M., Usrey, W. M., & Reid, R. C. (1996). Precisely correlated firing in cells of the lateral geniculate nucleus. *Nature*, 383(6603), 815–9.

[10] Alonso, L. M. & Mindlin, G. B. (2011). Average dynamics of a driven set of globally coupled excitable units. *Chaos*, 21(2), 023102.

[11] Arieli, A., Sterkin, A., Grinvald, A., & Aertsen, A. (1996). Dynamics of ongoing activity: explanation of the large variability in evoked cortical responses. *Science (New York, N.Y.)*, 273(5283), 1868–1871.

[12] Ashwin, P. & Timme, M. (2005). Unstable Attractors: Existence and Robustness in Networks of Oscillators With Delayed Pulse Coupling. *Nonlinearity*, 18(5), 29.

[13] Atallah, B. V. & Scanziani, M. (2009). Instantaneous Modulation of Gamma Oscillation Frequency by Balancing Excitation with Inhibition. *Neuron*, 62(4), 566–577.

[14] Atay, F. M., Jost, J., & Wende, A. (2004). Delays, connection topology, and synchronization of coupled chaotic maps. *Physical Review Letters*, 92(14), 144101–1.

[15] Barardi, A., Sancristobal, B., & Garcia-Ojalvo, J. (2014). Phase-Coherence Transitions and Communication in the Gamma Range between Delay-Coupled Neuronal Populations. *PLoS Computational Biology*, 10(7).

[16] Bartos, M., Vida, I., & Jonas, P. (2007). Synaptic mechanisms of synchronized gamma oscillations in inhibitory interneuron networks. *Nature reviews. Neuroscience*, 8(1), 45–56.

[17] Bastos, A. M. M., Vezoli, J., Bosman, C. A., Schoffelen, J. M., Oostenveld, R., Dowdall, J. R., DeWeerd, P., Kennedy, H., & Fries, P. (2015a). Visual areas exert feedforward and feedback influences through distinct frequency channels. *Neuron*, 85(2), 390–401.

[18] Bastos, A. M. M., Vezoli, J., & Fries, P. (2015b). Communication through coherence with inter-areal delays. *Current Opinion in Neurobiology*, 31, 173–180.

[19] Battaglia, D., Brunel, N., & Hansel, D. (2007). Temporal decorrelation of collective oscillations in neural networks with local inhibition and long-Range excitation. *Physical Review Letters*, 99(23), 14–17.

[20] Battaglia, D., Witt, A., Wolf, F., & Geisel, T. (2012). Dynamic effective connectivity of inter-areal brain circuits. *PLoS Computational Biology*, 8(3), 1–53.

[21] Başar, E. (1972). A study of the time and frequency characteristics of the potentials evoked in the acoustical cortex. *Kybernetik*, 10(2), 61–64.

[22] Benettin, G., Galgani, L., Giorgilli, A., & Strelcyn, J. M. (1980). Lyapunov Characteristic Exponents for smooth dynamical systems and for hamiltonian systems; A method for computing all of them. Part 2: Numerical application. *Meccanica*, 15(1), 21–30.

[23] Berg, R. W., Alaburda, A., & Hounsgaard, J. (2007). Balanced Inhibition and Excitation Drive Spike Activity in Spinal Half-Centers. *Science*, 315(5810), 390–393.

[24] Bimbard, C., Ledoux, E., & Ostojic, S. (2016). Instability to a heterogeneous oscillatory state in randomly connected recurrent networks with delayed interactions. *arXiv:1605.07977*, (pp. 1–9).

[25] Börgers, C. & Kopell, N. (2003). Synchronization in networks of excitatory and inhibitory neurons with sparse, random connectivity. *Neural computation*, 15, 509–538.

[26] Bosman, C. A., Schoffelen, J. M., Brunet, N. M., Oostenveld, R., Bastos, A. M. M., Womelsdorf, T., Rubehn, B., Stieglitz, T., De Weerd, P., & Fries, P. (2012). Attentional Stimulus Selection through Selective Synchronization between Monkey Visual Areas. *Neuron*, 75(5), 875–888.

[27] Bragin, A., Jandó, G., Nádasdy, Z., Hetke, J., Wise, K., & Buzsáki, G. (1995). Gamma (40-100 Hz) oscillation in the hippocampus of the behaving rat. *The Journal of neuroscience : the official journal of the Society for Neuroscience*, 15(1 Pt 1), 47–60.

[28] Bressler, S. L. & Seth, A. K. (2011). Wiener-Granger Causality: A well established methodology. *NeuroImage*, 58(2), 323–329.

[29] Brunel, N. (2000). Phase diagrams of sparsely connected networks of excitatory and inhibitory spiking neurons. *Neurocomputing*, 32-33(3), 307–312.

[30] Brunel, N. & Hakim, V. (1999). Fast Global Oscillations in Networks of Integrate-and-Fire Neurons with Low Firing Rates. *Neural Computation*, 11(7), 1621–1671.

[31] Brunel, N. & Hakim, V. (2008). Sparsely synchronized neuronal oscillations. *Chaos*, 18(1), 015113.

[32] Brunel, N. & Hansel, D. (2006). How noise affects the synchronization properties of recurrent networks of inhibitory neurons. *Neural computation*, 18(5), 1066–1110.

[33] Brunel, N. & Van Rossum, M. C. W. (2007). Lapicque's 1907 paper: From frogs to integrate-and-fire. *Biological Cybernetics*, 97(5-6), 337–339.

[34] Brunel, N. & Wang, X.-J. (2003a). What Determines the Frequency of Fast Network Oscillations With Irregular Neural Discharges? I. Synaptic Dynamics and Excitation-Inhibition Balance. *Journal of Neurophysiology*, 90(1), 415–430.

[35] Brunel, N. & Wang, X.-J. (2003b). What Determines the Frequency of Fast Network Oscillations With Irregular Neural Discharges? I. Synaptic Dynamics and Excitation-Inhibition Balance. *Journal of Neurophysiology*, 90(1), 415–430.

[36] Brunet, N. M., Bosman, C. A., Roberts, M. J., Oostenveld, R., Womelsdorf, T., De Weerd, P., & Fries, P. (2015). Visual cortical gamma-band activity during free viewing of natural images. *Cerebral Cortex*, 25(4), 918–926.

[37] Buehlmann, A. & Deco, G. (2010). Optimal information transfer in the cortex through synchronization. *PLoS Computational Biology*, 6(9).

[38] Buffalo, E. A., Fries, P., Landman, R., Buschman, T. J., & Desimone, R. (2011). Laminar differences in gamma and alpha coherence in the ventral stream. *Proceedings of the National Academy of Sciences of the United States of America*, 108(27), 11262–7.

[39] Buffalo, E. a., Fries, P., Landman, R., Liang, H., & Desimone, R. (2010). A backward progression of attentional effects in the ventral stream. *Proceedings of the National Academy of Sciences of the United States of America*, 107(1), 361–365.

[40] Bullock, T., Hofmann, M., Nahm, F., New, J., & Prechtl, J. (1990). Event-related potentials in the retina and optic tectum of fish. *Journal of Neurophysiology*, 64(3), 903–914.

[41] Burchell, T. R., Faulkner, H. J., & Whittington, M. A. (1998). Gamma frequency oscillations gate temporally coded afferent inputs in the rat hippocampal slice. *Neuroscience Letters*, 255(3), 151–154.

[42] Burkhalter, A. (2008). Many specialists for suppressing cortical excitation. *Frontiers in neuroscience*, 2(2), 155–167.

[43] Burns, S. P., Xing, D., & Shapley, R. (2011). Is gamma-band activity in the local field potential of V1 cortex a “clock” or filtered noise? *The Journal of neuroscience : the official journal of the Society for Neuroscience*, 31(26), 9658–9664.

[44] Burns, S. P., Xing, D., Shelley, M. J., & Shapley, R. (2010). Searching for autocoherence in the cortical network with a time-frequency analysis of the local field potential. *The Journal of neuroscience : the official journal of the Society for Neuroscience*, 30(11), 4033–4047.

[45] Buschman, T. J., Denovellis, E. L., Diogo, C., Bullock, D., & Miller, E. K. (2012). Synchronous Oscillatory Neural Ensembles for Rules in the Prefrontal Cortex. *Neuron*, 76(4), 838–846.

[46] Buschman, T. J. & Miller, E. K. (2007). Top-down versus bottom-up control of attention in the prefrontal and posterior parietal cortices. *Science (New York, N.Y.)*, 315(5820), 1860–1862.

[47] Buzsáki, G. (2005). Theta rhythm of navigation: Link between path integration and landmark navigation, episodic and semantic memory. *Hippocampus*, 15(7), 827–840.

[48] Buzsáki, G. (2006). *Rhythms of the Brain*. Oxford University Press.

[49] Buzsáki, G. (2010). Neural Syntax: Cell Assemblies, Synapsembles, and Readers. *Neuron*, 68(3), 362–385.

[50] Buzsáki, G. & Andreas, D. (2004). Neuronal Oscillations in Cortical Networks. *Science*, 304(5679), 1926.

[51] Buzsáki, G., Logothetis, N., & Singer, W. (2013). Scaling brain size, keeping timing: Evolutionary preservation of brain rhythms. *Neuron*, 80(3), 751–764.

[52] Buzsáki, G. & Wang, X.-J. (2012). Mechanisms of Gamma Oscillations. *Annual review of neuroscience*, 35(March), 203–225.

[53] Cardin, J. A., Carlén, M., Meletis, K., Knoblich, U., Zhang, F., Deisseroth, K., Tsai, L.-H., & Moore, C. I. (2009). Driving fast-spiking cells induces gamma rhythm and controls sensory responses. *Nature*, 459(7247), 663–7.

[54] Castelo-Branco, M., Goebel, R., Neuenschwander, S., & Singer, W. (2000). Neural synchrony correlates with surface segregation rules. *Nature*, 405, 685–689.

[55] Chakrabarti, S., Martinez-Vazquez, P., & Gail, A. (2014). Synchronization patterns suggest different functional organization in parietal reach region and the dorsal premotor cortex. *Journual Neurophys?*, 112(12), 3138–3153.

[56] Chalk, M., Gutkin, B., & Denève, S. (2016). Neural oscillations as a signature of efficient coding in the presence of synaptic delays. *eLife*, 5(2016JULY), 1–23.

[57] Chalk, M., Herrero, J. L., Gieselmann, M. A., Delicato, L. S., Gotthardt, S., & Thiele, A. (2010). Attention Reduces Stimulus-Driven Gamma Frequency Oscillations and Spike Field Coherence in V1. *Neuron*, 66(1), 114–125.

[58] Chaudhuri, R., Knoblauch, K., Gariel, M. A., Kennedy, H., & Wang, X. J. (2015). A Large-Scale Circuit Mechanism for Hierarchical Dynamical Processing in the Primate Cortex. *Neuron*, 88(2), 419–431.

[59] Colgin, L. L. (2013). Mechanisms and functions of theta rhythms. *Annual review of neuroscience*, 36, 295–312.

[60] Cover, T. M. & Thomas, J. A. (2005). *Elements of Information Theory.* Wiley Series in Telecommunications and Signal Processing.

[61] DeFelipe, J. (1999). Estimation of the number of synapses in the cerebral cortex: Methodological considerations. *Cerebral Cortex*, 9(7), 722–732.

[62] Denker, M., Timme, M., Diesmann, M., Wolf, F., & Geisel, T. (2004). Breaking synchrony by heterogeneity in complex networks. *Physical review letters*, 92(2), 074103.

[63] Dismone, R. & Duncan, J. (1995). Neural Mechanisms of Selective Visual Attention. *Annual Review of Neuroscience*, 18, 193–222.

[64] Dotson, N. M., Goodell, B., Salazar, R. F., Hoffman, S. J., & Gray, C. M. (2015). Methods, caveats and the future of large-scale microelectrode recordings in the non-human primate. *Frontiers in systems neuroscience*, 9(November), 149.

[65] Dotson, N. M., Salazar, R. F., & Gray, C. M. (2014). Frontoparietal correlation dynamics reveal interplay between integration and segregation during visual working memory. *The Journal of neuroscience : the official journal of the Society for Neuroscience*, 34(41), 13600–13.

[66] Ecker, A. S., Berens, P., Keliris, G. A., Bethge, M., Logothetis, N. K., & Tolias, A. S. (2010). Decorrelated neuronal firing in cortical microcircuits. *Science (New York, N.Y.)*, 327(5965), 584–7.

[67] Eckmann, J. P. & Ruelle, D. (1985). Ergodic theory of chaos and strange attractors. *Reviews of Modern Physics*, 57(3), 617–656.

[68] Engel, A. K. & Fries, P. (2010). Beta-band oscillations-signalling the status quo? *Current Opinion in Neurobiology*, 20(2), 156–165.

[69] Engel, A. K., Konig, P., Kreiter, A. K., & Singer, W. (1991a). Interhemispheric synchronization of oscillatory neuronal responses in cat visual cortex. *Science*, 252(5010), 1177–1179.

[70] Engel, A. K., Kreiter, A. K., König, P., & Singer, W. (1991b). Synchronization of oscillatory neuronal responses between striate and extrastriate visual cortical areas of the cat. *Proc. Natl. Acad. Sci. U. S. A.*, 88(14), 6048–6052.

[71] Engel, A. K. & Singer, W. (2001). Temporal binding and the neural correlates of sensory awareness. *Trends in Cognitive Sciences*, 5(1), 16–25.

[72] Engelken, R., Monteforte, M., & Wolf, F. (2016). The impact of single neuron biophysics on the collective chaotic dynamics of large scale neuronal circuits. *Unpublished Work*, (pp. 1–8).

[73] Ermentrout, B. (1996). Type I membranes, phase resetting curves, and synchrony. *Neural computation*, 8(5), 979–1001.

[74] Ermentrout, G. B. & Kopell, N. (1986). Parabolic Bursting in an Excitable System Coupled with a Slow Oscillation. *SIAM Journal on Applied Mathematics*, 46(2), 233–253.

[75] Ermentrout, G. B. & Terman, D. H. (2010). *Mathematical Foundation of Neuroscience*. Springer.

[76] Ernst, U., Pawelzik, K., & Geisel, T. (1995). Synchronization induced by temporal delays in pulse-coupled oscillators. *Physical Review Letters*, 74(9), 1570–1573.

[77] Ernst, U., Pawelzik, K., & Geisel, T. (1998). Delay-induced multistable synchronization of biological oscillators. *Physical Review E*, 57(2), 2150–2162.

[78] Farmer, J. D. (1982a). Chaotic attractors of an infinite-dimensional dynamical system. *Physica D: Nonlinear Phenomena*, 4(3), 366–393.

[79] Farmer, J. D. (1982b). Information Dimension and the Probabilistic Structure of Chaos.

[80] Farmer, J. D., Ott, E., & Yorke, J. A. (1983). The dimension of chaotic attractors. *Physica D: Nonlinear Phenomena*, 7(1-3), 153–180.

[81] Feng, J., Jirsa, V. K., & Ding, M. (2006). Synchronization in networks with random interactions: Theory and applications. *Chaos*, 16(1), 1–21.

[82] Fisahn, A., Pike, F. G., Buhl, E. H., & Paulsen, O. (1998). Cholinergic induction of network oscillations at 40|[thinsp]|Hz in the hippocampus in vitro. *Nature*, 394(6689), 186–189.

[83] Fourcaud-Trocmé, N., Hansel, D., van Vreeswijk, C., & Brunel, N. (2003). How spike generation mechanisms determine the neuronal response to fluctuating inputs. *J. Neurosci.*, 23(37), 11628–11640.

[84] Frederickson, P., Kaplan, J. L., Yorke, E. D., & Yorke, J. A. (1983). The liapunov dimension of strange attractors. *Journal of Differential Equations*, 49(2), 185–207.

[85] Frenzel, S. & Pompe, B. (2007). Partial mutual information for coupling analysis of multivariate time series. *Physical Review Letters*, 99(20), 1–4.

[86] Fries, P. (2005). A mechanism for cognitive dynamics: Neuronal communication through neuronal coherence.

[87] Fries, P., Reynolds, J. H., & Desimone, R. (2001). Modulation of Oscillatory Neuronal Synchronization by Selective Visual Attention. *Science*, 291(April 2016), 1560–1563.

[88] Froehling, H., Crutchfield, J. P., Farmer, D., Packard, N. H., & Shaw, R. (1981). On determining the dimension of chaotic flows. *Physica D: Nonlinear Phenomena*, 3(3), 605–617.

[89] Froyland, G., Lloyd, S., & Quas, A. (2013). A semi-invertible oseledets theorem with applications to transfer operator cocycles. *Discrete and Continuous Dynamical Systems- Series A*, 33(9), 3835–3860.

[90] Geisler, C., Brunel, N., & Xiao-Jing Wang (2005). Contributions of Intrinsic Membrane Dynamics to Fast Network Oscillations With Irregular Neuronal Discharges. *Journal of Neurophysiology*, 94(6), 4344–4361.

[91] Geist, K., Parlitz, U., & Lauterborn, W. (1990). Comparison of different methods for computing Lyapunov exponents. *Prog. Theor. Phys*, 83(5), 875–893.

[92] Gerstein, G. L. & Mandelbrot, B. (1964). Random Walk Models for the Spike Activity of a Single Neuron. *Biophysical journal*, 4(c), 41–68.

[93] Girardeau, G., Benchenane, K., Wiener, S. I., Buzsáki, G., & Zugaro, M. B. (2009). Selective suppression of hippocampal ripples impairs spatial memory. *Nature neuroscience*, 12(10), 1222–1223.

[94] Goedeke, S., Schuecker, J., & Helias, M. (2016). Noise dynamically suppresses chaos in neural networks. *arXiv*, (pp. 1–5).

[95] Golomb, D. & Hansel, D. (2000). The number of synaptic inputs and the synchrony of large, sparse neuronal networks. *Neural computation*, 12(5), 1095–1139.

[96] Golomb, D., Hansel, D., Shraiman, B., & Sompolinsky, H. (1992). Clustering in globally coupled oscillators. *Phys. Rev. A*, 45(6), 3516–3531.

[97] Golomb, D. & Rinzel, J. (1993). Dynamics of globally coupled inhibitory neurons with heterogeneity. *Physical Review E*, 48(6), 4810–4814.

[98] Gourévitch, B., Eggermont, J. J., Neymotin, S. A., Lazarewicz, M. T., Sherif, M., Contreras, D., Leif, H., Lytton, W. W., Reimer, A., Hubka, P., Engel, A. K., Kral, A., & Cortex, C. (2007). Evaluating Information Transfer Between Auditory Cortical Neurons. *Journal of Neurophysiology*, 97(January 2007), 2533–2543.

[99] Gray, C. M. (1994). Synchronous oscillations in neuronal systems: Mechanisms and functions. *Journal of Computational Neuroscience*, 1(1-2), 11–38.

[100] Gray, C. M., König, P., Engel, A. K., & Singer, W. (1989). Oscillatory responses in cat visual cortex exhibit inter-columnar synchronization which reflects global stimulus properties. *Nature*, 338(6213), 334–337.

[101] Gray, C. M. & Singer, W. (1989). Stimulus-specific neuronal oscillations in orientation columns of cat visual cortex. *Proceedings of the National Academy of Sciences of the United States of America*, 86(5), 1698–1702.

[102] Gregoriou, G. G., Gotts, S. J., & Desimone, R. (2012). Cell-type-specific synchronization of neural activity in FEF with V4 during attention. *Neuron*, 73(3), 581–594.

[103] Gregoriou, G. G., Gotts, S. J., Zhou, H., & Desimone, R. (2009). High-Frequency, Long-Range Coupling Between Prefrontal and Visual Cortex During Attention. *Science*, 324(5931), 1207–1210.

[104] Gross, J., Schmitz, F., Schnitzler, I., Kessler, K., Shapiro, K., Hommel, B., & Schnitzler, A. (2004). Modulation of long-range neural synchrony reflects temporal limitations of visual attention in humans. *Proceedings of the National Academy of Sciences of the United States of America*, 101(35), 13050–5.

[105] Grothe, I., Neitzel, S. D., Mandon, S., & Kreiter, A. K. (2012). Switching neuronal inputs by differential modulations of gamma-band phase-coherence. *Journal of Neuroscience*, 32(46), 16172–16180.

[106] Grothe, I., Rotermund, D., Neitzel, S. D., Mandon, S., Alexander, U., Kreiter, A. K., & Pawelzik, K. R. (2015). Attention selectively gates afferent signal transmission to area V4. *Biorxiv*, (pp. 1–24).

[107] Hafting, T., Fyhn, M., Bonnevie, T., Moser, M. B., & Moser, E. I. (2008). Hippocampus-independent phase precession in entorhinal grid cells. *Nature*, 453(7199), 1248–1252.

[108] Hahn, G., Bujan, A. F., Frégnac, Y., Aertsen, A., & Kumar, A. (2014). Communication through Resonance in Spiking Neuronal Networks. *PLoS Computational Biology*, 10(8), e1003811.

[109] Haider, B. (2006). Neocortical Network Activity In Vivo Is Generated through a Dynamic Balance of Excitation and Inhibition. *Journal of Neuroscience*, 26(17), 4535–4545.

[110] Hansel, D. & Mato, G. (1993). Patterns of synchrony in a heterogeneous Hodgkin-Huxley neural network with weak coupling. *Physica A: Statistical Mechanics and its Applications*, 200(1-4), 662–669.

[111] Hansel, D. & Mato, G. (2003). Asynchronous states and the emergence of synchrony in large networks of interacting excitatory and inhibitory neurons. *Neural computation*, 15(1), 1–56.

[112] Hansel, D., Mato, G., & Meunier, C. (1995). Synchrony in excitatory neural networks. *Neural computation*, 7(2), 307–337.

[113] Hansel, D. & Sompolinsky, H. (1992). Synchronization and computation in a chaotic neural network. *Physical Review Letters*, 68(5), 718–721.

[114] Hansel, D. & Sompolinsky, H. (1996). Chaos and synchrony in a model of a hypercolumn in visual cortex. *Journal of Computational Neuroscience*, 3(1), 7–34.

[115] Harnack, D., Ernst, U. A., & Pawelzik, K. R. (2015). A model for attentional information routing through coherence predicts biased competition and multistable perception. *Journal of neurophysiology*, 114(3), 1593–605.

[116] Harris, K., Csicsvari, J., Hirase, H., Dragoi, G., & Buzsáki, G. (2003). Organization of cell assemblies in the hippocampus. *Nature*, 424(July), 552–556.

[117] Heiligenthal, S., Dahms, T., Yanchuk, S., Jüngling, T., Flunkert, V., Kanter, I., Schöll, E., & Kinzel, W. (2011). Strong and weak chaos in nonlinear networks with time-delayed couplings. *Physical Review Letters*, 107(23), 1–5.

[118] Helmer, M., Chen, X. J., Wei, W., Wolf, F., & Battaglia, D. (2015). Connectome of a model local cortical circuit flexibly shapes layer-dependent multi-frequency oscillations. *bioRxiv*, (October 2015), 026674.

[119] Hermes, D., Miller, K. J., Wandell, B. A., & Winawer, J. (2015). Stimulus Dependence of Gamma Oscillations in Human Visual Cortex. *Cerebral cortex (New York, N.Y. : 1991)*, 25(9), 2951–9.

[120] Herrero, J. L., Gieselmann, M. A., Sanayei, M., & Thiele, A. (2013). Attention-induced variance and noise correlation reduction in macaque v1 is mediated by NMDA receptors. *Neuron*, 78(4), 729–739.

[121] Hiemeyer, P. (2009). On silent neurons: The dark matter of the brain.pdf. *Diploma Thesis.*

[122] Hodgkin, A. L. (1948). The local electric changes associated with repetitive action in a non-medullated axon. *Journal of Physiology*, 107(2), 165–181.

[123] Hodgkin, A. L. & Huxley, A. F. (1952). A quantitative description of membrane current and its application to conduction and excitation in nerve. *Bulletin of Mathematical Biology*, 52(1-2), 25–71.

[124] Hofman, M. A. (2014). Evolution of the human brain: when bigger is better. *Frontiers in neuroanatomy*, 8(March), 15.

[125] Honey, C. J., Kötter, R., Breakspear, M., & Sporns, O. (2007). Network structure of cerebral cortex shapes functional connectivity on multiple time scales. *Proceedings Of The National Academy Of Sciences Of The United States Of America*, 104(24), 10240–10245.

[126] Izhikevich, E. M. (2007). *Dynamical Systems in Neuroscience.* MIT Press.

[127] Izhikevich, E. M. & Edelman, G. M. (2008). Large-scale model of mammalian thalamocortical systems. *Proceedings of the National Academy of Sciences of the United States of America*, 105(9), 3593–8.

[128] Jahnke, S., Memmesheimer, R. M., & Timme, M. (2008). Stable irregular dynamics in complex neural networks. *Physical Review Letters*, 100(4), 2–5.

[129] Jahnke, S., Memmesheimer, R.-M., & Timme, M. (2009). How Chaotic is the Balanced State? *Frontiers in computational neuroscience*, 3(November), 13.

[130] Jain, M. (2011). A next-generation approach to the characterization of a non-model plant transcriptome. *Current Science*, 101(11), 1435–1439.

[131] Jensen, O., Kaiser, J., & Lachaux, J. P. (2007). Human gamma-frequency oscillations associated with attention and memory. *Trends in Neurosciences*, 30(7), 317–324.

[132] Jia, X. & Kohn, A. (2011). Gamma rhythms in the brain. *PLoS Biology*, 9(4), 2–5.

[133] Jia, X., Smith, M. A., & Kohn, A. (2011). Stimulus Selectivity and Spatial Coherence of Gamma Components of the Local Field Potential. *Journal of Neuroscience*, 31(25), 9390–9403.

[134] Jia, X., Tanabe, S., & Kohn, A. (2013a). Gamma and the Coordination of Spiking Activity in Early Visual Cortex. *Neuron*, 77(4), 762–774.

[135] Jia, X., Xing, D., & Kohn, A. (2013b). No Consistent Relationship between Gamma Power and Peak Frequency in Macaque Primary Visual Cortex. *Journal of Neuroscience*, 33(1), 17–25.

[136] Jirsa, V. K. & Ding, M. (2004). Will a large complex system with time delays be stable? *Physical Review Letters*, 93(7), 1–4.

[137] Jones, M. W. & Wilson, M. A. (2005). Phase precession of medial prefrontal cortical activity relative to the hippocampal theta rhythm. *Hippocampus*, 15(7), 867–873.

[138] Jüngling, T. & Kinzel, W. (2012). Scaling of Lyapunov exponents in chaotic delay systems. *arXiv preprint arXiv:1210.3528*, 0(7), 1–4.

[139] Kadmon, J. & Sompolinsky, H. (2015). Transition to chaos in random neuronal networks. *Physical Review X*, 5(4), 1–28.

[140] Kaplan, J. & Yorke, J. (1979). Chaotic behavior of multi-dimensional difference equations. *in {H. Peitgen and H. Walther (eds), Functional differential equations and approximation of fixed points, Lectures notes in Mathematics, Springer-Verlag}*, 730, 204–227.

[141] Kayser, C., Salazar, R. F., & Konig, P. (2003). Responses to natural scenes in V1. *J Neurophysiol*, 90(May 2003), 1910–1920.

[142] Kirst, C., Timme, M., & Battaglia, D. (2016). Dynamic information routing in complex networks. *Nature Communications*, 7(6), 11061.

[143] Koepsell, K. & Sommer, F. T. (2008). Information transmission in oscillatory neural activity. *Biological Cybernetics*, 99(4-5), 403–416.

[144] Kopell, N. & LeMasson, G. (1994). Rhythmogenesis, amplitude modulation, and multiplexing in a cortical architecture. *Proc Natl Acad Sci U S A*, 91(22), 10586–10590.

[145] Kreiter, A. K. & Singer, W. (1996a). Stimulus-Dependent Synchronization of Neuronal Responses in the Visual Cortex of the Awake Macaque Monkey. *Journal of Neuroscience*, 16(7), 2381–2396.

[146] Kreiter, A. K. & Singer, W. (1996b). Stimulus-Dependent Synchronization of Neuronal Responses in the Visual Cortex of the Awake Macaque Monkey. *Journal of Neuroscience*, 16(7), 2381–2396.

[147] Kumar, A., Rotter, S., & Aertsen, A. (2008). Conditions for propagating synchronous spiking and asynchronous firing rates in a cortical network model. *The Journal of neuroscience : the official journal of the Society for Neuroscience*, 28(20), 5268–80.

[148] Kuptsov, P. V. & Parlitz, U. (2012). Theory and computation of covariant lyapunov vectors. *Journal of Nonlinear Science*, 22(5), 727–762.

[149] Kuramoto, Y. (1981). Rhythms and turbulence in populations of chemical oscillators. *Physica A: Statistical Mechanics and its Applications*, 106(1-2), 128–143.

[150] Kuramoto, Y. (1983). *Chemical Oscillations, Waves and Turbulence.* Springer.

[151] Lachaux, J. P., Rodriguez, E., Martinerie, J., & Varela, F. J. (1999). Measuring phase-synchrony in brain signals. *Human Brain Mapp.*, 8, 194–208.

[152] Lajoie, G., Lin, K. K., & Shea-Brown, E. (2013). Chaos and reliability in balanced spiking networks with temporal drive. *Physical Review E - Statistical, Nonlinear, and Soft Matter Physics*, 87(5), 1–15.

[153] Le Berre, M., Ressayre, E., Tallet, A., & Gibbs, H. M. (1986). High-dimension chaotic attractors of a nonlinear ring cavity. *Physical Review Letters*, 56(4), 274–277.

[154] Le Berre, M., Ressayre, E., Tallet, A., Gibbs, H. M., Kaplan, D. L., & Rose, M. H. (1987). Conjecture on the dimensions of chaotic attractors of delayed-feedback dynamical systems. *Physical Review A*, 35(9), 4020–4022.

[155] Lepri, S., Giacomelli, G., Politi, A., & Arecchi, F. T. (1994). High-dimensional chaos in delayed dynamical systems. *Physica D: Nonlinear Phenomena*, 70(3), 235–249.

[156] Liedtke, J. (2013). Master ' s Thesis Geometrie und Organization von stabilen und instabilen Mannigfaltigkeiten in balancierten Netzwerken Geometry and organization of stable and unstable manifold in balanced networks. *Master Thesis*, (April).

[157] Lima, B., Singer, W., Chen, N. H., & Neuenschwander, S. (2010). Synchronization dynamics in response to plaid stimuli in monkey V1. *Cerebral Cortex*, 20(7), 1556–1573.

[158] Lisman, J. (2010). Working memory: The importance of theta and gamma oscillations. *Current Biology*, 20(11), R490–R492.

[159] Lisman, J. E. & Idiart, M. A. (1995). Storage of 7 +/- 2 short-term memories in oscillatory subcycles.

[160] London, M., Roth, A., Beeren, L., Häusser, M., & Latham, P. E. (2010). Sensitivity to perturbations in vivo implies high noise and suggests rate coding in cortex. *Nature*, 466(7302), 123–7.

[161] Luccioli, S., Olmi, S., Politi, A., & Torcini, A. (2012). Collective dynamics in sparse networks. *Physical Review Letters*, 109(13), 1–5.

[162] Lungarella, M., Pitti, A., & Kuniyoshi, Y. (2007). Information transfer at multiple scales. *Physical Review E - Statistical, Nonlinear, and Soft Matter Physics*, 76(5), 1–10.

[163] Mackey, M. C. & Glass, L. (1977). Oscillation and chaos in physiological control systems. *Science (New York, N.Y.)*, 197(4300), 287–9.

[164] Mainen, Z. F. & Sejnowski, T. J. (1995). Reliability of spike timing in neocortical neurons. *Science (New York, N.Y.)*, 268(5216), 1503–1506.

[165] Maris, E., Fries, P., & van Ede, F. (2016). Diverse Phase Relations among Neuronal Rhythms and Their Potential Function. *Trends in Neurosciences*, 39(2), 86–99.

[166] Markov, N. T., Ercsey-Ravasz, M., Lamy, C., Ribeiro Gomes, A. R., Magrou, L., Misery, P., Giroud, P., Barone, P., Dehay, C., Toroczkai, Z., Knoblauch, K., Van Essen, D. C., & Kennedy, H. (2013). The role of long-range connections on the specificity of the macaque interareal cortical network. *Proceedings of the National Academy of Sciences*, 110(13), 5187–5192.

[167] Markov, N. T., Ercsey-Ravasz, M. M., Ribeiro Gomes, A. R., Lamy, C., Magrou, L., Vezoli, J., Misery, P., Falchier, A., Quilodran, R., Gariel, M. A., Sallet, J., Gamanut, R., Huissoud, C., Clavagnier, S., Giroud, P., Sappey-Marinier, D., Barone, P., Dehay, C., Toroczkai, Z., Knoblauch, K., Van Essen, D. C., & Kennedy, H. (2014). A weighted and directed interareal connectivity matrix for macaque cerebral cortex. *Cerebral Cortex*, 24(1), 17–36.

[168] Marshall, L., Helgadóttir, H., Mölle, M., & Born, J. (2006). Boosting slow oscillations during sleep potentiates memory. *Nature*, 444(7119), 610–613.

[169] Massimo, C., Fabio, C., & Vulpiani, A. (2010). *Chaos from simple models to complex systems*. World Scientific Publishing Co.

[170] Mastrogiuseppe, F. & Ostojic, S. (2016). Intrinsically-generated fluctuating activity in excitatory-inhibitory networks. *arXiv*, (pp. 1–33).

[171] Mazzoni, A., Panzeri, S., Logothetis, N. K., & Brunel, N. (2008). Encoding of naturalistic stimuli by local field potential spectra in networks of excitatory and inhibitory neurons. *PLoS Computational Biology*, 4(12), e1000239.

[172] Mirollo, R. E. & Strogatz, S. H. (1990). Synchronization of pulse-coupled biological oscillators. *SIAM Journal on Applied Mathematics*, 50(6), 1645–1662.

[173] Monteforte, M. (2011). Chaotic Dynamics in Networks of Spiking Neurons in the Balanced State. *PhD Thesis*.

[174] Monteforte, M. & Wolf, F. (2010). Dynamical entropy production in spiking neuron networks in the balanced state. *Physical Review Letters*, 105(26), 268104.

[175] Monteforte, M. & Wolf, F. (2012). Dynamic flux tubes form reservoirs of stability in neuronal circuits. *Physical Review X*, 2(4), 041007.

[176] Moran, J. & Desimone, R. (1985). Selective attention gates visual processing in the extrastriate cortex. *Science (New York, N.Y.)*, 229(4715), 782–784.

[177] Motter, B. C. (1993). Focal attention produces spatially selective processing in visual cortical areas V1, V2, and V4 in the presence of competing stimuli. *Journal of neurophysiology*, 70(3), 909–919.

[178] Naundorf, B., Geisel, T., & Wolf, F. (2005). Action potential onset dynamics and the response speed of neuronal populations. *Journal of Computational Neuroscience*, 18(3), 297–309.

[179] Naundorf, B., Wolf, F., & Volgushev, M. (2006). Unique features of action potential initiation in cortical neurons. *Nature*, 440(7087), 1060–3.

[180] Naundorf, B., Wolf, F., & Volgushev, M. (2007). Neurophysiology: Hodgkin and Huxley model - still standing? (Reply). *Nature*, 445(7123), E2–E3.

[181] Neltner, L., Hansel, D., Mato, G., & Meunier, C. (2000). Synchrony in heterogeneous networks of spiking neurons. *Neural computation*, 12(7), 1607–1641.

[182] Niebur, E. & Koch, C. (1994). A model for the neuronal implementation of selective visual attention based on temporal correlation among neurons. *Journal of Computational Neuroscience*, 1(1-2), 141–158.

[183] Nischwitz, A. & Glunder, H. (1995). Local lateral inhibition: a key to spike synchronization? *Biological Cybernetics*, 73(5), 389–400.

[184] O'Keefe, J. & Recce, M. L. (1993). Phase relationship between hippocampal place units and the EEG theta rhythm. *Hippocampus*, 3(3), 317–330.

[185] Okun, M. & Lampl, I. (2008). Instantaneous correlation of excitation and inhibition during ongoing and sensory-evoked activities. *Nature neuroscience*, 11(5), 535–7.

[186] Okun, M., Steinmetz, N. a., Cossell, L., Iacaruso, M. F., Ko, H., Barthó, P., Moore, T., Hofer, S. B., Mrsic-Flogel, T. D., Carandini, M., & Harris, K. D. (2015). Diverse coupling of neurons to populations in sensory cortex. *Nature*, 521(7553), 511–515.

[187] Olmi, S., Livi, R., Politi, A., & Torcini, A. (2010). Collective oscillations in disordered neural networks. *Physical Review E - Statistical, Nonlinear, and Soft Matter Physics*, 81(4), 1–7.

[188] Olshausen, B. a., Anderson, C. H., & Van Essen, D. C. (1993). A neurobiological model of visual attention and invariant pattern recognition based on dynamic routing of information. *The Journal of neuroscience*, 13(11), 4700–19.

[189] Osborne, L. C., Palmer, S. E., Lisberger, S. G., & Bialek, W. (2008). The Neural Basis for Combinatorial Coding in a Cortical Population Response. *Journal of Neuroscience*, 28(50), 13522–13531.

[190] Oseledets, V. (2008). Oseledets theorem. *Scholarpedia*, 3(1), 1846.

[191] Ott, E. & Antonsen, T. M. (2008). Low dimensional behavior of large systems of globally coupled oscillators. *Chaos*, 18(3), 1–6.

[192] Pesaran, B., Pezaris, J. S., Sahani, M., Mitra, P. P., & Andersen, R. a. (2002). Temporal structure in neuronal activity during working memory in macaque parietal cortex. *Nature neuroscience*, 5(8), 805–811.

[193] Peters, A. (1987). Number of neurons and synapses in primary visual cortex. *Cerebral Cortex*, 6 Further, 267–294.

[194] Pikovsky, A., Rosenblum, M., & Kurths, J. (2003). Synchronization: A Universal Concept in Nonlinear Sciences. *Cambridge Nonlinear Science Series 12*, (pp. 432).

[195] Popescu, A. T., Popa, D., & Paré, D. (2009). Coherent gamma oscillations couple the amygdala and striatum during learning. *Nature neuroscience*, 12(6), 801–7.

[196] Popovych, O. V., Maistrenko, Y. L., & Tass, P. A. (2005). Phase chaos in coupled oscillators. *Physical Review E - Statistical, Nonlinear, and Soft Matter Physics*, 71(6), 3–6.

[197] Press, W., Teukolsky, S., Vetterling, W., Flannery, B., Ziegel, E., Press, W., Flannery, B., Teukolsky, S., & Vetterling, W. (1987). *Numerical Recipes: The Art of Scientific Computing*, volume 29. Cambridge University Press 1988,.

[198] Pritchett, D. L., Siegle, J. H., Deister, C. A., & Moore, C. I. (2015). For things needing your attention: The role of neocortical gamma in sensory perception. *Current Opinion in Neurobiology*, 31(July 2016), 254–263.

[199] Puelma Touzel, M. (2014). Cellular dynamics and stable chaos in balanced networks Dissertation for the award of the degreee Submitted by Maximilian Puelma Touzel. *PhD Thesis.*

[200] Raghavachari, S., Kahana, M. J., Rizzuto, D. S., Caplan, J. B., Kirschen, M. P., Bourgeois, B., Madsen, J. R., & Lisman, J. E. (2001). Gating of human theta oscillations by a working memory task. *The Journal of neuroscience : the official journal of the Society for Neuroscience*, 21(9), 3175–3183.

[201] Raghunathan, M. S. (1979). A proof of Oseledec's multiplicative ergodic theorem. *Israel Journal of Mathematics*, 32(4), 356–362.

[202] Rajan, K., Abbott, L., & Sompolinsky, H. (2010). Stimulus-dependent suppression of chaos in recurrent neural networks. *Physical Review E - Statistical, Nonlinear, and Soft Matter Physics*, 82(1), 1–5.

[203] Ray, S. & Maunsell, J. H. R. (2010). Differences in Gamma Frequencies across Visual Cortex Restrict Their Possible Use in Computation. *Neuron*, 67(5), 885–896.

[204] Ray, S. & Maunsell, J. H. R. (2011). Different origins of gamma rhythm and high-gamma activity in macaque visual cortex. *PLoS Biology*, 9(4), e1000610.

[205] Ray, S. & Maunsell, J. H. R. (2015). Do gamma oscillations play a role in cerebral cortex? *Trends in Cognitive Sciences*, 19(2), 78–85.

[206] Renart, A., de la Rocha, J., Bartho, P., Hollender, L., Parga, N., Reyes, A. D., & Harris, K. D. (2010). The asynchronous state in cortical circuits. *Science (New York, N.Y.)*, 327(5965), 587–90.

[207] Renart, A., Moreno-Bote, R., Wang, X.-j., & Parga, N. (2007). Mean-Driven and Fluctuation-Driven Persistent Activity in Recurrent Networks. *Neural Computation*, 19(1), 1–46.

[208] Richardson, M. J. E. (2007). Firing-rate response of linear and nonlinear integrate-and-fire neurons to modulated current-based and conductance-based synaptic drive. *Physical Review E - Statistical, Nonlinear, and Soft Matter Physics*, 76(2), 1–15.

[209] Roberts, M. J., Lowet, E., Brunet, N. M., TerWal, M., Tiesinga, P., Fries, P., & DeWeerd, P. (2013). Robust gamma coherence between macaque V1 and V2 by dynamic frequency matching.

[210] Rodriguez, E., George, N., Lachaux, J. P., Martinerie, J., Renault, B., & Varela, F. J. (1999). Perception's shadow: long-distance synchronization of human brain activity. *Nature*, 397(6718), 430–433.

[211] Roxin, A., Brunel, N., & Hansel, D. (2005). Role of delays in shaping spatiotemporal dynamics of neuronal activity in large networks. *Physical Review Letters*, 94(23), 1–4.

[212] Ruelle, D. (1982). The obsessions of time. *Communications in Mathematical Physics*, 85(1), 3–5.

[213] Saalmann, Y. B., Pigarev, I. N., & Vidyasagar, T. R. (2007). Neural Mechanisms of Visual Attention: How Top-Down Feedback Highlights Relevant Locations. *Science*, 316(5831), 1612–1615.

[214] Saalmann, Y. B., Pinsk, M. a., Wang, L., Li, X., & Kastner, S. (2012). The Pulvinar Regulates Information Transmission Between Cortical Areas Based on Attention Demands.pdf. *Science (New York, N.Y.)*, 337(6095), 753–6.

[215] Salazar, R. F., Dotson, N. M., Bressler, S. L., & Gray, C. M. (2012). Content-Specific Fronto-Parietal Synchronization During Visual Working Memory. *Science*, 338(6110), 1097–1100.

[216] Salinas, E. & Sejnowski, T. J. (2001). Correlated neuronal activity and the flow of neural information. *Nature reviews. Neuroscience*, 2(8), 539–50.

[217] Schaumlöffel, K.-U. (1991). Multiplicative Ergodic Theorems in Infinite Dimensions. *Lyapunov Exponents, Proceedings of a Conference held in Oberwolfach, May 28 - June 2, 1990*, 1486, 187–195.

[218] Schmolesky, M. T., Wang, Y., Hanes, D. P., Thompson, K. G., Leutgeb, S., Schall, J. D., & Leventhal, a. G. (1998). Signal timing across the macaque visual system. *Journal of neurophysiology*, 79(6), 3272–8.

[219] Schneidman, E., Berry, M. M. J., Segev, R., & Bialek, W. (2006). Weak pairwise correlations imply strongly correlated network states in a neural population. *Nature*, 440(7087), 1007–1012.

[220] Schoffelen, J.-M. (2005). Neuronal Coherence as a Mechanism of Effective Corticospinal Interaction. *Science*, 308(5718), 111–113.

[221] Schreiber, T. (2000). Measuring information transfer. *Physical Review Letters*, 85(2), 461–464.

[222] Schuster, H. G. & Just, W. (2005). *Deterministic Chaos*. WILEY-VCH Verlag GmbH & Co.

[223] Shadlen, M. N. & Newsome, W. T. (1994). Noise, neural codes and cortical organization. *Current Opinion in Neurobiology*, 4(4), 569–579.

[224] Shadlen, M. N. & Newsome, W. T. (1998). The variable discharge of cortical neurons: implications for connectivity, computation, and information coding. *The Journal of neuroscience : the official journal of the Society for Neuroscience*, 18(10), 3870–96.

[225] Shaw, R. (1981a). Strange attractors, chaotic behavior, and information flow.

[226] Shaw, R. (1981b). Strange Attractors, Chaotic Behavior, and Information Flow. *Zeitschrift für Naturforschung A*, 36(1), 80–112.

[227] Shu, Y., Hasenstaub, A., & McCormick, D. A. (2003). Turning on and off recurrent balanced cortical activity. *Nature*, 423(May), 288–293.

[228] Siegle, J. H., Pritchett, D. L., & Moore, C. I. (2014). Gamma-range synchronization of fast-spiking interneurons can enhance detection of tactile stimuli. *Nature Neuroscience*, 17(August), 1371–1379.

[229] Skaggs, W. E. & McNaughton, B. L. (1996). Replay of neuronal firing sequences in rat hippocampus during sleep following spatial experience. *Science (New York, N.Y.)*, 271(5257), 1870–1873.

[230] So, P., Luke, T. B., & Barreto, E. (2014). Networks of theta neurons with time-varying excitability: Macroscopic chaos, multistability, and final-state uncertainty. *Physica D: Nonlinear Phenomena*, 267, 16–26.

[231] Softky, W. R. & Koch, C. (1993). The highly irregular firing of cortical cells is inconsistent with temporal integration of random EPSPs. *The Journal of neuroscience : the official journal of the Society for Neuroscience*, 13(1), 334–50.

[232] Sohal, V. S., Zhang, F., Yizhar, O., & Deisseroth, K. (2009). Parvalbumin neurons and gamma rhythms enhance cortical circuit performance. *Nature*, 459(7247), 698–702.

[233] Sommers, H. J., Crisanti, A., Sompolinsky, H., & Stein, Y. (1988). Spectrum of large random asymmetric matrices. *Physical Review Letters*, 60(19), 1895–1898.

[234] Sompolinsky, H., Crisanti, A., & Sommers, H. J. (1988). Chaos in random neural networks. *Physical Review Letters*, 61(3), 259–262.

[235] Stefanski, A., Dabrowski, A., & Kapitaniak, T. (2005). Evaluation of the largest Lyapunov exponent in dynamical systems with time delay. *Chaos, Solitons & Fractals*, 23(5), 1651–1659.

[236] Steinmetz, P. N., Roy, a., Fitzgerald, P. J., Hsiao, S. S., Johnson, K. O., & Niebur, E. (2000). Attention modulates synchronized neuronal firing in primate somatosensory cortex. *Nature*, 404(6774), 187–190.

[237] Stetter, O., Battaglia, D., Soriano, J., & Geisel, T. (2012). Model-Free Reconstruction of Excitatory Neuronal Connectivity from Calcium Imaging Signals. *PLoS Computational Biology*, 8(8), e1002653.

[238] Stevens, C. F. & Zador, a. M. (1998). Input synchrony and the irregular firing of cortical neurons. *Nature neuroscience*, 1(3), 210–7.

[239] Stickgold, R. (2005). Sleep-dependent memory consolidation. *Nature*, 437(7063), 1272–1278.

[240] Stopfer, M., Bhagavan, S., Smith, B. H., & Laurent, G. (1997). Impaired odour discrimination on desynchronization of odour-encoding neural assemblies. *Nature*, 390(6655), 70–74.

[241] Strogatz, S. H. (2000). From Kuramoto to Crawford: exploring the onset of synchronization in populations of coupled oscillators. *Physica D: Nonlinear Phenomena*, 143(1-4), 1–20.

[242] Strong, S., Koberle, R., de Ruyter Van Steveninck, R., & Bialek, W. (1998). Entropy and Information in Neural Spike Trains. *Physical Review Letters*, 80(1), 197–200.

[243] Taylor, K., Mandon, S., Freiwald, W. A., & Kreiter, A. K. (2005). Coherent oscillatory activity in monkey area v4 predicts successful allocation of attention. *Cerebral Cortex*, 15(9), 1424–1437.

[244] ter Wal, M. & Tiesinga, P. (2013). Hippocampal Oscillations (PING, ING, sparse) - Encyclopedia of Computational Neuroscience.

[245] Thiele, A. & Stoner, G. (2003). Neuronal synchrony does not correlate with motion coherence in cortical area MT. *Nature*, 421(January), 366–370.

[246] Thomson (1999). Visual coding and the phase structure of natural scenes. *Network*, 10(2), 123–32.

[247] Tiesinga, P. & Sejnowski, T. J. (2009). Cortical Enlightenment: Are Attentional Gamma Oscillations Driven by ING or PING? *Neuron*, 63(6), 727–732.

[248] Tiesinga, P. P. H. & Sejnowski, T. J. (2010). Mechanisms for phase shifting in cortical networks and their role in communication through coherence. *Papers.Cnl.Salk.Edu*, 4(November), 1–14.

[249] Timme, M. & Wolf, F. (2008). The simplest problem in the collective dynamics of neural networks: is synchrony stable? *Nonlinearity*, 21(7), 1579–1599.

[250] Timme, M., Wolf, F., & Geisel, T. (2002a). Coexistence of regular and irregular dynamics in complex networks of pulse-coupled oscillators. *Physical review letters*, 89(25), 258701.

[251] Timme, M., Wolf, F., & Geisel, T. (2002b). Prevalence of Unstable Attractors in Networks of Pulse-Coupled Oscillators. *Physical Review Letters*, 89(15), 154105.

[252] Timme, M., Wolf, F., & Geisel, T. (2004). Topological Speed Limits to Network Synchronization. *Physical Review Letters*, 92(7), 074101.

[253] Traub, R. D., Miles, R., & Wong, R. K. (1989). Model of the origin of rhythmic population oscillations in the hippocampal slice. *Science*, 243(4896), 1319–1325.

[254] Treue, S. & Maunsell, J. H. R. (1996). Attentional modulation of visual motion processing in cortical areas MT and MST.

[255] Troyer, T. W. & Miller, K. D. (1997). Physiological gain leads to high ISI variability in a simple model of a cortical regular spiking cell. *Neural computation*, 9(5), 971–983.

[256] Tsodyks, M., Mitkov, I., & Sompolinsky, H. (1993). Pattern of synchrony in inhomogeneous networks of oscillators with pulse interactions.

[257] Tsodyks, M. & Sejnowski, T. (1995). Rapid state switching in balanced cortical network models. *Network: Computation in Neural Systems*, 6(2), 111–124.

[258] Uhlhaas, P. J. & Singer, W. (2012). Neuronal Dynamics and Neuropsychiatric Disorders: Toward a Translational Paradigm for Dysfunctional Large-Scale Networks. *Neuron*, 75(6), 963–980.

[259] Usrey, W. M., Alonso, J.-M., & Reid, R. C. (2000). Synaptic interactions between thalamic inputs to simple cells in cat visual cortex. *The Journal of neuroscience : the official journal of the Society for Neuroscience*, 20(14), 5461–5467.

[260] Vakorin, V. A., Krakovska, O. A., & McIntosh, A. R. (2009). Confounding effects of indirect connections on causality estimation. *Journal of Neuroscience Methods*, 184(1), 152–160.

[261] van Kerkoerle, T., Self, M. W., Dagnino, B., Gariel-Mathis, M.-A., Poort, J., van der Togt, C., & Roelfsema, P. R. (2014). Alpha and gamma oscillations characterize feedback and feedforward processing in monkey visual cortex. *Proceedings of the National Academy of Sciences*, 111(40), 14332–41.

[262] van Vreeswijk, C. (1996). Partial synchronization in populations of pulse-coupled oscillators. *Physical Review E*, 54(5), 5522–5537.

[263] Van Vreeswijk, C., Abbott, L., & Bard Ermentrout, G. (1994). When inhibition not excitation synchronizes neural firing. *Journal of Computational Neuroscience*, 1(4), 313–321.

[264] van Vreeswijk, C. & Sompolinsky, H. (1996). Chaos in neuronal networks with balanced excitatory and inhibitory activity. *Science (New York, N.Y.)*, 274(5293), 1724–6.

[265] van Vreeswijk, C. & Sompolinsky, H. (1998a). Chaotic balanced state in a model of cortical circuits. *Neural Comput*, 10(6), 1321–1371.

[266] van Vreeswijk, C. & Sompolinsky, H. (1998b). Chaotic balanced state in a model of cortical circuits. *Neural computation*, 10(6), 1321–71.

[267] Varela, F., Lachaux, J. P., Rodriguez, E., & Martinerie, J. (2001). The brainweb: phase synchronization and large-scale integration. *Nature reviews. Neuroscience*, 2(4), 229–239.

[268] Vicente, R., Wibral, M., Lindner, M., & Pipa, G. (2011). Transfer entropy-a model-free measure of effective connectivity for the neurosciences. *Journal of Computational Neuroscience*, 30(1), 45–67.

[269] Vinck, M., Lima, B., Womelsdorf, T., Oostenveld, R., Singer, W., Neuenschwander, S., & Fries, P. (2010). Gamma-Phase Shifting in Awake Monkey Visual Cortex. *Journal of Neuroscience*, 30(4), 1250–1257.

[270] Vinck, M., Womelsdorf, T., Buffalo, E. A., Desimone, R., & Fries, P. (2013). Attentional Modulation of Cell-Class-Specific Gamma-Band Synchronization in Awake Monkey Area V4. *Neuron*, 80(4), 1077–1089.

[271] Vogels, T. P. & Abbott, L. (2005). Signal Propagation and Logic Gating in Networks of Integrate-and-Fire Neurons. *The Journal of Neuroscience*, 25(46), 10786–10795.

[272] Vogels, T. P. & Abbott, L. (2007). Gating deficits in model networks: A path to schizophrenia? *Pharmacopsychiatry*, 40(SUPPL. 1), S73–7.

[273] Vogels, T. P. & Abbott, L. (2009). Gating multiple signals through detailed balance of excitation and inhibition in spiking networks. *Nature neuroscience*, 12(4), 483–91.

[274] Wang, X.-J. (2010). Neurophysiological and Computational Principles of Cortical Rhythms in Cognition. *Physiological Reviews*, 90(3), 1195–1268.

[275] White, J. A., Chow, C. C., Ritt, J., Soto-Trevino, C., & Kopell, N. (1998). Synchronization and oscillatory dynamics in heterogeneous, mutually inhibited neurons. *Journal of Computational Neuroscience*, 5(1), 5–16.

[276] Whittington, M. A., Cunningham, M. O., LeBeau, F. E. N., Racca, C., & Traub, R. D. (2011). Multiple origins of the cortical gamma rhythm. *Developmental Neurobiology*, 71(1), 92–106.

[277] Whittington, M. A., Traub, R. D., & Jefferys, J. G. (1995). Synchronized oscillations in interneuron networks driven by metabotropic glutamate receptor activation. *Nature*, 373(6515), 612–615.

[278] Whittington, M. A., Traub, R. D., Kopell, N., Ermentrout, B., & Buhl, E. H. (2000). Inhibition-based rhythms: Experimental and mathematical observations on network dynamics. *International Journal of Psychophysiology*, 38(3), 315–336.

[279] Wibral, M., Vicente, R., & Lizier, J. T. (2014). *Directed Information Measures in Neuroscience*. Springer Complexity.

[280] Wilson, M. A. & McNaughton, B. L. (1994). Reactivation of hippocampal ensemble memories during sleep. *Science (New York, N.Y.)*, 265(5172), 676–9.

[281] Winfree, a. T. (1967). Biological rhythms and the behavior of populations of coupled oscillators. *Journal of theoretical biology*, 16(1), 15–42.

[282] Witt, A., Palmigiano, A., Neef, A., Hady, A. E., Wolf, F., & Battaglia, D. (2013). Controlling the oscillation phase through precisely timed closed-loop optogenetic stimulation: a computational study. *Frontiers in Neural Circuits*, 7(April), 49.

[283] Womelsdorf, T. & Fries, P. (2007). The role of neuronal synchronization in selective attention. *Current Opinion in Neurobiology*, 17(2), 154–160.

[284] Womelsdorf, T., Fries, P., Mitra, P. P., & Desimone, R. (2006). Gamma-band synchronization in visual cortex predicts speed of change detection. *Nature*, 439(7077), 733–736.

[285] Xiao-Jing Wang & György Buzsáki (1996). Gamma Oscillation by Synaptic Inhibition in a Hippocampal Interneuronal Network Model. *The Journal of Neuroscience*, 16(20), 6402–6413.

[286] Xing, D., Shen, Y., Burns, S., Yeh, C.-I., Shapley, R., & Li, W. (2012). Stochastic Generation of Gamma-Band Activity in Primary Visual Cortex of Awake and Anesthetized Monkeys. *Journal of Neuroscience*, 32(40), 13873–13880.

[287] Yamamoto, J., Suh, J., Takeuchi, D., & Tonegawa, S. (2014). Successful execution of working memory linked to synchronized high-frequency gamma oscillations. *Cell*, 157(4), 845–857.

[288] Yeung, M. & Strogatz, S. (1999). Time Delay in the Kuramoto Model of Coupled Oscillators. *Physical Review Letters*, 82(3), 648–651.

[289] Yuste, R. (2015). From the neuron doctrine to neural networks. *Nature Reviews Neuroscience*, 16(8), 487–497.

[290] Zhou, H. & Desimone, R. (2011). Feature-Based Attention in the Frontal Eye Field and Area V4 during Visual Search. *Neuron*, 70(6), 1205–1217.

[291] Zhou, H., Schafer, R. J., & Desimone, R. (2016). Pulvinar-Cortex Interactions in Vision and Attention. *Neuron*, 89(1), 209–220.

[292] Zylberberg, A., Slezak, D. F., Roelfsema, P. R., Dehaene, S., & Sigman, M. (2010). The brain's router: A cortical network model of serial processing in the primate brain. *PLoS Computational Biology*, 6(4), e1000765.

Glossary

AMPA -amino-3-hydroxy-5-methyl-4-isoxazolepropionic acid, a glutamate receptor mediating fast synaptic transmission. 24, 25

CA3 Cornus ammonis 3 of the hippocampus. 28

CTC Communication through coherence. 12, 14, 15

EEG Electroencephalogram. 16

EI Excitatory Inhibitory networks.. 122, 124

eLIF Exponential integrate and fire. 20, 24

FEF Frontal eye fields. 13, 18

FS Fast spiking. 15

GABA$_{\mathrm{A}}$ gamma-Aminobutyric acid. 24, 25

ING Interneuron network gamma oscillation . 24–26, 59

IT Inferior temporal cortex. 14

LFP Local field potential. 11, 14–18, 28, 35–39, 41, 43–47, 49, 50, 53, 59, 61–64, 67, 69, 70, 76

LIF Leaky integrate and fire neuron model. 19–24, 29, 30, 80, 91, 92, 109, 110, 122, 124–127, 131, 138, 139

LIP Lateral intra-parietal cortex. 13

MSD Mean squared deviation. . 111, 112

MT Middle temporal area. 10, 13

MUA Multi-Unit Activity. 59, 101, 110, 111, 113, 119–128

PING Pyramidal-interneuron network gamma oscillation . 24–26, 59

PRC Phase Response Curve. 104

QIF Quadratic integrate and fire neuron model. 22, 30, 80, 93–97, 109–115, 118–121, 123–125, 127–130, 137–140

RF Receptive field. 9–11

rQIF ”Rapid” QIF, i.e. QIF with tunable onset rapidness.. 93, 94, 125–129, 131, 138, 139

SCA Single Compartment Axon. 80, 90, 98, 103–105, 116, 130

SI Synchronous irregular state. 23–25, 110–112, 125, 127, 128, 130, 131, 137

TEO Inferior temporal cortical area TEO. 14

V1 Primary visual cortex (striate). 12, 14, 16–18

V2 Visual area V2 (pre-striate). 10, 12, 14, 18

V4 Visual area V4 (extra-striate). 10–14, 18

WB Wang-Buzsáki neuron model. 22